Quantum Modelling of Ruthenium Chemistry in the field of Nuclear Power Plant Safety

A DISSERTATION SUBMITTED TO THE UNIVERSITÉ LILLE 1 BY

FAOULAT MIRADJI

IN ACCORDANCE WITH THE REQUIREMENTS OF THE DEGREE OF

DOCTOR OF PHILOSOPHY

DOCTORAL SCHOOL:

SCIENCES DE LA MATIÈRE, DU RAYONNEMENT ET DE L'ENVIRONNEMENT

FIELD:

OPTIQUE ET LASERS, PHYSICO-CHIMIE, ATMOSPHÈRE

DEFENDED ON DECEMBER 5TH 2016 IN FRONT OF JURY MEMBERS:

Pr. Gérard Cote	Chimie ParisTech -CNRS	President
Pr. Denis Jacquemin	Université de Nantes -CEISAM	Reviewer
Dr. Manuel Ruiz-Lopez	University of Lorraine - SRSMC	Reviewer
Dr. Florent Louis	Université de Lille 1 -PC2A	Director thesis
Dr. Valérie Vallet	Université de Lille 1 - PhLAM	Director thesis
Dr. Sidi Souvi	IRSN-PSN-RES/SAG/LETR	Supervisor
Dr. Laurent Cantrel	IRSN-PSN-RES/SEREX/L2EC	Supervisor

ABSTRACT

During a severe accident (SA) occurring to a pressurized water reactor (PWR), fission products (FPs) are released from the nuclear fuel and may reach the nuclear containment building. Among the FPs, ruthenium (Ru) is of particular interest due to its ability to form volatile oxide compounds in highly oxidizing conditions combined with its high radiotoxicity ([103]Ru and [106]Ru isotopes) at middle term after the accident. Uncertainties concerning evaluation releases of Ru are important and some R&D efforts are led to get a better understanding of ruthenium chemistry in such conditions. The thermodynamic database on ruthenium species used to estimate these releases shows some discrepancies for most ruthenium oxides and for other species such as oxyhydroxides, data are scarce and not reliable, calling for quantum chemical calculations. The most suitable approach corresponds to TPSSh-5%HF for geometry optimization, followed by CCSD(T) for the calculation of the total electronic energies. The energetics are combined with statistical physics to obtain the thermochemical properties of ruthenium oxides and ruthenium oxyhydroxide species as the latter may play an important role on the transport of ruthenium in the primary circuit due to high steam content. The revised thermodynamic database is then used to predict which species are most stable in representative severe accident conditions. Next, kinetic calculations are also performed to obtain pathways of formations for ruthenium trioxide and tetraoxide gaseous compounds, which are the most stable Ru volatile species in steam/air atmospheres.

RÉSUMÉ

Lors d'un Accident Grave (AG) survenant à un réacteur nucléaire à eau pressurisée, sous atmosphère fortement oxydante, des relâchements importants de ruthénium, depuis le combustible dégradé, sont attendus du fait de la formation d'oxydes gazeux. Les composés de Ru représentent un risque sanitaire lié aux isotopes ^{103}Ru et ^{106}Ru, radio-contaminants à court et moyen terme. En outre l'oxyde RuO_4, volatil à température ambiante, est susceptible d'être relâché à l'environnement via les fuites de l'enceinte de confinement. L'évaluation de ce rejet à l'environnement présente des incertitudes importantes, liées entre autres aux données thermochimiques des composés de ruthénium gazeux avec des disparités entre les valeurs de la littérature pour les oxydes. Concernant les oxyhydroxydes, les données sont trés parcellaires et celles disponibles sont sujettes à caution. Une première étape de ces travaux de thèse a consisté au développement d'une méthodologie de calcul pour obtenir les données thermochimiques des oxydes de ruthénium gazeux en fonction de la température, via des outils de chimie quantique, avec la fonctionnelle TPSSh-5%HF pour l'optimisation de géométrie, suivi de la méthode CCSD(T) pour le calcul des énergies électroniques. Cette méthodologie fut ensuite étendue aux oxyhydroxydes. Des calculs de spéciation chimique ont été effectués afin de prédire les espèces gazeuses les plus stables lors d'un AG. A l'aide des propriétés thermochimiques des espèces d'intérêts et des méthodologies développées, une étude cinétique a été conduite afin de déterminer les chemins réactionnels conduisant à la formation d'oxydes de Ru, espèces gazeuses les plus stables en conditions AG.

Contents

The global average temperature curve, which followed the natural curve of the sun's activity until the 1970's, is now completely uncorrelated thereof upwards and its slope is impressive, as illustrated in Fig. 1.1.

Global Surface Temperature
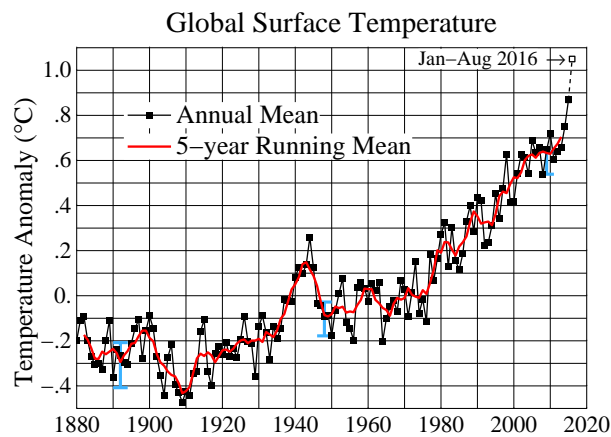
Figure 1.1: Average global surface temperatures since 1880.[1]

One of the main identified reasons for climate change is the production of greenhouse gases, such as nitrous oxide, fluorinated gases, and the well-known carbon dioxide. The latter is identified to be highly emitted through electricity production means, as modern society development and growth is mostly driven by this one. Thus the energy sources which can prevent CO_2 emissions should be chosen. Nuclear energy appears as reliable and very

1

efficient. Indeed, we can compare CO_2 emissions and electricity cost from several means of production [2, 3] :

► 9 g/kV/h and 24.1 €/MWh for nuclear power plant (NPP)

► 960 g/kV/h and 32.1€/MWh for coal

► 460 g/kV/h and 30.5 €/MWh for gas

► 11 g/kV/h and 50.1€/MWh for wind

It is shown that nuclear energy has the lowest cycle release of CO_2 emissions and electricity cost. However, some drawbacks are associated with the use of nuclear power plants, namely the storage of the radioactive waste remaining after the utilisation of the fuel and nuclear accidents which can lead to the release of artificial radioactivity into the environment. The radiological consequences of such an accident are influenced by its severity, which is classified into 7 levels by the International Nuclear Events Scale (INES) [4], according to the International Atomic Energy Agency (IAEA). Two accidents were classified as the highest level, the accidents of Chernobyl in 1986 and Fukushima-Daiichi in 2011. The following section gives details concerning phenomena leading to such severe nuclear power plant accident.

1.1   Nuclear Power Plant Severe Accident

In normal operations, fissions of fuel result in the accumulation of radionuclides called Fissions Products (FPs). The prevention of contamination is ensured by three barriers leading to the decrease of FPs release into the environment, as schematically represented in Figure 1.2.
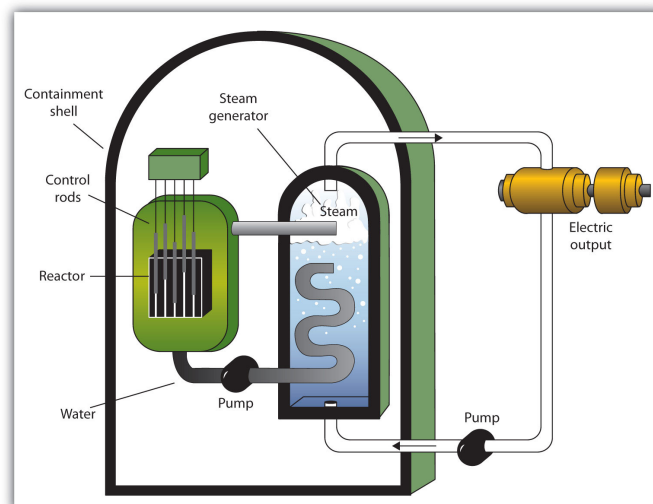
Figure 1.2: Schematic representation of nuclear power plant infrastructures [5].

The first barrier is the cladding of the nuclear fuel pellets, made in zircaloy. Due to the existence of some defects, small amounts of FPs are transferred in the water of the primary circuit (purified with resins ions exchange). This latter circuit, closed, constitutes the second barrier. Its role is to transfer the heat produced by fissions to the secondary water loop via the steam generators. It is composed of the reactor vessel that contains the fuel core, the pressuriser, the primary pumps and tubular beams of the steam generators. The final barrier preventing is the containment building, which encloses previously mentioned infrastructures. A major accident occurs when there is a combined and complete loss of safety systems. A typical scenario is the loss of coolant, induced by a break in the primary circuit. This loss of cooling leads to a temperature increase of the fuel rods and around 1200 °C, the fuel cladding rupture occurs. The core fuel then melts, resulting in the release of FPs than can reach the containment building. Depending on the state parameters (pressure, temperature,...), a significant amount of FPs can be released in the environment, which is called Term Source (TS). Among the released FPs, ruthenium isotope ^{103}Ru and ^{106}Ru can be released in oxidising conditions (mixture of steam/air), and they represent high radio contaminants in a case of outside releases. In the case of the Chernobyl accident, activity concentrations of Ru isotopes in the air and on the ground were found similar to that of ^{131}I and ^{137}Cs [6, 7], with activity ratios equal to 1.98 and 0.86 for ^{103}Ru/^{137}Cs and ^{106}Ru/^{137}Cs, respectively [8]. The release of ^{106}Ru was observed in the case of the Fukushima-Daiichi accident in the water with the activity ratio of ^{106}Ru/^{137}Cs ranging between 0.07-0.2 [9]. The most significant Ru releases were observed at the Hanford nuclear fuel waste reprocessing site, where a high release of the ^{103}Ru and ^{106}Ru isotopes was evidenced in 1950 [10]. The health hazards of these compounds are discussed in the next section.

1.2   Radiological Consequences of Ruthenium Mitigation

The chemical toxicity of the ruthenium itself and the radiological risk originating from its radioactive isotopes represent the primary factor of the health hazards of Ru release in case of severe accident conditions. Table 1.1 reports the radio-toxic parameters of isotopes ^{103}Ru and ^{106}Ru.

Table 1.1: Physical and toxicological characteristics of radionuclide ^{103}Ru and ^{106}Ru [11].

Isotope	Emission	Half-life	Mass Activity	DPUI public inhalation
		(d)	(Bq/g)	(Sv/Bq) (target tissue)
^{103}Ru	β^-	39.3	1.19×10^{15}	7.3×10^{-10} (colon)
^{106}Ru	β^-	368.2	1.24×10^{14}	7.0×10^{-9} (colon)

Regarding the chemical toxicity, it is assumed that ruthenium in its metallic state behaves in the human body in a similar way to the other platinum group metals. Under its volatile form RuO_4, after inhalation, it can be deposited into the lungs or throat. With half-lives of 39.3 and 368.2 days [11], ^{103}Ru and ^{106}Ru isotopes are important at short and medium term time scales from a radiological point of view: ^{103}Ru is associated to the medium toxicity

group, while [106]Ru to the high one, like ^{131}I and [137]Cs [11]. Ruthenium contamination was also observed in the form of "hot particles", within the Chernobyl accident [12]. The specific microscopic-sized of these particles allowed them to be quite mobile in the environment by reaching trajectory lengths of up to 1400-1800 km [13]. These observations mean that huge doses can be reached quickly if such particles are deposited on the skin [14]. All this information proved the importance of accurate evaluation to design mitigation means if needed.

1.3   Evaluation of Ru Source Term with ASTEC/SOPHAEROS module

The physicochemical speciation and isotopic inventory of radionuclides which could be release to the environment constitute the evaluation of the safety of nuclear power plant and management crisis of a severe accident. Many tools are used to reach these goals, such as accident code software to predict the behaviour of radionuclides during a potential accident. In this topic, the ASTEC (Accident Source Term Evaluation Code) code is dedicated to simulating accidents and predict source terms. [15]. In particular, the ASTEC/SOPHAEROS module simulates the transport of FPs from primary circuit to their released at the containment building. All models including aerosol physics and gas chemistry are illustrated in Fig. 1.3.
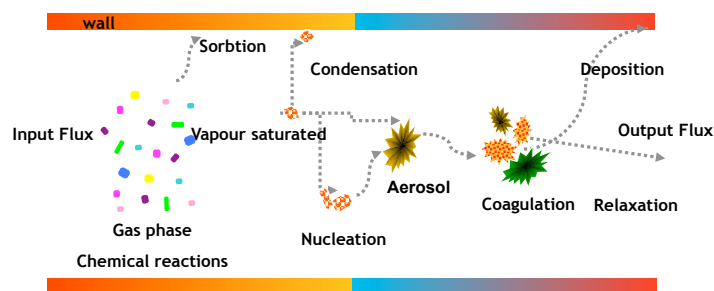
Figure 1.3: Schematic models transport included in ASTEC/SOPHAEROS module.

The gas phase chemistry is calculated mainly by considering equilibrium calculations except for iodine chemistry including kinetic limitations. Aerosol physics include nucleation processes, coagulation, sedimentation and resuspension. All processes describe above require trustful input data, based on fundamental data (thermodynamic parameters) coupled to experiments. In the case of Ru, the evaluation of Source Term is made with a lot of conservatisms, due to large uncertainties on the Ru thermokinetic chemistry in NPP severe accident conditions. The aim of this work is focused on consolidating/completing knowledge on Ru thermochemistry as well as kinetic parameters about possible chemical reactions occurring in the reactor coolant system (RCS).

References

(1) Hansen, J.; Ruedy, R.; Sato, M.; Imhoff, M.; Lawrence, W.; Easterling, D.; Peterson, T.; Karl, T. A closer look at United States and global surface temperature change. *Journal of Geophysical Research: Atmospheres* **2001**, *106*, 23947–23963, DOI: `10.1029/2001JD000354`.

(2) Sustainable development and nuclear power., IAEA report, Vienna, 2001.

(3) Holttinen, H. Optimal electricity market for wind power. *Energy Policy* **2005**, *33*, 2052 –2063, DOI: `10.1016/j.enpol.2004.04.001`.

(4) Scales for rating nuclear incidents and accidents and radiation protection events., Autorité de Sûreté Nucléaire (ASN), Annual report 2007, 2007.

(5) Nuclear chemistry., http://saylordotorg.github.io, 2016.

(6) Fry, F. A.; Clarke, R. H.; O' Riordan, M. C. *Nature* **May 1986**, *321*, 193–195.

(7) Denschlag, H. O.; Diel, A.; Gläsel, K.-H.; Heimann, R.; Kaffrell, N.; Knitz, U.; Menke, H.; Trautmann, N.; Weber, M.; Herrmann, G. Fallout in the Mainz Area from the Chernobyl Reactor Accident. *Radiochimica Acta* **1987**, *41*, DOI: `10.1524/ract.1987.41.4.163`.

(8) Beresford, N.; Smith, J, *Chernobyl: Catastrophe, Consequences and Solutions*; Springer Berlin Heidelberg: 2005.

(9) Schwantes, J. M.; Orton, C. R.; Clark, R. A. Analysis of a Nuclear Accident: Fission and Activation Product Releases from the Fukushima Daiichi Nuclear Facility as Remote Indicators of Source Identification, Extent of Release, and State of Damaged Spent Nuclear Fuel. *Environmental Science and Technology* **2012**, *46*, PMID: 22680069, 8621–8627, DOI: `10.1021/es300556m`.

(10) Walther, C.; Gupta, D., *Radionuclides in the Environment - Influence of chemical speciation and plant uptake on radionuclide migration*; Switzerland: Springer International Publishing Switzerland.: 2015.

(11) *Clefs CEA N° 48 : Radiological and Chemical Toxicology*; Commissariat à l'énergie atomique (CEA): Paris, France, 2003.

(12) Sandalls, F.; Segal, M.; Victorova, N. Hot particles from Chernobyl: A review. *Journal of Environmental Radioactivity* **1993**, *18*, 5 –22, DOI: `10.1016/0265-931X(93)90063-D`.

(13) Pöllänen, R.; Valkama, I.; Toivonen, H. Transport of radioactive particles from the chernobyl accident. *Atmospheric Environment* **1997**, *31*, 3575 –3590, DOI: `10.1016/S1352-2310(97)00156-8`.

(14) Pöllänen, P. Highly Radioactive Ruthenium Particles Released from the Chernobyl Accident: Particle Characteristics and Radiological Hazard. *Radiation Protection Dosimetry* **1997**, *71*, 23–32.

(15) Van Dorsselaere, J. P.; Seropian, C.; Chatelard, P.; Jacq, F.; Fleurot, J.; Giordano, P.; Reinke, N.; Schwinges, B.; Allelein, H. J.; Luther, W. The ASTEC Integral Code for Severe Accident Simulation. *Nucl. Technol.* **2009**, *165*, 293–307.

The aim of this chapter is to sum up the knowledge and uncertainties related to Ru behaviour under nuclear power plant (NPP) severe accident to gain insight into the origins of the limiting factors regarding the evaluation of the Ru Source Term. The modelling of ruthenium chemistry behaviour in severe accident conditions can be performed using the ASTEC software package [1] requiring accurate sets of thermodynamic properties ($\Delta_f H°(298\ K)$, $S°(298\ K)$, $C_P = f(T)$).

The first section is thus devoted to the general properties of Ru target species and analyses the origins of the thermodynamic data present in the databases. A second section concerns the literature review related to Ru release in the fuel matrix under nuclear power plant severe accident conditions. Transport through the reactor coolant system (RCS) is detailed later in the third section with the presentation of the experimental programs dedicated to reproducing Ru behaviour after its release from the damaged fuel. The fourth section reviews Ru interactions in the containment building leading to its release to the external environment. A synthesis and the main conclusions are assessed to introduce the objectives of this work in the final section.

2.1 Literature review of Ru properties and thermodynamic values

2.1.1 General properties

Ruthenium element, with atomic number of 44 and atomic mass around 101 g mol^{-1} was identified in 1844 by Karl Klaus [2], a Russian professor, who obtained a sample of pure oxide and called it ruthenium about the Latin name of Russia "Ruthenia". Ruthenium, which belongs to the platinum group metals, is relatively rare as its level is about 0.001 pm [3] in Earth's crust. It is found in ores with other platinum group metals in the Ural Mountains and in America. General physical properties of Ru are presented in Table 2.1.1.

Table 2.1: General properties of Ru element

Electron configuration	[Kr] $4d^7\ 5s^1$
Atomic radius	131.6 pm -134 pm
Covalent radius	124 pm
Ionic radius	VII: 36 pm, IV: 62 pm
Melting point	2607 K
Boiling point	4423 K
Electronegativity	2.2
Density	12.2 g.cm^{-3}
Vapour pressure	9.8×10^{-8} atm at ca. 1898 K

The major applications of ruthenium are in electrical contact field since this element hardens platinum and palladium alloys; a thin film is sufficient to achieve the wished properties, and it is cheaper than rhodium. Ruthenium presents very efficient catalytic properties, as do other platinum group metals. It is also used in electrolysing, often combined with another metal. In solar energy conversion, some ruthenium complexes absorb visible light, thus can offering possibilities for the fabrication of new low-cost solar cell systems [4]. In data storage, thin films produce by chemical vapour deposition of ruthenium on substrates show promising ways for its use in microchips and the giant magnetoresistive reading elements of hard disk drive.

Regarding nuclear properties, ruthenium has 7 stable isotopes and several radioisotopes with short periods. Only ^{103}Ru and ^{106}Ru have significative halftime towards nuclear safety issues [5], as discussed in Introduction.

2.1.2   Chemical reactivity

As ruthenium chemistry is very rich and varies from 0 to +VIII in most cases, we focused here on compounds that may be found in our conditions of study.

Ruthenium may forms ruthenates with alkaline or alkaline earth fission products, such as Cs_2RuO_4, $SrRuO_4$, $BaRuO_3$... Halide species can also be found like RuF_6, RuF_3, $RuCl_3$, $RuCl_2$, RuI_3, RuI_2, *etc.* [6]. In aqueous phase, oxidation states +VI, +VII and +VIII allow formation of tetraedric oxo-complexe like ruthenate ions $RuO_4{}^{2-}$, perruthenates $RuO_4{}^{-}$, RuO_4 and H_2RuO_5. Ruthenium can also form nitroso and nitrosyl compounds after reacting with nitric acid, nitrogen dioxide or oxide gases [7, 8], species that can be found under nuclear severe accident due to air radiolysis.

Ruthenium monoxide has been identified only in gaseous phase, at high temperatures (ca. 1500-1900 K) [9–13]. Ru dioxide is the most stable in solid form. It has tetragonal structural symmetry, forming grey-black crystal. The gaseous form of the dioxide can only appear at high temperature (>2000 K), according to some thermodynamic equilibrium calculations on Ru volatility [14].

The existence of gaseous trioxide has been evidenced by several experimental studies [9, 10], whereas the possibility of it forming a solid has not been validated by the literature

[15]. It appears in negligible amounts at temperature lower than 700 ° C, decomposing into ruthenium solid dioxide [12]. Ruthenium tetroxide is the most known oxide in the literature. It is a high volatility compound with toxic yellow vapour. It forms yellow prisms in its solid form [16]. RuO_4 appears to have strong affinity for different metal surfaces, reducing it into solid hydrated RuO_2 in slightly humid atmospheres [8, 17]. Some authors [18–20] predicted that gaseous ruthenium oxyhydroxides species, namely RuOH and RuO_3OH gases, may play a role under severe accident conditions either in reducing or oxidising environment. To our knowledge, such species have not been yet isolated experimentally.

Under severe accident conditions, the species susceptible to exist are ruthenium oxides (gaseous or solid form), aerosols (like Cs_2RuO_4) and metallic Ru itself [12]. We review hereafter the origins of the thermodynamic values of gaseous oxides and oxyhydroxides, as these quantities present the largest uncertainties.

2.1.3 Literature review on thermodynamic properties of Ru

2.1.3.1 Oxides species

Table 2.2 repertories the most cited references in the databases for the standard enthalpies of formation of ruthenium gaseous oxides. The corresponding standard molar entropies and heat capacities at room temperature are displayed in Table 2.3.

Table 2.2: Standard enthalpies of formation $\Delta_f H°(298K)$ in kJ mol^{-1}.

Species	Cordfunke and Konings [21]	Garisto [19]	Barin *et al.* [22]	Zimmerman [15]
$Ru_{(g)}$	649.0 ± 3.0	649.6 ± 13.0	651.4	640 ± 4
$RuO_{(g)}$	376 ± 25	372.0 ± 42.0	-	376 ± 4
$RuO_{2(g)}$	136 ± 10	133.7 ± 15.0	-	140 ± 4
$RuO_{3(g)}$	-64.1 ± 2.5	-48.4 ± 12.7	-78.2	-58 ± 4
$RuO_{4(g)}$	-188.0 ± 0.4	-187.1 ± 8.4	-183.1	-188 ± 4

Cordfunke and Konings data To calculate thermodynamic values of Ru oxides species, Cordfunke and Konings [21] determined Gibbs energy function ϕ (T) of each compound with selected spectrometric data and statistical thermodynamics using the rigid rotator harmonic oscillator. A third law analysis was applied to extract the enthalpies of formation from high-temperature vapour pressure data. For some species, they used tabulated ϕ (T) functions to derive the thermodynamic data.

To calculate the thermodynamic function of Ru gas, they used the atomic energy level given by Moore [23] and derived the standard entropy and heat capacity. To evaluate standard enthalpy of formation of $Ru_{(g)}$, they made a third law recalculation using vapour pressure data measured by different authors either using mass spectrometry [13, 24, 25] or with the Langmuir method [26]. They only retained the vapour pressure values of Panish and Magrave [24] and those of Carrera *et al.* [25], proposing an average value of 649.0 ± 3 kJ mol^{-1}.

The thermal function of RuO species was derived using vibrational frequencies taken from Pedley's review [27] which quotes the value derived by Norman *et al.* [13] by mass spectrometry. The latter took into account 3 points of measurement to derive the thermal constants of RuO, using the second law. Cordfunke and Konings [21] obtained a standard enthalpy of formation equal to 376 ± 25 kJ mol^{-1}. The obtained deviation can be thought underestimated, due to the few data used to extrapolate the thermal constants.

For the $RuO_{2(g)}$ species, they took the spectroscopic parameters analogous to those of $MoO_{2(g)}$ to derive the thermal functions. The enthalpy of formation calculated is equal to 136 ± 10 kJ mol^{-1}.

The study of the oxygen pressure effects on the vapour pressure of ruthenium species at 800 ° C and at ca. 1465-2090 ° C made by Schäfer *et al.* showed evidence for the gaseous RuO_3 and RuO_4 species. The latter dominated at high oxygen partial pressure and lower temperature. RuO_3 is stated to be in equilibrium with RuO_2 at low oxygen partial pressure and high temperature. Ruthenium behaviour was studied by Bell and Tagami [10] in the temperature range from 800 ° C to 1500 ° C at oxygen partial pressures of 0.01 to 1.0 atm. They found as stable condensed phase RuO_2 and vapour species as RuO_3 and RuO_4.

The thermodynamic functions of RuO_3 have been determined in a first step in 1990 by Cordfunke and Konings [21], assuming that its has similar spectrometric data to XeO_3, with a Ru-O bond length of 1.706 Å, an O-Ru-O bond angle of 103 ° and similar vibrational frequencies. They reevaluated these spectroscopic parameters in 1993 using data from ab initio calculations of Hameka *et al.* [28], which gives Ru-O bond length of 1.717 Å with a D_{3h} structural symmetry. With the first set of spectrometric parameters, Cordfunke and Konings [21] derived a $\Delta_f H°(298\ K)$ of -62.5± 2.5 kJ mol^{-1}, average value calculated using vapour pressure measurements from Bell and Tagami [10], Schäfer *et al.* [9, 29] and Alcok and Hooper [30] work. With the new spectrometric parameters, they derived a revised $\Delta_f H°(298\ K)$ equal to -64.1± 2.5 kJ mol^{-1}.

Heat capacity and entropy were calculated from the thermodynamic function of RuO_4 using Schäfer *et al.* spectrometric parameters [9], assuming the molecular structure to be tetrahedral with a Ru-O bond length of 1.706 Å. Levein and Abrahamovitch vibrational frequencies were used [31]. Average standard enthalpy of formation equal to -188.0 ± 0.4 was calculated with a third law extrapolation of the data from Penman and Hammer [32], Bell and Tagami [10] and Schäfer *et al.*, [9, 29] measurements, with a larger weight on the data from Penman and Hammer [32].

Garisto values   To derive ruthenium's ϕ (T) functions, Garisto used parameters from Pankratz study [33]. Tabulated Ru $\Delta_f H°(298\ K)$ value was taken from Rard [11, 34] review, who extended the reference data set with the mass spectrometry study of Krikorian *et al.* [20], leading to an average computed value of 649.6 ± 13.0 kJ mol^{-1}.

For $RuO_{(g)}$, Garisto used Pedley and Marshall's thermodynamic properties and thus calculated an enthalpy of formation equal to 372.0 ± 42.0 kJ mol^{-1}, which were been derived from Norman *et al.* [13] mass spectrometry work.

To obtain $RuO_{2(g)}$ Gibbs function, he applied statistical thermodynamics with the rigid rotator harmonic oscillator approximation, assuming that this species is a non linear mo-

lecule with a bond angle of 110 ° and a Ru-O bond length equal to 1.7 Å. He used $MoO_{2(g)}$ spectroscopic parameters from Glushko review [35], and then extracted RuO_2 ($\Delta_f H°(298\ K)$) using Rard's [11, 34] vapour pressure data. He obtained a value equal to 133.7 ± 15.0 kJ mol^{-1} 298.15 K.

RuO$_3$ and RuO$_4$'s ϕ (T) functions were derived as for the $RuO_{2(g)}$ molecule with the rigid rotator harmonic oscillator approximation. RuO$_3$ was assumed to have a pyramidal geometry (C$_{3v}$) with a Ru-O bond length equal to 1.7 Å and an O-Ru-O bond angle of 109.47 °. For RuO$_4$, he took the spectrometric data from Schäfer *et al.* like Cordfunke and Konings [21]. He used Shimanouchi [36] vibrational frequencies for both RuO$_3$ and RuO$_4$, assuming that the shifts were similar to those between XO_4^{2-} and XO_3, in which X refer to Cr, Mo or W, taken from Glushko [35] and Loewenschuss [37] studies. Extraction of $\Delta_f H°(298\ K)$ values were obtained by averaging the measurements of Bell and Tagami [10] and Schäfer *et al.* [9, 29], leading to a RuO$_3$ $\Delta_f H°(298\ K)$ equal to -48.4 ± 12.7 kJ mol^{-1} and a RuO$_4$ $\Delta_f H°(298\ K)$ equal to -187.1 ± 8.4 kJ mol^{-1}.

Table 2.3: Literature values for the standard molar entropies at 298 K ($S°(298\ K)$) and heat capacities at constant pressure ($C_p(298\ K)$) in J K^{-1} mol^{-1} for the gaseous ruthenium oxides.

(a)

Species	Cordfunke and Konings [21]		Garisto [19]	
	$S°(298\ K)$	$C_p(298\ K)$	$S°(298\ K)$	$C_p(298\ K)$
Ru$_{(g)}$	186.4	21.5	186.4 ± 1	/
RuO$_{(g)}$	242.1	31.5	242 ± 5	/
RuO$_{2(g)}$	267.4	44.1	283.9 ± 9	42.0
RuO$_{3(g)}$	281.9	59.4	291.4 ± 3.0	58.3
RuO$_{4(g)}$	289.1	75.2	289.0 ± 1.0	75.1

(b)

Species	Barin *et al.* [22]		Zimmerman [15]	
	$S°(298\ K)$	$C_p(298\ K)$	$S°(298\ K)$	$C_p(298\ K)$
Ru$_{(g)}$	186.4	21.5	186.4	-
RuO$_{(g)}$	/	/	241 ± 4	/
RuO$_{2(g)}$	/	/	275 ± 3	/
RuO$_{3(g)}$	276.1	/	287 ± 8	/
RuO$_{4(g)}$	290.1	75.6	289.1 ± 1.3	/

Barin *et al.* and Zimmerman values   The tabulated value of Barin *et al.* [22] review equals to 651.4 kJ mol^{-1} for $\Delta_f H°(298\ K)$(Ru) comes from different reference data selected for solid and liquid Ru in the the study of Hultgren [38]. RuO$_3$ and RuO$_4$ values are taken from Glushko's [35] compilation, which in turn refers to previously cited studies [9, 10, 13, 29, 30].

The thermodynamic properties of Ru oxides derived by Zimmerman [15] were partly based on Norman *et al.* measurements [13]. Zimmerman completed this previous work with low-temperature measurements [39, 40]. He stated that the deviation on his calculations results from the uncertainties in the bending vibrational frequencies, the ground state identifications, and the structural parameters like bond lengths.

2.1.3.2 Oxyhydroxides species

We reported the thermodynamic data of Krikorian [20] study in Table 2.4. He assumed that, the bond lengths of oxyhydroxides species are similar to those of Ru-F and Ru-Cl bonds. The Ru-O bond energies in hydroxide are assumed to be identical of those of Ru oxides, i.e 481 kJ mol^{-1} for $RuO(OH)_y$, $RuO_2(OH)_y$ and $RuO_3(OH)_y$. Ru−OH proposed bond energies are 364, 352, 335, 326, and 343 kJ mol^{-1} for the species $Ru(OH)_{(g)}$, $Ru(OH)_{2(g)}$, $Ru(OH)_{3(g)}$, $Ru(OH)_{4(g)}$, and $RuO_x(OH)_{y(g)}$ systems, respectively.

Table 2.4: Literature Values for Thermodynamic Data (Enthalpies of Formation $\Delta_f H°(298\,K)$, Molar Entropies $S°(298\,K)$ at 298 K and Gibbs Energy Functions) of Some Ruthenium Gaseous Oxyhydroxide Species [20].

Species	$\Delta_f H°(298\,K)$ (kJ mol^{-1})	$S°(298\,K)$ (J K^{-1} mol^{-1})	$-(G_T° - H°(298\,K))/T$ (J K^{-1} mol^{-1})		
			1000 K	1500 K	2000 K
$Ru(OH)_{(g)}$	327	266.5	303.9	330.6	357.2
$Ru(OH)_{2(g)}$	28	308.3	351.6	382.5	413.3
$Ru(OH)_{3(g)}$	-233	350.2	399.3	434.3	469.4
$Ru(OH)_{4(g)}$	-495	392.0	447.1	486.3	525.5
$RuO(OH)_{(g)}$	116	287.4	327.8	356.5	385.3
$RuO(OH)_{2(g)}$	-187	329.2	375.5	408.4	441.3
$RuO(OH)_{3(g)}$	-491	371.1	423.2	460.2	497.4
$RuO_2(OH)_{(g)}$	-116	308.3	351.6	382.5	413.3
$RuO_2(OH)_{2(g)}$	-419	350.2	399.3	434.3	469.4
$RuO_3(OH)_{(g)}$	-348	329.2	375.5	408.4	441.3

Some equilibrium calculations have been performed including the Ru database thermodynamic values of Tables 2.2, 2.3 and 2.4 [14, 19, 41]. The major conclusions of these calculations are the predominance of tetroxide in the vapour phase at low temperatures, as illustrated in Fig 2.1 presenting ruthenium speciation at equilibrium in air and 1 bar.

Calculations performed including hydroxides species in the equilibrium database stated that RuO_3OH is stable at temperatures ranging from 700 to ~1300 °C (see Fig. 2.2) in humid oxidising atmospheres and RuOH in reducing atmospheres (H_2/air environment) at high temperatures. However, Garisto [19] underlined that large uncertainties of up to ± 100 kJ mol^{-1} can be related on the standard enthalpy of formation of oxyhydroxides species. Taylor [14] found that these calculations lead to unrealistic high Gibbs energy expressions, with overestimated entropy and heat capacity, making it no possible to conclude about the existence of oxyhydroxide forms.

2.2 Release of Ru in fuel matrix

The Kleykamp *et al.* literature review [43] on the chemical state of irradiated fuel reveals that ruthenium is present as alloy precipitates. Metallic ruthenium is assumed to be a non-volatile
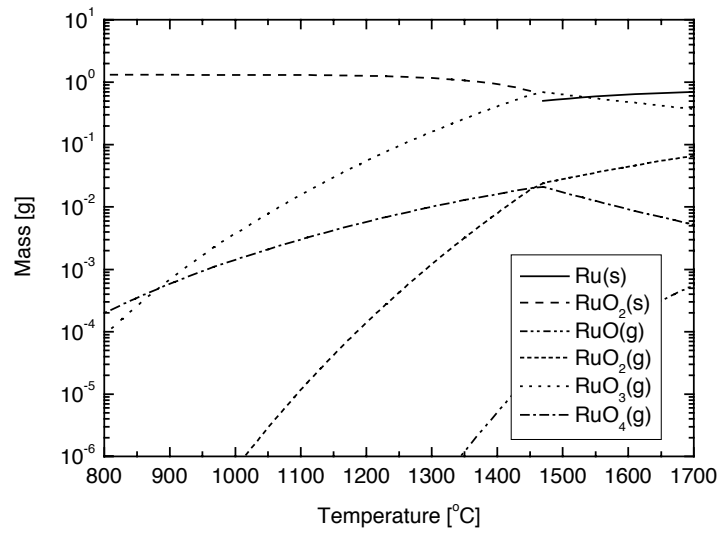
Figure 2.1: Ru thermodynamic equilibrium in air at 1 bar [42].
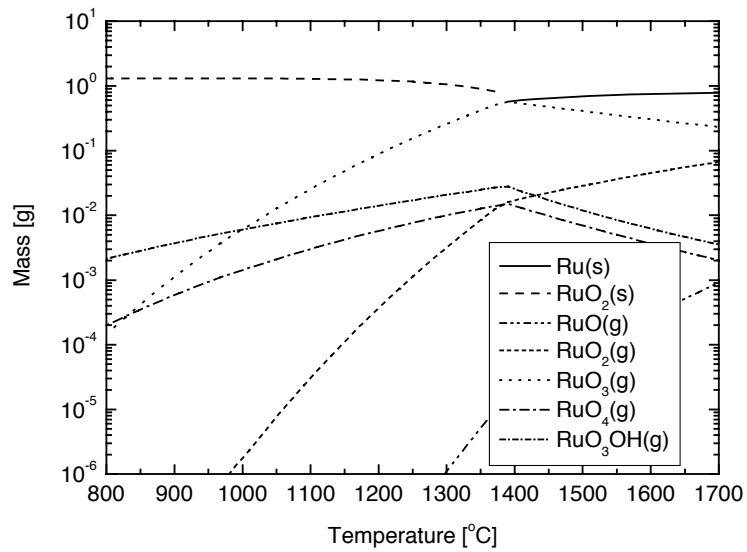
Figure 2.2: Ru thermodynamic equilibrium in 50% air/steam mixture at 1 bar [42].

element up to 2500 K [44]. As discussed in the introduction section, within the the Chernobyl

accident, the rate of Ru released by the nuclear fuel was similar to those of low volatile elements like Zr, Ce and U compounds; the emissions stopped ca. 9 days after the accident [45–47]. Later experimental work of Ronneau *et al.* [48] demonstrated that the oxygen content influenced the emission of radioactive ruthenium from the fuel matrix, occurring at relatively low temperatures (750-1000 °C). In these oxidising conditions, almost all ruthenium was released from the damaged fuel in volatile RuO_3 and RuO_4 forms. These observations can be explained with the Ellingham diagram in Fig. 2.3, allowing prediction of the behaviour of fission products (FP) by studying the relative stabilities of their oxides in the fuel matrix. According to the diagram, the presence of Ru oxide is unlikely until all uranium has been previously oxidised, implying a large excess of oxygen.
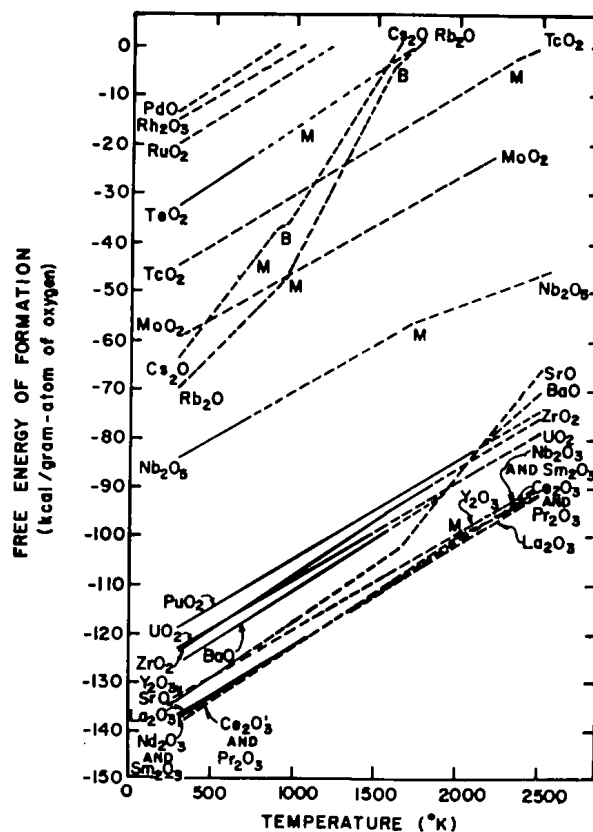
Figure 2.3: Elligham Diagram of oxygen potential of systems relevant to irradiated oxide fuels [49]

Many experimental studies were performed this two last decade to characterise fission products releases from melting fuel. The main programs are presented in the following section.

2.2.1 Experimental programs

The more relevant information relative to Ru release from the main experimental programs are presented in Table 2.5.

Table 2.5: % of Ru release with respect to fuel inventory for different experimental conditions [50].

Test	Fuel	Conditions	% Ru release [a]	% Ru at the break	Ref.
PHEBUS FPT1	UO2, ~ 23 GWd/tU	Steam, 2 g/s	~ 1.2	~ 0.5	[51]
PHEBUS FPT2	UO2, ~ 32 GWd/tU	Steam, 2 g/s	~ 11	~ 0.1	[51]
PHEBUS FPT3	UO2, ~ 24 GWd/tU	Steam, 0.5 g/s	~ 1.0	~ 0.3	[51]
VERCORS 5	UO2, ~ 38 GWd/tU	Steam, 1.5 g/min	6	/	[3-7-8]
VERCORS RT1	UO2, ~ 47 GWd/tU	H_2O (1.5 g/min) +H2 (0.03 g/min)	9	/	[52, 53]
VERCORS RT6	UO2, ~ 72 GWd/tU	H_2O (1.5 g/min) + H2 (0.03 g/min)	28	/	[52, 53]
VERCORS HT2	UO2, ~ 48 GWd/tU	H_2O (1.5 g/min)	~65	12[b]	[52, 53]
VERCORS RT8	UO2, ~ 70 GWd/tU	He + 10% air	~17	6[b]	[52, 53]
HC02	UO2, ~ 10 GWd/tU	air	87		[54, 55]
HC03	UO2, ~ 10 GWd/tU	steam	3.7		[54, 55]

[a] of the bundle
[b] value measured downstream the experimental line, at low temperature

In the frame of the VERCORS program at CEA, co-funded by IRSN and EDF [52, 53], 25 annealing tests were performed between 1983 and 2002 on irradiated PWR fuels. Usually, 3 irradiated pellets in their original cladding were involved. The major findings of this program are that most of the Ru release has occurred during the phase where the fuel rod was still intact because after the fuel melting Ru could be trapped in the liquid phase. The Canadian CANDU tests were performed by Atomic Energy of Canada Limited (now Canadian Nuclear Laboratories). HCE tests [54, 55] were conducted to study FP releases from clad CANDU fuel samples. The PHÉBUS-FP program was initiated by IRSN and JRC (Joint Research Center) of the Commission of European Communities [51]. The main objectives of this program were to simulate the full range of FP behaviour in conditions relevant to nuclear power plant accident, using a facility scaled down by a factor 5000 relative to a French 900 MWe PWR.

2.2.2 Main conclusions on Ru release

Experimental observations indicate that Ru can be potentially released to a great extent, all the most that the fuel burn-up is high and the gas is oxidative [53, 56]. High Bun-up fuel promotes the Ru release probably due to a higher oxygen potential inside fuel. The Ru release starts when temperature reaches at least 1900-2000 °C. Some modelling efforts were made [57] to predict Ru release in severe accident conditions, but these models do not consider the initial structure of fuel which depends on burn-up for instance.

In the next section, the transport of ruthenium compounds through the RCS toward the containment building will be discussed.

2.3   Ruthenium transport through the RCS

In severe accident conditions, the temperature in the reactor pressure vessel and the primary circuit ranges from ~1500 °C down 150 °C. The released volatile FPs from the fuel are then susceptible to be transported with the steam flow through RCS and reach the containment building. Few studies have examined the transport of ruthenium through the reactor coolant system [58], these showed that its transport is influenced by humidity, temperature and air flow rate in the RCS. Ru can be transported of either as condensed RuO_2 or as gaseous Ru tetroxide. Interactions with other elements released from the fuel may also impact the chemical composition and possibly the quantity of transported Ru [7].

We present here a literature review regarding the studies on Ru transport and the main experimental programs related on.

2.3.1   PHÉBUS program

The Phébus program, presented in Section 2.2.1, aims at reproducing PWR severe accident conditions at a smaller scale. A schematic representation of the experimental set-up is displayed in Fig. 2.4. The experimental circuit includes a hot leg heated at 700 °C, a single reverted U-tube simulating a steam generator, a cold leg at 150 °C and a $10m^3$ tank simulating the containment building.
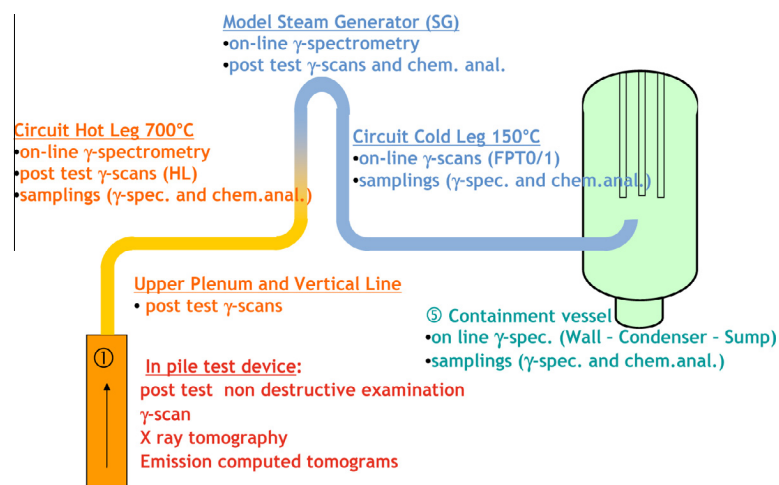
Figure 2.4:   Simplified schematic representation of the experimental circuits in the bundle tests FPT0/3 and localisation of on-line/post test measurements and samplings dedicated to material release/deposition/ transport in the circuit and up to the containment vessel (c-spec: c-spectrometry; chem. anal.: chemical analyses). [56]

These experiments showed that ruthenium is significantly and progressively deposited from the exit of the bundle to the entrance of the containment. The main processes observed in the circuit are chemical transformation of vapours, vapour condensation onto structures, nucleations to form aerosols, aerosol agglomeration and thermophoretic deposition. Transported ruthenium inside the containment was observed mostly as aerosols, with possible small amount of gaseous ruthenium but not measured in the absence of specific devices.

2.3.2 The RUSET-MTA EK program

The RUSET (RUthenium Separated Effects Tests) program [59] lead by the Hungarian team of AEKI institute (now MTA EK) aimed to study the impact of surfaces and other fission products on Ru transport using a bench-scale apparatus. The experimental set-up is illustrated in Fig. 2.5. It consists of heating mixtures of Ru powder (with or without FPs) in a ZrO_2 matrix, in a vertical quartz tube located in a furnace, with an air flow rate of $171N\ cm^3$/min to ensure fast vaporisation of Ru in isothermal conditions at $1100\,^\circ$C. The released ruthenium was collected in two places. The first one was located on a sampling tube of quartz/SS/alumina/E110 (Zr, 1.0 wt.% Nb, 0.05 wt.% O, 0.01 wt.% Fe, 0.01 wt.% Hf)) placed after the reaction chamber tube to determine the amount of deposited RuO_2 at the decreasing temperature. The second place consisted of an absorber solution at the final outlet to quantify gaseous ruthenium after cooling down. Each test lasted 360 min. To investigate vapour-surface reactions, quartz rod, alumina rod, SS plate, E110 plate into the quartz, alumina, SS and E110 sampling tubes were respectively introduced.

The main conclusions of these tests are that quartz surface catalyses reaction of RuO_4 and RuO_3 into solid ruthenium dioxide, with 6% of gaseous fraction evidenced at the outlet facility. This fraction increases to ca. 22% and 10%, when using stainless steel (SS) sampling tube and alumina one respectively. The deposits appear at temperature ranges of 865-510 $^\circ$C for the quartz tube, 910-365 $^\circ$C for alumina and 860-405 $^\circ$C for SS surfaces. Two peaks of deposits are noticed: a larger one at 900-600 $^\circ$C and a smaller one at 600-400 $^\circ$C. Re-evaporation of RuO_2 deposits were found to be higher from the SS tube than alumina or quartz ones. To study the influence of other fission products, they treated the surface of the tube with molybdenum and caesium coatings. With molybdenum, the detected fraction of the tetroxide in the absorber solution increases to 11% for quartz, 23% for SS surface and 24% for alumina tube. With caesium layers, this fraction is ca. 26% for quartz tube, 10% for alumina sampling and 18% for SS surface. Caesium compounds on quartz tube limit the catalytic effect of its surface on the decomposition of RuO_x to RuO_2. With SS surface, it was stated that caesium deposits seem to trap ruthenium, as observed in a previous study [61]. Concerning the alumina tube, caesium precipitation decreased the decomposition of RuO_x to RuO_2, increasing the fraction of transported gaseous tetroxide in the outlet air. With cladding material E110 placed in the decreasing temperature zone, almost no (ca. 1%) Ru is transported, even with oxidation. This demonstrates that zirconium tube has to be completely oxidised before Ru transmittance is detected. When adding other fission products, this fraction is slightly increased to 8% after zirconium oxidation.

To model the accidental situation of oxidised metal surfaces, tests were also performed with pre-oxidised SS surfaces, but the results showed no significant impact on the ruthenium
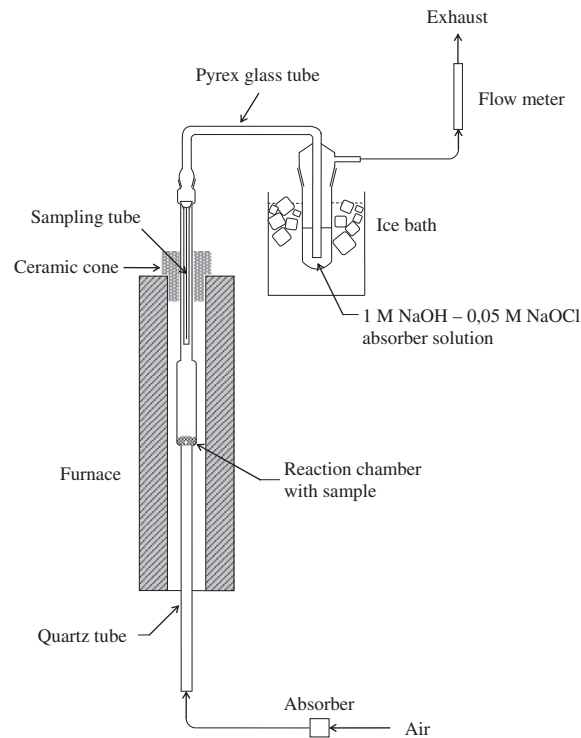
Figure 2.5: Experimental set-up of RUSET-MTA EK program [60]

transport by comparison with non-pre-oxidised SS.

Simulations of the RUSET test 17a, illustrated in Fig. 2.6 was made using ASTEC accident code [62]. It was assumed that the kinetic decomposition of RuO_4 to RuO_2 did not follow equilibrium. The transit time of transported ruthenium from the furnace to the tube outlet (liquid trap) was predicted to be about 1 s [63]. This is as fast as the transit time from the core outlet zone to the reactor containment for typical loss of coolant accident (LOCA) with a break at the hot leg of the RCS [58]. The simulation of the tests consisted of two phases:

- the first one was the injection phase during 45 min, corresponding to the evaporation of Ru, assumed to be in thermodynamic equilibrium. After 45 min, the Ru source was exhausted. In consequent, the only source of Ru was the deposits on the surfaces.

- the second phase corresponds to the revaporisation phase from the surfaces, between 45 and 360 min, at the end of the test.

Results of the simulation placed the temperature peak of deposit, around 727 °C. The mass deposit was underestimated as it is assumed that a significant amount of RuO_4 gas reaches
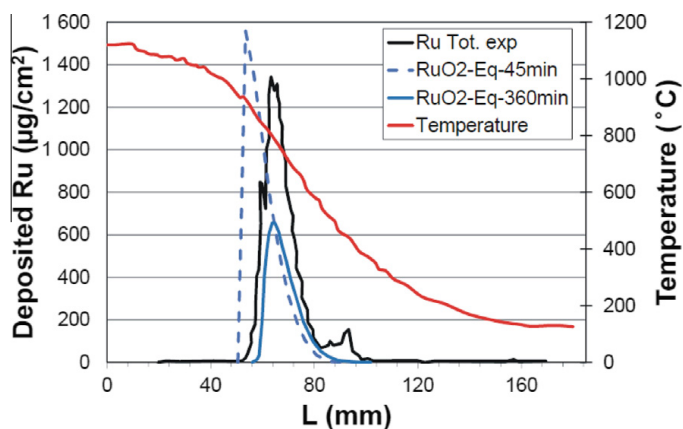
Figure 2.6: Simulation of RUSET test 17a using ASTEC/SOPHAEROS module [62].

the outlet. If one assumes the kinetics of the following reaction to be slow:

$$RuO_3 + 0.5 O_2 \rightleftharpoons RuO_4 \tag{2.1}$$

with a kinetic constant k $= k^0 \exp(-E^a/RT)$, k^0 = 0.5 molecule^{-1} s^{-1} and E^a = 300 kJ mol^{-1}, which has been fitted on experiments, the simulated results are much closer to the experimental ones, therefore indicating that kinetics limit the formation of gaseous RuO$_4$ in the reactor cooling system and that the equilibrium decomposition is not reached in the second phase of the tests.

2.3.3 VTT experiments

VTT Finnish institute carried out experiments on ruthenium transport through a small-scale simulated RCS since 2002 [58]. We will describe hereafter the two principal phases of this project.

2.3.3.1 Experimental program 2002-2004

The bench-scale apparatus, illustrated in Fig. 2.7, was built to conduct experiments consisting in heating the inlet source composed of ruthenium dioxide powder (about one gramme) in a ceramic crucible with a maximal gradient between 1427 °C and 25 °C, inside an alumina tube furnace or stainless steel one (SS). The carrier gas was pure air or air-steam with seed particles of AgNO$_3$ to simulate condensation or nucleation. The flow rate was about of

5L/min, each test lasted about 50 min. When heating RuO_2 powder, RuO_3 and RuO_4 gas are formed, assuming thermodynamic equilibrium [41, 64].
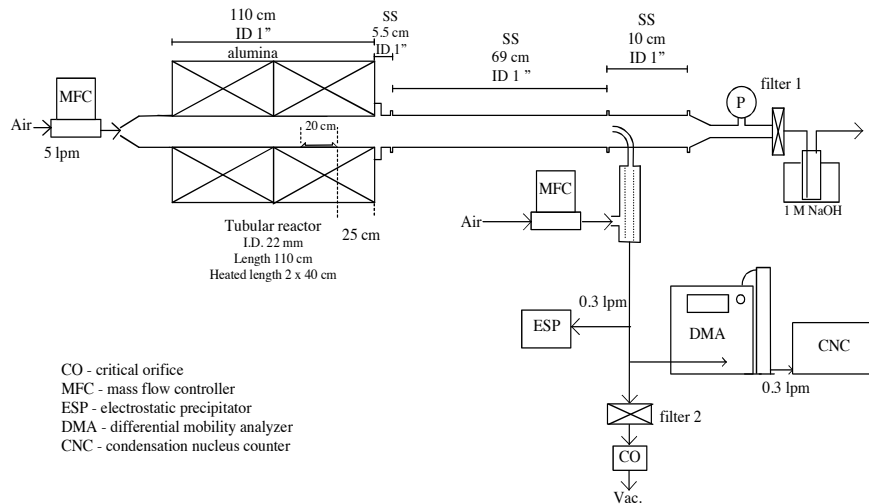
Figure 2.7: VTT-processes schematic experimental set-up [41]

Large quantities of Ru deposited on the tube were measured: 94% was attributed to the decomposition of gaseous RuO_3 into RuO_2, and small fraction of gaseous RuO_4. At the outlet, aerosol and gaseous forms of ruthenium reach the bubbler, 0.1-0.2% with SS tube and around 4% with alumina tube. This demonstrates that SS tube catalyses the decomposition of RuO_4 into RuO_2. These results agree with those of the Hungarian team in the RUSET program, which observed a larger peak deposit onto SS in comparison with alumina tube. It is stated that this result indicates that solid RuO_2 does not have a strong catalysis effect on the decomposition of RuO_4 gas, in contrast to the predictions of previous studies [65].

When using an air-steam carrier gas with seed particles, the amount of RuO_4 gas reaching the trapping bottle with SS tube is the same as that found with the alumina tube. The deposition profile along the thermal gradient tube (TGT) exhibits three peaks of deposition: the first one around 500 °C is attributed to the thermal dissociation of RuO_3 gas to RuO_2 solid, as no RuO_3 is expected to be stable at temperatures below 700 °C; the second peak at ca. 150 °C is attributed to thermophoretic deposition of particles; the third peak at ca. 30 °C. is assigned to the decomposition of RuO_4.

Depending on the performed tests, an amount of 12-35% of the released ruthenium was trapped in the outlet filter as RuO_2 particles, increased by seed particles and a higher temper-

ature gradient.

To draw conclusions from these experiments for a reactor accident, ruthenium release increases as oxidised gaseous species RuO_3 and RuO_4 are formed. The major part of the released ruthenium is deposited on RCS. With steam and aerosol particles, substantial amount of Ru may be released into the containment atmosphere as gaseous RuO_4 and aerosols.
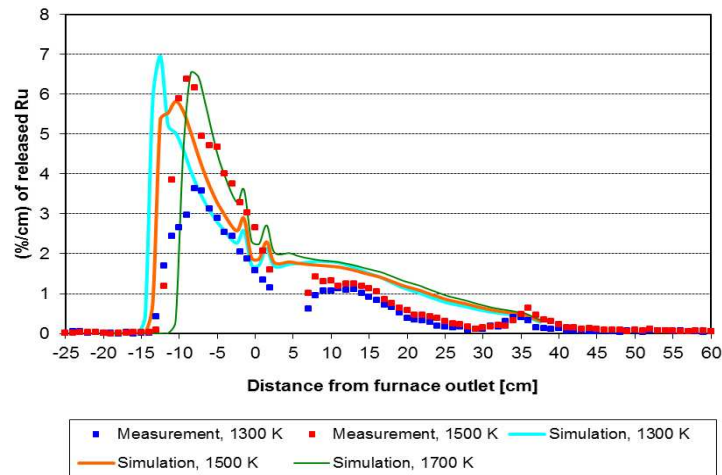
Figure 2.8: Simulation of VTT- tests 1, A and B using CFD/FLUENT code [61].

Simulation of VTT tests 1, A and B, was made using CFD/FLUENT code [58, 61]. In these tests, the diffusion-limited transport and deposition onto TGT surfaces of RuO_2 and RuO_3 were analysed, where the kinetics of ruthenium conversion to RuO_4 are negligible. As in the RUSET simulation, the decomposition of tetroxide to dioxide was not in equilibrium. Evaluated transient time from the release source to the cold zone is about 3 s [63]. Comparing to RUSET test, the VTT tests present a tube furnace diameter larger, as well as the overall apparatus. However, this time is in the range of those observed for a LOCA [58]. The three peaks of depositions observed in experiments are reproduced by the simulations. From the simulation, the formation of RuO_4 is expected to appear at lower temperatures, 1027 °C, than in the experiment, 1227 °C. The predicted quantities of RuO_4 are 25% and 9% at 1027 °C and 1227 °C, respectively.

2.3.3.2 Experimental program 2007-2014

The second phase of the VTT program focuses on the impact of air radiolysis products on the speciation and transport of Ru. The results have been recently published in the PhD thesis and article by Kajan [66]. As discussed in section 2.4, air radiolysis can occur in the containment in severe nuclear accident conditions, leading to the formation of N_2O, NO_2

and HNO_3. These species might oxidise RuO_2 and RuO_3 gaseous compounds into gaseous RuO_4 and thus possibly increase the release and transport of gaseous Ru [67].

The experimental set up is similar to the one illustrated in Fig. 2.7, except that the flow rate is much lower (2 L/min) and the air radiolysis products added after the furnace. In a humid air atmosphere, the transport of Ru tetroxide in gaseous form, amount to 0.024% with an initial temperature of 1300 K, 0.010% at 1500 K and 0% at 1700 K, it decreases with higher temperature whereas the transport of aerosols forms of condensed Ru dioxide increases. The amount of transported Ru is lower due to smaller Ru release rate comparing to those of air flow rate of 5 L/min of previous experiments [41]. This phenomenon was attributed to the fewer amount of oxygen reaching the crucible.

With an atmosphere containing 50 ppmV of NO_2, the transport of ruthenium tetroxide increased by 92% at 1300 K and 42% at 1500 K, by comparison to humid air atmospheres. The increase of RuO_4 fraction is due to the reaction between NO_2 and RuO_3, as expressed in equation 2.2:

$$RuO_3 + NO_2 \longrightarrow RuO_4 + NO \tag{2.2}$$

.

The equilibrium constant K_{eq} calculated for this reaction were equal to 28.55, 16.85, and 11.3 at 1300, 1500, and 1700 K, respectively. The decreasing at higher temperatures results from the decomposition of NO_2 with temperature [68, 69].

With an atmosphere containing 50 ppmV of N_2O, they observed a reduction of gaseous fractions. A modest increase is observed in higher temperatures, in comparison to humid air atmosphere. These effects are attributed to reaction of N_2O with RuO_4 to form gaseous RuO_3 or dioxide with NO gas species. The effect of N_2O is weak on ruthenium chemistry in these experimental conditions.

With 5 ppmV of HNO_3 in the atmosphere, the transport of RuO_4 is enhanced compared to humid atmospheres tests. However, these amounts are lower than the expected values of the equilibrium constants derived from equation 2.3 equal to 1.65×10^{11} at 1300 K, 4.57×10^{10} at 1500 K and 1.66×10^{10} at 1700 K. This effect is stated to result from the thermal decomposition of HNO_3 to the lower nitrogen oxide, reducing the amount of precursor in the gas phase [70, 71].

$$3\,RuO_{3\,(g)} + 2\,HNO_{3\,(g)} \rightleftharpoons 3\,RuO_{4\,(g)} + H_2O_{(g)} + 2\,NO_{(g)} \tag{2.3}$$
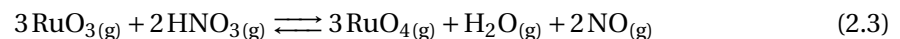
Most of the released ruthenium was deposited inside the apparatus, mainly at the outlet of the furnace. Transported ruthenium aerosols are under solid dioxide form, according to XPS and XRD characterisations.

2.3.4   OECD STEM/START program

To improve the knowledge on Ru transport through RCS in case of NPP severe accident, an OECD/NEA program is led by IRSN. This program includes the START project (Study of the TrAnsport of RuThenium in the primary circuit) [72, 73]. The START objectives are to study

ruthenium transport, to provide database about the quantification of gaseous ruthenium released at the breach of the primary circuit. The experimental set-up and measurements steps are illustrated in Figure 2.9.
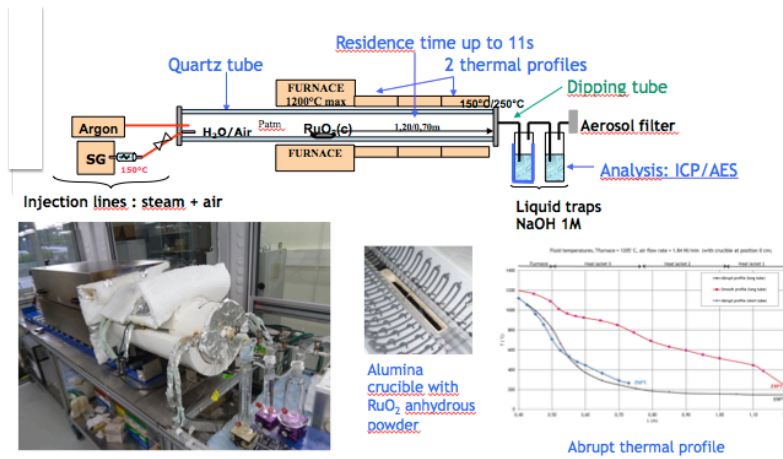
(a)
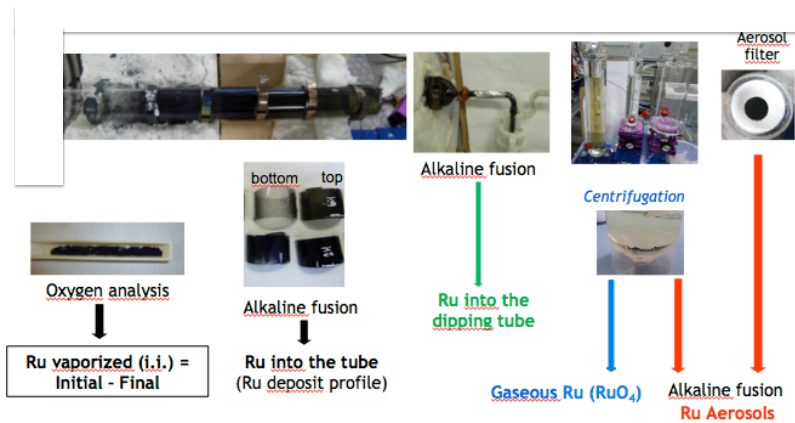
(b)

Figure 2.9: Experimental set-up (a) and measurements steps (b) in the START facility [74]

The release amount of Ru was determined by weighting the alumina crucible of anhydrous dioxide powder before and after the tests. The analysis of the deposits involved alkaline fusion. Absorber solution of NaOH trap the gaseous ruthenium fraction at the outlet, centrifugation is then conducted, and ICP/AES analysis is performed. Aerosols are trapped in a filter at the outlet of the quartz tube. The first phase of the experiment consists in the measurement of Ru vaporisation and direct transport. The second phase corresponds to the vaporisation tests, in which the only source of Ru was the deposits along the tube.

The main experimental data measured during START experiments are quantification and speciation of Ru species (gaseous and condensed form) at the break, quantification of Ru deposits along the thermal transport tube and quantification of revaporisation phenomena from the Ru deposits. 16 tests were performed with abrupt thermal profiles and 2 with smooth thermal profiles. The carrier gas corresponded to different percentages of air/steam mixtures. The duration of the main vaporisation tests was one hour except for two tests lasting 7 hours. The revaporisation tests lasted 4h, except for the 2 long tests, lasting 26 hours.

The amount of Ru deposit is around 90% of the initial inventory (i.i) whatever the carrier gas mixture on the vaporisation tests. XPS and Raman's spectroscopy identified the deposits as RuO_2. A first peak is detected at high temperatures (ca. 850 °C after vaporisation and revaporisation phases). A second peak is observed at 535-380 °C, this profile is attributed to the decomposition of gaseous RuO_4 into solid RuO_2.

With 60% of steam in the carrier gas, the amount of transported Ru is enhanced in comparison with tests performed with dry air. After a vaporisation phase of 7 hours, the amount of transported Ru is always the same whatever the carrier gas mixture. Regarding the revaporisation phase, Ru is transported only in dry air in increasing amount even after 26 hours. With mixed steam/air atmosphere, the amount of transported Ru seems to reach a plateau. With smooth thermal profile, the amount of transported gaseous tetroxide is lower.

A follow-up experimental program, STEM2/START, has just started to investigate impact of the surface with stainless steel tube and more oxidising conditions with air radiolysis products like nitrogen oxides to the transport of ruthenium through RCS in severe accident conditions [75].

2.3.5   Synthesis of knowledge

All experimental studies performed so far reveal that the release rate of Ru is enhanced by high oxygen partial pressure and high temperature. Volatile species are determined to be gaseous ruthenium RuO_3 and RuO_4. The major part of Ru release is deposited along the thermal gradient tube, forming distinct peaks at higher temperatures (ca. 800 °C) and lower ones (ca. 400 °C). The first deposition profile is attributed to the thermal decomposition of RuO_3 into solid RuO_2.The average deposition peak arises from the dissociation of RuO_4 into solid RuO_2. The other conclusion that has been highlighted from theses experiments is related to the kinetic limitation encountered on the dissociation of ruthenium tetroxide into dioxide. It reveals that this procedure has not reached equilibrium. Enhancement of transported Ru was observed with steam-air mixture, raising the question of the possible role of Ru oxyhydroxides into Ru transport through RCS. This enhancement was visible in the VTT tests by the formation of the layer of hydrogen due to the decomposition of water molecule into the

tube surfaces preventing catalysed reactions of RuO_x gas into solid dioxide. An enhancement of transported tetroxide gas is also observed with SS, and alumina surfaces, which are both less efficient at catalysing RuO_2 condensation than the quartz tube. The addition of surface coatings of fission products such as molybdenum or caesium promotes gaseous Ru species at the outlet. The cladding tube E110 stopped volatilisation of gaseous ruthenium, until the tube is completely oxidised. Air radiolysis products NO_2 and HNO_3 promote transportation of gaseous tetroxide ruthenium fractions, even if the amount of total transported Ru (under aerosols or gas forms) remain similar to those found in humid atmosphere. These observations evidenced that a fraction of ruthenium can reach the nuclear containment building either under gaseous form or aerosol form.

2.4 Ru behaviour in reactor containment building

Under severe accident conditions, in the containment building, the temperature ranges from 40 °C to 140 °C, relative humidity varies from 0 to 100% and pH in the sump ranges from 4 to 10. All these boundary conditions depend on the accidental sequence.

Due to emission of radiations from FPs, the dose rate after the release peak is in the order of 10 kGy.h^{-1}, leading to radiolysis of atmosphere and sump. Atmosphere radiolysis inside the containment building leads to the formation of NO_2, N_2O, O_3, HNO_3 species [76, 77]. Some studies estimate the values of NO_2 and N_2 concentrations to be around 50 ppmV [78]. Radiolysis of the sump leads to the decomposition of water to form molecular products and radicals. In particular, radiolysis of water leads to the formation of nitric acid HNO_3. The radiations impact the building surfaces by first damaging the paints. Stainless steel surfaces can also be damaged due to fragility and swelling.

In the containment building, we learnt from the previous sections that Ru can exist either as volatile species or as aerosols. When the temperature inside remains under 140 °C, ruthenium is mostly found as RuO_4, according to the thermodynamic equilibrium speciation (see section 2.1.3). The decomposition of $RuO_{4\,(g)}$ in moist air is quite slow; the half-life of RuO_4 is found to be 5 h at 90 °C in presence of steam [79]. As aerosols are trapped by the Filtering Containment Venting System (FCVS), their contribution is negligible to the effective dose outside. Nevertheless, solid ruthenium dioxide oxidised by the air radiolysis products of containment building can cause formation of gaseous RuO_4.

In the aqueous phase, oxidative reactions of dissolved ruthenium species can occur, potentially leading to volatile Ru species. These dissolved species come from aerosols, forming ruthenate and perruthenate, thermodynamically stable in wide conditions [80].

Ruthenium behaviour inside the containment building was the subject of the PhD thesis of Mun [81]. He proposed reaction schemes leading to the release of tetroxide outside containment building and implemented his models in the ASTEC code. He estimated Ru source term (ST) contribution to the radiological dose for several accidental parameters. Unfortunately, as Ru behaviour models in the RCS were limited to provide the code with quantifications of the fraction of transported Ru, his modelling was performed using assumptions regarding fraction of gaseous tetroxide and dioxide aerosols reaching the containment build-

ing. Mun proposed that reactions in the aqueous phase may be integrated into accident code software, as they can influence evaluation of the Ru ST.

2.5 Synthesis and objectives

The behaviour of ruthenium species in including relevant experiments has been reviewed in this chapter in order to identify the origins of uncertainties in evaluation of Ru Source Term in case of severe accident conditions. The release of Ru from fuel matrix has been characterised by several experimental programs, which concluded that its release is controlled by the oxygen potential, leading to oxidation of the fuel matrix, enhanced with high burn-up. Modelling with the ASTEC code has been performed and is in reasonable agreement with experimental data.

Ruthenium transport through RCS, after its release from the damaged fuel, has also been the topic of several experimental programs. Ruthenium is mainly deposited along the thermal gradient tube, but also transported as aerosols of RuO_2 and gaseous RuO_4 at low temperature. The gaseous fraction increases with humid atmosphere, and also with molybdenum and caesium FP deposited on the primary circuit surfaces. Air radiolysis products like nitrogen dioxide also promote the gaseous transport of RuO_4 by oxidising gaseous RuO_3. The simulations of several experimental tests with the ASTEC code overestimated the fractions of gaseous release at low temperature. It has been showed that including kinetic limitations in the formation of RuO_4 yielded results in better agreement with experiment.

Concerning ruthenium behaviour inside the containment building, models have been developed to assess Ru source term; that correspond to the release of radioactive Ru species to the environment. However, as this evaluation of the source term with accident code software directly depends on the simulation of the transported Ru species, these simulations might not be trusted.

These conclusions motivate my research topic to investigate ruthenium behaviour through its transport in the primary circuit of a nuclear power plant under severe accident conditions.

Regarding the uncertainties in the thermodynamic properties of Ru gaseous oxides, a first step, is to consolidate thermodynamic data existing in actual Ru databases. A second step will be the determination of thermodynamic properties of oxyhydroxides for which the data are very scarce. The literature review highlights limitations in simulation of Ru transport through RCS in severe accident conditions under oxidising atmosphere, hence reaction pathways leading to the formation of RuO_3 and RuO_4 gases will be studied, potentially involving some kinetic limitations.

The adopted strategy is the use of quantum chemical methods associated with statistical physics in order to obtain the desired thermodynamic and kinetic values. In fact, highly correlated quantum chemical theories offers a promising way to provide ruthenium species properties, as long as attention is paid to the accuracy of the theoretical method used because ruthenium is a transition metal and electronic structure of some oxides could be quite complex [82].

References

(1) Van Dorsselaere, J. P.; Seropian, C.; Chatelard, P.; Jacq, F.; Fleurot, J.; Giordano, P.; Reinke, N.; Schwinges, B.; Allelein, H. J.; Luther, W. The ASTEC Integral Code for Severe Accident Simulation. *Nucl. Technol.* **2009**, *165*, 293–307.

(2) Weeks, M. E. The discovery of the elements. VIII. The platinum metals. *Journal of Chemical Education* **1932**, *9*, 1017, DOI: `10.1021/ed009p1017`.

(3) Greenwood; Earnshaw.

(4) Daibin, K.; Seigo, I.; Bernard, W.; Cedric, K.; Jacques, E.-M.; Robin, H.-B.; Zakeeruddin, S. M.; Grätzel, M. High Molar Extinction Coefficient Heteroleptic Ruthenium Complexes for Thin Film Dye-Sensitized Solar Cells. *Journal of the American Chemical Society* **2006**, *128*, PMID: 16551124, 4146–4154, DOI: `10.1021/ja058540p`.

(5) W., S.-E.; G., P.; H., M., Karlsruher Nuklidkarte, Gesellsch. f. Kernforschung, Karlsruhe, 1974.

(6) Cotton, W., Advanced Inorganic Chemistry, 1972; Vol. 3rd Edition.

(7) Lemma, F. D.; Colle, J.; Benes, O.; Konings, R. A separate effect study of the influence of metallic fission products on CsI radioactive release from nuclear fuel. *Journal of Nuclear Materials* **2015**, *465*, 499 –508, DOI: `10.1016/j.jnucmat.2015.05.037`.

(8) Kajan, I.; Kärkelä, T.; Tapper, U.; Johansson, L.-S.; Gouëllo, M.; Ramebäck, H.; Holmgren, S.; Auvinen, A.; Christian, E. Impact of Ag and NOx compounds on the transport of ruthenium in the primary circuit of nuclear power plant in a severe accident., Submited to Annals of Nuclear Energy, 2016.

(9) Schäfer, H.; Schneidereit, G.; Gerhardt, W. Zur Chemie Der Platinmetalle. RuO_2 Chemischer Transport, Eigenschaften, Thermischer Zerfall. *Z. Anorg. Allg. Chem.* **1963**, *319*, 327–336, DOI: `10.1002/zaac.19633190514`.

(10) Bell, W. E.; Tagami, M. High-Temperature Chemistry of the Ruthenium-Oxygen System. *J. Phys. Chem.* **1963**, *67*, 2432–2436, DOI: `10.1021/j100805a042`.

(11) Rard, J. A. Chemistry and Thermodynamics of Ruthenium and Some of Its Inorganic Compounds and Aqueous Species. *Chem. Rev.* **1985**, *85*, 1–39, DOI: `10.1021/cr00065a001`.

(12) Eichler, B.; Zude, F.; Fan, W.; et al. Volatization and Deposition of Ruthenium Oxides in a Temperature Gradient Tube. *Radiochimica Acta* **1992**, *56*, 133–140, DOI: `10.1524/ract.1992.56.3.133`.

(13) Norman, J. H.; Staley, H. G.; Bell, W. E. In *Advances in Chemistry – Mass Spectrometry in Inorganic Chemistry*, Margrave, J. L., Ed.; American Chemical Society: Washington, D. C., 1968; Vol. 72; Chapter 8, pp 101–114, DOI: `10.1021/ba-1968-0072.ch008`.

(14) Taylor, P. Thermochemical data and calculations for Ruthenium volatility, with particular interest to the Phebus STLOC-1 TEST., 2004.

(15) Zimmerman, G. L.; Riviello, S. J.; Glauser, T. A.; Kay, J. G. Photochemical Decomposition of Ruthenium Tetroxide. *J. Phys. Chem.* **1990**, *94*, 2399–2404, DOI: `10.1021/j100369a039`.

(16) D.R., L., *CRC Handbook of chemistry and physics*, 84th Ed.; CRC Press, Inc.: 2003.

(17) Holm, J.; Glänneskog, H.; Ekberg, C. Deposition of RuO4 on various surfaces in a nuc-
      lear reactor containment. *Journal of Nuclear Materials* **2009**, *392*, 55 –62, DOI: `10.`
      `1016/j.jnucmat.2009.03.047`.

(18) Jackson, D. D. Thermodynamics of the gaseous hydroxides, report UCRL-51137., Laurence
      Livermore National Laboratory, 1971.

(19) Garisto, F. *AECL-9552* **1988**.

(20) Krikorian, O. H.; Carpenter, J. H.; Newbury, R. S. A Mass Spectrometric Study of the
      Enthalpy of Sublimation of Technetium. *High Temp. Sci.* **1969**, *1*, 313–330.

(21) Cordfunke, E. H. P.; Konings, R. J. M. Thermochemical Data for Reactor Materials and
      Fission Products: The ECN Database. *J. Phase Equilib.* **1993**, *14*, 457–464, DOI: `10.`
      `1007/BF02671964`.

(22) Barin, I.; Knacke, O.; Kubaschewski, O., *Thermochemical properties of inorganic sub-
      stances*; Springer-Verlag: Berlin, Heidelberg, New York, 1977, p 861.

(23) Moore, C. E. Atomic Energy Levels as Derived from the Analyses of Optical Spectra. *Nat.
      Stand. Ref. Data Ser.* **1971**, *35*, 245.

(24) Panish, M. B.; Reif, L. Vaporization of Ruthenium and Osmium. *J. Chem. Phys.* **1962**, *37*,
      128, DOI: `10.1063/1.1732934`.

(25) Carrera, N. J.; Walker, R. F.; Plante, E. R. Vapor Pressures of Ruthenium and Osmium. *J.
      Res. Natl. Bur. Stand. Sect.* **1964**, *68A*, 325.

(26) Paule, R. C.; Margrave, J. L. Vapor Pressures of Platinum Metals. III. Iridium and Ruthenium.
      J. Phys. Chem. **1963**, *67*, 1896–1897, DOI: `10.1021/j100803a040`.

(27) Pedley, J. B.; Marshall, E. M. Thermochemical Data for Gaseous Monoxides. *J. Phys.
      Chem. Data.* **1983**, *12*, 967–1031.

(28) Hameka, H. F.; Jensen, J. O.; Kay, J. G.; Rosenthal, C. M.; Zimmerman, G. L. Theoretical
      Prediction of Geometries and Vibrational Infrared Spectra of Ruthenium Oxide Mo-
      lecules. *J. Mol. Spectrosc.* **1991**, *150*, 218–221, DOI: `10.1016/0022-2852(91)`
      `90204-N`.

(29) Schäfer, H.; Tebben, A.; Gerhardt, W. Zur Chemie Der Platinmetalle. V Gleichgewichte
      Mit $Ru_{(f)5}$ $RuO_{2(f)5}$ $RuO_{3(g)}$ Und $RuO_{4(g)}$. *Z. Anorg. Allg. Chem.* **1963**, *321*, 41–55, DOI:
      `10.1002/zaac.19633210105`.

(30) Alcock, C. B.; Hooper, G. W. Thermodynamics of the Gaseous Oxides of the Platinum-
      Group Metals. *Proc. R. Soc. A* **1960**, *254*, 551–561, DOI: `10.1098/rspa.1960.0040`.

(31) Levin, I. W.; Abramowitch, S. *J. Chem. Phys.* **1969**, *50*, 4860.

(32) Penman, B. D.; Hammer, R. R. *The Ruthenium Dioxide-Oxygen-Ruthenium Tetroxide
      Equilibrium*; Report IN 1013; 1968.

(33) Pankratz, L. Thermodynamic Properties of Elements and Oxides., U.S. Bureau of Mines,
      Bulletin 672, 1982.

(34) Rard, J. A. Correction - Chemistry and Thermodynamics of Ruthenium and Some of Its Inorganic Compounds and Aqueous Species. *Chem. Rev.* **1986**, *86*, 731–731, DOI: `10.1021/cr00074a600`.

(35) Glushko, V. P.; Gurvich, L. V.; Veits, I. V.; Medvedev, V. A.; Khachkuruzov, G. A.; Yungman, V. S.; Bergman, G. A., *Termicheskie Konstanty Veshchestv*; Glushko, V. P., Ed.; Nauka: Moscow, 1978-1982; Vol. 1-4.

(36) Shimanouchi, T. Table of Molecular vibrational Frequencies. Consolidated Volume II. *J. Phys. Chem.* **1977**, *6*, 1024.

(37) A., L.; Y., M. The entropies of Polyatomic Gaseous Ions. *Chem. Rev.* **1984**, *84*, 89.

(38) Hultgren, R.; Orr, R.; Anderson, D.; Kelley, K. Selected Values of Thermodynamic Properties of Metals Alloys., ed. by Wiley, J.; Sons, 1974.

(39) Green, D.; Kay, J.; Duca, K.; Zimmerman, G. L.; Balko, B. *J. Mol. Spectrosc.* **1989**, *138*, 62.

(40) Kay, J.; Green, D.; Duca, K.; Zimmerman, G. L. *J. Mol. Spectrosc.* **1989**, *138*, 49.

(41) Backman, U.; Lipponen, M.; Auvinen, A.; Unto, T.; Riitta, Z.; Jorma, K. J. On the transport and speciation of ruthenium in high temperature oxidising conditions. *Radiochimica Acta* **2005**, *93*, 297–304, DOI: `10.1524/ract.93.5.297.64280`.

(42) Backman, U.; Lipponen, M.; Auvinen, A.; Jokiniemi, J.; Zilliacus, R. Ruthenium behaviour in severe nuclear accident conditions - final report., VTT Processes, Report No. PRO3/P27/04, Finland, 2004.

(43) Kleykamp, H. The chemical state of the fission products in oxide fuels. *Journal of Nuclear Materials* **1985**, *131*, 221 –246, DOI: `10.1016/0022-3115(85)90460-X`.

(44) Bowsher, B. Fission product chemistry and aerosol behaviour in the primary circuit of a pressurised water reactor under severe accident conditions. *Prog. Nuclear Energy* **1987**, *20*, 199 –233.

(45) ApSimon, H. M.; Wilson, J. J. N.; Simms, K. L. Analysis of the Dispersal and Deposition of Radionuclides from Chernobly Across Europe. *Proceedings of the Royal Society of London A: Mathematical, Physical and Engineering Sciences* **1989**, *425*, 365–405, DOI: `10.1098/rspa.1989.0111`.

(46) H., A. Radioactivity Emission from the Chernobyl Accident in Comparison with the Results of the SASCHA Program. *Radiochimica Acta* **1987**, *41*, 141, DOI: `10.1524/ract.1987.41.4.141`.

(47) Broda, R.; Mietelski, J. W.; Sieniawski, J. Radioactive [125]Sb and ^{60}Co in "ruthenium" hot particles from Chernobyl fallout. *Journal of Radioanalytical and Nuclear Chemistry* **1992**, *166*, 173–180, DOI: `10.1007/BF02164740`.

(48) Ronneau, C.; Cara, J.; Rimski-Korsakov, A. Oxidation-enhanced emission of ruthenium from nuclear fuel. *Journal of Environmental Radioactivity* **1995**, *26*, 63 –70, DOI: `10.1016/0265-931X(95)91633-F`.

(49)   Potter, P. Some phase equilibria and thermodynamic considerations for irradiated oxide nuclear fuels., JNRC, IAEA Panel meeting on the Behavior and Chemical State of Fission Products in irradiated Fuels, Wien, 1972.

(50)   Miradji, F.; Cousin, C.; Souvi, S.; Vallet, V.; Denis, J.; Tanchoux, V.; Cantrel, L. Modelling of Ru behaviour in oxidative accident conditions and first source term., Proceeding in European Review Meeting on Severe Accident Research (ERMSAR 2015), Marseille, March 24-26, 2015.

(51)   March, P.; Simondi-Teisseire, B. Overview of the facility and experiments performed in Phébus FP. *Annals of Nuclear Energy* **2013**, *61*, Special Issue : Phebus {FP} Final Seminar, 11 –22, DOI: `10.1016/j.anucene.2013.03.040`.

(52)   Ducros, G; Malgouyres, P.; Kissane, M; Boulaud, D; Durin, M Fission product release under severe accidental conditions: general presentation of the program and synthesis of VERCORS 1-6 results. *Nuclear Engineering and Design* **2001**, *208*, 191 –203, DOI: `10.1016/S0029-5493(01)00376-4`.

(53)   Ducros, G.; Pontillon, Y.; Malgouyres, P. Synthesis of the VERCORS experimental programme: Separate-effect experiments on Fission Product release, in support of the PHEBUS-FP programme. *Annals of Nuclear Energy* **2013**, *61*, Special Issue : Phebus {FP} Final Seminar, 75 –87, DOI: `10.1016/j.anucene.2013.02.033`.

(54)   Cox, D. S.; Hunt C. E. L.and Liu, Z.; Keller N. A.and Barrand, R. D.; O' Connor, R. F.; Iglesias, F. C. Fission product releases from UO2 in air and inert conditions at 1700-2350 K: analysis of the MCE-1 experiment., Int. Topical Meeting, Portland, 1991.

(55)   Hunt, C. E. L.; Cox, D. S.; Liu, Z.; Keller, N. A.; Barrand, R. D.; O'Connor, R. F.; Iglesias, F. C. Ruthenium release in air., Saskatoon, Saskatchewan, 1991.

(56)   Material release from the bundle in Phébus FP.

(57)   Brillant, G.; Marchetto, C.; W., P. Ruthenium release from fuel in accident conditions. *Radiochimica Acta* **2010**, *98*, 267, DOI: `10.1524/ract.2010.1719`.

(58)   Kärkelä, T.; Vér, N.; Haste, T.; Davidovich, N.; Pyykönen, J.; Cantrel, L. Transport of Ruthenium in Primary Circuit Conditions During a Severe {NPP} Accident. *Ann. Nucl. Energy* **2014**, *74*, 173–183, DOI: `10.1016/j.anucene.2014.07.010`.

(59)   Vér, N.; Matus, L.; Pintér, A.; Osán, J.; Hózer, Z. Effects of different surfaces on the transport and deposition of ruthenium oxides in high temperature air. *Journal of Nuclear Materials* **2012**, *420*, 297 –306, DOI: `10.1016/j.jnucmat.2011.09.030`.

(60)   Vér, N.; Matus, L.; Pintér, A.; Osán, J.; Hózer, Z. Effects of Different Surfaces on the Transport and Deposition of Ruthenium Oxides in High Temperature Air. *J. Nucl. Mater.* **2012**, *420*, 297–306, DOI: `10.1016/j.jnucmat.2011.09.030`.

(61)   Kärkelä, T.; Backman, U.; Auvinen, A.; Zilliacus, R.; Lipponen, M.; Kekki, T.; Tapper, U.; Jokiniemi, J. Experiments on the Behaviour of Ruthenium in Air Ingress Accidents - Final Report., SARNET-ST-P58, VTT-R-01252-07, 2007.

(62)   Demenay, A. Etude du transport et de la réactivité du ruthénium dans le circuit primaire en conditions accidentelles., IRSN internal document, 2012.

(63) Davidovich, N. Comparative Analysis and Determination of Thermo-Hydraulic Conditions for SARNET Ruthenium Release Experiments in Air Environment., SARNET-ST-P22, 2008.

(64) Bale, C. et al. FactSage thermochemical software and databases, 2010-2016. *Calphad* **2016**, *54*, 35 –53, DOI: 10.1016/j.calphad.2016.05.002.

(65) De Bettencourt A., O.; A, J. Ruthenium volatility during vitrification of fission products. Part II Fixation on a steel tube. Peroxide decomposition., Report CEA-R-3663 (II), 1969.

(66) Kajan, I.; Kärkelä, T.; Auvinen, A.; Ekberg, C. Ruthenium chemistry and transport in a RCS due to air radiolysis products., submitted to J. Radioanalytical and Nuclear Chem., 2016.

(67) Mun, C.; Cantrel, L.; Madic, C. Review of Literature on Ruthenium Behavior in Nuclear Power Plant Severe Accidents. *Nucl. Technol.* **2006**, *156*, 332–346.

(68) Polanyi, J. C. Erratum: Isotopic Reaction Rates Between Methyl and Hydrogen. *J. Chem. Phys.* **1956**, *24*, 493–493, DOI: 10.1063/1.1742533.

(69) Huffman, R. E.; Davidson, N. Shock Waves in Chemical Kinetics: The Thermal Decomposition of NO21a. *Journal of the American Chemical Society* **1959**, *81*, 2311–2316, DOI: 10.1021/ja01519a008.

(70) Harrison, H.; Johnston, H. S.; Hardwick, E. R. Kinetics of the Thermal Decomposition of Nitric Acid Vapor. IV. A Shock Tube Study Between 800-1200°K. *Journal of the American Chemical Society* **1962**, *84*, 2478–2482, DOI: 10.1021/ja00872a004.

(71) Ellis, W. R.; Murray, R. C. The thermal decomposition of anhydrous nitric acid vapour. *Journal of Applied Chemistry* **1953**, *3*, 318–322, DOI: 10.1002/jctb.5010030706.

(72) B, C.; B., S. T. STEM: An IRSN Project on Source Term Evaluation and Mitigation. *American Nuclear Society* **2010**, *103*, 475–476.

(73) NEa Source Term Evaluation and Mitigation (STEM) Project., Nuclear Energy Agency, 2015.

(74) Leroy, O.; Ohnet, M.; Planteur-Kieffer, S. Study of the Ruthenium transport under prevailing conditions in the primary circuit in case of a PWR severe accident., ERMSAR 2015, Marseille, March 24-26, 2015.

(75) Mun, C.; Bosland, L.; Cantrel, L.; Colombani, J.; Leroy, O.; Ohnet, M.-N.; Albiol, T. OECD/STEM PROJECT AND ITS FOLLOW-UP STEM2., Proceedings of the International OECD-NEA/NUGENIA-SARNET, Marseille, March 30- April 1, 2015.

(76) Graham, R.; Johnston, H. *J. Phys. Chem.* **1978**, *82*, 254–268.

(77) Girault, N.; Cantrel, L. *Proposition d'étude expérimentale de la radiolyse de l'air et son interaction avec la chimie de l'iode en phase gaz*; tech. rep., Programme PARIS, Note technique IRSN 02-05; 2002.

(78) Kajan, I.; Kärkelä, T.; Tapper, U.; Johansson, L.-S.; Gouëllo, M.; Ramebäck, H.; Holmgren Stina andAuvinen, A.; Ekberg, C. Impact of Aerosols on the Transport of Ruthenium in the primary circuit of nuclear power plant., VTT Processes, Report No. AFT/NKS-R(14)111/1, Finland, 2015.

(79) Mun, C.; Cantrel, L.; Madic, C. Study of RuO$_4$ Decomposition in Dry and Moist Air. *Radiochim. Acta* **2007**, *95*, 643–656.

(80) Schruoffeneger, B.; tech. rep., Communication interne IRSN/DPAM/SEMIC; 2002.

(81) C., M. Etude du comportement du produit de fission ruthénium dans l'enceinte de confinement d'un réacteur nucléaire, en cas d'accident grave., Université de PARIS-XI ,U.F.R. SCIENTIFIQUE D'ORSAY, 2007.

(82) Krauss, M.; Stevens, W. J. *J. Chem. Phys.* **1985**, *82*, 5584.

THEORETICAL TOOLS

The thermodynamic properties of Ru target species are very scarce, as discussed in the previous Chapter. These uncertainties are related to the molecular properties used by authors [1–4] to derive the thermodynamic functions. The few experimental measurements available to determine the Ru gaseous compounds structural and thermodynamical properties present huge differences, due to the difficulties in isolating these systems at room temperature. In this work, we proposed to obtain the desired molecular energy states and properties using quantum chemistry methods.

Computational chemistry has emerged as a valuable tool for investigating atomic and molecular properties. It is currently widely used by specialists or non-specialists at universities and industries. In fact, this modelling tool, with methods based upon the fundamental laws of quantum mechanics, allows us to solve problems related to molecular structures and reactivities as well as spectroscopic parameters, and other molecular properties, obtained by using of sophisticated program packages that implement advanced computational electronic-structure theories. With the continuous development of modelling theories algorithms and computer power, tackling chemical problems that only a few years ago seemed for beyond the reach of a rigorous quantum-mechanical treatment has become routinely.

Nevertheless, one of the main problems in computational chemistry is the selection of a suitable level of theory for a given problem, and the ability to evaluate the quality of the obtained results.

Some examples of criteria that might be of importance when a method is discussed are:

- *Size-extensive* - the energy has a correct linear scaling with the number of electrons. A size-extensive method makes it possible to compare calculations involving different numbers of electrons, as when describing ionisation processes or when calculations with the various numbers of electrons need to be compared. For a homogeneous system, the solutions for an isolated subsystem can be used to construct the solution for

the compound system since the energy has the proper scaling. A commonly used, less well defined, term is *size-consistent*, where the calculated energy scales correctly for a molecular system that consists of two separated, non-interacting subsystem. Size-consistency usually, implies correct dissociation into fragments.

- *Variational* - the energy from a variational method is an upper bound to the correct ground state energy.

- Efficient - useful/applicable for reasonably sized systems with proper basis sets.

- Accurate - in the sense that it should give an adequate approximation to the best available method together with a high-quality basis set expansion.

In fact, depending on the desired accuracy and the nature of the system at hand, calculations may reveal limitations and suggest improvements in the underlying theory, possibly resulting in more computationally simulations. Consequently, high levels of theory are limited to relatively small molecules with few valence electrons. For heavy atoms like Ru which is a transition metal, the large number of electrons (44) and the high nuclear charge imposes the use of relativistic methods with accurate treatments of electron correlation effects. The challenge of this study is to find a tradeoff between the accuracy of calculation and computational cost.

Most of the following calculations will focus on the description of individual molecules. The link between the properties of a single molecule, or a small collection of molecules, and the macroscopic observables (derived from experiment) is statistical mechanics. In fact, macroscopic properties, such as heat capacity, entropy, *etc*, are related to large ensemble of molecules having a certain distribution of energies. If all the possible energy states can be determined for an individual molecule or a small collection of molecules, statistical mechanics can be used to calculate macroscopic properties.

This chapter provides an introductory overview of the theory underlying the methodologies for these goals.

We will introduce the basic theoretical background in quantum chemistry in the first section. The main electronic structure methods used in this work will be presented, in the three next sections. Relativistic quantum chemistry effects are discussed in the fifth section. The theories used in statistical physics to obtain the thermodynamic and kinetic parameters will be briefly reviewed in the last section.

3.1   Introduction to Quantum Chemistry

According to the fundamental postulates in quantum mechanics, the state n of a system is fully described by a wave function $\Psi_n(r_1, r_2, ..., t)$ where $r_1, r_2, ...$ are the spatial coordinates of particles $1, 2, ...$ that constitute the system and t is the time. Ψ is called the time-dependent wave function of the system. The product of Ψ with its complex conjugate ($\Psi^*\Psi$, or $|\Psi|^2$) is interpreted as the probability distribution of the particle. As we are interested in stationary states of our systems, the wave function will refer to its time-independent formulation denoted $\psi_n(r_1, r_2, ...)$.

The total energy is obtained by applying the Hamiltonian operator to the wave function [5]:

$$\boldsymbol{H}\psi_n = E\psi_n \tag{3.1}$$

It is the time-independent Schrödinger equation [6], where the Hamiltonian $\mathbf{H} = \mathbf{T} + \mathbf{V}$, is the sum of $\mathbf{T}$ the kinetic operator of the system and $\mathbf{V}$ the potential energy one. Depending on the formulation of $\mathbf{H}$, equation 3.1 can be relativistic [7, 8] or not. Relativistic effects become important when the particle velocity approaches the speed of light, as a result of a high nuclear charge. This aspect will be described in section 3.4. For a molecular system, the non relativistic Hamiltonian can be written (in atomic units) as:

$$\mathbf{H} = \underbrace{-\sum_i \frac{1}{2}\boldsymbol{\nabla}_i^2}_{\text{electrons kinetic energy}} \underbrace{-\sum_A \frac{1}{2M_A}\boldsymbol{\nabla}_A^2}_{\text{nuclei kinetic energy}} \underbrace{-\sum_{i,A} \frac{Z_A}{\boldsymbol{r}_{iA}}}_{\text{electron-nucleus coulomb attraction}}$$

$$\underbrace{+\sum_{i<j} \frac{1}{\boldsymbol{r}_{ij}}}_{\text{electron-electron repulsion}} \underbrace{+\sum_{A<B} \frac{Z_A Z_B}{\boldsymbol{R}_{AB}}}_{\text{nuclear repulsion}} \tag{3.2}$$

where i, j stand for electrons and A, B for nuclei. Equation 3.1 can be resolved analytically for a system with one particle, or hydrogen-like atoms. For many-body systems, the solutions are approached with mathematical techniques. The Born-Oppenheimer [9] approximation is the first of several approximations used to simplify Schrödinger equation.

3.1.1 Born-Oppenheimer approximation

To overcome the difficulties of solving Schrödinger equations for many-body systems, the Born-Oppenheimer [9] approximation takes advantage of the significant difference between the masses of electrons and nuclei. Because of this difference, the electrons can respond almost instantaneously to displacements of the nuclei. Therefore, instead of trying to solve the Schrödinger equation for all the particles simultaneously, we regard the nuclei as fixed in position and solve the Schrödinger equation for the electrons in the static electric potential arising from the nuclei in that particular arrangement. Thus the electron distribution within a molecular system depends on the positions of the nuclei, and not on their velocities. The role of the stationary nuclei is to generate an electrostatic potential in which the electron moves. So we can construct an electronic Hamiltonian which neglects the kinetic energy term of the nuclei, equation 3.2 becomes:

$$\boldsymbol{H_{el}} = -\sum_i \frac{1}{2}\boldsymbol{\nabla}_i^2 - \sum_{i,A} \frac{Z_A}{\boldsymbol{r}_{iA}} + \sum_{A<B} \frac{Z_A Z_B}{\boldsymbol{R}_{AB}} + \sum_{i<j} \frac{1}{\boldsymbol{r}_{ij}} \tag{3.3}$$

The nuclear positions only enter as parameters in the Born-Oppenheimer approximation. The motion of electrons in the field of fixed nuclei is described as:

$$\boldsymbol{H_{el}}\psi_{el}(\boldsymbol{r},\boldsymbol{R}) = E_{el}(\boldsymbol{R})\psi_{el}(\boldsymbol{r},\boldsymbol{R}) \tag{3.4}$$

By varying the nuclear coordinates in equation 3.3, a so-called electronic potential energy surface of E_{el} is obtained. The optimal geometry of a molecule is found at the minimum of the potential energy surface, and the derivatives describe the vibrational and rotational properties. The Born-Oppenheimer approximation is very reliable for electronic ground states (seek on this work) however, breaks down when two (or more) solutions to the electronic Schrödinger equation become nearly degenerate.

3.1.2 Restrictions on the Wave function

The electrons being fermions, the wave function must be anti-symmetric with respect to exchange of the particles:

$$\psi(i,j) = -\psi(j,i) \tag{3.5}$$

This antisymmetric property also refers to the Pauli principle stating that two identical fermionic particles cannot occupy the same quantum state simultaneously. For a n-particle function it reads:

$$\psi(r_1,...,r_i,...,r_j,...,r_n) = -\psi(r_1,...,r_j,...,r_i,...,r_n) \tag{3.6}$$

An exact solution of the Schrödinger equation that fulfils all these conditions is impossible for any but hydrogen-like atoms or the di-hydrogen cation H_2^+. Some assumptions and procedures have been developed to make an approximate solution possible for a broad range of molecules, starting with the Hartree-Fock approximation.

3.1.3 Hartree-Fock approach

3.1.3.1 The independent particle approximation

A useful approximation when solving the Schrödinger equation for a n-electron system, is the *independent particle approximation*, where the n-electron wave function is described as a product of n one-electron functions. The description of one electron moving in an average field generated by the rest of the $(n-1)$ electrons is called the *mean field approximation*. Since the electrons are fermions with spin 1/2, the electronic wave function needs to fulfil the requirement of being anti-symmetric under particle interchange and the Pauli exclusion principle, stating that two identical fermions can not occupy the same quantum state simultaneously. A trial wave function that satisfies both requirements is the Slater Determinant (SD), a single determinant built up from orthonormal spin-orbitals[1]

$$\psi(r_1, r_2, ..., r_N) = \frac{1}{\sqrt{N!}} \begin{pmatrix} \phi_2(r_1) & \phi_2(r_1) & ... & \phi_N(r_1) \\ \phi_1(r_2) & \phi_2(r_2) & ... & \phi_N(r_2) \\ \vdots & \vdots & \ddots & \vdots \\ \phi_1(r_N) & \phi_2(r_N) & ... & \phi_N(r_N) \end{pmatrix}; \langle \phi_i | \phi_j \rangle = \delta_{ij} \tag{3.7}$$

with the electron coordinates in rows and the spin-orbitals in columns.

---

[1] A one-electron wave function including electron spin.

3.1.3.2 Basis sets approximation

In practice, the unknown molecular spin-orbitals are expressed regarding a finite set of known basis functions. Any basis functions may in principle be used: exponential, Gaussian, polynomial, cube functions, wavelets, plane waves, etc. For bound atomic and molecular systems, the functions should vanish to zero as the distance between the nucleus and the electron increases. In atomic and molecular calculations, the basis functions are usually centred on the atomic nuclei, since such functions are known to be exact solutions for the hydrogen atom and therefore bear resemblance to atomic orbitals. Actually, more general mathematical treatment is used to describe an individual molecular orbital, any set of appropriately defined functions may be used.

The molecular orbital (MO) ϕ_i is expanded in terms of the basis functions χ, conventionally called atomic orbital (MO=LCAO, Linear Combination of Atomic orbitals [10]):

$$\phi_i = \sum_{\mu=1}^{N} c_{\mu i} \chi_{\mu} \tag{3.8}$$

where the coefficients $c_{\mu i}$ are known as the molecular orbital expansion coefficients. To represent the different MOs, we have to consider three areas on systems as depicted in figure 3.1.
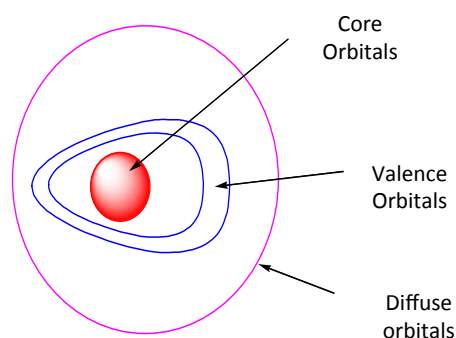
Figure 3.1: Illustration of areas treatment in basis set conception [11]

- **Core orbitals:** This region can be described as hydrogen-like orbitals, the spherical symmetry is important, as defined in the Slater Orbital Type (STO) basis set:

$$\chi(\boldsymbol{r}) = N\boldsymbol{r}^{n-1}e^{-\zeta r}Y_{lm_l}(\boldsymbol{\theta},\boldsymbol{\phi}). \tag{3.9}$$

N is a normalisation constant and Y_{lm_l} are spherical harmonic functions. To manage calculation, the exponential can be replaced by a gaussian function $exp(-\alpha r^2)$, with $\alpha > 0$.

$$\chi(\boldsymbol{r}) = R(\boldsymbol{r})e^{-\alpha r^2}Y_{lm_l}(\boldsymbol{\theta},\phi) \tag{3.10}$$

The fact that products of two STOs on distinct atoms are more difficult to express than those of Gaussian functions (which give a displaced Gaussian) has led many to expand them in terms of Gaussians. STO-nG basis are minimal basis sets, where n primitive Gaussian orbitals are fitted to a single Slater-type orbital (STO). For example an STO-3G basis set for the $1s$, $2s$, and $2p$ orbitals of the carbon atom are all linear combination of 3 primitive Gaussian functions. However, this minimal basis set remains inadequate to describe molecules with more than two centre electrons; STOs do not have any radial nodes.

Extended basis set approaches, called gaussian type orbitals (GTO), are usually used. In theses formulations, the radial part of the STO basis set is replaced by linear combinations of n gaussian functions.

$$\sum_{i=1}^{n} d_i e^{-\alpha_i r^2} \tag{3.11}$$

This description is appropriate to describe electronic core orbitals which present spherical symmetry when using a lot of gaussian functions. For valence zone, we need further improvements.

- **Valence orbitals** The minimal basis set contains one basis function to each occupied atomic orbital, defined as basis set of $Single-\zeta$ quality. To improve the description of systems where the charge distribution is delocalised away from the spherical core orbitals, the basis set can be split into two basis functions to describe each atomic orbital, defined as basis set of $Double-\zeta$ quality. Additional splittings lead to the $Triple-\zeta$, $Quadruple-\zeta$ and so on qualities. Polarisation functions can also be added to the basis set, consisting of higher angular momentum functions, essential for the description of electronic correlation.

- **Diffuse orbitals** At long distances, to improve the description of the tail portion of each atomic orbitals, we can add diffuse basis functions, which have small α exponents. These functions can be substantial when considering negatively charged molecules and van der Waals complexes.

For a chemical reaction, the most important orbitals are the bonding orbitals that involve combination of the valence orbitals of the bonded atoms. When performing quantum calculation, a significant computational effort is spent on determining the MO expansion coefficients in front of core orbitals that change very little depending on the chemical bonding situation, so these inner basis functions also change marginally.

To reduce this computational cost and apply it on chemical interesting part of the wave function, an approach is to combine the full set of basis functions, known as the primitive

GTOs (PGTOs), into a smaller set of functions by forming fixed linear combinations, known as basis set contractions, and the resulting functions are called contracted GTOs (CGTOs). The basis sets are segmented or general contracted type:

- In a segmented contraction each primitive is used only in one contracted function, i.e. the primitive set of functions is partitioned into disjoint sets. This approach leads to produce multiple minima, and selecting a suitable "optimum" solution may be non-trivial.

- In a general contraction all primitives (on a given atom) enter all the contracted functions, but with different contraction coefficients.

Examples of general contracted basis sets are the Atomic Natural Orbitals (ANOs)[12], while for segmented basis sets, the correlation consistent (cc) proposed by Dunning[13] exist almost for the whole periodic table. Both ANOs and cc basis sets are optimised on correlated atomic calculations and are geared towards recovering the correlation energy of the valence electrons. Their size, VXZ (X=3...6) increases by adding shells (or sets) of functions that contribute similar amounts of correlation energy. They are designed to converge smoothly towards the Complete Basis Set (CBS) limit. Aug-cc basis sets have diffuse functions for negatively charged species.

The quality of basis set expansion is critical for the accuracy of a quantum chemical calculation, the greater the expansion of the basis set, the better the resulting MOs and the closer one approaches the exact wave function.

3.1.3.3   Variational principle

To describe the stationary states of the molecular system as Slater determinants, the energy is required to be stationary with respect to the variation of the spin orbitals. According to the variational principle, the determinant giving the lowest energy is the solution closest to the exact wave function of the ground state. In other words, the spin orbitals should be chosen such that they minimise the expectation value of the electronic Hamiltonian H_{el}.

The mean value of $\boldsymbol{H}$ in a given state $|\psi\rangle$ is always upper or equal to those of system ground state E_0:

$$E = \langle \boldsymbol{H} \rangle = \frac{\langle \psi | \boldsymbol{H} | \psi \rangle}{\langle \psi | \psi \rangle} \geq E_0 \tag{3.12}$$

For a normalized wave function the denominator is 1, and therefore $E = \langle \psi | \boldsymbol{H} | \psi \rangle \geq E_0$.

3.1.3.4   The Hartree-Fock equations

If a single Slater determinant is used as a trial wave function, pseudo-eigenvalue equations for the molecular spin-orbitals ϕ_i, $i = 1, n$, the Hartree-Fock equations are derived:

$$\boldsymbol{F_i} \phi_i = \epsilon_i \phi_i \tag{3.13}$$

where $\boldsymbol{F_i}$, the Fock operator for one electron, can be written as:

$$\boldsymbol{F_i}(\boldsymbol{r}) = \boldsymbol{h_i}(\boldsymbol{r}) + \sum_{j=1}^{n} |\boldsymbol{J}_j(\boldsymbol{r}) - \boldsymbol{K}_j(\boldsymbol{r})| \tag{3.14}$$

In equation 3.14, $\boldsymbol{h_i}(\boldsymbol{r})$ refers to one-electron Hamiltonian sum of the kinetic energy of electron i and the electron-nuclei potential energy:

$$\boldsymbol{h_i}(\boldsymbol{r}) = \frac{1}{2}\Delta_i + \sum_{K=1}^{N} \frac{Z_K}{r_{iK}} \tag{3.15}$$

The electron-electron repulsion is contained in the two-electron J_j and K_j operators: the Coulomb operator J_j gives the electrostatic interaction of an electron in orbital ϕ_i with the average charge distribution from the others, while the exchange operator K_j is a purely non-classical term–it arises from the antisymmetry conditions and prevents electrons with parallel spins from occupying the same position in space.

$$\boldsymbol{J}_j\phi_i(\boldsymbol{r}_1) = \left[\int \frac{\phi_j^*(\boldsymbol{r}_2)\phi_j(\boldsymbol{r}_2)}{r_{12}} dr_2 \right]\phi_i(\boldsymbol{r}_1)$$
$$\boldsymbol{K}_j\phi_i(\boldsymbol{r}_1) = \left[\int \frac{\phi_j^*(\boldsymbol{r}_2)\phi_i(\boldsymbol{r}_2)}{r_{12}} dr_2 \right]\phi_j(\boldsymbol{r}_1) \tag{3.16}$$

If ϕ_i is the eigenfunction, the eigenvalue of equation 3.13 is:

$$\epsilon_i = \langle\phi_i|\boldsymbol{h}_i|\phi_i\rangle + \sum_{j=1}^{n} \left[\boldsymbol{J}_{ij} - \boldsymbol{K}_{ij} \right] \tag{3.17}$$

where $\boldsymbol{J}_{ij} = \langle\phi_i|\boldsymbol{J}_j|\phi_i\rangle$ and $\boldsymbol{K}_{ij} = \langle\phi_i|\boldsymbol{K}_j|\phi_i\rangle$.
Finally, the Hartree-Fock energy is written as:

$$\boldsymbol{E}_{HF} = \sum_{i=1}^{n} \epsilon_i - \frac{1}{2}\sum_{i=1}^{n}\sum_{j=i}^{n}(\boldsymbol{J}_{ij} - \boldsymbol{K}_{ij}) = \sum_{i=1}^{n} \epsilon_i - \frac{1}{2}\sum_{i=1}^{n}\sum_{j=i}^{n}\langle ij||ij\rangle \tag{3.18}$$

Solving equation 3.18 allows us to find a set of n eigenvalues $\{\epsilon_i\}$.

The resolution of these equations, when taking account of basis set approximations has been derived by Roothaan and Hall [14]. The problem set in equation 3.13 becomes a matrix equation with the basis functions:

$$\boldsymbol{F}\boldsymbol{C} = \mathrm{S}\boldsymbol{C}\epsilon \tag{3.19}$$

where ϵ is the diagonal matrix of orbital energies, each of its elements ϵ_i is the one-electron orbital energy of molecular orbital χ_i, $\boldsymbol{F}$ is the Fock matrix, representing the average effects of the field of all electrons in each orbital.
The S matrix is the overlap matrix between the spin-orbitals and the orbitals and the C matrix represents the molecular orbital expansion coefficients. As $\boldsymbol{F}$ depends on the solutions of ϕ_i, the Roothan equation are solved iteratively. The procedure which does so is called the Self Consistent Field (SCF) method [15]: to determine the unknown MO coefficients $c_{\mu i}$, an initial

set of orbitals are used to generate a new set, the process is then repeated until an energy convergence criteria is fulfilled; in each iteration step the Fock matrix must be diagonalised. For the N occupied orbitals, the ground state wave function is optimised with the lowest orbital energies, included in the Slater determinant. The remaining $M - N$ MOs are called virtual orbitals. The highest occupied (HOMO) and lowest unoccupied (LUMO) molecular orbitals are the most likely to be involved and change along a chemical reaction path.

3.1.3.5 Restricted and Unrestricted Hartree Fock

The Slater determinant has been written in terms of products of a spatial orbital and a spin function (α or β). For systems with one or more open shell electrons, spin-orbital with individual spatial coordinates for each spin function can be used,

$$\phi_i(r) = \begin{cases} \phi_i^\alpha(r)\alpha(\omega) \\ \phi_i^\beta(r)\beta(\omega) \end{cases} \tag{3.20}$$

where $\alpha(\omega)$ and $\beta(\omega)$ correspond to spin-up and spin-down respectively, and ω is an unspecified spin variable. It is the *Unrestricted Hartree-Fock* (UHF) approach. The UHF wave function is usually not an eigenfunction of the total spin $\hat{S}^2$ and the method can suffer from effects due to *spin contamination*. It is an artefact due to a mixing of higher spin states in the resulting wave function. This means that a "singlet" UHF wave function may also contain contributions from higher lying triplet, quintet, *etc*, states. Similarly, a "doublet" UHF wave function will contain spurious (non-physical) contributions from higher lying quartet, sextet, ..., states. A high spin contamination can strongly affect the result of a geometry optimisation or reaction energies.

One can also impose the spatial orbitals of the $\alpha(\omega)$ and $\beta(\omega)$ spins to be identical:

$$\phi_i(r) = \begin{cases} \phi_j(r)\alpha(\omega) \\ \phi_j(r)\beta(\omega) \end{cases} \tag{3.21}$$

This is the *Restricted Hartree-Fock* (RHF) theory which applies to closed-shell systems, this approach being variational and size-extensive. Open-shell systems may also be described by restricted type wave functions, where the spatial part of the doubly occupied orbitals is forced to be the same, and this is known as *Restricted Open-shell Hartree-Fock* (ROHF). The various HF schemes are illustrated by Figure 3.2.

As restricted type wave functions put constraints on the variation parameters, the energy of a UHF wave function is always lower than or equal to a corresponding R(O)HF type wave function. By default, RHF solution is a particular solution of UHF ones, but obtaining a real UHF solution (if exists) requires often an additional effort beyond RHF one. For higher multiplets systems, UHF solution is easily obtained, regardless the initial guess of orbitals since α and β orbitals are subject to a different exchange potential. For singlet systems, the obtention of the UHF solution depends extremely on an initial guess of orbitals, since for closed shell, α and β orbitals are subject to the same exchange potential. For first row species, the UHF solution is usually similar to RHF one near the equilibrium and disagreement appear along
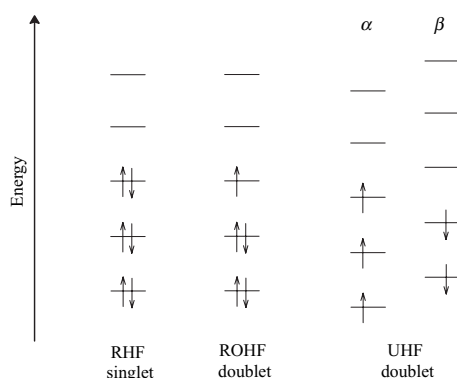
Figure 3.2: Illustrating an RHF singlet, ROHF and UHF doublet states [16]

dissociation pathway. For transition metal, the UHF may have a solution different from the RHF one, even near the equilibrium. Some procedures can be used to obtain the UHF solution. One way to obtain the UHF solution for singlet is to allow UHF calculation to start with a suitable initial guess, such as using initial charge density obtained from higher multiplicity calculations (see Section 3.3.5).

3.2   Electron correlation methods

3.2.1   Generalities concerning electronic correlation

The Hartree-Fock method calculates the energy in the mean-field approximation. It overestimates the exact energy E, as the single-determinant description of the wave function in the HF method lacks the flexibility to account for explicit electron-electron interactions other than that of same-spin electrons, captured in the exchange term. The deviation of the HF energy with respect to the exact energy defines the *correlation energy* [17].

Physically, we have electronic repulsion between two electrons due to their negative charge. Each electron possesses what is called Coulomb hole and Fermi hole that "prevent" particles of the same charge or spin value to be simultaneously at the same position. Electronic correlation is due to this instantaneous repulsion. This effect can by dynamical (essentially atomic-like) or non-dynamical (essentially molecular-like). The dynamical correlation refers to the cases where the electrons avoid each other by occupying different electronic configurations. It results in improvements of the description of the electron cusp, as well as core and valence polarisation effects. The non-dynamical correlation is often renamed as left-right correlation

as it is associated with the failure of single-reference methods (like Hartree-Fock) in describing covalent bond dissociations.

Altogether to approach the exact correlation energy E_{corr}, the wave function needs to acquire flexibility by being expanded over several Slater determinants. This mixing of electronic configurations is important in transition metal compounds, where many electronic levels often have similar energies, and there are strong overlaps between metal and ligand valence orbitals. Excited states may also require a multi-determinant description of the wave function.

Any exact n-electron wave function can be expanded in an infinite number of Slater determinants [15, 18, 19]:

$$|\Psi_n\rangle = C_0^{(n)}|\Phi_0\rangle + \sum_{ar} C_a^{r(n)}|\Phi_a^r\rangle + \sum_{\substack{r<s \\ a<b}} C_{ab}^{rs(n)}|\Phi_{ab}^{rs}\rangle + \sum_{\substack{r<s<t \\ a<b<c}} C_{abc}^{rst(n)}|\Phi_{abc}^{rst}\rangle + ..., \qquad (3.22)$$

where all possible ways of arranging the electrons in the Hartree-Fock orbitals that are empty in the HF determinant $|\Phi_0\rangle$ are included as *singly* excited determinants $|\Phi_a^r\rangle$, *doubly* excited determinants $|\Phi_{ab}^{rs}\rangle$, *triply* excited determinants $|\Phi_{abc}^{rst}\rangle$, ..., as shown by Figure 3.3 in which one or more occupied spin-orbitals $|\phi_a\rangle$ is replaced by a virtual one $|\phi_r\rangle$. These determinants are often referred as Singles (S), Doubles (D), Triples (T), Quadruples (Q), etc. Provided that the basis set is complete, the solution of this *configuration interaction* (CI) method is exact.
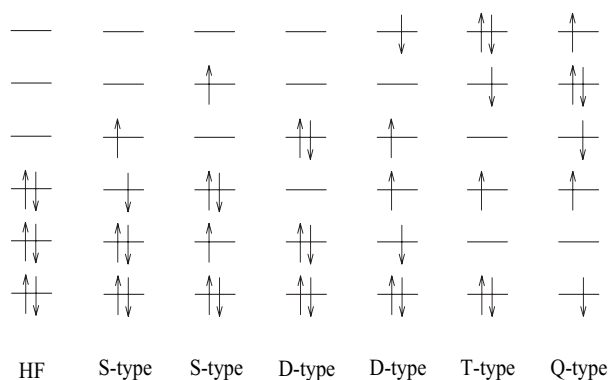
Figure 3.3: Excited Slater determinants generated from an HF reference [16].

$C^{(n)}$ terms refers to the expansion coefficients of wave function $|\psi_n\rangle$, obtained by variational principle, similar to Roothan-Hall equations in Hartree-Fock approach, leading to derive matrix equations. When all possible determinants are considered, interaction configuration is called a *full* CI, in this way all types of correlation are treated, thus leading the exact wave function, within the size of the used basis set. However, even for small systems, the

number of determinants of full CI rapidly becomes enormous and exceeds currently available computational capacities. The common approach is to use a truncated CI, i.e., to limit the number of determinants to a given excitation level. A single and double CI (CISD) includes only single and double excitations. Following some methods used in this work allowing that truncation and determine the $C^{(n)}$ coefficients.

3.2.2 The multi-reference and complete active space (MC-SCF and CASSCF) methods

Some chemical systems can not be correctly described with a single determinant wave function. Low-lying excited states, bond dissociation processes, ground and excited states of d and f metal molecules are examples where a multi-reference wave function is needed for a correct description. A standard approach is to take linear combinations of Slater determinants or configuration state functions into account as in the multi-configurational self-consistent field (MCSCF) [15] wave function can be expressed as follows:

$$|\Phi_{MCSCF}\rangle = \sum_I C_I |\Psi_I\rangle, \qquad (3.23)$$

where $|\Psi_I\rangle$ are the Configurations States Functions (CSFs) [20–22] which are defined as linear combinations of Slater determinants. Both the wave function and the orbital coefficients, $\{c_i\}$, are variationally determined. The multireference wave functions are capable to handling non-dynamic correlation effects, while the recovered amount of dynamical correlation depends on the size of the *active space*.

The complete active space SCF (CASSCF) method [23, 24] was developed for taking the most important determinants into account. The complete space of MOs is divided into three subspaces: *inactive orbitals* that are all doubly occupied, *active orbitals*, and *secondary orbitals* that are all empty. A full CI wave function is generated within the active space by letting all possible configurations that can be obtained from electron permutations consistent with the number of electrons and spin multiplicity in the active orbitals contribute to the wave function. At the same time, the orbital coefficients are optimised via all possible rotations between the inactive-active, active-virtual, and inactive-virtual orbitals.

As for any full CI expansion, the number of determinants grows rapidly with the number of active orbitals considered, which makes CASSCF a computationally challenging method. To reduce the computational cost, a variation of the CASSCF procedure has been proposed: the Restricted Active Space Self-Consistent Field (RASSCF) method [25]. Here the active MOs are divided into three subspaces, RAS1, RAS2 moreover, RAS3, each having restrictions on the occupation numbers (excitations) allowed (see figure 3.4), and thus limiting the number of excited configurations included.

There are many factors governing the choice of the active MOs. An important consideration is the nature of the chemical problem that is to be addressed. For example, if a chemical reaction is to be studied, then all orbitals involved in bond breaking/formation must be considered. If, instead, excited state properties are of interest, for example in the simulation of absorption processes, then orbitals whose occupations differ significantly between the ground and excited state must be included.
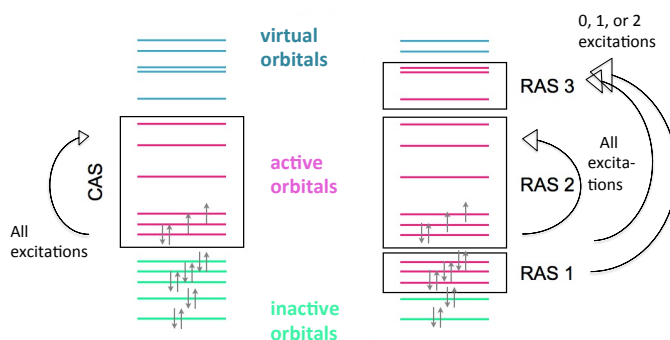
Figure 3.4: Illustrating the CAS and RAS orbital partitions

Björn Roos proposed rules to aid in the construction of active spaces [26] and we can briefly review those important for the ruthenium molecules we will consider in this work:

- Include $2s$ and $2p$ orbitals for light atoms such as Li, B, and C. For N, O, and F, only include $2p$ orbitals.

- Include the valence d-shell of transition metals

3.2.3 Multi-reference configuration interaction methods (MRCI)

The CI methods described so far consider only CSFs generated by exciting electrons from a single determinant. This corresponds to having an HF type wave function as reference. However, a MCSCF wave function may also be chosen as the reference. In that case, a CISD involves excitations of one or two electrons out of all the determinants that enter the MCSCF expansion, defining the Multi-Reference Configuration Interaction (MRCI) method:

$$|\Phi_{MRCI}\rangle = \sum_R C_R|R\rangle + \sum_i C_i|A_i\rangle, \tag{3.24}$$

with $|R\rangle$ represents the MCSCF references configurations and $|A_i\rangle$ refers to all configurations obtained by singly and doubly excitations on the references configurations. In this case, MRCI is called MRCI-SD. If a CASSCF wave function is used as starting point, the reference determinants certainly correspond to at least single or double excitations with respect to the HF determinant $|\Psi_0\rangle$. As a result, the final MRCI wave function will include determinants that are triply and quadruply excited from $|\Psi_0\rangle$. This implies that a large fraction of the exact correlation energy can be recovered from MRCI calculations with a much smaller number of

determinants than the full CI expansion. However, MRCI is not size-extensive since it does not include any contributions from higher than double excitations. The size-extensivity is strongly dependent on contributions from fourth-order excitations, see Refs. [27, 28] and reference therein. A dominating part of the quadruple excitations can be recovered by contributions from two double excitations taking place simultaneously, and based on this, corrections to the size-extensive error can be obtained.

One among the possible corrections is the Davidson correction [29, 30]. It is defined as

$$E_D^n = E_{corr}^n \frac{1 - c_n^2}{c_n^2}, \tag{3.25}$$

where c_n is the coefficient of the reference function in the MRCI wave function. Other size-extensive procedures have also been proposed, such as the MR-ACPF (Multi- Reference Averaged Coupled-Pair Functional) and MR-AQCC (Multi-Reference Averaged Quadratic Coupled Cluster) [31–33] ones. They are efficient for ground states systems calculations but presents deficiency for excited states. All these approaches will be tested in our study.

3.2.4   Perturbation theory methods

One important feature of CI methods is that they are variational, but one disadvantage is their lack of size-extensivity. Perturbation theory (PT) provides an alternative approach to finding the correlation energy. While these approaches are size-consistent, they are not variational in that they do not in general give energies that are upper bounds of the exact energy. As we are interested in energy differences on our chemical systems, the absence of a variational bound can allow for error cancellations. The lack of size extensivity of CI methods is disadvantageous in this respect. In perturbation theory [34], the Hamiltonian is partitioned into a reference Hamiltonian H^0 whose solutions are known, and a H' perturbation operator, defined as follows:

$$\begin{aligned} H &= H^0 + H' \\ H^0 |\Psi_i^{(0)}\rangle &= E_i^{(0)} |\Psi_i^{(0)}\rangle \end{aligned} \tag{3.26}$$

As H' is considered very "small" compared to H^0, the wave function, eigenvector of H, and the energy can be written as a Taylor expansion in powers of a perturbation parameter λ:

$$|\Psi_i\rangle = |\Psi_i^{(0)}\rangle + \sum_j \lambda^j |\Psi_i^{(j)}\rangle; E_i = E_i^{(0)} + \sum_j \lambda^j E_i^{(j)}. \tag{3.27}$$

λ, which values are between 0 and 1, determines the strength of the perturbation so that

$$H = H^0 + \lambda H'. \tag{3.28}$$

The unperturbed wave function $\Psi_i^{(0)}$ and energy $E_i^{(0)}$ are corrected by terms that are of various orders in the perturbation. The correction terms $\Psi_i^{(1)}$ and energy $E_i^{(1)}$, $\Psi_i^{(2)}$ and energy $E_i^{(2)}$,... are called first-order, second-order, ..., corrections to the wave function and energy, respectively. In order to apply perturbation theory to the calculation of correlation energy,

the unperturbed Hamiltonian $\boldsymbol{H}_0$ operator must be selected. The most common choice is to take this as a sum over the Fock operators, leading to Møller-Plesset (MP) perturbation theory [34]. The first order correction of energy in MP method lead to the HF energy. So the second order for the energy, and first-order for the wave function are defined as:

$$
\begin{aligned}
|\Psi_i^{(1)}\rangle &= |\Phi_i^{(0)}\rangle + \sum_{j \neq i} \frac{\langle \Psi_j^{(0)}|\boldsymbol{H'}|\Psi_i^{(0)}\rangle}{E_i^{(0)} - E_j^{(0)}}|\Psi_j^{(0)}\rangle \\
E_i^{(2)} &= \sum_j \frac{|\langle \Psi_j^{(0)}|\boldsymbol{H'}|\Psi_i^{(0)}\rangle|^2}{E_i^{(0)} - E_j^{(0)}}
\end{aligned}
\tag{3.29}
$$

As single-reference CI can be extended to MRCI, it is also possible to use perturbation methods with a multi-determinant reference wave function.

3.2.4.1 Complete Active Space Second Order Perturbation Theory (CASPT2)

The CASPT2 method is one expansion of MP2 approach, that uses as reference wave function $|\Psi_0\rangle$ for a given state $|\Psi_a\rangle$, a CASSCF wave function [35, 36]:

$$
\boldsymbol{H}|\Psi_a\rangle = E_a|\Psi_a\rangle, a = 1, ..., ncf,
\tag{3.30}
$$

where ncf refers to the active space of active orbitals on the CAS. The extension of the method to an RASSCF reference wave function is denoted RASPT2 [37]. The first-order wave function correction is defined in equation 3.31:

$$
|\Psi_a^{(1)}\rangle = \sum_{A \in CAS} \boldsymbol{C}_A|A\rangle + \sum_{\alpha \notin CAS} \boldsymbol{C}_\alpha|\alpha\rangle,
\tag{3.31}
$$

where $|A\rangle$ determinants belong to the CAS space, and $|\alpha\rangle$ are excited determinants with respect to the $|A\rangle$ determinants. $\boldsymbol{C}_\alpha$ coefficients are solutions of equation 3.32:

$$
\sum_{\alpha \notin CAS} \langle \beta|\boldsymbol{H}_0 - E_0|\alpha\rangle \boldsymbol{C}_\alpha = -\langle \beta|\boldsymbol{H}|\Psi_0\rangle, \beta \notin CAS,
\tag{3.32}
$$

where $E_0 = \langle \Psi_0|\boldsymbol{H}|\Psi_0\rangle$. A first solution of $\boldsymbol{H}_0$ is to choose the Generalized Fock Hamiltonian. However, when the excited determinants $\Psi_j^{(i)}$ are close in energy to the reference determinant $\Psi_j^{(0)}$, their contribution to the CASPT2 wave function will diverge, leading to intruder state problems. To reduce these errors, a modified zeroth order Hamiltonian [38] has been proposed. It introduces a shift (the Ionization Potential Electron Affinity, IPEA shift) that modifies the energies of active orbitals such that they become closer to ionization energies when excited from and closer to electron affinities when excited out of.

3.2.4.2 N-Electron Valence state Perturbation Theory (NEVPT2) methods

Another way of avoiding the intruder state problem rests on the use of the Dyall Hamiltonian [39] as zeroth-order Hamiltonian, which has the particularity to contain two-electron

terms, leading to the N-Electron Valence state Perturbation Theory (NEVPT2). It is a form of second-order multireference perturbation theory which can be applied to CASSCF wave-functions or, more generally, to CAS-CI wave functions [40–42]. The most relevant feature of this method consists in that the first order correction to the wave function is expanded over a set of properly chosen multireference functions which correctly take into consideration the two-electron interactions within the active electrons. The other feature of NEVPT2 theory is that the CAS space can be strongly contracted (SC), partially contracted (PC) or totally decon-tracted (CASPT2 has only decontracted CAS). The variants differ by the number of perturber functions employed in the perturbation summation. Because of the two-electron nature of H_0, this method is computationally more demanding. We also performed calculations us-ing the variant of NEVPT2, QDNEVPT2 [43], the Quasi-degenerate Second Order N-Electron Valence State Perturbation Theory, which allows the treatment of cases where the electronic states are nearly degenerate causes artefacts in the zeroth-order description. All these per-turbation methods have been used in this work.

3.2.5 The Coupled Cluster method

In Coupled Cluster (CC) methods [44–47], the idea is to include all corrections of a given type to infinite order. This approach is single reference and non variational, allows to recover dynamical correlation energy. This theory introduces the cluster operator T, which relates the exact electronic wave function Ψ to the HF wave function Ψ_0 through:

$$\Psi = e^{T}\Psi_0, \tag{3.33}$$

where the exponential operator e^{T} can be expressed as a power expansion:

$$1 + T + \frac{1}{2!}T^2 + \frac{1}{3!}T^3 + ... \tag{3.34}$$

In particular, T is the sum of the one-electron excitation operator T_1, two-electron excitation operator T_2 , ..., N-electron excitation operator T_N, as defined in equation 3.35:

$$T = T_1 + T_2 + T_3 + ... + T_{N_{elec}}. \tag{3.35}$$

An excitation operator T_i acting on HF wave function products all ith excited Slater's determin-inants.

$$\begin{aligned}
T_1\Phi_0 &= \sum_{i}^{occ} \sum_{a}^{virt} t_i^a \Phi_i^a \\
T_2\Phi_0 &= \sum_{i<j}^{occ} \sum_{a<b}^{virt} t_{ij}^{ab} \Phi_{ij}^{ab}
\end{aligned}. \tag{3.36}$$

The t_i^a are called single-excitation amplitudes, t_{ij}^{ab} double-excitation amplitudes, and so on. No operators beyond T_N appear because Ψ_0 has all electrons in N occupied spin-orbitals.

The excitation amplitudes are determined by solving the coupled cluster equations; the latter set of equations is derived by substituting $e^{T}\Psi_0$ into the electronic Schrödinger equation [48]. If all cluster operators up to T_N are included in T, all possible excited determinants are generated, and the coupled cluster wave function is equivalent to a full CI. This is impossible for all but the smallest systems. The cluster operator must, therefore, be truncated at some excitation level. One approximate CC method developed by Purvis and Bartlett [49], suggesting to limit T to $T = T_1 + T_2$, it is the Coupled Cluster Singles and Doubles model (CCSD). Whatever the truncation of the CC wave function the power expansion ensures that the approximation is size-extensive [49]. The CCSD energy can be expressed as:

$$E_{CCSD} = \langle\Psi_0|e^{-T}He^{T}|\Psi_0\rangle. \tag{3.37}$$

Computing CC energy variationally like CI leads to series of non-vanishing terms all the way up to order N_{elec}, that increasing computational time hardly. Equation 3.37 is then *projected* onto a space of excited determinants Ψ, thus generating the amplitudes. Starting from a single-reference determinant, the CCSD energy is computed. It directly depends on the single and double amplitudes, with indirect contributions from higher excitations. The calculation of the energy depending on the amplitudes, themselves depending on energy, the process is iterative. A further improvement of the CCSD approximation is to include triples excitations in a perturbative manner, CCSD(T) [50], based on evaluation of fifth order Møller-Plesset and CI correlation energy.

The next CC level uses $T = T_1 + T_2 + T_3$, leading to the CCSDT model [51]. This involves more demanding computational resources. It (and higher order methods such as CCSDTQ) can consequently only be used for small systems, and CCSD and CCSD(T) are the only generally applicable coupled cluster method. Even if CC method is very accurate and size-consistent, it is single-determinant based approach and not variational. In order to have an idea of the multi-reference character of the system, some authors proposed the T_1 diagnostic [52], defined as $T_1 = \frac{\|t_1\|}{\sqrt{N_{elec}}}$, where t_1 are the single-excitation amplitudes. An other diagnostic, D_1 [53, 54] has been defined for the same purpose. If the T_1 and D_1 diagnostic are larger the limits defined for single-reference system [55], other methods should be used to check whether this reveals a multi-configurational character of the wave function. The Brueckner Coupled Cluster Theory [56], uses so-called Brueckner orbitals where the reference orbitals are rotated to make the T_1 amplitudes vanish. All these methods have been applied to our Ru gaseous compounds.

3.3 Density functional theory

The wave-function methods described above all start with the Hartree-Fock approximation in that the HF equations are first solved to find spin-orbitals that can then be used to construct configuration state functions. Limitations are encountered using these methods, in particular, the computational difficulty of performing accurate calculations with large basis sets on molecules containing many atoms and many electrons. An alternative to the wave function methods is density functional theory (DFT). In contrast to the methods described above, DFT begins with the concept of the electron density, instead of CSFs. This procedure

allows to take into account electron correlation while being less demanding computationally, as electron density, and therefore the energy, only depends on the three spatial coordinates. Hohenberg and Khon [57] derived the fundamental theorems behind DFT methods, stating that an electronic system of n electrons can be written in terms of its total electron density, ρ:

$$
\rho(x) = N \sum_{x_p = s_p, r_p} \Psi^*(r_1, s_1, x_2, ..., x_n) \Psi(r_1, s_1, x_2, ..., x_n) ds_1, dx_2, ..., dx_n .
\tag{3.38}
$$

The electronic energy E is said to be a functional of the electron density, denoted $E[\rho]$. For a given external potential $v(r)$, the energy of the ground state is:

$$
E[\rho] \equiv \int v(r) \rho(r) dr + F[\rho].
\tag{3.39}
$$

For a system composed of nuclei and electrons, $v(r)$ corresponds to the Coulomb attraction between them, and $F[\rho]$ corresponds to the sum of kinetic energy, the electron-electron repulsion, exchange and correlation terms. We can rewrite 3.39 as:

$$
E[\rho] \equiv \int v(r) \rho(r) dr + \frac{1}{2} \iint \frac{\rho(r) \rho(r)'}{|r - r'|} + G[\rho],
\tag{3.40}
$$

where $G[\rho] = T[\rho] + E_{xc}[\rho]$ $T[\rho]$ is the kinetic energy term and $E_{xc}[\rho]$ is the exchange and correlation term. $E_{xc}[\rho]$ can be defined as:

$$
E_{xc}[\rho] = \int \rho(r) \epsilon_{xc}(\rho(r)) dr.
\tag{3.41}
$$

If the density has fluctuations, $E_{xc}[\rho]$ is expanded in a serial terms. We obtain then corrections depending on successive density derivatives.

For a system with N electrons, Kohn and Sham [58] derived a variational expression to calculate density. If the wave function is represented by a Slater determinant composed of orthonormal spin orbitals ϕ_i, then we have:

$$
\rho(r) = \sum_i^N \phi_i^*(r) \phi_i(r).
\tag{3.42}
$$

The application of the variational principle to equation 3.39 leads to a system of N coupled equations:

$$
\left\{ -\frac{1}{2} \nabla^2 + \varphi(r) + \mu_{xc}(\rho(r)) \right\} |\phi_i\rangle = \epsilon_i |\phi_i\rangle,
\tag{3.43}
$$

similar to Hartree-Fock ones and named the Kohn-Sham equations, which includes:

$$
\varphi(r) = v(r) + \int \frac{\rho(r')}{|r - r'|} dr',
\tag{3.44}
$$

and

$$
\mu_{xc}(\rho(r)) = \frac{d}{d\rho(r)} (\rho(r) \epsilon_{xc}(\rho(r))).
\tag{3.45}
$$

All the difficulty is to resolve the equation of exchange-correlation potential term $\mu_{xc}(\rho(r))$, due to the expression of $\epsilon_{xc}(\rho(r))$, as we can see later, that cannot be calculated analytically but only with numerical grids.

3.3.1 Exchange-correlation functionals

The main source of error in DFT usually stems from the approximate nature of E_{xc}. Starting from equation 3.41, the exchange-correlation energy can be decomposed into an exchange and a correlation part,

$$E_{xc} = E_x + E_c. \tag{3.46}$$

E_{xc} can also be expressed in terms of exchange and correlation energy per particle:

$$
\begin{aligned}
E_x[\rho] &= \int \rho(\boldsymbol{r})\epsilon_x([\rho];\boldsymbol{r})d\boldsymbol{r} \\
E_c[\rho] &= \int \rho(\boldsymbol{r})\epsilon_c([\rho];\boldsymbol{r})d\boldsymbol{r}
\end{aligned}
. \tag{3.47}
$$

The Local Density Approximation (LDA) method was the first approximation for the exchange-correlation energy, where the energy is a local function of the energy density [59–61]. A uniform electron gas system has a constant electron density and the exchange energy is proportional to the electron density, as given by the Dirac formula:

$$E_x^{LDA}[\rho] = -\frac{3}{2}(\frac{3}{4\pi})^{\frac{1}{3}} \int \rho_\sigma(\boldsymbol{r})^{\frac{3}{4}} \mathrm{d}^3\boldsymbol{r}. \tag{3.48}$$

The use of this approximation induced to consider that the effect of the exchange-correlation hole can be estimated by replacing it by a uniform density inside a small sphere and zero elsewhere, neglecting corrections to the exchange-correlation energy due to inhomogeneities in the electron density. This assumption leads to the self-correlation or self-interaction error (SIE), that arises from an interaction of a single electron with its own density. LDA is reliable for describing molecular structural properties, especially for solid systems [62, 63]. In case of open-shell systems, LDA is replaced by the Local Spin Density Approximation (LSDA) [64]. The accuracy of the local approximation density method decreases with varying electron density in the system and for many molecules.

3.3.2 The generalised gradient approximation

To account for the inhomogeneity of the electron density, a non-local correction involving the gradient of ρ is often added to the exchange-correlation energy, these methods are called generalized gradient approximation (GGA) [65]:

$$E_{xc}^{GGA}[\rho] = \int \rho \epsilon_{xc}^{GGA}(\rho;|\nabla\rho|)d\boldsymbol{r}. \tag{3.49}$$

As the exchange-correlation function can be expressed as the sum of exchange and correlation terms, several approximations have been developed for both terms.
The exchange term can be written as:

$$E_x^{GGa} = \int \rho(r)\epsilon_x^{unifgas}(\rho(r))f(\zeta)dr, \tag{3.50}$$

where f is an enhancement factor, and ζ is a dimensionless variable:

$$\zeta = \frac{|\Delta\rho|^2}{(2(3\pi^2)^{\frac{1}{3}})^2 \rho^{\frac{8}{3}}}. \tag{3.51}$$

"Two families" of exchange functionals can be found:

- empirical functionals: suggested by Becke [64, 66, 67], one of these functionals, B88x, is defined as:

$$f_{B88x}(\zeta) = 1 + \frac{a\zeta}{1 + b\sqrt{\zeta}\sinh^{-1}\left[2(6\pi^2)^{\frac{1}{3}}\sqrt{\zeta}\right]}, \tag{3.52}$$

  where parameter a had been adjusted on exact exchange energy of rare gas, and parameter b allows to ensure asymptotic behaviour of exchange energy.

- rational functionals: suggested by Perdew, one example is the the PW86x functional [65], defined as:

$$f_{PW86x}(\zeta) = (1 + 1.296\zeta + 14\zeta^2 + 0.2\zeta^3)^{\frac{1}{15}}. \tag{3.53}$$

Regarding correlation energy functional, the most famous one is the LYP functional [68]. It contains empirical parameters, adjusted on correlation energy of the helium atom. Comparing to LDA functionals, the GGA functionals enhance the descriptions of bonding energies, bonding distances and more, but they present some restrictions on other fields, due to the truncated Taylor series in the expression of the gradient density. The functional can be enhanced by taking account the Laplacian of the density leading to the so-called meta-GGA functionals.

3.3.3   The meta-generalised gradient approximation

We will describe here one example of meta-GGA functional, the TPSS [69] developed by Tao *et al.*, as we have used it extensively in our molecular investigations. This functional uses an exchange energy functional with parameters determined from a fit of the atomisation energies of 20 small molecules. Furthermore, the correlation part of this functional is self-interaction-free. However, the exchange functional still has small amount of self-interaction, which may be helpful in some systems to artificially mimic the non-dynamic correlation [70, 71].

3.3.4   Hybrid functionals

The Hartree-Fock theory allows calculation of exact exchange energy. Hybrid functionals approach takes advantages of that by combining exchange-correlation functionals with explicit Hartree-Fock exchange to express the exchange functional. The DFT exchange functional is partially replaced by HF one. In this work, the aim is to derive thermodynamic properties of ruthenium compounds with reactions pathways including air vapour species. Knowing that ruthenium metallic compounds may have significant amounts of non-dynamical correlation, they will be better described by DFT via SIE correcting non-dynamical correlation whereas

the air/vapour species are known to be single-reference, so the hybrid approach with HF exchange allows minimising SIE. To take account all specificities induced by the several species regarding electronic correlation effects, we will combine TPSS functional with different percentage of Hartree Fock amount, it is the TPSSh functional [69].

3.3.5   Unrestricted DFT Broken Symmetry Approach

As described previously, DFAs take account electronic correlation in their definition, and by mean of S.I.E the static electronic correlation. Nevertheless, these corrections are not sufficient to taking account for all electronic correlation. Analogous to UHF approach, UDFT approximation leads to different spatial orbitals for α and β in the Khon Sham matrix. Hence, this wave function is not an eigenvalue of the total spin $\hat{S}^2$, but in DFT approach, the definition of this quantity does not exactly correspond to $S_z(Sz+1)$[72], consequence of electron correlation being included in the single determinantal wave function (by means of E_{xc}). For open-shells systems, this solution is affordable. For singlet, to reach the lowest energy, we can add to the UDFT approach the *broken symmetry* procedure, in which the calculations of singlet ground states are performed using higher multiplicities that breaks the initial system symmetry.

3.4   Relativistic effects

All methods described above use the non-relativistic formulation of the Hamiltonian. However, in the presence of heavier nuclei, the speed of electrons increases as a result of relativistic effects. One can make a distinction between *scalar relativistic effects*, associated with the relativistic mass increase of the electron due to its high speed in the vicinity of heavy nuclei, and *spin-orbit effects*, associated with the interaction of the electron spin with the magnetic field induced by charges (e.g., nuclei and other electrons) in relative motion. The direct consequences of relativistic effects on the electronic structure are a contraction and stabilisation of s (and p) shells and the spin-orbit splitting of the p, d, f and higher shells. The indirect effect, which arises from the contraction of the inner shells, results in a screening of the nuclear charge for the outer shells leading to a decreased effective nuclear charge and an expansion and destabilisation of valence d, f, and higher shells. In molecules consisting of lighter atoms, the magnitude of relativistic effects is small and can in many cases be neglected. For heavier atoms, beyond the first-row transition metals, these effects have a large impact on the electronic structures and molecular properties. For instance, in the ruthenium atom we are interested in, relativistic effects result in close-lying $s^2 d^n$ and $s^1 d^{n+1}$ [73], impacting bond lengths, binding energies and vibrational constants. The relativistic contributions due to spin-orbit coupling will affect both molecular and atomic states, all the more when ground-state wave function has unpaired electrons. This will thus impact reaction energies and thermodynamics.

Quantum chemistry theory for relativistic effects is based on the four-component Dirac equation, which combines quantum mechanics with relativity laws of physics. The next section will briefly introduce the four-component Dirac Hamiltonian. We will then discuss re-

lativistic two-component Hamiltonians that result from eliminations of the positronic degrees of freedom of the Dirac Hamiltonian. We will also mention effective core potentials methods.

3.4.1 Dirac Hamiltonian

Using the relativistic energy expression, $E^2 = p^2 c^2 + m^2 c^4$, and the operators for energy momentum, $E = i\hbar \frac{d}{dt}$ and $\hat{p} = \frac{\hbar}{i}\nabla$, Klein and Gordon [74–76] proposed a relativistic analogue to the Schrödinger equation based on E^2, the Klein-Gordon equation for a free particle,

$$(\nabla^2 - \frac{\partial^2}{c^2 \partial t^2} - m^2 c^2)\Psi(r,t) = 0. \tag{3.54}$$

Equation 3.54 is a scalar equation of the second-order in time and spatial coordinates and it yields a time-dependent probability for the location of the particle. Dirac [77, 78] suggested an Ansatz linear in both time and space, leading to the Dirac equation:

$$\left(i\frac{\partial}{dt} - c\boldsymbol{\alpha}.\hat{\boldsymbol{p}} + \beta mc^2\right)\Psi(r,t) = 0$$
$$\boldsymbol{\alpha} = \left(\begin{array}{cc} 0 & \boldsymbol{\sigma} \\ \boldsymbol{\sigma} & 0 \end{array}\right), \beta = \left(\begin{array}{cc} \boldsymbol{I} & 0 \\ 0 & -\boldsymbol{I} \end{array}\right). \tag{3.55}$$

where $\boldsymbol{\alpha}$ and β are matrices defined in terms of the Pauli spin matrices $\boldsymbol{\sigma}$ and the 2×2 identity and null matrices.

Like the non-relativistic Schrödinger equation see previously, the Dirac equation can be separated in terms of time and spatial coordinates expressions. Thus we obtain the time-independent Dirac operator which be used to solve the eigenvalue equation for a free particle:

$$\boldsymbol{D}\Psi(r) = E\Psi(r)$$
$$\boldsymbol{D}\Psi(r) = (c\boldsymbol{\alpha}.\hat{\boldsymbol{p}} + \beta mc^2)\Psi(r). \tag{3.56}$$

Ψ is a four-component Dirac spinor with the corresponding energy eigenvalue E. It can be expressed as follows:

$$\Psi(r) = \begin{pmatrix} \Psi^L_\uparrow(r) \\ \Psi^L_\downarrow(r) \\ \Psi^S_\uparrow(r) \\ \Psi^S_\downarrow(r) \end{pmatrix} = \begin{pmatrix} \Psi^L(r) \\ \Psi^S(r) \end{pmatrix}, \tag{3.57}$$

where L and S are the large and small components of the wave function describing the positive and negative energy solutions respectively. The spin degree of freedom is symbolized by $\uparrow$ and $\downarrow$. For one electron, equation 3.57 can be rewritten in a matrix form, shifting the large component energy to zero:

$$\begin{pmatrix} V & c\boldsymbol{\sigma}.\boldsymbol{p} \\ c\boldsymbol{\sigma}.\boldsymbol{p} & -2mc^2 + V \end{pmatrix}\begin{pmatrix} \Psi^L \\ \Psi^S \end{pmatrix} = E\begin{pmatrix} \Psi^L \\ \Psi^S \end{pmatrix}. \tag{3.58}$$

3.4.2 Many-particle relativistic Hamiltonian

The extension of the Dirac Hamiltonian to an n-electron Hamiltonian leads to Dirac-Coulomb-Breit Hamiltonian [79, 80], an equation of a sum of even, δ, and odd, θ, operators with respect to intrinsic parity:

$$\boldsymbol{H} = \beta mc^2 + \delta + \theta. \tag{3.59}$$

The even operators have no matrix elements coupling the large and small components, whereas the odd operators only consist of such matrix elements. The Foldy-Wouthuysen (FW) [81] transformation is then applied to equation 3.59, to eliminate the odd terms. The first order of this FW transformation leads to the Pauli Hamiltonian, expanded in a power series in c^{-2}, as following:

$$\boldsymbol{H}^{Pauli} = V + \frac{p^2}{2m} \underbrace{- \frac{p^4}{8m^3c^2}}_{\text{mass-velocity}} \underbrace{+ \frac{1}{8m^2c^2}\left(\nabla^2 V\right)}_{\text{Darwin}} \underbrace{+ \frac{1}{4m^2c^2}\boldsymbol{\sigma}\cdot\left[\left(\nabla V\right)\times\boldsymbol{p}\right]}_{\text{spin-orbit}}. \tag{3.60}$$

The first two terms correspond to the non-relativistic Schrödinger equation, the third one is the mass velocity, the fourth term the Darwin correction representing the scalar relativistic corrections and the last one the spin-orbit coupling term.

The Pauli Hamiltonian has no lower bound and is therefore not recommended for variational calculations. It is nowadays mostly used in low-order perturbation calculations on light atoms ($Z < 40$) [82].

Another way of decoupling the large and small components, and using an expansion in the power series in $E/(2c^2 - V)$, lead to the zeroth-order regular approximation (ZORA) [83] Hamiltonian. In addition to the Pauli Hamiltonian, it includes the two-electron Darwin term and the two-electron spin-orbit terms.

The Douglas-Kroll-Hess approximation (DKH) [84, 85] is an alternative transformation, most used in quantum theories, allowing relativistic equation respect the variation principle. This DKH Hamiltonian results from a series of unitary transformations applied to the one-electronic Dirac Hamiltonian, leading to the following matrix:

$$\boldsymbol{h}^D_{DKH\infty} = \sum_{k=0}^{\infty}\boldsymbol{\epsilon}_k = \sum_{k=0}^{\infty}\begin{pmatrix} \epsilon_{k+} & 0 \\ 0 & \epsilon_{k-} \end{pmatrix}, \tag{3.61}$$

where the $\{\epsilon_k\}$ terms are scalar operators, composed by a spin dependent part, ϵ_k^{SD} and a spin free part ϵ_k^{SF}:

$$\boldsymbol{h}^D_{DKH\infty} = \sum_{k=0}^{\infty}\boldsymbol{\epsilon}_k = \sum_{k=0}^{\infty}\begin{pmatrix} \epsilon_{k+}^{SF} + \epsilon_{k+}^{SD} & 0 \\ 0 & \epsilon_{k-}^{SF} + \epsilon_{k-}^{SD} \end{pmatrix}, \tag{3.62}$$

3.4.3 Scalar relativistic effects and spin-orbit coupling

As indicated by equation 3.62, the DKH Hamiltonian includes scalar relativistic effects, by neglecting the spin dependent terms in the matrix. It is the quasi-relativistic approximation, where the relativistic corrections are applied only on one-electron interaction operators.

In calculations starting from a scalar-relativistic Hamiltonian, the spin-orbit effects can be taken into account by applying a variation-perturbation method, such as the CASSI-SO, or more generally RASSI-SO method [86, 87]. The reference is obtained with CASSCF, and the Hamiltonian is then diagonalised. As for the two-step SO-CI method, dynamic electron correlation effects can be added by the "dressing" of the Hamiltonian. In these calculations, either the spin-orbit integrals are computed with the ad hoc spin-orbit effective core potential (See Section 3.4.4), or whenever the DKH relativistic Hamiltonian is used, the spin-orbit integrals are calculated in the mean field approximation [88] using the AMFI code [89] implemented in the MOLCAS suite of programs.

3.4.4 Effective Core Potentials

The electrons in an atom, can be divided into two categories, the core electrons, located closer to the nucleus and the valence electrons, located in the outermost part and actively participating in chemical bonding. The core orbitals are considered as chemically inert, so they can be frozen in electron correlation structure calculation. By replacing the core electrons with an effective core potential (ECP) the size of the basis set is reduced, an advantage especially for the heavier atoms. A general form of ECP (in one-component form) is provided in equation 3.63:

$$V_{ecp} = -\frac{Z_{eff}}{r} + \sum_{l_i}(\sum_k a_{l_j,k} r^{n_{l_j}k^{-2}} e^{\alpha_{l_j,k}r^2})P_{l_j}$$

$$P_{l_j} = \sum_{m_l=l_i}^{l} |lm_l(i)\rangle\langle lm_l(i)| \quad , \qquad (3.63)$$

where $Z_{eff} = Z - N_{core}$, the parameters a, n and α, related to the angular momentum, are determined by a fitting procedure of a n-term polynomial, in particular for molecular systems gaussians functions are used.

For energy-consistent effective core potentials (used in this work), the parameters are derived from all electron multi-configuration Dirac Hartree-Fock (MDF) calculations based on the Dirac-Coulomb or Dirac-Coulomb-Breit Hamiltonian. These calculations are performed for a multitude of electronic configuration states of both the neutral atoms and the low-charged ions. Almost all elements of the periodic table have been made available by Dolg *et al.* [90].

For geometries, binding energies and reaction energetics, the difference in accuracy between all-electron and valence-only core-potential calculations is negligible, as long as the size of the frozen core is kept small or medium, that includes all orbitals with principal numbers smaller than that found in the valence orbitals. For Ru atom, the pseudo-potential used is the ECP28-MDF [91], a small-core potential with 28 frozen electrons, leaving the $4s^2 4p^6 4d^7 5s^1$ electrons to be treated explicitly.

3.5 Statistical physics tools

The purpose of this work is to determine thermodynamic properties and kinetic parameters for gaseous ruthenium compounds.

By performing the electronic structure calculations described above, we obtain stationary states and optimised structures of our compounds, with their specific electronic energies.

These obtained properties of a single molecule will be connected to the macroscopic ones by the use of statistical mechanics that exploits the topology of the potential energy surface as detailed in the first part of this section. Then reaction pathway calculations can be performed by mean of transition state theory, as described in the second part of this section, and after one can derive the desired thermodynamic and kinetic data, by use of statistical mechanics laws developed in last part of this section.

3.5.1 Potential energy surface

The potential energy surface (PES) is defined within the Born Oppenheimer approximation (see Section 3.1.1, equation 3.4).
In particular, for an N atoms system, the PES is functions of $3N - 6$ (non-linear) or $3N - 5$ (linear-system) coordinates.
The stationary points of the PES have their energy gradients equal to zero regarding all co-ordinates:

$$G_i = \left(\frac{\partial E(x_1, x_2, ..., x_n)}{\partial x_i} \right) = 0, \forall i. \tag{3.64}$$

The nature of the molecular structure at a PES stationary point is defined by the convexity or concavity, which is given by the Hessian matrix, denoted H. The matrix elements are the second derivatives of the potential energy surfaces points:

$$H_{ij} = \left(\frac{\partial^2 E(x_1, x_2, ..., x_n)}{\partial x_i \partial x_j} \right). \tag{3.65}$$

The Hessian matrix is diagonalised, the eigenvectors obtained are normal modes of vibrations Q_i of the molecules and the eigenvalues are force constants k_i related of each vibrational mode, in the harmonic oscillator approximation (see Section 3.5.3). The obtained eigenvalues allows to defined the nature of stationary points along the PES:

- if no negative value is obtained, it is a minimum,

- if one negative value is obtained, it is a first-order saddle point,

- if n ($n > 1$) negative values are obtained, it is a n-order saddle point.

A chemical reaction can be described as nuclei moving from one minimum to another on the potential energy surface within the Born-Oppenheimer approximation. Reactants, products and intermolecular systems corresponds to minima and transition states (TS) to first-order saddle points [92]. In the lowest level of approximation, the motion is assumed to occur along the path of least energy, and this path forms the basis for the transition state theory.

3.5.2   Transition state theory

The transition state theory or activated complex theory was proposed by Eyring, Polanyi and Evans in 1935 [93].

If one considers a chemical reaction of the type A + B $\longrightarrow$ C + D. The rate constant k can be written as:

$$-\frac{d[A]}{dt} = -\frac{d[B]}{dt} = \frac{d[C]}{dt} = \frac{d[D]}{dt} = k[A][B]. \tag{3.66}$$

The concentration of the various species can be calculated at any given time from the initial concentrations if k is known. For systems in equilibrium, the probability of finding a molecule in a certain state depends on its energy according to the Boltzmann distribution, and the macroscopic rate constant thereby becomes a function of temperature. Assuming that
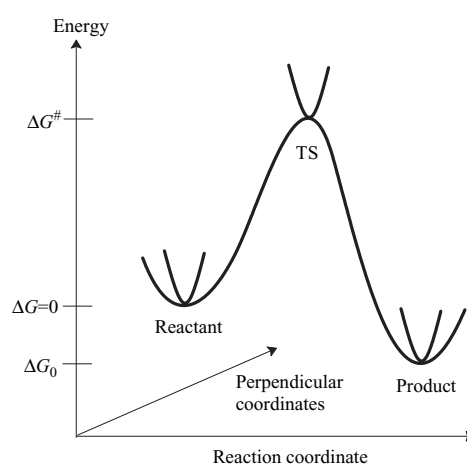
Figure 3.5: Schematic illustration of a reaction path [16]

the molecules at the TS are in equilibrium with the reactant, the macroscopic rate constant can be expressed as:

$$k_{rate} = \frac{k_B T}{h} e^{-\Delta G^{\ddagger}/RT}$$
$$\Delta G^{\ddagger} = G_{TS} - G_{reactant} \tag{3.67}$$

$\Delta G^{\ddagger}$ is the activation Gibbs free energy that corresponds to the difference between the Gibbs free energies of the TS and reactant along the reaction path drawn in Figure 3.5, h is Planck's constant and k_B is Boltzmann's constant.

Equation 3.67 is available if all molecules that pass from the reactant over the TS go on to product. For more complicated cases, for example "re-crossings" where a molecule passes over the TS but is reflected back to the reactant side, a transmission coefficient κ [94] is sometimes introduced. The equilibrium constant for a reaction can be calculated from the free energy difference between the reactant(s) and product(s) as:

$$K_{eq} = e^{-\Delta G^{\ominus}/RT}.$$ (3.68)

$G^{\ominus}$ represents the Gibbs free energy at standard state conditions. It is the sum of enthalpy and entropy terms, $G = H - TS$, and the enthalpy and entropy for a macroscopic ensemble of particles may be calculated from properties of a relatively few molecules using statistical mechanics. The transition state is a macroscopic ensemble with a Boltzmann energy distribution, while the transition structure refers to the microscopic system. At the microscopic level, the rate constant is a function of the quantum states of A, B, C and D, i.e. the electronic, translational, rotational and vibrational quantum numbers. The macroscopic rate constant is an average over such "microscopic" rate constants, weighted by the probability of finding a molecule in a given set of quantum numbers.

3.5.3 Statistical mechanics

The connection between properties of a microscopic system and a macroscopic sample is provided by statistical mechanics. At a temperature of 0 K, all molecules are in their energetic ground state but at a finite temperature, there is a distribution of molecules in all possible (quantum) energy states. The relative probability P of a molecule to be in a state with an energy ϵ at a temperature T is given by a Boltzmann factor (illustrated in figure 3.6):

$$P \propto e^{-\epsilon/k_B T}.$$ (3.69)

The partition function is the key feature of statistical mechanics, allowing calculation of all macroscopic functions related to microscopic level.
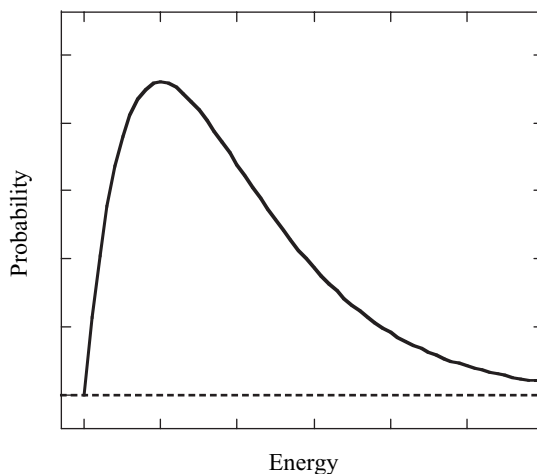
Figure 3.6: Boltzmann energy distribution [16]

For a single molecule, this function is denoted q and is defined as a sum of exponential terms involving all possible quantum energy states.

$$q = \sum_{i=states}^{\infty} e^{-\epsilon_i/k_B T}. \tag{3.70}$$

q can also be written as a sum over all distinct energy levels, multiplied with a degeneracy factor g_i that indicates how many states have the same energy ϵ_i.

$$q = \sum_{i=levels}^{\infty} g_i e^{-\epsilon_i/k_B T}. \tag{3.71}$$

It may also be viewed as the normalisation factor for the Boltzmann probability distribution, as q can be considered as an average excited state number-operator, since it is the probability-weighted sum of energy states, each counted with a factor of 1. The partition function for N non-interacting particles (ideal gas), denoted Q is given by:

$$\begin{aligned} Q &= q^N \text{(different particles, non interacting)} \\ Q &= \frac{q^N}{N!} \text{(identical particles, non interacting)} \end{aligned} \tag{3.72}$$

Starting from Q, we can derived the thermodynamic functions, such as the internal energy U and Helmholtz free energy $A(A = U - TS)$.

$$\begin{aligned} U &= k_B T^2 \left(\frac{\partial \ln Q}{\partial T} \right)_V. \\ A &= -k_B T \ln Q \end{aligned} \tag{3.73}$$

Macroscopic observables such as the pressure P or the heat capacity C_v can then be calculated as derivatives of thermodynamic functions:

$$\begin{aligned} P &= -\left(\frac{\partial A}{\partial V} \right)_T = k_B T \left(\frac{\partial \ln Q}{\partial V} \right)_T \\ C_v &= \left(\frac{\partial U}{\partial T} \right)_V = 2k_B T \left(\frac{\partial \ln Q}{\partial T} \right)_V + k_B T^2 \left(\frac{\partial \ln^2 Q}{\partial T^2} \right)_V \end{aligned} \tag{3.74}$$

From these relations, the thermodynamic functions, such as the enthalpy H, the entropy S and Gibbs free energy G can be constructed.

$$\begin{aligned} H &= U + PV = k_B T^2 \left(\frac{\partial \ln Q}{\partial T} \right)_V + k_B T V \left(\frac{\partial \ln Q}{\partial V} \right)_T \\ S &= \frac{U - A}{T} = k_B T \left(\frac{\partial \ln Q}{\partial T} \right)_V + k_B \ln Q \\ G &= H - TS = k_B T V \left(\frac{\partial \ln Q}{\partial V} \right)_T - k_B T \ln Q \end{aligned} \tag{3.75}$$

To calculate the partition function, $q(Q)$, all possible quantum states for the system are needed. In principle, they can be computed by solving the nuclear Schrödinger equation, with the suitable potential energy surface, obtained from solving the electronic Schrödinger

equation. Such a rigorous approach is only possible for di- and triatomic systems. As our study is focused on gaseous compounds, the partition function can be calculated within the rigid-rotator harmonic oscillator (RRHO) approximation [95], where the electronic, vibrational and rotational degrees of freedom are assumed to be separable.

This assumption implies that the partition function can be written as a product of terms. As the enthalpy and entropy contributions involve the logarithm of q, the product of $q's$ thus transforms into sums of enthalpy and entropy contributions.

$$
\begin{aligned}
\epsilon_{tot} &= \epsilon_{trans} + \epsilon_{rot} + \epsilon_{vib} + \epsilon_{elec} \\
q_{tot} &= q_{trans} \times q_{rot} \times q_{vib} \times q_{elec} \\
H_{tot} &= H_{trans} + H_{rot} + H_{vib} + H_{elec} \\
S_{tot} &= S_{trans} + S_{rot} + S_{vib} + S_{elec}
\end{aligned}
\tag{3.76}
$$

The expression of translational, rotational, vibrational and electronic contributions for each term (ϵ, q, H, S) are detailed in Appendix A.

3.6   Conclusions

To compute our molecular structure properties, the overall methods reviewed will be used, as Ru atomic compound presents electronic configuration with open-shell d orbitals, implies much electronic correlation and relativistic effects. We will adjust the methodology on RuO and RuO_2 species, less computationally expensive systems, in which the several methods can be applied. Then the thermodynamic properties will be derived, once the electronic energies and the geometries of our systems obtained.

References

(1)   Garisto, F. *AECL-9552* **1988**.

(2)   Barin, I.; Knacke, O.; Kubaschewski, O., *Thermochemical properties of inorganic substances*; Springer-Verlag: Berlin, Heidelberg, New York, 1977, p 861.

(3)   Rard, J. A. Chemistry and Thermodynamics of Ruthenium and Some of Its Inorganic Compounds and Aqueous Species. *Chem. Rev.* **1985**, *85*, 1–39, DOI: `10.1021/cr00065a001`.

(4)   Cordfunke, E. H. P.; Konings, R. J. M. Thermochemical Data for Reactor Materials and Fission Products: The ECN Database. *J. Phase Equilib.* **1993**, *14*, 457–464, DOI: `10.1007/BF02671964`.

(5)   Schaefer III, H. F., *Methods of Electronic Structure Theory*; Springer US: 1977, DOI: `10.1007/978-1-4757-0887-5`.

(6)   Schrödinger, E. Quantisierung als Eigenwertproblem. *Ann. Phys.* **1926**, *385*, 437–490, DOI: `10.1002/andp.19263851302`.

(7)   Das, T. P., *Relativistic Quantum Mechanics of Electrons*; Harper & Row: New York, 1973.

(8)   Feynman, R.-P., *Quantum electrodynamics*. WA Benjamin: New York, 1961.

(9)   Born, M.; Oppenheimer, R. Zur Quantentheorie der Molekeln. *Ann. Phys.* **1927**, *389*, 457–484, DOI: `10.1002/andp.19273892002`.

(10)   Eschrig, H., *Optimized LCAO method and the electronic structure of extended systems*; Research reports in physics; Springer-Verlag: 1989.

(11)   Chaquin, P. Pratique de la Chimie Théorique., accessed June 6, 2016.

(12)   Almlöf, J.; Taylor, P. R. In, Per-Olov Löwdin, J. R. S., Zerner, M. C., Eds.; Advances in Quantum Chemistry, Vol. 22; Academic Press: 1991, pp 301 –373, DOI: `10.1016/S0065-3276(08)60366-4`.

(13)   Dunning Jr., T. H. Gaussian Basis Sets for Use in Correlated Molecular Calculations. I. the Atoms Boron Through Neon and Hydrogen. *J. Chem. Phys.* **1989**, *90*, 1007–1023, DOI: `10.1063/1.456153`.

(14)   Roothaan, C. C. J. New Developments in Molecular Orbital Theory. *Rev. Mod. Phys.* **1951**, *23*, 69–89, DOI: `10.1103/RevModPhys.23.69`.

(15)   Szabo, A.; Ostlung, N. S., *Modern Quantum Chemistry*; Dover Puplications Inc.: 1996.

(16)   Jensen, F., *Introduction to computational chemistry*; Wiley: 2007.

(17)   Löwdin, P.-O. Quantum Theory of Many-Particle Systems. III. Extension of the Hartree-Fock Scheme to Include Degenerate Systems and Correlation Effects. *Phys. Rev.* **1955**, *97*, 1509–1520, DOI: `10.1103/PhysRev.97.1509`.

(18)   Siegbahn, P. E. M. Generalizations of the direct CI method based on the graphical unitary group approach. I. Single replacements from a complete CI root function of any spin, first order wave functions. *J. Chem. Phys.* **1979**, *70*, 5391–5397, DOI: `10.1063/1.437473`.

(19)   Roos, B. O. A new method for large-scale Cl calculations. *Chem. Phys. Lett.* **1972**, *15*, 153 –159, DOI: `10.1016/0009-2614(72)80140-4`.

(20)   Werner, H.-J.; Meyer, W. A quadratically convergent multiconfiguration-self-consistent field method with simultaneous optimization of orbitals and CI coefficients. *J. Chem. Phys.* **1980**, *73*, 2342–2356, DOI: `10.1063/1.440384`.

(21)   Werner, H. J.; Meyer, W. A quadratically convergent MCSCF method for the simultaneous optimization of several states. *J. Chem. Phys.* **1981**, *74*, 5794–5801, DOI: `10.1063/1.440892`.

(22)   Werner, H.-J.; Knowles, P. J. A second order multiconfiguration SCF procedure with optimum convergence. *J. Chem. Phys.* **1985**, *82*, 5053–5063, DOI: `10.1063/1.448627`.

(23)   Roos, B. O.; Taylor, P. R.; Siegbahn, P. E. A complete active space SCF method (CASSCF) using a density matrix formulated super-CI approach. *Chem. Phys.* **1980**, *48*, 157 –173, DOI: `10.1016/0301-0104(80)80045-0`.

(24)   Roos, B. O. In *Advances in Chemical Physics*; John Wiley & Sons, Inc.: 1987, pp 399–445, DOI: `10.1002/9780470142943.ch7`.

(25)   Olsen, J.; Roos, B. O.; Jørgensen, P.; Jensen, H. J. r. A. Determinant based configuration interaction algorithms for complete and restricted configuration interaction spaces. *J. Chem. Phys.* **1988**, *89*, 2185–2192, DOI: `10.1063/1.455063`.

(26)   Veryazov, V.; Malmqvist, P.-Å.; Roos, B. O. How to select active space for multiconfigurational quantum chemistry? *Int. J. Quantum Chem.* **2011**, *111*, 3329–3338, DOI: `10.1002/qua.23068`.

(27)   Bartlett, R. J. Many-body perturbation theory and coupled cluster theory for electron correlation in molecules. *Annu. Rev. Phys. Chem.* **1981**, *32*, 359–401, DOI: `10.1146/annurev.pc.32.100181.002043`.

(28)   Dush, W.; Diercksen, G. H. Size-extensivity corrections in configuration interaction methods. *J. Chem. Phys.* **1994**, *101*, 3018–3030, DOI: `10.1063/1.467615`.

(29)   Davidson, E. R. In *The World of Quantum Chemistry*, Daudel, R., Pullman, B., Eds.; Reidel: Dortretch, 1974.

(30)   Langhoff, S. R.; Davidson, E. R. Configuration interaction calculations on the nitrogen molecule. *Int. J. Quantum Chem.* **1974**, *8*, 61–72, DOI: `10.1002/qua.560080106`.

(31) Gdanitz, R. J.; Ahlrichs, R. The averaged coupled-pair functional (ACPF): A size-extensive modification of MR CI(SD). *Chem. Phys. Lett.* **1988**, *143*, 413 –420, DOI: `10.1016/0009-2614(88)87388-3`.

(32) Laidig, W. D.; Bartlett, R. J A multi-reference coupled-cluster method for molecular applications. *Chem. Phys. Lett.* **1984**, *104*, 424 –430, DOI: `10.1016/0009-2614(84)85617-1`.

(33) Szalay, P. G.; Bartlett, R. J. Multi-reference averaged quadratic coupled-cluster method: a size-extensive modification of multi-reference CI. *Chem. Phys. Lett.* **1993**, *214*, 481 –488, DOI: `10.1016/0009-2614(93)85670-J`.

(34) Møller, C.; Plesset, M. S. Note on an Approximation Treatment for Many-Electron Systems. *Phys. Rev.* **1934**, *46*, 618–622, DOI: `10.1103/PhysRev.46.618`.

(35) Andersson, K.; Malmqvist, P.-Å.; Roos, B. O. Second-Order Perturbation Theory with a Complete Active Space Self-Consistent Field Reference Function. *J. Chem. Phys.* **1992**, *96*, 1218–1226, DOI: `10.1063/1.462209`.

(36) Andersson, K.; Malmqvist, P.-Å.; Roos, B. O.; Sadlej, A. J.; Wolinski, K. Second-order perturbation theory with a CASSCF reference function. *J. Chem. Phys.* **1990**, *94*, 5483–5488, DOI: `10.1021/j100377a012`.

(37) Malmqvist, P.-Å.; Pierloot, K.; Shahi, A. R. M.; Cramer, C. J.; Gagliardi, L. The restricted active space followed by second-order perturbation theory method: Theory and application to the study of CuO_2 and Cu_2O_2 systems. *J. Chem. Phys.* **2008**, *128* 204109, DOI: `10.1063/1.2920188`.

(38) Ghigo, G.; Roos, B. O.; Malmqvist, P.-Å. A modified definition of the zeroth-order Hamiltonian in multiconfigurational perturbation theory (CASPT2). *Chem. Phys. Lett.* **2004**, *396*, 142 –149, DOI: `10.1016/j.cplett.2004.08.032`.

(39) Dyall, K. G. The choice of a zeroth-order Hamiltonian for second-order perturbation theory with a complete active space self-consistent-field reference function. *J. Chem. Phys.* **1995**, *102*, 4909–4918, DOI: `10.1063/1.469539`.

(40) Angeli, C.; Cimiraglia, R.; Evangelisti, S.; Leininger, T.; Malrieu, J.-P. Introduction of n-electron valence states for multireference perturbation theory. *J. Chem. Phys.* **2001**, *114*, 10252–10264, DOI: `10.1063/1.1361246`.

(41) Angeli, C.; Cimiraglia, R.; Malrieu, J.-P. n-electron valence state perturbation theory: A spinless formulation and an efficient implementation of the strongly contracted and of the partially contracted variants. *J. Chem. Phys.* **2002**, *117*, 9138–9153, DOI: `10.1063/1.1515317`.

(42) Angeli, C.; Pastore, M.; Cimiraglia, R. New perspectives in multireference perturbation theory: the n-electron valence state approach. *Theor. Chem. Acc.* **2007**, *117*, 743–754, DOI: `10.1007/s00214-006-0207-0`.

(43) Angeli, C.; Borini, S.; Cestari, M.; Cimiraglia, R. A Quasidegenerate Formulation of the Second Order N-Electron Valence State Perturbation Theory Approach. *J. Chem. Phys.* **2004**, *121*, 4043–4049, DOI: `10.1063/1.1778711`.

(44) Čížek, J. On the Correlation Problem in Atomic and Molecular Systems. Calculation of wavefunction Components in Ursell-type Expansion Using Quantum-Field Theoretical Methods. *J. Chem. Phys.* **1966**, *45*, 4256–4266, DOI: `10.1063/1.1727484`.

(45) Cizek, J.; Paldus, J. Correlation problems in atomic and molecular systems III. Rederivation of the coupled-pair many-electron theory using the traditional quantum chemical methodst. *Int. J. Quantum Chem.* **1971**, *5*, 359–379, DOI: `10.1002/qua.560050402`.

(46) Knowles, P. J.; Hampel, C.; Werner, H.-J. Erratum: "Coupled Cluster Theory for High Spin, Open Shell Reference Wave Functions". *J. Chem. Phys.* **2000**, *112*, 3106–3107, DOI: `10.1063/1.465990`.

(47) Knowles, P. J.; Hampel, C.; Werner, H.-J. Coupled Cluster Theory for High Spin, Open Shell Reference Wave Functions. *J. Chem. Phys.* **1993**, *99*, 5219–5227, DOI: `10.1063/1.465990`.

(48) Bartlett, R. J. Coupled-cluster approach to molecular structure and spectra: a step toward predictive quantum chemistry. *J. Chem. Phys.* **1989**, *93*, 1697–1708, DOI: `10.1021/j100342a008`.

(49) Purvis, G. D.; Bartlett, R. J. A full coupled-cluster singles and doubles model: The inclusion of disconnected triples. *J. Chem. Phys.* **1982**, *76*, 1910–1918, DOI: `10.1063/1.443164`.

(50) Raghavachari, K.; Trucks, G. W.; Pople, J. A.; Head-Gordon, M. A fifth-order perturbation comparison of electron correlation theories. *Chem. Phys. Lett.* **1989**, *157*, 479 –483, DOI: `10.1016/S0009-2614(89)87395-6`.

(51) Watts, J. D.; Bartlett, R. J. Triple excitations in coupled-cluster theory: Energies and analytical derivatives. *Int. J. Quantum Chem.* **1993**, *48*, 51–66, DOI: `10.1002/qua.560480809`.

(52) Lee, T. J.; Taylor, P. R. A diagnostic for determining the quality of single-reference electron correlation methods. *Int. J. Quantum Chem.* **1989**, *36*, 199–207, DOI: `10.1002/qua.560360824`.

(53) Janssen, C. L.; Nielsen, I. M. New diagnostics for coupled-cluster and Møller-Plesset perturbation theory. *Chem. Phys. Lett.* **1998**, *290*, 423 –430, DOI: `10.1016/S0009-2614(98)00504-1`.

(54) Lee, T. J. Comparison of the {T1} and {D1} diagnostics for electronic structure theory: a new definition for the open-shell {D1} diagnostic. *Chem. Phys. Lett.* **2003**, *372*, 362 –367, DOI: `10.1016/S0009-2614(03)00435-4`.

(55) Jiang, W.; DeYonker N, J.; Wilson, A. K. Multireference Character for 3d Transition-Metal-Containing Molecules. *J. Chem. Theory Comput.* **2012**, *8*, 460–468, DOI: `10.1021/ct2006852`.

(56) Lee, T. J.; Scuseria, G. E. In *Quantum Mechanical Electronic Structure Calculations with Chemical Accuracy*, Langhoff, S. R., Ed.; Springer Netherlands: Dordrecht, 1995, pp 47–108, DOI: `10.1007/978-94-011-0193-6_2`.

(57) Hohenberg, P.; Kohn, W. Inhomogeneous Electron Gas. *Phys. Rev.* **1964**, *136*, B864–B871, DOI: `10.1103/PhysRev.136.B864`.

(58) Kohn, W.; Sham, L. J. Self-Consistent Equations Including Exchange and Correlation Effects. *Phys. Rev.* **1965**, *140*, A1133–A1138, DOI: `10.1103/PhysRev.140.A1133`.

(59) Vosko, S. H.; Wilk, L.; Nusair, M. Accurate spin-dependent electron liquid correlation energies for local spin density calculations: a critical analysis. *Can. J. Phys.* **1980**, *58*, 1200–1211, DOI: `10.1139/p80-159`.

(60) Perdew, J. P.; Wang, Y. Accurate and simple analytic representation of the electron-gas correlation energy. *Phys. Rev. B* **1992**, *45*, 13244–13249, DOI: `10.1103/PhysRevB.45.13244`.

(61) Vosko, S. H.; Wilk, L A comparison of self-interaction-corrected local correlation energy functionals. *J. Phys. B: At. Mol. Phys.* **1983**, *16*, 3687, DOI: `10.1088/0022-3700/16/20/006`.

(62) R. G., P.; W., Y., *Density-Functinal Theory of Atoms and Molecules*; Oxford University Press: 1989.

(63) J. K., L.; W. J., A., *Density Functional Methods in Chemistry*; Springer-Verlag: 1991.

(64) Slater, J. C. A simplification of the Hartree-Fock method. *Phys. Rev.* **1951**, *81*, 385, DOI: `10.1103/PhysRev.81.385`.

(65) Perdew, J. P.; Burke, K.; Ernzerhof, M. Generalized gradient approximation made simple. *Phys. Rev. Lett.* **1996**, *77*, 3865, DOI: `10.1103/PhysRevLett.77.3865`.

(66) Becke, A. D. Density-functional exchange-energy approximation with correct asymptotic behavior. *Phys. Rev. A* **1988**, *38*, 3098–3100, DOI: `10.1103/PhysRevA.38.3098`.

(67) Dirac, P. A. M. In *Proceedings of the Royal Society of London A: Mathematical, Physical and Engineering Sciences*, 1929; Vol. 123, pp 714–733, DOI: `10.1098/rspa.1929.0094`.

(68) Lee, C.; Yang, W.; Parr, R. G. Development of the Colle-Salvetti correlation-energy formula into a functional of the electron density. *Phys. Rev. B* **1988**, *37*, 785–789, DOI: `10.1103/PhysRevB.37.785`.

(69) Tao, J.; Perdew, J. P.; Staroverov, V. N.; Scuseria, G. E. Climbing the Density Functional Ladder: Nonempirical Meta-Generalized Gradient Approximation Designed for Molecules and Solids. *Phys. Rev. Lett.* **2003**, *91*, 146401, DOI: `10.1103/PhysRevLett.91.146401`.

(70) Grafenstein, J.; Kraka, E.; Cremer, D. Effect of the self-interaction error for three-electron bonds: On the development of new exchange-correlation functionals. *Phys. Chem. Chem. Phys.* **2004**, *6*, 1096–1112, DOI: `10.1039/B311840A`.

(71) Polo, V.; Kraka, E.; Cremer, D. Some thoughts about the stability and reliability of commonly used exchange–correlation functionals – coverage of dynamic and nondynamic correlation effects. *Theor. Chem. Acc.* **2002**, *107*, 291–303, DOI: `10.1007/s00214-002-0331-4`.

(72) Pople, J. A.; Gill, P. M. W.; Handy, N. C. *Int. J. Quant. Chem.* **1995**, *56*, 303.

(73) Pelissier, M.; Daudey, J. P.; Malrieu, J. P.; Jeung, G. H. In; Springer Netherlands: Dordrecht, 1986; Chapter The Electronic Structure of Transition Metal Atoms and Diatoms Through Pseudopotential Approaches, pp 37–51, DOI: `10.1007/978-94-009-4656-9_3`.

(74) Klein, O. Z Elektrodynamik und Wellenmechanik vom Standpunkt des Korrespondenzprinzips. *Z. Phys.* **1927**, *41*, 407–442, DOI: `10.1007/BF01400205`.

(75) Gordon, W. Der Strom der Diracschen Elektronentheorie. *Z. Phys.* **1928**, *50*, 630–632, DOI: `10.1007/BF01327881`.

(76) Gordon, W. Der Comptoneffekt nach der Schrödingerschen Theorie. *Z. Phys.* **1926**, *40*, 117–133, DOI: `10.1007/BF01390840`.

(77) Dirac, P. The Quantum Theory of the Electron. *Proceedings of the Royal Society of London Series A* **Feb. 1928**, *117*, 610–624, DOI: `10.1098/rspa.1928.0023`.

(78) Dirac, P. A. M., *The Principles of Quantum Mechanics*; Clarendon Press Oxford: 1958.

(79) Malli, G.; Oreg, J Relativistic self-consistent-field (RSCF) theory for closed-shell molecules. *J. Chem. Phys.* **1975**, *63*, 830–841, DOI: `10.1063/1.431364`.

(80) Grant, I. Relativistic calculation of atomic structures. *Adv. Phys.* **1970**, *19*, 747–811, DOI: `10.1080/00018737000101191`.

(81) Foldy, L. L.; Wouthuysen, S. A. On the Dirac Theory of Spin 1/2 Particles and Its Non-Relativistic Limit. *Phys. Rev.* **1950**, *78*, 29–36, DOI: `10.1103/PhysRev.78.29`.

(82) Vallet, V. Traitement Electronique des Molécules Contenant des Atomes Lourds., Ph.D. Thesis, Université Paul Sabatier, 2001.

(83) Lenthe, E. v.; Baerends, E. J.; Snijders, J. G. Relativistic regular two-component Hamiltonians. *J. Chem. Phys.* **1993**, *99*, 4597–4610, DOI: `10.1063/1.466059`.

(84) Douglas, M.; Kroll, N. M. Quantum electrodynamical corrections to the fine structure of helium. *Ann. Phys.* **1974**, *82*, 89 –155, DOI: `10.1016/0003-4916(74)90333-9`.

(85) Wolf, A.; Reiher, M.; Hess, B. A. The generalized Douglas -Kroll transformation. *J. Chem. Phys.* **2002**, *117*, 9215–9226, DOI: `10.1063/1.1515314`.

(86) Malmqvist, P.-Å.; Roos, B. O. The CASSCF state interaction method. *Chem. Phys. Lett.* **1989**, *155*, 189 –194, DOI: `10.1016/0009-2614(89)85347-3`.

(87) Malmqvist, P.-Å.; Roos, B. O.; Schimmelpfennig, B. The restricted active space (RAS) state interaction approach with spin-orbit coupling. *Chem. Phys. Lett.* **2002**, *357*, 230 –240, DOI: `10.1016/S0009-2614(02)00498-0`.

(88) Heß, B. A.; Marian, C. M.; Wahlgren, U.; Gropen, O. A mean-field spin-orbit method applicable to correlated wavefunctions. *Chem. Phys. Lett.* **1996**, *251*, 365–371, DOI: `10.1016/0009-2614(96)00119-4`.

(89) Schimmelpfennig, B. AMFI, an Atomic Mean-Field Integral program., 1996.

(90) Dolg, M. In *Modern Methods and Algorithms of Quantum Chemistry*, 2000, pp 479–508.

(91)   Peterson, K. A.; Figgen, D.; Dolg, M.; Stoll, H. *J. Chem. Phys.* **2007**, *126.*

(92)   Laidler, K. J.; King, M. C. Development of transition-state theory. *J. Chem. Phys.* **1983**, *87*, 2657–2664, DOI: 10.1021/j100238a002.

(93)   Eyring, H. The Activated Complex in Chemical Reactions. *J. Chem. Phys.* **1935**, *3*, 107–115, DOI: 10.1063/1.1749604.

(94)   Truhlar, D. G.; Garrett, B. C. Variational transition-state theory. *Acc. Chem. Res.* **1980**, *13*, 440–448, DOI: 10.1021/ar50156a002.

(95)   Rashid, M. A.; Mahmood, A. Transition amplitudes for time-dependent linear harmonic oscillators. *J. Phys. A: Math. Gen.* **2001**, *34*, 8185, DOI: 10.1088/0305-4470/34/39/316.

RESEARCH OF COMPUTATIONAL METHODOLOGY FOR RU COMPOUNDS

Chapter 3 established the molecular electronic structure theory that will be used to derive the Ru target properties. In the first section, a literature review of ruthenium species electronic structure from quantum chemistry calculations is presented. Section 2 reveals the structural parameters that were obtained with several levels of theory and the choice of the basis set used to compute the optimised geometries of the stationary states (ground states). Natural population analysis and chemical bonding are also examined. In Section 3, the electronic energies of Ru, RuO, and RuO_2, as determined with several methods, are tabulated. Section 4 discusses relativistic effects treated either with pseudo-potential and all-electron relativistic Hamiltonians, such as the Douglas-Kroll approximation. The final section in this chapter presents the choice of methodology in order to validate the derivation of the thermodynamic properties of Ru species.

4.1 Literature review on structural calculations for Ru compounds

4.1.1 Ruthenium electronic configuration specificities

In quantum chemistry, particular difficulties affect the accuracy of calculations with transition metals, since, due to the large number of electrons, correlation effects are not negligible. As seen in the previous chapter [1], the origin of these difficulties for Ru compounds is attributed to the existence of the electrons of the d open-shells, which is common to all transition metal atoms. The presence of this open d shell translates in a unique feature in the atomic spectra, namely the existence of two very close electronic configurations ($s^2 d^n$ and $s^1 d^{n+1}$). Hence, quantitative *ab initio* calculations on transition metal atoms will need special care since those distinct configurations have to be evaluated with high accuracy. In the $s^1 d^{n+1}$ configuration, the d orbitals are more diffuse than in the $s^2 d^n$ configuration. This difference in spatial extension requires a large d atomic basis functions to treat both config-

urations properly. A correct description of differential correlation effects will need another extension of the atomic basis set, including f type orbitals for the angular correlation of the d shells.

In the construction of molecular bonds, the above mentioned special features of transition metal atoms induce the same type of complexity. That being said, there has been a lot of progress that has been made, which allows a clearer understanding of the electronic structure and a fair quantitative reproduction of experimental data. As one moves from second to third-row transition metals, where Ru stands, the effects of relativity on the core and valence orbitals start playing a crucial role.

Daniel (2003) [2] provides some recommendations on how to find a reliable methodology to compute transition metal electronic structures. In the review, it is stated that the main difficulties to overcome arise from the size of the molecular system, its symmetry, the density of states, the number of metal centre d shells and the metal-ligand interactions. The choice of the method satisfies a compromise between the feasibility and the computational cost, the validity of some approximations, the desired level of accuracy, and the control that can be performed on the analysis of the results. Four types of theoretical methods are designed available for treating electronic spectroscopy in transition metal complexes:

- the DFT methods [3–5] and time-dependent DFT(TD-DFT) [6–8];

- the variational approaches such as the self-consistent-field [9], configuration interaction (CI) [10], multi configuration SCF (MC-SCF) [11], multireference CI (MR-CI) [12];

- the cluster expansion methods such as the equation of motion coupled cluster single double (EOM-CCSD) [13, 14], the symmetry adapted cluster CI (SAC-CI) [15];

- the single state (SS) or multistate (MS) Second Order Perturbational approaches applied to zeroth-order variational wavefunctions and so-called SS-CASPT2 [16, 17] and MS-CASPT2 [18].

The goal is to provide for electronic spectroscopy transition energies with an accuracy of 0.10 /0.15 eV and reliable dipole transition moments. In the DFT approach, the ground state chemical properties can be accurately predicted and the reactivity can be interpreted with the development of the Kohn-Sham DFT method. However, in transition metal complexes, large correlation effects affect the electron density, in particular, because several electronic configurations are nearly degenerate, requesting the use of a multi-configurational scheme including static electronic correlation effects. The MC-SCF method and its extension CAS-SCF or RASSCF methods have been derived from resolving this fundamental problem. These methods provide zero-order wave functions used as references in subsequent CI, MR-CI, or MS-CASPT2 calculations, which take into account dynamical correlation effects (in the "cusp region"). Note that in practice, the size of the active space defined by m active electrons and n active orbitals, noted (m/n) can vary from (2/2) up to (16/16). With the largest active spaces, the partitioning between static and dynamical correlation is not straightforward. The validity of the subsequent MR-CI or MS-CASPT2 treatments depends entirely on the quality of the

CASSCF waves function. The MRCI method converges quite slowly, however, and this increases dramatically with the number of references and the lack of size-extensivity, and leads to incorrect scaling of the energy with the number of correlated electrons. This prevents the use of this method for electronic spectroscopy to a large transition metal complexes. The CASPT2 method and its multistate extension MS-CASPT2 methods are size-extensive and that gives very accurate transition energies. That being said, the presence of intruder states, which interact with the reference space, leads to an erratic behaviour of the perturbation and to transition energy predictions that are out of range by more than 2.0 eV. One can either increase the size of the active space (strong intruder states) or introduce a carefully chosen level shift (weak intruder state) to lift near-degeneracies. Cluster expansions method as CCSD(T) are size-extensive by definition. Although these methods converge efficiently, it 's hard to generalise them to multi-reference starting wave functions. Consequently, some approximations have to be made, which may destroy the size-extensitivity. It is highlighted in the Daniel paper (2003) [2] that relativistic effects have to be taken into account with transition metals, and it is mandatory for systems with 5d shells.

Use of effective core potentials as described before is in line with the chemist's view that valence electrons of an element mainly determine its chemical behaviour. Spin-orbit coupling is necessary for electronic spectroscopy and chemical reactivity. These effects can be corrected by the use of ECP including relativistic effects and associated valence basis sets for 2nd and 3rd-row transition metal complexes.

Concerning the determination of equilibrium geometries, transition states, and reaction pathway, for instance, many levels of calculation (SCF, MP2, DFT, MC-SCF, CCSD, CI) are considered as suitable [19]. However, post-HF methods encountered difficulties when optimising systems more than ten atoms limited to hydrogen and 2nd-row atoms. Density functional methods are competitive with the above wave-function methods for the computation of ground state potential energy surface (PES).

4.1.2   Literature review of theoretical calculations concerning Ru target species

A literature review concerning computational chemistry calculations around Ru target species is presented here to give a summary of the structural properties of these compounds.

Krauss and Stevens (1985) [20] examined the electronic structure of RuO with multiconfigurational SCF calculations. They used relativistic effective core potentials (RECP) [21–23] to replace core electrons. They predicted the ground state to be a $^5\Delta$ and bonding correlated in a generalised sense to Ru^+ and O^- fragments, with doubly occupied sigma bonding orbital. At equilibrium, they predicted the zero-point average distance Ru-O to be equal to 1.693 Å, and the calculated Born-Oppenheimer distance R_B is 1.741 Å. The stretching frequency w_e was equal to 814 cm^{-1} and molecular constant $w_e x_e$ was equal to 5.0 cm^{-1}. Spin-orbit lowers the RuO ground state by $-3.04 \text{ kJ mol}^{-1}$.

Siegbhan *et al.* (1993) [24] performed calculations for second row transitions metals, including RuO_2, RuO_3, and RuO_4 systems. The geometry optimisations were performed with small basis sets for the metal atoms, with an RECP according to Hay and Wadt basis set [25], and for the rest of the atoms by regular double-zeta basis set. To perform correlated calculations, the Huzinaga primitive basis [26] was used for metal atoms basis sets, extended by

adding one diffuse function. The core orbitals were entirely contracted except for the $4s$ and $4p$ orbitals, described by two functions each to mimic the relativistic effects. The correlated calculations were performed using the modified coupled pair functional (MCPF) method, which is a size-consistent single reference state method. The metal $4d$ and $5s$ electrons and all electrons on the oxygen ligands except the $1s$ electrons were correlated. The ground state of RuO_2 corresponds to $^1A_1$. It has a bent structure attributed to the interaction between the oxygen lone pairs and empty or half-empty $4d$-orbitals on the metal, forming double covalent bonds. Bond distance Ru-O is 1.670 Å and bond angle O-Ru-O is equal to 152.8°. The binding energy is equal to 100.6 kcal mol^{-1} in Ru-O bonding and 90.6 kcal mol^{-1} for the second oxygen.

Regarding the RuO_3 system, the origin of the planarity D_{3h} symmetry found is claimed to be a mixing of metal $4s$ and $4p$ orbitals, bond distances Ru-O are equal to 1.680 Å . Finally, for the RuO_4 compound, the Ru-O bonds involve five $4d$ orbitals mixed with oxygen $2p$ orbitals. The Ru-O bond distance is equal to 1.670 Å. At the SCF level, the ground states for RuO_3 and RuO_4 were found to be a triplet. With the correlated MCPF method, the energy difference between the singlet and the triplet placed the singlet as the ground state, lower by 177.8 kJ mol^{-1} for RuO_3 and 120.5 kJ mol^{-1} for RuO_4. It was underlined that to increase the accuracy of this study significantly, regarding the ruthenium oxides, it would probably not be enough to include triple excitations in the valence correlation treatment, and the metal $4p$-electrons would also have to be correlated. In addition to the cost of including the triples in the correlation treatment, this would also require much larger basis sets.

Hameka *et al*. (1991) [27] performed optimised geometries, evaluation of energies, and vibrational frequencies on RuO_2, RuO_3, and RuO_4 with the HF theory. They used the Hay and Wadt RECP to describe ruthenium [25, 28], and for oxygen, a Dunning/Huzinaga valence double-zeta function [29]. For RuO_2, a closed shell singlet state was first obtained with a bond angle of 150.6°, and a bond length of 1.595 Å. There were three vibrational modes located at 306.8 cm^{-1} (IR intensity = 55 km mol^{-1}), 817.2 cm^{-1} (IR intensity = 816 km mol^{-1}), and 1098.2 cm^{-1} (IR intensity = 21 km mol^{-1}). They derived a number of possible triplet configurations by performing single configuration unrestricted HF computations. They found that one of the triplet states, with the unpaired electrons in (B_1) and (A_2) orbitals, has an optimised geometry with a bond angle of 122.7° and a bond length of 1.800 Å and an energy 42.4 kJ mol^{-1} lower than the closed shell singlet state. It was highlighted that the vibrational frequencies and geometries computed in singlet states agree better with their experimentally observed configuration of RuO_2 in the argon matrix [30], with bond angle of 149± 2 ° and IR lines at 926 and 902 cm^{-1}. They attributed the ground state to be the singlet state.

For RuO_3, a planar symmetric structure D_{3h} is predicted with a Ru-O bond length of 1.610 Å. They obtained six vibrational modes, 2 two-fold degenerate modes at 329.8 cm^{-1} (IR intensity = 13 km mol^{-1}) and at 758.6 cm^{-1} (IR intensity = 146 km mol^{-1}), and two non-degenerate modes at 185.0 cm^{-1} (IR intensity= 27 km mol^{-1}) and at 1054.9 cm^{-1} (IR intensity = 0 km mol^{-1}). For RuO_4, Hameka *et al*. [27] predicted a tetrahedral structure T_d with a Ru-O bond length of 1.608 Å. Nine vibrational frequencies were found: a two-fold degenerate mode at 398.1 cm^{-1} with relative IR intensity of 22 km mol^{-1}, another three-fold degenerate mode at 923.1 cm^{-1} with relative IR intensity of 297 km mol^{-1}, and a non-degenerate mode

at 1065.9 cm^{-1} with zero IR intensity.

Density functional calculations (DFT) were carried out by Zhou *et al.* (2000) [31] on metal oxides and anions with the BP86 and B3LYP functionals [32]. For O atoms, they used the 6-31+G(d) basis set and Los Alamos RECP plus DZ for metal atoms [25]. Calculations for monoxides and dioxides were done using both BP86 and B3LYP functional, and for RuO_3 and RuO_4 using the BP86 functional only. RuO was found to have a $^5\Delta$ ground state with BP86 and B3LYP functionals, as in MC-SCF calculations [20]. The Ru-O bond distance is equal to 1.748 and 1.745 Å with BP86 and B3LYP methods, respectively. The vibrational frequencies were found at 859.9 (BP86) and 862.7 cm^{-1} (B3LYP). Concerning the RuO_2 system, the ground state $^1A_1$ was obtained with both density functionals, the triplet state $^3B_1$ had an upper energy of 27.2 kJ mol^{-1} in the BP86 calculations, and of 34.7 kJ mol^{-1} in the B3LYP calculations. Bond lengths and bond angles for the singlet ground state were found to be 1.709 Å and 150.1 $°$at the BP86 level, 1.697 Å and 152.4°at the B3LYP functional. Vibrational frequencies and intensities (in parenthesis km mol^{-1}) were equal to 947.8 cm^{-1} (7) for the v_1 mode, 196.2 cm^{-1} (30) for the v_2 mode, and 964.8 cm^{-1} (354) for the v_3 mode. RuO_3 was found to have an $^1A_1$ state in D_{3h} symmetry with the BP86 functional. Bond lengths were equal to 1.717 Å. Vibrational frequencies and intensities (in parenthesis in km mol^{-1}) were found at 949.7 (125) cm^{-1}, 948.0 (125) cm^{-1}, 915.8 (0) cm^{-1}, 289.8 (1) cm^{-1}, 289.7 (1) cm^{-1}, and 77.5 (9) cm^{-1}. The species O_2RuO_2 was observed in solid neon matrix isolation at 946.9 and 928.5 cm^{-1}, blue-shifted 6.7 and 7.8 cm^{-1} from the argon matrix values. The DFT calculations performed with the BP86 functional assigned the ground state for O_2RuO_2 to be $^1A_1$ in C_{2v} symmetry, and with Ru-O bond length equal to 1.924 Å. The vibrational frequencies were found at 928.7 (92,a_1) and 912.6 (162, b_2) cm^{-1}, for isotope $^{18}O_2$. The a_1 and b_2 modes were identified at 983.7 (92) and 956.4 (177) cm^{-1}, respectively, for isotope $^{16}O_2$. The ground state of RuO_4 species was found to be $^1A_1$ in T_d symmetry, and with the Ru-O bond length equal to 1.723 Å. The vibrational frequencies for isotope $^{18}O_2$ were determined at 906.0 (92, t_2) and 852.2 (0,a_1) cm^{-1}. With isotope $^{16}O_2$, the t_2 and a_1 stretching were found at 950.2 (100) and 904.0 (0,a_1) cm^{-1}, respectively. The calculated vibrational frequencies in the BP86 functional were stated to be scaled by 0.965 and 0.971 factors in order to match the argon and neon matrix values, respectively.

A recent article on MO_4 molecules by Huang *et al.* (2016) [33] proposed molecular properties for RuO_4 species, with a ground state found to be $^1A_1$ in T_d symmetry and a Ru-O bond length optimised by CASPT2 calculations equal to 710 Å, greater than all the previous studies presented here, using for O atom the aug-cc-VDZ2d basis set and Ru atom LANL RECP LANL2-VDZ basis set. The active space was obtained using 12 electrons with three weakly occupied metallic d-t_2 type orbitals, six strongly, and three weakly occupied orbitals of O-2p type. The weights of the two most important configurations in the CASSCF wave function were found to be 89% and 1% for C_0 and C_1 coefficients, respectively. CCSD(T) calculation was also performed giving T_1 Diag value equal to 0.03 and D_1 Diag value equal to 0.10 . Vibrational harmonic frequencies provide the A_1 state at 943 cm^{-1}. Relativistic effects were evaluated with B3LYP ADF package [34] by the zero-order regular approximation, and the atomic small-core-shells were frozen from atomic Dirac-Slater calculations.

All these molecular properties will be compared to our results. The first step is to find a suitable level of theory to investigate the structural features. The methodology will be assessed for Ru, RuO, and RuO_2 species, due to their affordable system size for a large panel of quantum chemistry levels of theory.

4.2   Structural properties

The literature review of Ru quantum chemical calculations highlights the fact that wavefunction based methods, even if they allow to take into account the multi-reference (MR) character generated by metal transitions can be computationally expensive in deriving optimised geometries, and unmanageable when the size of the basis sets and/or the number of atoms increases. DFT method seems the best compromise to compute equilibrium geometries. For small systems RuO and RuO_2, optimised geometries are calculated with different wave functions to evaluate the potential impact on the results.

4.2.1   Choice of density functional approximation (DFA)

All the species used to derive the thermodynamic quantities, H_2, H_2O, OH, and O_2 have been investigated with Ru compounds in order to define the most suitable DFAs. Preliminary work [35] led us to choose the Dunning basis set to represent the MOs of our systems, this type of basis set being energy consistent. For the Ru atom, an ECP28MDF RECP is used as presented in Section 3.4.4 of Chapter 3. The geometries are computed in several methods and compared in Table 4.1. The obtained results lead us to choose the hybrid functional TPSSh with 5 % of HF amount in exchange functional, as the latter provides fair geometries for all studied molecules.

The Ru ground state is found to be a ^{5}F as described in the NIST database [40]. Concerning RuO, the ground state is determined to be $^5\Delta$, as described in previous works [20, 31]. Bond length is equal to 1.713 Å, shorter than B3LYP [31] and MCSCF [20] determinations, but much closer to experimental work, whose value is about 1.716 Å [39] and 1.714 Å [38]. Vibrational stretching frequency, computed in harmonic formulation, is equal to 895.0 cm^{-1} with an intensity of about 133 km mol^{-1}. This result is slightly higher by ca. 33 cm^{-1} than in the previous *ab initio* studies. The experimental value derived by Wang *et al.* [38] (855.82 cm^{-1}) is closer to our calculations.

The RuO_2 system is found to be a $^1A_1$ ground state, as in the studies by Hameka *et al.* [27] and Zhou *et al.* [31]. The triplet state is found to be 24.8 kJ mol^{-1} greater than the singlet state at TPSSh-5%HF level. The TPSSh-5%HF geometric parameters (1.685 Å, 149.8 °) are close to the geometries optimised at the B3LYP level (1.697 Å, 152.4 °) [31]. The derived O-Ru-O angle is close to the value of $149 \pm 2°$ predicted by argon matrix isolation of Kay *et al.* [30]. The computed vibrational harmonic frequencies are equal to 972 cm^{-1} for the symmetric stretching frequency, above the antisymmetric stretching equal to 964 cm^{-1}. B3LYP calculations predict these vibrational modes at 990.1 and 989.7 cm^{-1}. Both TPSSh-5%HF and B3LYP values are about 60 cm^{-1} larger than those measured by Kay *et al.* in argon matrix (926 and 902 cm^{-1}).

Table 4.1: Bond distance (Å) and bond angles (°) of target species computed with several DFAs with the basis set aug-cc-pVTZ (aVTZ) for O and H, and aVTZ -PP for Ru, compared to literature values and wave function optimised geometries.

Method	H$_2$	OH	H$_2$O	O$_2$	RuO	RuO$_2$
	r_{H-H}	r_{O-H}	r_{O-H} ; θ_{H-O-H}	r_{O-O}	r_{Ru-O}	r_{Ru-O} ; θ_{O-Ru-O}
DFT-TPSS	0.744	0.983	0.969;104.2	1.220	1.718	1.690;149.2
DFT-TPSSh-5% HF	0.742	0.980	0.967; 104.4	1.215	1.713	1.685;149.8
DFT-TPSSh-10% HF	0.742	0.978	0.964; 104.5	1.209	1.709	1.680;150.3
DFT-M06L	0.742	0.971	0.959; 104.0	1.207	1.721	1.683; 151.3
DFT-M11L	0.746	0.964	0.951;103.6	1.181	1.712	1.657; 159.4
DFT-SOGGA-11L	0.749	0.974	0.960;104.6	1.211	1.706	1.672; 150.7
MCSCF	0.755	0.975	0.964; 102.9	1.218	1.725	1.695;162.1
MRCI	0.743	0.975	0.964; 103.1	1.217	1.712	1.691;155.6
CASPT2	0.745	0.974	0.966;103.3	1.218	1.710	1.689;153.3
Literature [a]	0.741	0.970	0.958;104.5[b]	1.208	1.714[c]-1.716[d]	*; 149±2[e]

* No data
[a] experimental values from Ref. [36] for H$_2$, OH, and O$_2$
[b] Experimental values from Ref. [37]
[c] Experimental value from Ref. [38]
[d] Experimental value from Ref. [39]
[e] Experimental value from Ref. [30]

Zhou *et al.* observed the antisymmetric stretching mode at 918.4 and 905.1 cm^{-1} in neon and argon matrices, respectively.

4.2.2   Level of basis set used for optimised geometries

The calculated electronic energy for each compound in DFA method TPSSh-5%HF is presented at optimised geometries in aug-cc-pVTZ (aVTZ), aug-cc-pVQZ (aVQZ), and aug-cc-pV5Z (aV5Z) basis set respectively in Table 4.3 in order to evaluate the influence of the level of basis set on the computed equilibrium geometries. The results shown in Table 4.3 underline that using optimised geometries from aVTZ basis set to compute single point energy calculations in aVQZ and aV5Z level provide the same total electronic energy as that obtained when the geometries are optimised with the corresponding basis sets. These observations illustrate Daniel's paper [2] recommendations stating that quantum calculation with transition metals using a triple zeta quality basis set give accurate energy closer to higher basis set expansion. Hence, the electronic energy calculations with the several methods will be computed in single point using aVTZ optimised geometries.

4.2.3   Natural population Analysis and Chemical Bonding

Natural population analysis (NPA) were carried out with the Gaussian package [41]. The topological analysis was performed with the AIMall package [42].

Table 4.2: Bond distances (Å), O-Ru-O angles (θ, deg), vibrational frequencies (cm^{-1}), and infrared intensities (km mol^{-1}) in parenthesis for RuO and RuO$_2$ compared to literature values. Ground states and symmetry are also provided.

Species	Method	r,θ	frequencies (IR intensity)
RuO ($^5\Delta$; $C_{\infty v}$)	TPSSh-5%HF[a]	1.713	895.0 (133)
	B3LYP[b]	1.745	862.7 (130)
	MCSCF[c]	1.740	814 (-)
	Exp.[d]	1.714	855.82(2)
RuO$_2$ ($^1A_1$; C_{2v})	TPSSh-5%HF[a]	1.685,149.8	972.4 (a_1, 5); 964.3 (b_2, 358); 191.7 (a_1, 21)
	B3LYP[b]	1.697,152.4	990.1 (8); 989.7 (466); 206.1 (35)
	HF[e]	1.595,150.6	1098 (21); 817 (816); 307 (55)
	Exp.[f]	-;149±2	926 ($\nu_1(A_1)$); 902.2 ($\nu_3(B_1)$)

[a] This work
[b] Ref. [31]
[c] Ref. [20]
[d] Ref. [38] with laser ablation/reaction free-jet expansion technique and laser induced fluorescence (LIF) spectroscopy. Ground state: $^5\Delta_4$
[e] Ref. [27]
[f] Ref. [30] with argon matrix isolation and Fourier Transform InfraRed Spectroscopy

For the RuO compound, the QTAIM analysis is presented in Table 4.4 and occupied orbitals in Fig. 4.1. We can see that the bonding orbitals have strong covalent bond with δ(Ru,O)

(a) σ (2)   (b) π (4)   (c) δ (1.5)

(d) π^* (2)   (e) σ^* (1)
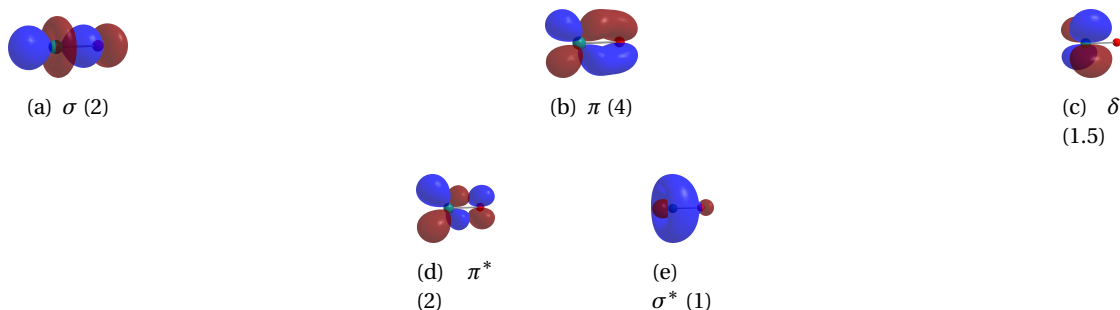
Figure 4.1: The DFT (TPSSh-5%HF) molecular orbitals forming the chemical bond between ruthenium (on the left) and oxygen (on the right) in RuO. The orbital label is given below each orbital, together with the number of electrons occupying this orbital or pair of orbitals in the case of degeneracy. Red is for negative charges and blue for positives charges

equal to 2.25, with equivalent charges q(Ru) = 0.62 and q(O) = -0.62. The bonding orbitals involve doubly occupied σ bond as discussed by Krauss *et al.* [20] and two degenerated doubly occupied π bonds.

Table 4.3:   Comparison of electronic energy (au) computed in DFT TPSSh-5%HF with optimised geometries in basis set level aVXZ, X= (3,5).

Species	Basis set	E_{elec} in aVTZ	E_{elec} in aVQZ	E_{elec} in aV5Z
	aVTZ	-1.179571	-1.1800218	-1.180173
H_2	aVQZ	-	-1.1800223	-
	aV5Z	-	-	-1.1801736
	aVTZ	-75.7690217	-75.7746909	-75.7760489
OH	aVQZ	-	-75.7746911	-
	aV5Z	-	-	-75.7760496
	aVTZ	-76.462387	-76.4684778	-76.4699344
H_2O	aVQZ	-	-76.468479	-
	aV5Z	-	-	-76.4699369
	aVTZ	-150.3963402	-150.4076146	-150.4101874
O_2	aVQZ	-	-150.4076187	-
	aV5Z	-	-	-150.4101929
	aVTZ	-169.7519032	-169.7581361	-169.7600483
RuO	aVQZ	-	-169.7581361	-
	aV5Z	-	-	-169.7600529
	aVTZ	-245.0512516	-245.0632871	-245.0667289
RuO_2	aVQZ	-	-245.0635089	-
	aV5Z	-	-	-245.0667375

Table 4.4:   Ru–O bond distances (Å), natural population analysis (NPA) charges, and bond critical points (BCP) parameters: ρ_b and $\nabla^2\rho_b$ are the electron density and the Laplacian at the BCP given in e^-/bohr^3 and e^-/bohr^5, δ(Ru,O) is the delocalisation index, H_b (au) is the energy density at the critical point. All values are computed at the TPSSh-5%HF/aVTZ level of theory.

Species	r_e	q(Ru)	q(O)	δ(Ru,O)	ρ_b	$\nabla^2\rho_b$	H_b
RuO ($^5\Delta, C_{\infty v}$)	1.713	0.62	-0.62	2.25	0.24	0.76	-0.153
RuO_2 ($^1A_1; C_{2v}$)	1.685	0.99	-0.49	1.93	0.26	0.91	-0.174
RuO_2 ($^3B_1; C_{2v}$)	1.686	0.99	-0.50	2.01	0.26	0.93	-0.172

The RuO_2 molecule is bent as a result of the interaction between the oxygen lone pairs and empty, or half-empty, $4d$ ruthenium orbitals, as seen in Hameka *et al.* [27] and Siegbahn [24] studies. The bonding orbitals are found to be doubly covalent with a delocalisation index δ(Ru,O) equal to 1.93 and 2.01 for singlet and triplet states, respectively. In Fig. 4.2, the triplet state shows two single occupied $4d$ ruthenium orbitals, whereas the distribution charge q(Ru) and q(O) present equal values for both singlet and triplet states of RuO_2, which means that bonding involves empty $4d$ Ru orbitals.

(a) $^1A_1$-σ (2)   (b) $^1A_1$-π (2)   (c) $^1A_1$-π (d) $^1A_1$-π (2)   (e) $^1A_1$-π
                                           (2)   (2)

(f) $^1A_1$-δ (g) $^3B_1$-δ (h) $^3B_1$-δ
(2)   (1)   (1)
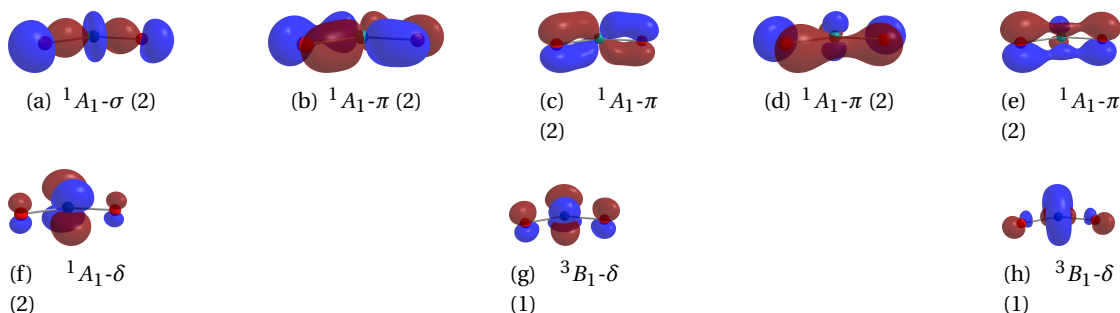
Figure 4.2: DFT (TPSSh-5%HF) forming the chemical bond between ruthenium (at the center) and the two oxygen atoms in RuO_2 in the $^1A_1$ ground-state (a)-(f), and in the singly occupied orbitals in the $^3B_1$ orbital. The orbital label is given below each orbital and the occupation number is in parenthesis.

4.3   Electronic energy calculations

The computational procedures used to perform the calculations in each theory are first disccused. Then the derived electronic energies for Ru, RuO, and RuO_2 systems, are tabulated with variation of the level of theory.

4.3.1   Computational details

DFT calculations   The unrestricted broken symmetry (UDFT-BS) formulation is used for all DFT calculations. This procedure allows to include some multi-configurational character on the single Kohn-Sham determinant artificially, by allowing mixing of configurations of different multiplicities. This approach ensures to find the lowest energetically ground state, which can be contaminated by higher multiplicities state [43]. Electronic energies obtained with aVTZ, aVQZ and aV5Z basis set expansion have been extrapolated to the Complete Basis Set (CBS) limit using the following formula [44]:

$$E(n) = E(CBS) + A\exp-(n-1) + B\exp-(n-1)^2. \tag{4.1}$$

Computational analyses are presented in Section B.4.1 of Appendix B. The calculations were done using the Gaussian 09 program [41], with 8 processors and 1 node. Table B.3 underlines that the computational costs increase both with the molecular system size and the basis set quality. The use of aVTZ basis sets to optimise the geometry allows one to keep the calculation time short, and the memory needs is then smaller than 1GB.

Multi-Reference (MR) calculations   CASSCF and post-CASSCF calculations were performed using a full valence active space (oxygen $2s$ and $2p$, ruthenium $5s$ and $4d$). MRCI calculations were determined with the Davidson's size-consistent correction [45]. CASPT2 electronic energies were derived with the ionisation potential electron affinity (IPEA) corrected zeroth-order Hamiltonian [46], equal to 0.25. CBS extrapolations were done using a three-point ex-

ponential formula for E_{CASSCF} [47, 48]:

$$E_{\text{CASSCF}}(n) = E_{\text{CASSCF}}^{\text{CBS}} + A \exp(-Bn), \tag{4.2}$$

and a two-point extrapolation for E_{corr} [49]:

$$E_{\text{corr}}(n) = E_{\text{corr}}^{\text{CBS}} + An^{-3}. \tag{4.3}$$

The MR calculations were performed with the Molpro package [50], using 8 processors with one node. MCSCF (CASSCF) calculations are not expensive, as presented in Table B.4. MRCI +Q calculations appear more expensive than MCSCF ones, but still affordable. AQCC and ACPF methods are two times more computationally expensive than MRCI theory, as displayed in Table B.5. The computational time increases with the basis set expansion and system size in all perturbative theories (Section B.4.4 of Appendix B). For all methods, most of the time is used to build the integral matrices, and it together with memory requirements increases with the basis set size and the number of atoms.

Coupled Cluster expansions   Coupled cluster calculations were performed using TPSSh-5%HF/aVTZ geometries with Molpro package [50]. Energies are extrapolated to Complete Basis Set limit using Equations 4.2 and 4.3. The overall computed cluster expansions total electronic energies were derived starting from R(O)HF total energies, that are quite similar for CCSDT and CCSDTQ calculations. The potential multi-reference character of the wave function was also estimated by UDFTBS-UHF-CCSD(T) calculations performed with Gaussian09 software [41]: starting from the UDFT broken symmetry (BS) charge density, we ensure that the cluster excitations will be carried out on the lowest open-shell UHF state. Derived energies of Ru, RuO, and RuO_2 using this methodology are presented in Table B.1 of Appendix B. It is worth noticing that the UDFTBS-UHF-CCSD(T) procedure is computationally expensive, aVQZ calculations taking more than 75 hours, comparing to the 6 min (see Section B.4.5) taken in RHF-CCSD(T) Molpro procedure to perform all level basis sets (aVTZ, aVQZ, and aV5Z) calculations. The multireference cluster expansion is tremendously expensive, taking for example 10 days for RuO_2 in the aVTZ basis set for an MR-CCSDT calculation. BCCD(T) calculations were performed for closed-shell systems with the Molpro package. This method cancels T1 contributions, thus providing a way to check the validity of CCSD calculations, as explained in Chapter 3 Section 3.2.5.

4.3.2   Electronic energies of Ru

Table 4.5 presents the total electronic energies computed at different levels of theory for Ru system. Ru S^2 eigenvalue is equal to 6.002. The T_1 and D_1 Diag value are equal to 0.02 and 0.04, respectively. They are in agreement with the recommended values by Jiang *et al.* for single reference calculations, (0.05 and 0.15, respectively) [51]. With MR calculations, the ground state of Ru is found to be a ^{5}F. The computed C_0^2 for the leading configuration is larger than 0.9, reflecting that MR character is negligible for the ground state wave function of this system, in agreement with the non-contaminated S^2 operator, T_1 and D_1 Diag values. As displayed in Table 4.5, the total electronic energies computed in DFA, HF and CAS-

Table 4.5: Electronic energies of Ru compound performed at the HF, DFT, MR methods, and Coupled Cluster theories, using TPSSh-5%HF optimised geometries.

Method	E_{TOT} (CBS) [au]	ΔE [kJ mol^{-1}][a]		
		CBS - aVTZ	CBS - aVQZ	CBS - aV5Z
HF	-93.8094	-1.8	-1.3	-0.8
TPSSh-5%HF	-94.4657	-4.4	-2.3	-0.8
CCSD(T)	-94.0398	-70.1	-31.3	-16.2
MR-CCSDT	-94.0396	-69.1	-30.8	-15.9
MR-CCSDTQ	-94.0282	-38.5	0.0	0.0
CASSCF	-93.8061	-0.3	0.0	0.0
MRCI +Q	-94.0316	-65.0	-28.9	-14.8
ACPF	-94.0291	-64.4	-28.7	-14.7
AQCC	-94.0256	-63.3	-28.2	-14.4
CASPT2	-94.0379	-80.5	-37.9	-19.4
QDNEVPT2-PC	-94.0033	-73.9	-35.3	-18.1

[a] Difference in total energies derived at CBS and AVXZ basis set level

SCF theories converge with basis set expansion, with a maximum difference in energy less than 5 kJ mol^{-1}. The post-CASSCF theories have minimal ΔE about 20 kJ mol^{-1}. Regarding UDFTBS-UHF-CCSD(T) calculations performed with Gaussian software [41] (see Table B.1), the UHF total energies are closed to R(O)HF ones. Additional excitation with UCSSDT and UCCSDTQ methods led to calculated values close to those obtained with the CCSD(T) theory. As we are interested in relative energies, the final accuracy of these approaches will be obtained while deriving the thermodynamic values.

4.3.3 Electronic energies of RuO system

RuO system did not exhibit any spin contamination, with S^2 eigenvalue equal to 6.008. The ground state was found doubly degenerated by MR calculations, with one state in A_1 symmetry and the other one in B_1 symmetry, using C_2 point group symmetry. For both states, the associated wave-function is mainly described by a reference to a weight of larger than 0.9. Multireference character seems negligible for this system, confirmed by T_1 and D_1 Diag values of 0.05 and 0.13, respectively, in UCCSD(T) calculations. The computed electronic energies are presented in Table 4.6. The smaller deviations in energy differences are observed in HF, DFT and CASSCF calculations. Here again, the final accuracy can be evaluated by computing the relative energies. Although, the ΔE values decrease with basis set level in all theories, confirming convergence of calculated electronic energies with basis set expansion. The UDFTBS-UHF-CCSD(T) calculations (see Table B.1) provide UHF total energies similar to those of ROHF-UCCSD(T) theory.

4.3.4 Electronic energies of RuO$_2$ system

For RuO$_2$ species, the UDFT-BS approach provides a S^2 eigenvalue about 0.460, contaminated with triplet low-lying state. In fact, the optimisation step leads us to unstable wave func-

Table 4.6: Electronic energies of RuO compound performed at the HF, DFT, MR methods, and Coupled Cluster theories, using TPSSh-5%HF geometries.

Method	E_{TOT} (CBS) [au]	ΔE [kJ mol^{-1}][a]		
		CBS - aVTZ	CBS - aVQZ	CBS - aV5Z
HF	-168.6435	-19.3	-5.9	-1.8
DFT	-169.7611	-24.3	-8.0	-2.9
CCSD(T)	-169.2258	-155.2	-64.6	-31.9
CASSCF	-168.7333	-18.7	-5.4	-1.6
MRCI +Q	-169.1995	-135.8	-61.6	-31.6
ACPF	-169.2008	-135.9	-61.7	-31.6
AQCC	-169.1923	-133.7	-60.8	-31.1
CASPT2	-169.2212	-166.9	-79.5	-40.7
QDNEVPT2-PC	-169.1793	-157.9	-75.8	-38.8

[a] Difference in total energies derived at CBS and AVXZ basis set level

tion and stabilisation procedure lead to a contaminated singlet ground state. At the CASSCF level of theory, a singlet state ($^1A_1$) and a doubly degenerated triplet state ($^3A_1$ and $^3B_1$) were found to have the lowest energies. Their leading configuration show a C_0^2 larger than 0.9, in agreement with the T_1 and D_1 Diag values of 0.04 and 0.10, respectively. The treatment of dynamical correlation with the MRCI +Q calculations leads to a singlet ground state, lower to the triplet state by about 38.8 kJ mol^{-1}. With the perturbative CASPT2 calculation, a singlet ground state is also found, and is lower than the triplet state by about 29.2 kJ mol^{-1}. These results underline that inclusion of dynamical correlation to CASSCF reference states stabilises the singlet ground state more. The calculated electronic energies are shown in Table 4.7. Table 4.7 highlights ΔE values decreasing with the level of basis set in all theories. The

Table 4.7: Electronic energies of RuO$_2$ compound performed at the HF, DFT, MR methods, and Coupled Cluster theories, using TPSSh-5%HF optimised geometries.

Method	E_{TOT} (CBS) [au]	ΔE [kJ mol^{-1}][a]		
		CBS - aVTZ	CBS - aVQZ	CBS - aV5Z
HF	-243.4714	-39.8	-11.4	-3.3
DFT	-245.0686	-45.6	-13.4	-4.9
CCSD(T)	-244.4379	-248.1	-101.3	-49.3
BCCD(T)	-244.4379	-248.4	-101.2	-49.2
CASSCF	-243.7250	-38.8	-11.0	-3.1
MRCI +Q	-244.4104	-236.8	-111.0	-56.8
ACPF	-244.4153	-239.2	-112.2	-57.5
AQCC	-244.4049	-235.5	-110.6	-56.6
CASPT2	-244.4419	-279.8	-136.2	-69.8
QDNEVPT2-PC	-244.3917	-267.5	-131.1	-67.1

[a] Difference in total energies derived at CBS and AVXZ basis set level

cluster calculations were performed with the restricted formalism CCSD(T). The UDFTBS-

UHF-CCSD(T) calculations provided total UHF potential energies equivalent to RHF-CCSD-(T) ones (see Table B.1). We noticed that the BCCD(T) calculations provide energies similar to the CCSD(T) ones. We can confirm that the R(O)HF-CCSD(T) procedure implemented in Molpro package [50] provide reliable CCSD(T) energies easily, closer to the UDFTBS charge density starting UHF-CCSD(T) calculations performed with Gaussian software [41] and computationally more demanding.

4.4   Study on spin-orbit coupling

As discussed previously in Section 4.1, the relativistic effects are taken into account using RECP and the corresponding basis sets. The spin-orbit coupling is evaluated in two steps as described in Chapter 3 Section 3.4. The first step consists in building the wave functions of all the potential multiplicities of spin-free states, while in the second step the spin-orbit Hamiltonian is constructed by taking into account the dynamical correlation estimated with CASPT2, QDNEVPT2-PC, or MRCI+Q methods. To assess the accuracy of the stabilising contribution of the spin-orbit coupling to the ground state energies, either pseudo-potential spin-orbit integrals or all-electron mean-field integrals calculations were used.

For Ru, RuO, and RuO_2 compounds, the evaluation of spin -orbit coupling was performed as implemented in the MOLPRO package using the CASSCF, MRCI +Q, CASPT2, and QD-NEVPT2 energies. The state-interaction SOC matrix was built for Ru coupling 15 quintet, 36 triplet, and 36 singlet states bridged by the full-valence active space, as these states differ in term of energy by less than 3 eV at all levels of theories aforementioned. The CASSCF, MRCI +Q , and CASPT2 computed spin free electronic energies are illustrated with an energy level diagram in Fig. B.1, B.2, and B.3, respectively, of Appendix B. The SOC matrix was built for RuO by coupling the seven lowest-lying state of singlet, triplet, and quintet multiplicities with the oxygen 2s and 2p orbitals, and the ruthenium 5s and 4d orbitals included in the active space. The energy level diagrams are presented in Fig. B.4 for CASSCF, MRCI +Q, and CASPT2 spin free electronic energies. For the RuO_2 system, the CASSCF reference states were built starting with 5 singlet, 5 triplet, and 5 quintet states in each symmetry, since the molecular geometry belongs to the C_{2v} symmetry group. Energy levels diagrams for RuO_2 are displayed in Fig. B.5, B.6, and B.7 for CASSCF, MRCI +Q, and CASPT2 theories calculated spin free electronic energies, respectively. The SOC contributions to ground states for all species are tabulated in Table 4.8. The results shown in this table highlight the fact that all levels of theory predict a SOC contribution, given as the difference between the spin-orbit ground-state and the spin-orbit free ground state, without any variation with the basis set expansion.

The SOC values are about -16, -10, and -0.7 kJ mol^{-1} for Ru, RuO, and RuO_2, respectively. ANO all-electron basis sets and the relativistic Douglas-Kroll Hamiltonian yield the same value of the energy lowering by SOC for the ruthenium oxide, confirming the good description of core electrons with RECP and of valence SOC. For all compounds, we observe that SOC values are already evaluated with the lower method (CASSCF) and with the lower basis set expansion (aVTZ). The Ru electronic spectrum is illustrated only for the first J levels in Table 4.9 to evaluate the accuracy of the treatment of correlation effects and spin-orbit coupling. This latter lifts the degeneracy of the ^{5}F ground state, and the first four excitation

Table 4.8: Spin-orbit contributions ΔE_{SO} in kJ mol^{-1} to the ground-state energies of Ru, RuO, and RuO$_2$ with variation of theory and basis set levels using optimised geometries with TPSSh5%HF level of theory.

Level of theory	ΔE_{SO}		
	Ru	RuO	RuO$_2$
CASSCF/aVTZ	-16.12	-10.46	-1.60
CASSCF/aVQZ	-16.14	-10.48	-1.40
CASSCF/aV5Z	-16.13	-10.67	-1.40
CASPT2/aVTZ	-15.82	-10.42	-0.77
CASPT2/aVQZ	-15.87	-10.45	-0.73
CASPT2/aV5Z	-15.88	-10.45	-0.72
CASPT2/ANO-VTZ	-	-11.82	-
MRCI/aVTZ	-15.30	-10.33	-0.70
MRCI/aVQZ	-15.41	-10.42	-
MRCI/aV5Z	-15.46	-	-

energies agree well with the experimental values, indicating that there is a weak interplay between electron correlation and the SOC. Thus the latter has been accurately treated by the spin-orbit effective core potential.

Table 4.9: Excitation energies (cm^{-1}) and mean signed error (MSE) with respect to the experimental data of the first five J levels of Ru. Spin-orbit free correlated energies obtained at the MRCI+Q,CASPT2, or QD-NEVPT2 levels are used to dress the state-interaction SOC matrix.

Configuration	J	SO-MRCI+Q	SO-CASPT2	SO-QDNEVPT2	Exp. [40]
	5	0	0	0	0
	4	1022	1187	1078	1191
$4d^7(a^5F)5s$	3	1849	2023	1904	2092
	2	2548	2691	2486	2713
	1	2874	2986	2853	3105
MSE		-161	-20	-153	

The RuO$_2$ electronic spectrum illustrated in Table 4.10 shows that the spin-orbit electronic ground state is dominated by a singlet character, in agreement with the spin free states correlated calculations including dynamical corrections.

From Table 4.8, we remark that SOC contributions are only sizeable for Ru and RuO and negligible for RuO$_2$ that has a closed shell ground-state. We thus neglect SOC effects on energies for all other species studies in this manuscript.

Table 4.10: Excitation energies in cm^{-1} of the low-lying energy levels of RuO_2 computed at the SO-CASSCF, SO-MRCI+Q, and SO-CASPT2.

Composition	SO-CASSCF	Composition	SO-MRCI+Q	Composition	SO-CASPT2
$51\% \, {}^3A_1 + 49\% \, {}^3B_1$	0	$99\% \, {}^1A_1$	0	$99\% \, {}^1A_1$	0
$52\% \, {}^3A_1 + 48\% \, {}^3B_1$	1	$48\% \, {}^3A_1 + 52\% \, {}^3B_1$	3163	$52\% \, {}^3A_1 + 48\% \, {}^3B_1$	1649
$62\% \, {}^1A_1 + 40\% \, {}^3B_1$	653	$48\% \, {}^3A_1 + 52\% \, {}^3B_1$	3164	$52\% \, {}^3A_1 + 48\% \, {}^3B_1$	1650
$99\% \, {}^3A_1$	732	$99\% \, {}^3B_1$	3871	$99\% \, {}^3A_1$	2361
$38\% \, {}^1A_1 + 62\% \, {}^3B_1$	856	$98\% \, {}^3A_1$	3942	$98\% \, {}^3B_1$	2425

4.5 Validation of methodology

The several energetics computed with DFA and wave-function based methods will be used to derive thermodynamic quantities of RuO and RuO_2. Calculated standard enthalpy of formation at 298 K will be compared to their literature counterparts leading us to validate our computational procedure given the accuracy of the results.

4.5.1 Choice of equations

To obtain the standard enthalpy of formation of RuO and RuO_2, we will use the known standard enthalpy of formation of Ru derived by Cordfunke and Konings [52] with the reaction enthalpies of the following four reactions:

$$R_1(n) : Ru + n\,O \longrightarrow RuO_n \tag{4.4a}$$

$$R_2(n) : Ru + n\frac{1}{2}O_2 \longrightarrow RuO_n \tag{4.4b}$$

$$R_3(n) : Ru + n\,HO \longrightarrow RuO_n + n\,H \tag{4.4c}$$

$$R_4(n) : Ru + n\,H_2O \longrightarrow RuO_n + n\,H_2 \tag{4.4d}$$
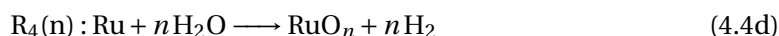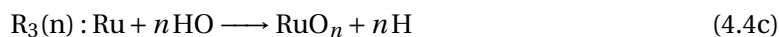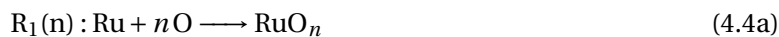
The values of the standard enthalpies of formation for H, H_2, H_2O, OH, O, and O_2 have been taken from the literature [53].

4.5.2 Results for RuO

Table 4.11 presents the computed standard enthalpies of formation with variation of the basis set level for the RuO species.

The average standard enthalpy of formation of RuO equal to 403.5 ± 12.8 kJ mol^{-1} at TPSSh-5%HF/CBS level calculation is larger than the literature value by about 30 kJ mol^{-1}, with a standard deviation across the four chemical reactions of about 13 kJ mol^{-1}, slightly larger than the expected accuracy of quantum chemical methods [54]. CASPT2 calculations present less deviation around 4 kJ mol^{-1}, smaller than QDNEVPT2 values about 8 kJ mol^{-1} at CBS level. Average standard enthalpies of formation derived in perturbation methods are

Table 4.11: Computed standard enthalpies of formation $\Delta_f H°(298\ K)$ for RuO obtained at the DFT, CCSD(T), and MR correlated levels using TPSSh-5%HF optimised geometries, for Reactions 4.4. $\overline{\Delta_f H°}(298K) \pm \sigma$ represents the average and the standard deviation of computed standard enthalpies of formation.

$\Delta_f H°(298\ K)$lit = 376 ± 25 kJ mol^{-1} (Ref. [52])				
Level of theory	R_1	R_2	R_3	R_4	$\overline{\Delta_f H°}(298K) \pm \sigma$
DFT					
TPSSh5%HF/aVTZ	411.9	417.9	407.5	377.6	403.7 ± 13.1
TPSSh5%HF/aVQZ	411.0	418.5	407.8	378.1	403.9 ± 12.9
TPSSh5%HF/aV5Z	410.8	418.2	407.6	377.9	403.7 ± 12.9
TPSSh5%HF/CBS	410.7	418.1	407.5	377.8	403.5 ± 12.8
Variational methods					
MRCI+Q/aVTZ	497.3	482.8	485.3	476.0	485.4 ± 6.0
MRCI+Q/aVQZ	488.4	479.9	482.4	476.3	481.8 ± 3.7
MRCI+Q/aV5Z	482.7	475.7	478.1	472.6	477.3 ± 3.1
MRCI+Q/CBS	476.9	471.4	473.7	468.8	472.7 ± 2.6
ACPF/aVTZ	482.5	470.5	470.1	461.1	471.0 ± 5.7
ACPF/aVQZ	472.8	467.1	466.5	460.6	466.7 ± 3.2
ACPF/aV5Z	466.8	462.7	461.9	456.6	462.0 ± 2.8
ACPF/CBS	460.8	458.2	457.2	452.5	457.2 ± 2.3
AQCC/aVTZ	488.9	475.9	475.6	466.4	476.7 ± 6.1
AQCC/aVQZ	479.5	472.6	472.2	466.1	472.6 ± 3.5
AQCC/aV5Z	473.7	468.3	467.7	462.2	468.0 ± 3.0
AQCC/CBS	467.8	463.9	463.2	458.2	463.3 ± 2.6
Perturbation theory					
CASPT2/aVTZ	431.8	433.8	421.5	419.2	426.6 ± 6.2
CASPT2/aVQZ	420.5	428.1	416.1	415.9	420.2 ± 4.2
CASPT2/aV5Z	414.2	423.3	411.4	411.4	415.1 ± 4.1
CASPT2/CBS	407.8	418.4	406.6	406.8	409.9 ± 4.2
QDNEVPT2-PC/aVTZ	406.1	414.0	403.8	412.5	409.1 ± 4.1
QDNEVPT2-PC/aVQZ	394.6	407.9	397.9	408.6	402.2 ± 6.0
QDNEVPT2-PC/aV5Z	388.2	403.0	393.2	404.1	397.1 ± 6.4
QDNEVPT2-PC/CBS	381.8	398.0	388.3	398.9	391.8 ± 6.7
Cluster expansions					
CCSD(T)/aVTZ	446.1	435.2	436.3	433.0	437.7 ± 4.2
CCSD(T)/aVQZ	437.1	432.7	433.6	433.6	434.2 ± 1.4
CCSD(T)/aV5Z	433.8	431.3	431.9	432.5	432.4 ± 0.8
CCSD(T)/CBS	431.1	430.3	430.7	432.0	431.0 ± 0.5
CCSDT/aVTZ	446.5	434.3	436.6	432.6	437.5 ± 4.5

greater than literature value by ca. 30 kJ mol^{-1}. Size-extensive MRCI methods (MRCI+Q, ACPF, and AQCC) predict $\Delta_f H°(298\ K)$ values that are about 100 kJ/mol larger than the perturbative methods. The standard deviation is however only 2 kJ mol^{-1}. In Ref. [55], we have explained that MRCI methods failed because they do not include contributions from

triple excitations which turn out to be significant for these molecules. CCSD(T) calculations present minor deviation only equal to 0.5 kJ mol^{-1} at the CBS level. Even in aVTZ calculation, the derived average deviation is about 4 kJ mol^{-1}. Computed CCSDT values are similar to CCSD(T) ones, which implies good approximation of triple excitations by perturbative triple excitations. The derived standard enthalpies are larger than the literature value by 30 kJ mol^{-1} if the literature uncertainties are taken into consideration.

4.5.3   Results for RuO$_2$

Table 4.12 presents the computed standard enthalpies of formation with variation of the basis set level for the RuO$_2$ species.

The computed average standard enthalpy of formation obtained at CCSD(T) level of 150.9 ± 1.0 turns out to be only 10 kJ mol^{-1} higher that the literature value. DFT values in average are close to literature ones, the standard deviation across the various reactions is always larger, than with CCSD(T) methods. Regarding perturbative calculations, the derived standard enthalpies of formation are at least 60 kJ mol^{-1} smaller than literature values, with a reaction standard deviation of about 20 kJ mol^{-1}, similar to the DFT one, knowing that both methods haven't boundaries on derived electronic energies since they are not variational. MRCI+Q, AQCC, and ACPF methods present fewer deviations than DFAs method, but as for RuO the predicted enthalpies are 20-40 kJ mol^{-1} larger than the literature values, it may be due to the fact that dynamical correlation is not enough taken account into these methods. Performing calculations by adding one more ruthenium d shell orbital in the active space for MRCI +Q and CASPT2 calculations (see Table B.2 of Appendix B) converged to results that tend towards the CCSD(T) ones, indicating that very large active spaces are needed in MRCI+Q or CASPT2 to reach CCSD(T) accuracy. In fact, these calculations bring previous standard enthalpy of formation of RuO from 488.5 ± 4.6 kJ mol^{-1} down to 433.5 ± 4.6 kJ mol^{-1} with the MRCI+Q method, but the computational cost is expensive: around 4 days to compute MRCI calculation in aVTZ basis set for RuO compound, besides, and for RuO$_2$, the calculation could not be handled because it to be far too large (about 300 million CSFs).

At this stage, the coupled cluster approach appears to be the best estimated level of theory to compute our thermodynamic properties, with optimised geometries at the TPSSh-5%HF method.

Table 4.12: Computed standard enthalpies of formation $\Delta_f H°(298 \, K)$ for RuO_2 obtained at the DFT, CCSD(T), and multi-reference correlated levels using TPSSh-5%HF optimised geometries, for Reactions 4.4. $\overline{\Delta_f H°}(298K) \pm \sigma$ represents the average and the standard deviation of computed standard enthalpies of formation.

Level of theory	R_1	R_2	R_3	R_4	$\overline{\Delta_f H°}(298K) \pm \sigma$
$\Delta_f H°(298 \, K)$lit = 136 ± 10 kJ mol^{-1} (Ref. [52])
DFT					
TPSSh5%HF/aVTZ	151.0	163.1	142.3	82.4	134.7 ± 26.2
TPSSh5%HF/aVQZ	147.7	162.7	141.4	81.9	133.4 ± 25.7
TPSSh5%HF/aV5ZZ	147.5	162.4	141.1	81.8	133.2 ± 25.7
TPSSh5%HF/CBS	147.4	162.2	140.9	81.6	133.0 ± 25.7
Variational methods					
MRCI+Q/aVTZ	271.1	242.1	247.0	228.5	247.2 ± 12.0
MRCI+Q/aVQZ	238.1	221.1	226.1	214.0	224.8 ± 7.3
MRCI+Q/aV5Z	218.3	204.3	209.1	198.2	207.5 ± 6.2
MRCI+Q/CBS	198.3	187.2	191.8	182.0	189.8 ± 5.2
ACPF/aVTZ	243.6	219.7	218.9	200.7	220.7 ± 11.4
ACPF/aVQZ	208.4	196.9	195.7	183.9	196.2 ± 6.4
ACPF/aV5Z	187.7	179.4	177.8	167.2	178.0 ± 5.5
ACPF/CBS	166.7	161.4	159.5	150.1	159.4 ± 4.7
AQCC/aVTZ	247.8	221.9	221.3	202.9	223.5 ± 12.2
AQCC/aVQZ	213.4	199.6	198.7	186.6	199.6 ± 6.9
AQCC/aV5Z	193.0	182.4	181.2	170.2	181.7 ± 6.0
AQCC/CBS	172.5	164.7	163.3	153.4	163.5 ± 5.1
Perturbation theory					
CASPT2/aVTZ	151.3	155.3	130.6	126.1	140.8 ± 12.5
CASPT2/aVQZ	116.0	131.2	107.1	106.6	115.2 ± 8.3
CASPT2/aV5Z	95.6	113.9	90.1	90.0	97.4 ± 8.2
CASPT2/CBS	75.0	96.1	72.7	73.0	79.2 ± 8.5
QDNEVPT2-PC/aVTZ	101.2	117.0	96.6	114.1	107.2 ± 8.3
QDNEVPT2-PC/aVQZ	65.8	92.5	72.6	94.0	81.2 ± 12.0
QDNEVPT2-PC/aV5Z	45.7	75.3	55.6	77.5	63.5 ± 12.9
QDNEVPT2-PC/CBS	25.4	57.7	38.4	59.5	45.2 ± 13.4
Cluster expansions					
CCSD(T)/aVTZ	188.9	167.1	169.3	162.7	172.0 ± 8.5
CCSD(T)/aVQZ	166.4	157.8	159.5	159.5	160.8 ± 2.8
CCSD(T)/aV5Z	158.3	153.3	154.5	155.7	155.4 ± 1.6
CCSD(T)/CBS	151.0	149.4	150.3	152.8	150.9 ± 1.0
CCSDT/aVTZ	204.4	179.9	184.6	176.6	186.3 ± 9.0

4.6 Conclusions

Despite their large number of correlated electrons, Ru, RuO, and RuO_2 are found to have negligible amounts of multi-reference character, according to CASSCF, post-CASSCF, MRCI+Q,

and CASPT2 calculations proving that the wave function is 90% dominated by a single determinant. DFAs methods with UDFT-BS procedure provide good predictions of geometries and spectroscopic parameters. Regarding the accuracy of the computed thermodynamic properties, CCSD(T) calculations present fewer deviations decreasing with increasing basis set quality. The calculated standard enthalpies of formation are homogeneous against reaction schemes. To compute the molecular properties, thermodynamic, and kinetic data of the remaining Ru species, the coupled cluster theory CCSD(T) associated with geometries computed at the TPSSh-5%HF DFA is found to be the most accurate computational procedure.

References

(1) Pelissier, M.; Daudey, J. P.; Malrieu, J. P.; Jeung, G. H. In; Springer Netherlands: Dordrecht, 1986; Chapter The Electronic Structure of Transition Metal Atoms and Diatoms Through Pseudopotential Approaches, pp 37–51, DOI: `10.1007/978-94-009-4656-9_3`.

(2) Daniel, C. Electronic spectroscopy and photoreactivity in transition metal complexes. *Coord. Chem. Rev.* **2003**, *238-239*, 143 –166, DOI: `10.1016/S0010-8545(02)00295-3`.

(3) Von Barth, U. Local-density theory of multiplet structure. *Phys. Rev. A* **1979**, *20*, 1693–1703, DOI: `10.1103/PhysRevA.20.1693`.

(4) Von Barth, U Local-Density Theory of Exchange and Correlation Energies for Valence Electrons. *Phys. Scripta* **1980**, *21*, 585.

(5) Daul, C.; Baerends, E. J.; Vernooijs, P. A Density Functional Study of the MLCT States of [Ru(bpy)3]2+ in D3 Symmetry. *Inorg. Chem* **1994**, *33*, 3538–3543, DOI: `10.1021/ic00094a017`.

(6) Erich, R.; U., G. E. K. Density -Functional Theory for Time-Dependent Systems. *Phys. Rev. Lett.* **1984**, *52*, 997–1000, DOI: `10.1103/PhysRevLett.52.997`.

(7) Gross, E.; Kohn, W. In *Density Functional Theory of Many-Fermion Systems*, Löwdin, P.-O., Ed.; Advances in Quantum Chemistry, Vol. 21; Academic Press: 1990, pp 255 –291, DOI: `10.1016/S0065-3276(08)60600-0`.

(8) Gross, E. K. U.; Dobson, J. F.; Petersilka, M. In *Density Functional Theory II: Relativistic and Time Dependent Extensions*, Nalewajski, R. F., Ed.; Springer Berlin Heidelberg: Berlin, Heidelberg, 1996, pp 81–172, DOI: `10.1007/BFb0016643`.

(9) Roothaan, C. C. J. New Developments in Molecular Orbital Theory. *Rev. Mod. Phys.* **1951**, *23*, 69–89, DOI: `10.1103/RevModPhys.23.69`.

(10) Roos, B. O. A new method for large-scale Cl calculations. *Chem. Phys. Lett.* **1972**, *15*, 153 –159, DOI: `10.1016/0009-2614(72)80140-4`.

(11) Roos, B. O. In *Methods in Computational Molecular Physics*, Diercksen G. H. F.and Wilson, S., Ed.; Springer Netherlands: Dordrecht, 1983, pp 161–187, DOI: `10.1007/978-94-009-7200-1_6`.

(12) Werner, H.-J.; Knowles, P. J. A second order multiconfiguration SCF procedure with optimum convergence. *J. Chem. Phys.* **1985**, *82*, 5053–5063, DOI: `10.1063/1.448627`.

(13) Geertsen, J.; Rittby, M.; Bartlett, R. J. The equation -of- motion coupled-cluster method Excitation energies of Be and CO. *Chem. Phys. Lett.* **1989**, *164*, 57 –62, DOI: `10.1016/0009-2614(89)85202-9`.

(14) Stanton, J. F.; Bartlett, R. J. The equation of motion coupled-cluster method. A systematic biorthogonal approach to molecular excitation energies, transition probabilities, and excited state properties. *J. Chem. Phys.* **1993**, *98*, 7029–7039, DOI: `10.1063/1.464746`.

(15) Nakatsuji, N. Cluster expansion of the wavefunction. Excited states. *Chem. Phys. Lett.* **1978**, *59*, 362 –364, DOI: `10.1016/0009-2614(78)89113-1`.

(16) Andersson, K.; Malmqvist, P.-Å.; Roos, B. O. Second-Order Perturbation Theory with a Complete Active Space Self-Consistent Field Reference Function. *J. Chem. Phys.* **1992**, *96*, 1218–1226, DOI: `10.1063/1.462209`.

(17) Andersson, K.; Malmqvist, P.-Å.; Roos, B. O.; Sadlej, A. J.; Wolinski, K. Second-order perturbation theory with a CASSCF reference function. *J. Chem. Phys.* **1990**, *94*, 5483–5488, DOI: `10.1021/j100377a012`.

(18) Finley, J.; ke Malmqvist, P.-A.; Roos, B. O.; Serrano-Andrés, L. The multi-state {CASPT2} method. *Chem. Phys. Lett.* **1998**, *288*, 299 –306, DOI: `10.1016/S0009-2614(98)00252-8`.

(19) Shepard, R In, Yarkony, D. R., Ed.; Advanced Series in Physical Chemistry; World Scientific: Singapore, 1995, pp 345–458.

(20) Krauss, M.; Stevens, W. J. *J. Chem. Phys.* **1985**, *82*, 5584.

(21) Lee, Y. S.; Ermler, W. C.; Pitzer, K. S. Abinitio effective core potentials including relativis=effects. I. Formalism and applications to the Xe and Au atoms. *J. Chem. Phys.* **1977**, *67*, 5861–5876, DOI: `10.1063/1.434793`.

(22) Christiansen, P. A.; Lee, Y. S.; Pitzer, K. S. Improved abinitio effective core potentials for molecular calculations. *J. Chem. Phys.* **1979**, *71*, 4445–4450, DOI: `10.1063/1.438197`.

(23) Ermler, W. C.; Lee, Y. S.; Christiansen, P. A.; Pitzer, K. S. Ab initio effective core potentials including relativistic effects. A procedure for the inclusion of spin-orbit coupling in molecular wavefunctions. *Chem. Phys. Lett.* **1981**, *81*, 70 –74, DOI: `10.1016/0009-2614(81)85329-8`.

(24) Siegbahn, P. E. M. Binding in Second-Row Transition Metal Dioxides, Trioxides, Tetraoxides, Peroxides, and Superoxides. *J. Phys. Chem.* **1993**, *97*, 9096–9102.

(25) Hay, P. J.; Wadt, W. R. Ab initio effective core potentials for molecular calculations. Potentials for the transition metal atoms Sc to Hg. *J. Chem. Phys.* **1985**, *82*, 270–283, DOI: `10.1063/1.448799`.

(26) Huzinaga, S. *Chem. Phys.* **1977**, *66*, 4245.

(27) Hameka, H. F.; Jensen, J. O.; Kay, J. G.; Rosenthal, C. M.; Zimmerman, G. L. Theoretical Prediction of Geometries and Vibrational Infrared Spectra of Ruthenium Oxide Molecules. *J. Mol. Spectrosc.* **1991**, *150*, 218–221, DOI: `10.1016/0022-2852(91)90204-N`.

(28) Hay, P. J.; Wadt, W. R. Ab initio effective core potentials for molecular calculations. Potentials for the transition metal atoms Sc to Hg. *J. Chem. Phys.* **1985**, *82*, 284–310, DOI: `10.1063/1.448799`.

(29) Dunning, T. H.; Hay, P. J. In *Methods of Electronic Structure Theory*, Schaefer, H. F., Ed.; Springer US: Boston, MA, 1977, pp 1–27, DOI: `10.1007/978-1-4757-0887-5_1`.

(30) Kay, J.; Green, D.; Duca, K.; Zimmerman, G. L. *J. Mol. Spectrosc.* **1989**, *138*, 49.

(31) Zhou, M.; Citra, A.; Liang, B.; Andrews, L. Infrared Spectra and Density Functional Calculations of MO_2, MO_3, $(O_2)MO_2$, MO_4, MO_2^- (M = Re, Ru, Os) and ReO_3^-, ReO_4^- in Solid Neon and Argon. *J. Phys. Chem. A* **2000**, *104*, 3457–3465, DOI: 10.1021/jp993026p.

(32) Lee, C.; Yang, W.; Parr, R. G. Development of the Colle-Salvetti correlation-energy formula into a functional of the electron density. *Phys. Rev. B* **1988**, *37*, 785–789, DOI: 10.1103/PhysRevB.37.785.

(33) Huang, W.; Xu, W.-H.; Schwarz, W. H. E.; Li, J. On the Highest Oxidation States of Metal Elements in MO4 Molecules (M = Fe, Ru, Os, Hs, Sm, and Pu). *Inorg. Chem* **2016**, *55*, PMID: 27074099, 4616–4625, DOI: 10.1021/acs.inorgchem.6b00442.

(34) Baerends, E.; Ziegler, T; Autschbach, J; Bashford, D; Bérces, A; Bickelhaupt, F.; Bo, C; Boerrigter, P.; Cavallo, L; Chong, D. et al. ADF2013. 01. *Scientific Computing & Modeling NV* **2013**.

(35) Faoulat, M. Calculs de propriétés thermodynamiques de composés de ruthénium., MA thesis, Université Claude Bernard Lyon 1, 2003.

(36) Huber, K.; Herzberg, G., *Molecular Spectra and Molecular Structure. IV. Constants of Diatomic Molecules*; Van Nostrand Reinhold Co.: 1979.

(37) Hoy, A.; Bunker, P. A precise solution of the rotation bending Schrödinger equation for a triatomic molecule with application to the water molecule. *Journal of Molecular Spectroscopy* **1979**, *74*, 1–8, DOI: 10.1016/0022-2852(79)90019-5.

(38) Wang, N.; Ng, Y. W.; Cheung, A. S. C. Electronic Transitions of Ruthenium Monoxide. *J. Phys. Chem. A* **2013**, *117*, 13279–13283.

(39) Scullman, R.; Thelin, B. The Emission Spectrum of RuO between 5000 and 6000 Å. *J. Mol. Spectrosc.* **1975**, *56*, 64–75.

(40) Moore, C. E. Atomic Energy Levels as Derived from the Analyses of Optical Spectra. *Nat. Stand. Ref. Data Ser.* **1971**, *35*, 245.

(41) Frisch, M. J. et al. Gaussian 09 Revision C.01., Gaussian Inc. Wallingford CT, 2009.

(42) Keith, T. A. AIMAll (Version 14.11.23), Todd A. Keith, TK Gristmill Software, Overland Park KS, USA, 2014., http://aim.tkgristmill.com.

(43) Souvi, S. O.; Danset, D.; Alikhani, M. E.; Manceron, L. Formation and Structure of Co_2O_4: A Combined IR Matrix Isolation and Theoretical Study. *J. Phys. Chem. A* **2010**, *114*, 11399–11407, DOI: 10.1021/jp104873j.

(44) Peterson, K. A.; Woon, D. E.; Dunning, T. H. Benchmark calculations with correlated molecular wave functions. IV. The classical barrier height of the H+H2 -> H2+H reaction. *J. Chem. Phys.* **1994**, *100*, 7410–7415, DOI: 10.1063/1.466884.

(45) Langhoff, S. R.; Davidson, E. R. Configuration interaction calculations on the nitrogen molecule. *Int. J. Quantum Chem.* **1974**, *8*, 61–72, DOI: 10.1002/qua.560080106.

(46) Ghido, G.; Roos, B. O.; Malmqvist, P.-Å. A Modified Definition of the Zeroth-Order Hamiltonian in Multiconfigurational Perturbation Theory (CASPT2). *Chem. Phys. Lett.* **2004**, *396*, 142–149, DOI: `10.1016/j.cplett.2004.08.032`.

(47) Feller, D. Application of Systematic Sequences of Wave Functions to Water Dimer. *J. Chem. Phys.* **1992**, *96*, 6104–6114, DOI: `10.1063/1.462652`.

(48) Feller, D. The Use of Systematic Sequences of Wave Functions for Estimating the Complete Basis Set, Full Configuration Interaction Limit in Water. *J. Chem. Phys.* **1993**, *98*, 7059–7071, DOI: `10.1063/1.464749`.

(49) Helgaker, T.; Klopper, W.; Koch, H.; Noga, J. Basis-Set Convergence of Correlated Calculations on Water. *J. Chem. Phys.* **1997**, *106*, 9639–9646.

(50) Werner, H.-J.; Knowles, P. J.; Knizia, G.; Manby, F. R.; Schütz, M. Molpro: A General Purpose Quantum Chemistry Program Package. *WIREs Comput. Mol. Sci.* **2012**, *2*, 242–253, DOI: `10.1002/wcms.82`.

(51) Jiang, W.; DeYonker N, J.; Wilson, A. K. Multireference Character for 3d Transition-Metal-Containing Molecules. *J. Chem. Theory Comput.* **2012**, *8*, 460–468, DOI: `10.1021/ct2006852`.

(52) Cordfunke, E. H. P.; Konings, R. J. M. Thermochemical Data for Reactor Materials and Fission Products: The ECN Database. *J. Phase Equilib.* **1993**, *14*, 457–464, DOI: `10.1007/BF02671964`.

(53) Cox, J.; Wagman, D.; Medvedev, V., *CODATA Key Values for Thermodynamics*; Hemisphere: 1989.

(54) Jensen, F., *Introduction to computational chemistry*; Wiley: 2007.

(55) Miradji, F.; Souvi, S.; Cantrel, L.; Louis, F.; Vallet, V. Thermodynamic Properties of Gaseous Ruthenium Species. *J. Phys. Chem. A* **2015**, *119*, 4961–4971, DOI: `10.1021/acs.jpca.5b01645`.

THERMODYNAMIC PROPERTIES OF RU GASEOUS COMPOUNDS

C hapter 4 proposed the validation of the methodology to derive the thermodynamic properties of the ruthenium oxides. The cluster expansion CCSD(T) with the TPSSh-5% HF method was found to be the most appropriate. This Chapter will provide molecular structural properties and thermodynamic quantities for ruthenium gaseous oxides and other species such as oxyhydroxides, which, as discussed in Chapter 2, are suspected to play a role in the transport of RuO_4, under an atmosphere consisting of a combined air/steam mixture.

In the first section, the molecular structural properties will be presented and compared to the literature data. The derived electronic energies will be tabulated in Section 5.2, with stepwise binding energies of Ru oxides. Then, in Section 5.3, the standard enthalpies of formation, molecular entropies, and heat capacities are calculated. Ruthenium speciation calculations at thermodynamic equilibrium in conditions of a nuclear power plant severe accident will be presented in the last section, with sensitivity analysis regarding theoretical standard enthalpy of formation.

5.1   Structural properties

Optimised geometries calculations were performed in the previous chapter aVTZ basis set expansion while exploring the molecular properties of RuO and RuO_2 oxides. In this chapter, we optimise the geometries in the aVQZ basis set, knowing that discrepancies in this level of basis set compared to CBS one are less than at aVTZ expansion. In this way, the accuracy of computed geometries is improved for cluster expansion calculations, in particular regarding the increasing size of our systems with oxyhydroxide species and dimer ones. The structural properties of Ru oxides (RuO_3, RuO_4, and its dimer O_2RuO_2) are first presented. Then the bond lengths, the nature of chemical bonding, and the molecular orbitals in the Ru oxyhy-

droxide compounds are analysed. The geometric parameters and the topological analyses of Ru dimer species are provided in the last subsection.

5.1.1   Structural properties of Ru oxides

5.1.1.1   Geometries and vibrational frequencies

The pseudo-potential ECP28MDF is used combined with the Dunning basis set aVQZ to describe the Ru atom. O and H species are also described with the aVQZ basis set expansions. RuO and RuO_2 oxides had been already investigated in Chapter 4, this study focuses on remaining oxides.

     DFA TPSSh-5%HF calculations provided RuO_3 and RuO_4 ground states to be a $^1A_1$ state. This ground state was also predicted by Zhou *et al.* [1] work's with DFT BP86 calculations, Hameka *et al.* study [2] with Hartree Fock theory, and Siegbahn one [3] with MCPF calculations, as described on Section 4.1.2 of Chapter 4. Siegbahn found that the electronic ground states of RuO_3 and RuO_4 corresponded to be triplet using non-correlated SCF level of theory. With the DFA TPSSh-5%HF approach, the total electronic energy of triplet state for RuO_3 and RuO_4 species is found to be greater than singlet one by 62 and 170 kJ mol^{-1}, respectively.

     Bond lengths displayed in Table 5.1 are equal to 1.687 and 1.691 Å for RuO_3 and RuO_4, respectively. They are longer compared to those derived by HF calculations equal to 1.610 and 1.609 Å, respectively, and shorter compared to those derived by BP86 functional equal to 1.717 and 1.723 Å, respectively. CCSD(T) and CASPT2 optimized calculations by Huang *et al.* [4] predicted Ru-O bond distance of RuO_4 species equal to 1.710 Å, closer to our TPSSh-5%HF value. Structure of RuO_3 is planar with D_{3h} symmetry and for RuO_4 tetrahedral with T_d symmetry, as found in previous literature works except Garisto [5] one, in which a C_{3v} pyramidal structure for RuO_3 is proposed. Computed vibrational frequencies for RuO_3 species, given in Table 5.1, show that the antisymmetric mode at 963.0 cm^{-1} is slightly larger than the one computed at BP86 level, equal to 948.0 cm^{-1}, or the one measured experimentally in argon matrix by Kay *et al.* [6] (893.4 cm^{-1}) and by Zhou *et al.* [1] in neon matrix (901.1 cm^{-1}). TPSSh-5%HF theory predicted RuO_4 vibrational t_2 mode at 974.2 cm^{-1}, higher than infrared measurements [1] values in solid argon (916.9 cm^{-1}) and in neon matrix (923.0 cm^{-1}). Like our DFA results, BP86 functional predicted this stretching mode higher than experimental measurements (950.2 cm^{-1}). As presented in Chapter 3, the vibrational frequencies are calculated using the rigid rotator harmonic oscillator, that could explain the observed differences between the calculated values and their experimental counterparts. Ru–O bond length in O_2RuO_2 species at TPSSh-5%HF level is slightly shorter than the derived one at BP86 DFA, in opposite with calculated bond angle $\angle$ O-Ru-O value similar in both theories.

5.1.1.2   Nature of chemical bonding in RuO_3, RuO_4 and O_2RuO_2 system

Table 5.2 presents the QTAIM parameters for RuO_3, RuO_4, and O_2RuO_2 species and relies on the quantitative analysis of the topology of density in the interatomic region. The value of ρ_b is equal to 0.27, which indicates a strong covalent bond between Ru and O atoms. This feature is confirmed by H_b quantities of -0.173 and -0.175 for RuO_3 and RuO_4, respectively, negative

Table 5.1: Bond distances (Å), O-Ru-O angles (θ, deg), vibrational frequencies (cm^{-1}), and infrared intensities (km mol^{-1}) in parenthesis for the Ru oxides.

Species	Method	r, θ	vibrational frequencies (IR intensities) (intensity)
RuO$_3$ ($^1A_1'$; D$_{3h}$)	TPSSh-5%HF[a]	1.687	963.9 (0); 963.0 (264); 298.2 (e', 2); 71.3 (a_2'', 71)
	HF[b]	1.610	1055(0); 759 (146); 330 (13); 185 (27)
	BP86[c]	1.717	949.7 (125); 948.0 (125); 915.8 (0); 289.8 (1);289.7 (1); 77.5 (9)
	Exp.		893.4[d] ; 901.1[e]
RuO$_4$ ($^1A_1$; T$_d$)	TPSSh-5%HF[a]	1.691	974.3 (t_2, 254); 952 (a_1, 0), 350 (t_2, 2154); 327 (e, 0)
	HF[b]	1.608	1066(0); 923 (273); 413 (22); 398 (0)
	BP86[c]	1.723	950.2 (100); 904.0 (0)
	Exp.		916.4[d] ; 923.0[e](t_2)
O$_2$RuO$_2$ (^1A; C$_2$)	TPSSh-5%HF[a]	1.674, 122.2 [f]	992(a, 78); 986(a, 55); 970(b, 199); 613(b, 3); 611(a, 7); 328(a, 0); 294(a, 6); 231(b, 3); 227(b, 2)
O$_2$RuO$_2$ ($^1A_1$; C$_{2v}$)	BP86[c]	1.708, 121.1 [g]	983.7 (a_1, 92); 956.4 (b_2, 177);949.3 (a_1, 44)

[a] This work
[b] Ref. [2]
[c] Ref. [1] with BP86 functional
[d] argon matrix measurements from [6]
[e] neon matrix measurements from [1]
[f] O-O 1.415 Å, Ru–(O$_2$) 1.885 Å
[g] O-O 1.407 Å, Ru–(O$_2$) 1.924 Å

for interactions where electrons are being closely shared. The delocalisation indice δ(Ru,O) that measuring bond order between atom Ru and O is equal to 1.89 for RuO$_3$ and 1.68 for RuO$_4$, confirming covalent bond predicted by ρ_b and H_b parameters. Remembering values of 2.25 and 1.93 for RuO and RuO$_2$ oxides respectively, we can conclude that this parameter slightly decreases for oxides at higher oxidation states.

Table 5.2: Ru–O bond distances in Å, natural population analysis (NPA) charges, and bond critical points (BCP) parameters: ρ_b and $\nabla^2\rho_b$ are the electron density and the Laplacian at the BCP given in e$^-$/bohr^3 and e$^-$/bohr^5, respectively. δ(Ru,O) is the delocalization index. H_b (au) is the energy density at the critical point.

Species	r_e	q(Ru)	q(O)	δ(Ru,O)	ρ_b	$\nabla^2\rho_b$	H_b
RuO$_3$ ($^1A_1'$; D$_{3h}$)	1.687	0.99	-0.33	1.89	0.27	0.94	-0.173
RuO$_4$ ($^1A_1$; T$_d$)	1.691	1.05	-0.26	1.68	0.27	0.83	-0.175
O$_2$RuO$_2$ Ru–O bond	1.674	0.85	-0.27	1.86	0.28	0.93	-0.187
O$_2$RuO$_2$ Ru–O$_2$ bond	1.885	0.85	-0.15	0.97	0.16	0.53	-0.079

Fig. 5.1 illustrates six bonding orbitals in RuO$_3$ species, showing three Ru=O double bonds

quite close to the δ(Ru,O) value of 1.89. In RuO$_4$, there are five bonding orbitals shown in Fig. 5.2, making up an average bond order of 1.25, slightly lower compared to the δ(Ru,O) value of 1.68. This result underlines that the BCP analysis study had to be completed with chemical bonding orbitals analysis. As suggested by its structural symmetry, the O$_2$RuO$_2$ species presents topological parameters that are closer to those of RuO$_3$. In fact, the δ(Ru,O) value of 1.86 is in good agreement with those of RuO$_3$ (1.89). The ρ_b and H_b parameters, equal to 0.28 and -0.187 respectively, indicate strong covalent bonding. By contrast, the Ru$-$O$_2$ bond presents values for the ρ_b and H_b factors equal to 0.16 and -0.079, respectively, corresponding to less sharing of electrons corroborated by δ(Ru,O) value of 0.97 typical of a simple covalent bond.

(a) a'_1 (b) e'' (c) e''

(d) e' (e) e' (f) a'_1
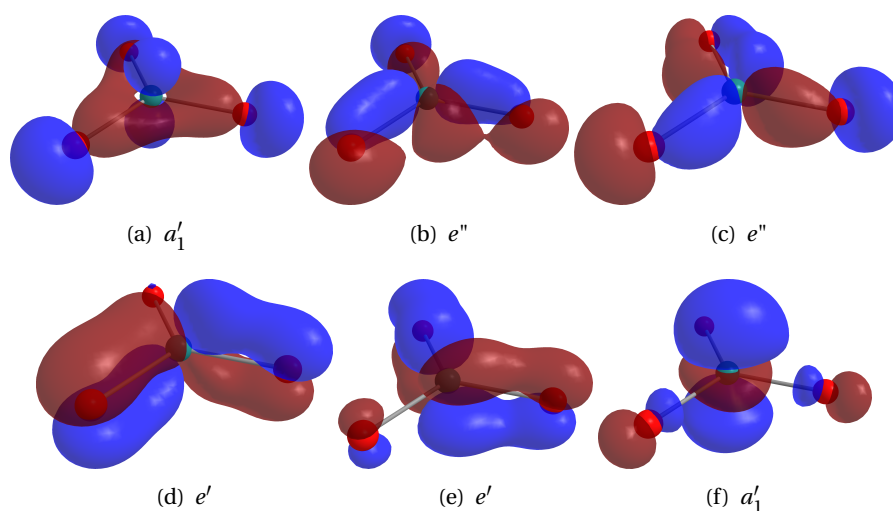
Figure 5.1: DFT (TPSSh-5%HF) molecular bonding orbitals in RuO$_3$. The symmetry is given below each orbital.

(a) e (b) e (c) t_2 (d) t_2 (e) t_2
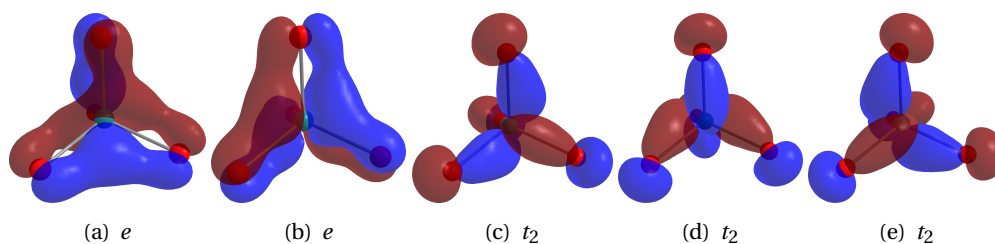
Figure 5.2: DFT (TPSSh-5%) molecular bonding orbitals in RuO$_4$. The symmetry is given below each orbital.

5.1.2 Geometries and nature of chemical bonding in Ruthenium oxyhydroxide species

Several stoichiometries of the RuO_xH_y species involving oxides, hydroxides, and water ligands are presented here while varying with ruthenium oxidation level. For each stoichiometry, all possible conformers were explored, although only the most stable ones at 298.15 K are shown here. All different species considered are detailed in Tables C.2, C.3, and C.4 of Appendix C. Geometric parameters reported in Table 5.3 were optimised at the TPSSh-5%HF/aVQZ level of theory.

5.1.2.1 Geometric parameters

The computed bond distances, molecular symmetry, and multiplicity of RuO_xH_y species are displayed in Table 5.3.

Table 5.3: Ru–O, Ru–OH, and Ru–H_2O bond distances in Å, molecular symmetry, and multiplicity in ruthenium oxyhydroxide systems.

Species	Bond Lengths (Å)			Symmetry	Multiplicity
	Ru–O	Ru–OH	Ru–OH_2		
$Ru(OH)$	/	1.899	/	C_1	4
$Ru(OH)_2$	/	1.910	/	C_2	5
$Ru(OH)_3$	/	1.864	/	C_1	2
$Ru(OH)_4$	/	1.841-1.951	/	C_1	1
$RuO(H_2O)$	1.728	/	2.278	C_1	5
$RuO(OH)$	1.643	1.828	/	C_s	2
$RuO(OH)(H_2O)$	1.673	1.874	2.079	C_1	2
$RuO(OH)_2$	1.650	1.870	/	C_s	2
$RuO(OH)_2(H_2O)$	1.656	1.904-1.924	2.176	C_1	1
$RuO(OH)_3$	1.666	1.872-1.899	/	C_1	2
$RuO_2(H_2O)$	1.677-1.682	/	2.095	C_s	1
$RuO_2(H_2O)_2$	1.704-1.716	/	2.145-2.193	C_1	1
$RuO_2(OH)$	1.678	1.868	/	C_s	2
$RuO_2(OH)(H_2O)$	1.677-1.715	1.924	2.235	C_1	2
$RuO_2(OH)_2$	1.680	1.874-1.893	/	C_s	1
$RuO_2(OH)_4$	1.697-1.712	1.900-1.983	/	C_1	1
$RuO_3(H_2O)$	1.688-1.713	/	2.331	C_1	1
$RuO_3(OH)$	1.688-1.726	1.872	/	C_1	2
$RuO_3(OH)_2$	1.680-1.735	1.924	/	C_1	1

The coordination of a water molecule does not change the oxidation state of the species, while the negatively charged hydroxide groups induce an oxidation of the ruthenium metal, leading to different electronic ground states than in the ruthenium oxides. Major oxyhydroxide compounds have a low spin singlet or doublet ground state, except for Ru(OH) (quartet), $Ru(OH)_2$ and $RuO(H_2O)$ (quintet).

The Ru(OH)$_3$ species, found with a doublet ground state has been for the first time evidenced by XPS characterisations in the recent Morgan *et al.* study [7].

Ru−O bond distances vary from 1.64 to 1.73 Å, close to the ruthenium oxide species range from 1.68 to 1.71 Å, revealing that the lower the oxidation state of Ru, the longer the Ru−O bond length. Ru−OH bond length ranges from 1.83 to 1.92 Å, slightly longer that those reported (1.75 Å) in the gas phase[8]. They are slightly shorter compared to those reported for platinum equal to 2.10 Å [9]. Our calculated Ru−OH bond lengths slightly differ from those reported in the aqueous phase study of Yamaguchi *et al.*(2.02±0.01 Å) [10]. Reported Ru−OH$_2$ bond lengths varying from 2.08 and 2.33 Å are very similar to those of iron and platinum water ligand, equal to 2.01 and 2.2 Å respectively [8, 11, 12].

5.1.2.2 Nature of the chemical bonds and topological analysis

Tables 5.4 , 5.5, and 5.6 show the BCP parameters for Ru−O, Ru−OH, and Ru−OH$_2$ bonding, respectively.

Table 5.4: Ru−O Bond Critical Points (BCP) Parameters: ρ_b and $\nabla^2\rho_b$ are the electron density and its Laplacian at the BCP given in e$^-$/bohr^3 and e$^-$/bohr^5, respectively. δ(Ru,O) is the delocalization index, H_b (au) is the energy density at the critical point.

Species	ρ_b	$\nabla^2\rho_b$	H_b	δ(Ru,O)
RuO(H$_2$O)	0.24	0.79	-0.149	2.12
RuO(OH)	0.30	1.01	-0.234	2.26
RuO(OH)(H$_2$O)	0.28	0.80	-0.203	2.12
RuO(OH)$_2$	0.29	0.92	-0.230	2.16
RuO(OH)$_2$(H$_2$O)	0.29	0.88	-0.225	2.08
RuO(OH)$_3$	0.28	0.79	-0.213	1.93
RuO$_2$(H$_2$O)	0.27	0.89	-0.193	1.94
RuO$_2$(H$_2$O)$_2$	0.25	0.96	-0.155	1.75
RuO$_2$(OH)	0.28	0.89	-0.200	1.95
RuO$_2$(OH)(H$_2$O)	0.25	0.78	-0.166	1.81
RuO$_2$(OH)$_2$	0.28	0.85	-0.199	1.81
RuO$_2$(OH)$_4$	0.25	0.78	-0.168	1.57
RuO$_3$(H$_2$O)	0.25	0.80	-0.169	1.75
RuO$_3$(OH)	0.27	0.82	-0.195	1.74
RuO$_3$(OH)$_2$	0.25	0.84	-0.166	1.63

The Ru−O bonding of the oxyhydroxide systems presents a delocalization index δ(Ru,O), which lies between 1.75 and 2.26. The energy density parameter H_b presents values between -0.15 and -0.22. Added to this, the electron density ρ_b, which ranges between 0.25 and 0.30, corroborates covalent bonding of Ru−O determined by previous parameters. All these values are similar to that found in the ruthenium oxides species RuO, RuO$_2$, RuO$_3$, and RuO$_4$.

Table 5.5: RuO_x–(OH) Bond Critical Points (BCP) Parameters: ρ_b and $\nabla^2\rho_b$ are the electron density and its Laplacian at the BCP given in e^-/bohr^3 and e^-/bohr^5, respectively. δ(Ru,O) is the delocalization index. H_b (au) is the energy density at the critical point.

Species	ρ_b	$\nabla^2\rho_b$	H_b	δ(Ru,O)
Ru(OH)	0.16	0.57	-0.063	1.32
Ru(OH)$_2$	0.14	0.62	-0.054	1.12
Ru(OH)$_3$	0.17	0.57	-0.080	1.20
Ru(OH)$_4$	0.16	0.61	-0.069	1.10
RuO(OH)	0.17	0.79	-0.070	1.17
RuO(OH)(H$_2$O)	0.16	0.59	-0.070	1.14
RuO(OH)$_2$	0.17	0.59	-0.073	1.11
RuO(OH)$_2$(H$_2$O)	0.15	0.53	-0.056	0.96
RuO(OH)$_3$	0.16	0.56	-0.067	1.06
RuO$_2$(OH)	0.17	0.60	-0.075	1.09
RuO$_2$(OH)(H$_2$O)	0.14	0.52	-0.056	0.95
RuO$_2$(OH)$_2$	0.17	0.54	-0.075	1.07
RuO$_2$(OH)$_4$	0.14	0.40	-0.058	0.87
RuO$_3$(OH)	0.17	0.54	-0.077	1.02
RuO$_3$(OH)$_2$	0.15	0.43	-0.065	0.91

Concerning the Ru–OH bonding, the δ(Ru,O) values are ranging from 0.84 to 1.32, typical for single covalent bonding. H_b values between -0.05 and -0.07 confirmed that result by revealing less sharing of electrons as compared to Ru–O bonds. The ρ_b values varying from 0.15 to 0.17 are all greater than 0.1 (e^-/bohr^3) and lower than 0.2 (e^-/bohr^3), highlighting single bonds between Ru and hydroxide groups.

Table 5.6: RuO_x–(H$_2$O) Bond Critical Points (BCP) Parameters: ρ_b and $\nabla^2\rho_b$ are the electron density and its Laplacian at the BCP given in e^-/bohr^3 and e^-/bohr^5, respectively. δ(Ru,O) is the delocalization index. H_b (au) is the energy density at the critical point.

Species	ρ_b	$\nabla^2\rho_b$	H_b	δ(Ru,O)
RuO(H$_2$O)	0.05	0.26	-0.007	0.44
RuO(OH)(H$_2$O)	0.09	0.42	-0.021	0.61
RuO(OH)$_2$(H$_2$O)	0.07	0.32	-0.013	0.47
RuO$_2$(H$_2$O)	0.09	0.40	-0.021	0.57
RuO$_2$(H$_2$O)$_2$	0.07	0.29	-0.014	0.51
RuO$_2$(OH)(H$_2$O)	0.07	0.26	-0.013	0.42
RuO$_3$(H$_2$O)	0.05	0.19	-0.007	0.32

For Ru–OH$_2$ bonding, the delocalization index is around 0.5, the ρ_b parameter ranges from 0.05 to 0.09, lower than 0.1 (e$^-$/bohr^3), reflecting together with the H_b values (-0.007 to -0.021), closed-shell interactions. These factors reveal that there is no sharing of electrons between the water oxygen atoms and ruthenium, highlighting ionic bonds.

It can be concluded from this analysis that ruthenium forms single bond with the hydroxide ligands and interacts ionically with the water molecules in the oxyhydroxide species, according to the QTAIM parameters. To complete these topological results the bonding molecular orbitals of some representative ruthenium oxyhydroxides are presented (RuO$_2$(OH), RuO$_2$(H$_2$O), and RuO$_2$(OH)(H$_2$O)). Features of the bonding characteristics discussed previously, are illustrated in Fig. 5.3, 5.4, and 5.5, respectively.
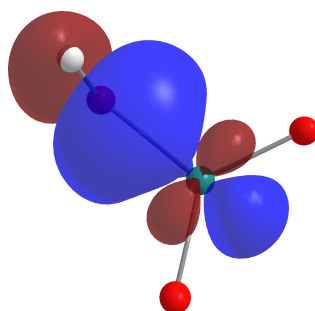
Figure 5.3: DFT (TPSSh-5%HF) natural bonding orbital in RuO$_2$(OH) between the ruthenium dioxide cation (right) and the hydroxide (left).
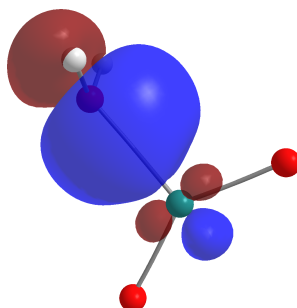
Figure 5.4:   DFT (TPSSh-5%HF) natural lone pair water orbital in RuO$_2$(H$_2$O) of the coordinated water molecule (left) pointing toward ruthenium (right).

In Fig. 5.3, the natural bonding involved in the Ru–OH chemical bonding of the RuO(OH) species, formed by the Ru 4d orbital and the oxygen 2p orbital, confirming the covalent nature suggested by the topological analysis. Fig. 5.4 shows one of the oxygen water lone pair pointing toward ruthenium without making a covalent bond. Subfigure 5.5(a) represents the bonding between Ru and (OH) of RuO$_2$(OH)(H$_2$O) species and Subfigure 5.5(b) shows the oxygen water lone pair pointing in the direction of Ru. These results can be compared with

(a)   (b)
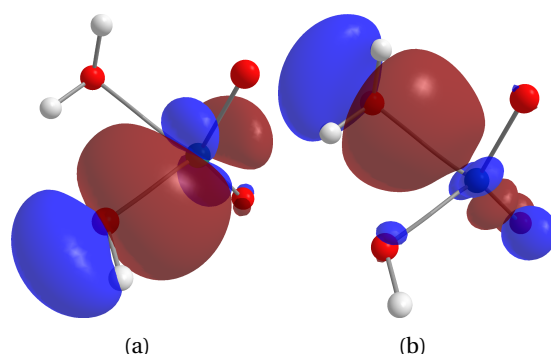
Figure 5.5: DFT (TPSSh-5%HF) natural bonding orbital in $RuO_2(OH)(H_2O)$ between ruthenium dioxide cation (right) and hydroxide (left front); lone pair of the coordinated water molecule pointing toward ruthenium

the work of Magnela *et al.* [11], who demonstrates that depending on the transition metal cation, hydroxide forms bonds either with the $3d$ orbitals of the metal (as iron), or with the $4s$ orbital in gas phase.

5.1.3 Topological study of Ru dimer oxides species

Among the reaction pathways leading to the formation of Ru oxides, the Ru dimer oxide species may play a significant role. To derive their thermodynamic and kinetic parameters, the molecular structural properties of dimer species have been determined. The Ru_2O_4, dimer of RuO_2 oxide, and Ru_2O_6, dimer of RuO_3 oxide, will be discussed here, and are illustrated in Fig. 5.6. The study indicates that RuO_4 dimerisation does not lead to a Ru_2O_8 complex lower in energy compared to that of two RuO_4 combined. The most stable Ru_2O_8 complexes are shown in Table C.1 of Appendix C.

Fig. 5.6 illustrates the several bond distances involved in Ru_2O_4 and Ru_2O_6 species. The topological analyses for these bond lengths are reported in Table 5.7.

Ru–Ru (B1) bonding in Ru_2O_4 complex seems to be a single covalent bond, with $\delta(A,B)$ value equal to 0.79. ρ_b and H_b parameters with 0.08 and -0.03 values, respectively, show fewer electrons shared between the 2 Ru atoms, suggesting bonding orbitals formed by a Ru lone pair with the other one. B2 and B3 bond lengths range from 1.87 to 1.92 Å, similar to those found between hydroxyl ligand and ruthenium in oxyhydroxides species. In addition, ρ_b and H_b values equal to 0.16 and -0.07 respectively, confirm the single covalent characteristic of B2 and B3 bonding. Ru–O bonding B4 and B5 have bond length of 1.66, close to those of RuO_2 oxide and O_2RuO_2 species (1.67 Å). The O–Ru–O bond angle in Ru_2O_4 varying from 130 to 133 ° is closer to the one in O_2RuO_2 (122.2 °) than the 149.8 ° value in RuO_2. QTAIM parameters present $\delta(A,B)$ value range from 1.97 to 2.04, ρ_b values between -0.67 and -0.65 and H_b equal to -0.22. All these parameters highlight that Ru–O bonding B4 and B5 are strongly covalent bond.

Figure 5.6: Schematic drawing of Ru_2O_4 and Ru_2O_6 dimers with the label of bondings displayed in Table 5.7.

Table 5.7: Ru_xO_y Bonding NPA charges (Natural Population Analysis) and Bond Critical Points (BCP) Parameters. ρ_b and $\nabla^2\rho_b$ are the electron density and its Laplacian at the BCP given in $e^-/bohr^3$ and $e^-/bohr^5$, respectively. $\delta(A,B)$ is the delocalization index and H_b (au) is the energy density at the critical point. Lengths are given in Å.

Species	bonding	length	q(A)	q(B)	ρ_b	$\nabla^2\rho_b$	H_b	$\delta(A,B)$
	B1	2.51	0.89	0.99	0.08	0.16	-0.03	0.79
	B2	1.92	0.99	-0.57	0.15	0.54	-0.06	1.03
Ru_2O_4	B3	1.87	0.89	-0.57	0.17	0.61	-0.07	1.14
	B4	1.66	0.89	-0.37	0.29	0.89	-0.22	1.97
	B5	1.66	0.99	-0.37	0.29	0.81	-0.22	2.04
	B1 (RCP)[a]	2.97	1.11	1.11	0.05	0.22	-0.06	0.12
	B2	1.90	1.11	-0.49	0.16	0.48	-0.07	0.98
Ru_2O_6	B3	1.90	1.11	-0.49	0.16	0.48	-0.07	0.98
	B4	1.68	1.11	-0.31	0.28	0.87	-0.20	1.83
	B5	1.68	1.11	-0.31	0.28	0.87	-0.20	1.83

[a] RCP: Ring Critical Point between $O_2 - Ru_1 - O_5 - Ru_6$

In Ru_2O_6 complex, a ρ_b value of 0.05, and an H_b parameter with lower magnitude value of -0.06 for Ru – Ru bonding, implies that there is no sharing of electrons between the two atoms. It is confirmed by $\delta(A, B)$ quantity suggesting a bond order of zero between the two Ru, and the longer bond length Ru – Ru of 2.97 Å. The QTAIM calculations found this bond length to be a ring critical point between $Ru_1 - O_1 - Ru_2 - O_4$ atoms. The parameters of B2 and B3 bond distances, concerning the oxygen atoms on the ring bond, translate covalent bond with $\delta(A, B)$ value of 0.98. Regarding the ρ_b and H_b factors values, a few electrons are expected to be shared; the bonding orbital seems formed by oxygen lone pair with the Ru atom. We can add

that Ru–O bond length of 1.90 Å is similar to the one found between hydroxyl ligand and ruthenium in oxyhydroxides species, that corroborates the single covalent characteristic of B2 and B3 bonding. B4 and B5 bond lengths of 1.68 Å are similar to RuO_3 oxide one (1.687 Å). The δ(A,B) value of 1.83 indicate double covalent bond, like suggested by the ρ_b and H_b quantities.

5.2 Calculated electronic energies

5.2.1 Derived electronic energies for Ru oxides

Table 5.8 reports computed single-point electronic energies with cluster expansions CCSD(T) using TPSSh-5%HF/aVQZ optimised geometries.

Table 5.8: Electronic energies of Ru oxides performed at the CCSD(T)/CBS//TPSSh-5%HF level of theory.

Species	T_1 Diag	D_1 Diag	$< S^2 >$	E_{TOT} (CBS) [au]	ΔE [kJ mol^{-1}]		
					CBS - aVTZ	CBS - aVQZ	CBS - aV5Z
RuO_3	0	0.03	0.09	-319.6132	-324.6	-130.5	-63.1
RuO_4	0	0.03	0.11	-394.7672	-407.2	-162.3	-78.1
O_2RuO_2	0	0.04	0.13	-394.7154	-408.3	-163.2	-78.7

O_2RuO_2 species is 152.9 kJ mol^{-1} higher than RuO_4 species at the TPSSh-5%HF/aVQZ level of theory, and 135.9 kJ mol^{-1} using the CCSD(T)/CBS extrapolated total energy. Zhou *et al.* calculations found this species with C_{2v} symmetry structure . The isomer was found 116.3 kJ mol^{-1} higher in energy than RuO_4 with the BP86 calculations [1]. Average S^2 values are all equal to 0.00, traducing no spin contamination of singlet ground state by higher multiplets, revealing single reference character of the fundamental state. T_1 values are all below the recommended 0.05 upper limit confirming the single reference character of the ground state. The ΔE values decrease with basis set expansion. Calculation of the relative energies will allow us to evaluate the accuracy of the provided CCSD(T) electronic energies.

Table 5.9 presents the binding energies and enthalpies at 298 K of oxygen to ruthenium oxide calculated at CCSD(T) level of theory, compared with those derived by Siegbahn [3] with MCPF approach neglecting spin-orbit coupling.

Study of binding energies, through reaction $RuO_{n-1} + O = RuO_n$, can provide some hint on the nature of bond strength between Ru and O. MCPF calculations reported monotonically decreasing bond strengths. It differs from our results indicating that the Ru–O bond strength reaches a maximum for RuO_2 and decreases when additional oxygen atoms bind ruthenium. This effect should lead to decrease Ru-O bond lengths in the oxides. The previous topological study does not exhibit a variation of the Ru-O bond length despite the fact that the covalent character drops with higher oxidation state. But the Ru charge increases with greater oxidation state, enhancing the purely electrostatic interactions with the neighbouring oxygens. We

Table 5.9: Stepwise binding energies $-\Delta E_{n-1,n}$ and binding enthalpies at 298 K in kJmol^{-1} of oxygen to ruthenium oxide Ru$_{n-1}$, for reaction RuO$_{n-1}$ + O = RuO$_n$, computed at the CCSD(T) level, using TPSSh5%HF geometries.

	$n=1$	$n=2$	$n=3$	$n=4$
$-\Delta E_{n-1,n}$	481	532	443	385
$-\Delta E_{n-1,n}$ [a]	421	379	355	270
$-\Delta H_{n-1,n}$ (298 K)	472	528	440	384

[a] Ref. [3]

can conclude that these two competing effects keep the Ru-O distance constant in the RuO$_n$ species.

5.2.2   Ru oxyhydroxides total electronic energies

Table 5.10 lists the calculated electronic energies for most stable oxyhydroxides. Energetics were derived at CCSD(T)/CBS//TPSSh-5%HF level of theory. For some singlet ground states, where a multi-reference character was suggested by S^2 eigenvalue, T_1 diag, and/or D_1 Diag values, and BCCD(T) calculations were performed to ensure suitable approximation by single reference method of ground state wave function, presented in Table 5.11.

Table 5.10: Derived electronic energies on Ru oxyhydroxides compounds at CCSD(T)/CBS//TPSSh-5%HF level of theory.

(a) Part 1

Species	T_1 Diag	D_1 Diag	$<S^2>$	E_{TOT} (CBS) [au]	ΔE [kJ mol^{-1}]		
					CBS - aVTZ	CBS - aVQZ	CBS - aV5Z
Ru(OH)	0.04	0.09	3.77	-169.8199	-161.9	-65.9	-32.5
Ru(OH)$_2$	0.03	0.08	6.01	-245.6716	-243.1	-96.3	-46.8
Ru(OH)$_3$	0.03	0.1	0.75	-321.4657	-339.0	-134.3	-65.0
Ru(OH)$_4$	0.03	0.1	0	-397.2566	-425.1	-167.4	-80.8
RuO(H$_2$O)	0.04	0.13	6.01	-245.6322	-245.3	-98.1	-47.8
RuO(OH)	0.04	0.11	0.77	-245.0491	-250.3	-100.6	-48.9
RuO(OH)(H$_2$O)	0.05	0.18	0.78	-321.4446	-338.9	-134.0	-64.9
RuO(OH)2	0.04	0.15	0.48	-320.8589	-334.7	-132.9	-64.3
RuO(OH)$_2$(H$_2$O)	0.04	0.18	0	-397.2543	-423.8	-166.1	-80.1

(b) Part 2

Species	T_1 Diag	D_1 Diag	$<S^2>$	E_{TOT} (CBS) [au]	ΔE [kJ mol^{-1}]		
					CBS - aVTZ	CBS - aVQZ	CBS - aV5Z
RuO(OH)$_3$	0.04	0.12	0.76	-396.6408	-419.4	-165.3	-79.7
RuO$_2$(H$_2$O)	0.04	0.12	0	-320.8534	-336.0	-133.8	-64.7
RuO$_2$(H$_2$O)$_2$	0.03	0.12	0	-397.2448	-423.8	-166.5	-80.3
RuO$_2$(OH)	0.05	0.2	0.76	-320.2379	-329.4	-131.6	-63.6
RuO$_2$(OH)(H$_2$O)	0.07	0.3	0.76	-396.6273	-417.8	-164.5	-79.3
RuO$_2$(OH)$_2$ – Cs	0.03	0.1	0	-396.0269	-415.5	-164.5	-79.3
RuO$_2$(OH)$_2$ – C$_2$v	0.03	0.1	0	-396.0215	-415.7	-164.6	-79.3
RuO$_2$(OH)$_4$	0.05	0.23	0	-547.4393	-577.5	-225.5	-108.4
RuO$_3$(H$_2$O)	0.04	0.13	0.48	-395.9908	-412.9	-163.6	-78.9
RuO$_3$(OH)	0.07	0.31	0.76	-395.3751	-410.0	-163.0	-78.5
RuO$_3$(OH)$_2$	0.07	0.34	0.17	-471.1046	-491.7	-194.0	-93.3

Ru(OH), Ru(OH)$_2$, Ru(OH)$_3$, and Ru(OH)$_4$ systems have T_1 Diag values less than 0.05, and D_1 Diag values less than 0.10. Average S^2 eigenvalues are equal to 3.77, 6.01, 0.75, and 0.0 respectively, traducing the absence of spin contamination by higher multiplets. All these factors highlight that single reference method CCSD(T) is suitable to provide good approximations of the ground states for these systems.

RuO(H$_2$O) and RuO(OH) systems have T_1 Diag value equivalent to 0.04 and D_1 Diag to 0.13 and 0.11 respectively, with average $<S^2>$ eigenvalues equivalent to 6.01 and 0.76. In opposite, the RuO(OH)$_2$ system presents $<S^2>$ eigenvalue equal to 0.48, contaminated by higher multiplets states. However, RuO(OH)$_2$ T_1 Diag and D_1 Diag values equal to 0.04 and 0.15, respectively . BCCD(T) total electronic energies are similar to CCSD(T) ones differ only by 1.45 kJ mol^{-1} at aVQZ basis set.

Table 5.11: Electronic energies computed at the BCCD(T) level of theory using TPSSh-5%HF optimised geometries.

Species	E$_{TOT}$ (aVTZ) [au]	E$_{TOT}$ (aVQZ) [au]	ΔE (BCCD(T) -CCSD(T))[kJ mol^{-1}]	
			aVTZ	aVQZ
RuO(OH)$_2$	-320.7307	-320.8078	1.9	1.5
RuO(OH)$_2$(H$_2$O)	-397.0926	-397.1909	0.6	0.2
RuO$_2$(OH)$_4$	-547.2242	-547.3584	-12.9	-13.2
RuO$_3$(OH)$_2$	-470.9156	-471.02917	4.4	3.9

RuO$_2$(H$_2$O) and RuO$_2$(H$_2$O)$_2$ systems present T_1 and D_1 Diag quantities of 0.04, 0.03, and 0.12, respectively. $<S^2>$ eigenvalue equals 0.00, confirming that single reference method CCSD(T) is suitable to describe ground state for these species. The same conclusions can be made for RuO$_2$(OH)$_2$−Cs and RuO$_2$(OH)$_2$−C$_{2v}$ systems having both T_1 and D_1 Diag values equal to 0.03 and 0.10, with average S^2 equivalent to 0.00.

RuO(OH)(H$_2$O), RuO$_2$(OH), and RuO$_2$(OH)(H$_2$O) species present great D_1 Diag values of 0.18, 0.20, and 0.30 respectively. Nevertheless, the average S^2 eigenvalues of 0.78, 0.76 and 0.76 did not exhibit spin contamination, which allows us to confirm the appropriateness of the CCSD(T) method. The RuO(OH)$_2$(H$_2$O) species presents a large D_1 Diag value (0.18), but $<S^2>$ eigenvalue equivalent to 0.00 shows no contamination by higher multiplets. BCCD(T) total electronic energies are close to CCSD(T) ones, with a difference with the aVQZ basis set of about 0.2 kJ mol^{-1}, confirming that this species can be described with the single reference method CCSD(T).

For RuO$_3$(H$_2$O) species, a singlet state with average S^2 eigenvalue equal to 0.17 was first derived by DFAs calculations. This system was found higher in energy to triplet state by 2.4 kJ mol^{-1} at TPSSh5%HF/aVQZ level of theory, but UCCSD(T) calculation brings the singlet state as ground state. Lower energetics of the singlet state is reached at the UDFT-BS-TPSSh-5%HF/aVQZ level of theory by using initial triplet charge density. As shown in Table 5.10, the latter species has an average $<S^2>$ eigenvalue of 0.48, which emphasises that UDFTBS pro-

cedure is mandatory to ensure lower ground state for singlet systems, and cluster expansion CCSD(T) gives reliable energy regardless DFAs approach provided geometries. T_1 Diag and D_1 Diag quantities of 0.04 and 0.13, respectively, highlight that CCSD(T) approach is suitable to describe this system ground state despite spin contamination provided by DFA method.

For $RuO_3(OH)_2$ species, all factors tend to a non negligible multireference character, with T_1 Diag and D_1 Diag values equal to 0.07 and 0.34, respectively, and $<S^2>$ eigenvalue equivalent to 0.17. The difference between BCCD(T) and CCSD(T) methods associated with the aVQZ basis set is about 3.9 kJ mol^{-1}. $RuO_2(OH)_4$ species did not exhibit spin contamination, despite large amounts of T_1 and D_1 Diag values (0.05 and 0.23, respectively). The BCCD(T) total electronic energies slightly differ from the CCSD(T) ones with a difference of 13.16 kJ mol^{-1} using the aVQZ basis set, translate reasonable approximation of ground state by CCSD(T) method.

5.2.3 Electronic energies of Ru_2O_4 and Ru_2O_6 species

The total electronic energies at different levels of theory for Ru dimer compounds are displayed in Table 5.12.

Table 5.12: Derived electronic energies on Ru dimers compounds with TPSSh-5%HF/aVQZ geometries.

Species	T_1 Diag	D_1 Diag	S^2	Method	E_{TOT}	ΔE [a]
					[au]	[kJ mol^{-1}]
				UCCSD(T)/aVTZ	-488.7712	-
Ru_2O_4	0.06	0.19	2.04	UCCSD(T)/aVQZ	-488.8823	-291.6
				UCCSD(T)/aV5Z	-488.9214	-102.5
				UCCSD(T)/CBS	-488.9584	-97.3
Ru_2O_6	0.04	0.13	0.00	UCCSD(T)/aVTZ	-639.0520	-
				UCCSD(T)/aVQZ	-639.2007	-390.5

[a] ΔE corresponds to the difference in computed energy at aVXZ and aV(X-1)Z basis set.

Potential energies for Ru_2O_4 show convergence with basis set expansion, regarding ΔE values. T_1 Diag and D_1 Diag appear quite large (0.06 and 0.19), but DFA calculations did not exhibit spin contamination, confirming that a good approximation of ground state wave function can be made with the single reference method. Ru_2O_6 species did not show spin contamination with an average S^2 eigeinvalue of 0.00. T_1 and D_1 Diag values indicate that CCSD(T) is suitable to provide reliable energy for this compound. Calculations have been managed until the aVQZ basis set level. The standard enthalpies of formation calculated at aVQZ and aV5Z basis set present only 9 kJ mol^{-1} of deviation, for Ru oxides and oxyhydroxides. This means that the calculated total electronic energies at aVQZ basis set expansion are accurate to derive thermodynamic data.

5.3   Thermodynamic properties

In Chapter 4, standard enthalpies of formation of RuO and RuO_2 were obtained using the standard enthalpy of formation of Ru provided by the literature review of Cordfunke and Konings [13]. These properties will be calculated using the known enthalpy of formation of RuO_4 species (average of literature values), 185.5 ± 3.1 kJ mol^{-1} [5, 13, 14], for which literature values are very close, with small deviation from each other. Hence, all the following thermodynamic properties will be derived using RuO_4 $\Delta_f H°(298\ K)$ literature value. The standard enthalpy of formation of Ru will also be computed, thus providing not only a direct validation of the reaction schemes, but also an assessment of the accuracy of the electronic structure approaches.

5.3.1   Theoretical thermodynamic properties of Ru oxides

5.3.1.1   Standard enthalpy of formation at 298 K

We use the reaction enthalpies of the following dissociation reactions to obtain the standard enthalpy of formation of Ru oxides:

$$R_1(m,n) : RuO_m \longrightarrow RuO_n + (m\text{-}n)\,O \tag{5.1a}$$

$$R_2(m,n) : RuO_m \longrightarrow RuO_n + (m\text{-}n)\,\frac{1}{2}O_2 \tag{5.1b}$$

$$R_3(m,n) : RuO_m + (m\text{-}n)\,H \longrightarrow RuO_n + (m\text{-}n)\,HO \tag{5.1c}$$

$$R_4(m,n) : RuO_m + (m\text{-}n)\,H_2 \longrightarrow RuO_n + (m\text{-}n)\,H_2O, \tag{5.1d}$$
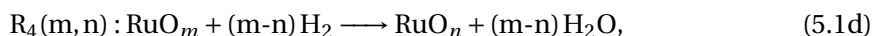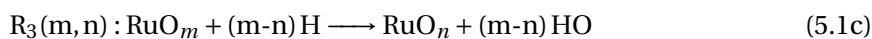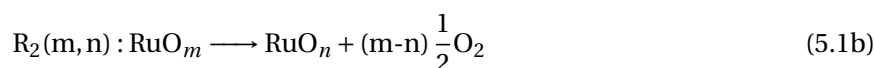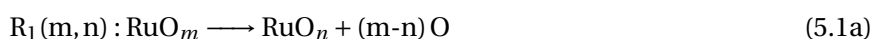
m is equal to 4 and n is equal to 0 for Ru, 1 for RuO, 2 for RuO_2, and 3 for RuO_3 species. Table 5.13 portrays the standard enthalpies of formation of Ru, RuO, RuO_2, and RuO_3 derived at CCSD(T)/CBS level of theory.

The standard enthalpy of formation of Ru is equal to 638 ± 2 kJ mol^{-1} in these calculations, about 10 kJ mol^{-1} lower than Cordfunke and Konings [13], Garisto [5], and Barin *et al.* [14] values of 649 ± 3, 649 ± 13, and 651.4 kJ mol^{-1}, respectively, and in good agreement with the one taken from Zimmerman [15] (640 ± 4 kJ mol^{-1}).

Comparing the calculated standard enthalpy of formation of RuO to those of previous cited authors, the value is 44 kJ mol^{-1} higher than Cordfunke and Konings [13] one (376 ± 25 kJ mol^{-1}) and Zimmerman's one (376 ± 4 kJ mol^{-1}) [15]. Garisto's evaluation (372.0 ± 42.0 kJ mol^{-1}) is close to our value especially if we consider the associated uncertainties.

The standard enthalpy of formation of RuO_2 at CCSD(T)/CBS level, 140.2 ± 1.0 kJ mol^{-1}, is similar to those of Zimmerman equal to 140 ± 4 kJ mol^{-1} [15], in good agreement with the one estimated by Cordfunke and Konings (136 ± 10 kJ mol^{-1}) [13] and by Garisto (133.7 ± 15.0 kJ mol^{-1}) [5].

The average calculated standard enthalpy of formation of RuO_3 species is -50.7 ± 0.5 kJ mol^{-1}. It differs by about 14 kJ mol^{-1} from Cordfunke and Konings' estimation (-64.1 ± 2.5 kJ mol^{-1}) [13], and by 25 kJ mol^{-1} with the one of Barin *et al.* (-78.2 kJ mol^{-1}) [14]. Our calculated value is in excellent agreement with Garisto(-48.4 ± 12.7 kJ mol^{-1}) [5]. Zimmerman value of -58 ± 4 kJ mol^{-1} [15] only differs from ours by about 8 kJ mol^{-1}.

With the CCSD(T) approach, the standard enthalpy of formation of RuO_4 is equal to -186.5 kJ mol^{-1} when taking account Ru spin-orbit correction, and, -202.7 kJ mol^{-1} without SOC corrections. The former is close to literature values derived by Cordfunke and Konings [13], Zimmerman [15], Garisto [5] and Barin *et al.* [14] of -188.0 ± 0.4, -188 ± 4 , -187.1 ± 8.4, and -183.1 kJ mol^{-1}, respectively.

Table 5.13: Standard enthalpies of formation for Ru, RuO, RuO_2, RuO_3 in kJ mol^{-1} computed at the CCSD(T) level of theory for the various reactions 5.1, using TPSSh-5%HF optimised geometries and the experimental standard enthalpy of formation of RuO_4. $\overline{\Delta_f H°}(298K) \pm \sigma$ represents the average and the standard deviation of computed standard enthalpies of formation. The literature values are taken from Cordfunke and Konings [13]

Species	method	R_1	R_2	R_3	R_4	$\overline{\Delta_f H°}(298K) \pm \sigma$
Ru		$\Delta_f H°(298\,K)$lit = 649 ± 3 kJ mol^{-1}				
	UCCSD(T)	638.0	641.4	639.5	634.6	638.4 ± 2.1
RuO		$\Delta_f H°(298\,K)$lit = 376 ± 25 kJ mol^{-1}				
	UCCSD(T)	420.1	422.7	421.3	417.6	420.4 ± 1.6
RuO_2		$\Delta_f H°(298\,K)$lit =136 ± 10 kJ mol^{-1}				
	UCCSD(T)	140.1	141.8	140.8	138.3	140.3 ± 1.0
RuO_3		$\Delta_f H°(298\,K)$lit = -64.1 ± 2.5 kJ mol^{-1}				
	CCSD(T)	-50.8	-49.9	-50.4	-51.6	-50.7 ± 0.5

To compute O_2RuO_2 standard enthalpies of formation, the following reactions are used:

$$R_1 : Ru + 4\,O \longrightarrow O_2RuO_2 \tag{5.2a}$$

$$R_2 : RuO_4 \longrightarrow O_2RuO_2 \tag{5.2b}$$

$$R_3 : Ru + 2\,O_2 \longrightarrow O_2RuO_2 \tag{5.2c}$$

$$R_4 : Ru + 4\,OH \longrightarrow O_2RuO_2 + 4\,H \tag{5.2d}$$

$$R_5 : Ru + 4\,H_2O \longrightarrow O_2RuO_2 + 4\,H_2 \tag{5.2e}$$
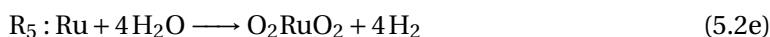
with Ru $\Delta_f H°(298\,K)$ equal to 638 ± 2 kJ mol^{-1} derived from our calculations and standard enthalpy of formation for RuO_4 extrapolate from literature equal to 185.5 ± 3.1 kJ mol^{-1} ([5, 13, 14]). Results shown in Table 5.14 present an average value of O_2RuO_2 $\Delta_f H°(298\,K)$ of -50.9 ± 5.2 kJ mol^{-1}, similar to RuO_3 $\Delta_f H°(298\,K)$. These results corroborate the topological analyses (see Table 5.1 and 5.2) that highlight similarities between RuO_3 and O_2RuO_2 (see Table 5.8).

5.3.1.2 Standard entropy and heat capacity

Table 5.15 displays the standard molar entropies ($S°(298\,K)$) and heat capacities at constant pressure $C_p(298\,K)$ derived from the molecular properties obtained at the TPSSh-5%HF/aVQZ

Table 5.14: Standard enthalpies of formation for O_2RuO_2 in kJ mol^{-1} computed at the CCSD(T) level of theory using TPSSh-5%HF optimised geometries.

R_1	R_2	R_3	R_4	R_5	$\overline{\Delta_f H°}$(298K) $\pm \sigma$
-50.5	-51.0	-53.8	-52.0	-47.2	-50.9 $\pm$ 5.2

level. The coefficients of the following heat capacity function are also fitted:

$$C_p(T) = a + bT + cT^2 + dT^{-2} \tag{5.3}$$

Data for Ru, RuO, RuO_2 , RuO_3, and RuO_4 are shown in Table C.5 of Appendix C.

Table 5.15: Calculated standard molar entropies at 298 K $S°$(298 K) and heat capacities C_p(298 K) in J K^{-1} mol^{-1} for the gaseous ruthenium oxides computed at the TPSSh-5%HF/aVTZ level of theory with unscaled vibrational frequencies.

Species	Ru	RuO	RuO_2	RuO_3	RuO_4	O_2RuO_2
			$S°$(298 K)			
This work	186.6	242.3	266.4	291.0	287.5	307.7
Literature [a]	186.4	242.1	267.4	281.9	289.1	
			C_p(298 K)			
This work	21.52	31.22	44.46	60.79	73.51	75.51
Literature [a]	21.5	31.5	44.1	59.4	75.2	

[a] Data taken from Cordfunke and Konings [13]

Computed standard molar entropy and heat capacity of Ru atom agree well with the literature values [13, 14]. The degeneracy of Ru ground-state was taken into account while calculating the temperature evolution of the heat capacity. Thus we observed slightly deviations between the calculated values and those of literature for temperatures greater than 900 K [16]. RuO and RuO_2 standard molar entropies and heat capacities agree well with the Cordfunke and Konings [13] tabulated values. Calculated values for RuO_3 and RuO_4 are slightly different from those of literature, as shown in Table 5.15. Differences were observed at temperatures either lower than 1000 K and higher than 1500 K [16]. In particular, RuO_3 species present the larger differences; we predict for this species a standard molar entropy value of 291 J K^{-1} mol^{-1} slightly larger than the one of Barin *et al.* [14] (276 J K^{-1} mol^{-1}) and Cordfunke and Konings [13] (281.96 J K^{-1} mol^{-1}). The computed result is much closer to the Garisto [5] one (291.4 $\pm$ 3.0 J K^{-1} mol^{-1}).

5.3.2 Computed thermodynamic properties of Ru oxyhydroxide compounds

To derive the standard enthalpy of formation of Ru oxyhydroxide species, the standard enthalpy of formation of RuO_4 from literature is used as well as our calculated standard enthalpy of $Ru_{(g)}$ (638.4 ± 2.1 kJ mol^{-1}), in the following chemical reactions:

$$R_1 : RuO_4 + yOH \longrightarrow RuO_xH_y + (4-x+y)O \tag{5.4a}$$

$$R_2 : RuO_4 + y\frac{1}{2}H_2O \longrightarrow RuO_xH_y + (4-x+y\frac{1}{2})O \tag{5.4b}$$

$$R_3 : Ru + xO + yH \longrightarrow RuO_xH_y \tag{5.4c}$$
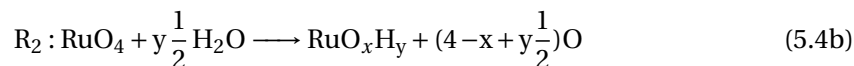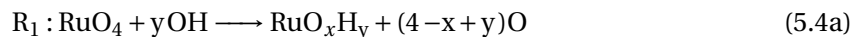
with x = 0-6 and y the complementary values to balance the equations. Table 5.16 reports the standard enthalpies of formation of the most stables Ru oxyhydroxides compared with those derived by Krikorian *et al.* [17]. The differences between the calculated values and that proposed by this author differ by 10 up to 100 kJ mol^{-1}, the higher the oxidation state, the larger the difference. Values computed at the CBS limit result in further changes in the correlation contributions by at most 10 kJ mol^{-1} compared to the aVQZ results. The most negative standard enthalpies correspond to species with an oxidation state equal or higher to four, while species containing less than two oxygen atoms have positive standard enthalpies of formation.

Table 5.16: Computed Standard Enthalpies of Formation[a] at CBS-CCSD(T) Level of Theory for the Various Reactions 5.4, using TPSSh-5%HF Optimized Geometries. Comparison with the experimental standard enthalpies of formation from ref. [17]

Species	R_1	R_2	R_3	$\overline{\Delta_f H°}$(298K) $\pm \sigma$	$\Delta_f H°$(298K) [17]
Ru(OH)	421.6	422.1	422.5	422.1 ± 2.5	327
Ru(OH)$_2$	5.2	6.2	6.4	5.9 ± 2.7	28
Ru(OH)$_3$	-253.7	-252.1	-252.1	-252.6 ± 0.7	-233
Ru(OH)$_4$	-505.7	-503.7	-503.8	-504.4 ± 3.1	-495
RuO(H$_2$O)	113.8	114.8	115.0	114.5 ± 2.7	-
RuO(OH)	88.9	89.5	89.8	89.4 ± 2.5	116
RuO(OH)(H$_2$O)	-196.6	-195.0	-195.0	-195.6 ± 2.9	-
RuO(OH)$_2$	-215.6	-214.3	-214.4	-214.9 ± 2.8	-187
RuO(OH)$_2$(H$_2$O)	-499.4	-497.4	-497.5	-498.1± 3.1	-
RuO(OH)$_3$	-443.5	-441.9	-441.9	-442.5 ± 2.9	-491
RuO$_2$(H$_2$O)	-197.0	-195.9	-195.8	-196.3 ± 2.7	/
RuO$_2$(H$_2$O)$_2$	-480.5	-478.4	-478.6	-479.2 ± 3.1	-
RuO$_2$(OH)	-138.3	-137.8	-137.5	-137.8 ± 2.5	-116
RuO$_2$(OH)(H$_2$O)	-407.4	-405.8	-405.8	-406.4 ± 2.9	-
RuO$_2$(OH)$_2$–C$_s$	-384.6	-383.5	-383.4	-383.8 ± 2.7	-419
RuO$_2$(OH)$_2$–C$_{2v}$	-372.0	-371.0	-370.8	-371.3 ± 2.7	-419
RuO$_2$(OH)$_4$	-448.6	-446.6	-446.7	-447.3 ± 3.1	-
RuO$_3$(H$_2$O)	-291.12	-290.1	-289.9	-290.4 ± 2.7	-
RuO$_3$(OH)	-229.2	-228.7	-228.4	-228.8 ± 2.5	-348
RuO$_3$(OH)$_2$	-321.9	-320.9	-320.8	-321.2 ± 2.7	-

[a] $\overline{\Delta_f H°}$(298K) represents the average of computed standard enthalpies of formation in kJ mol^{-1}. σ represents the standard deviation of the computed standard enthalpies of formation, including the experimental error.

Table 5.17: Computed standard entropies and heat capacity at constant pressure, in J K^{-1} mol^{-1}

Species	$S°(298\ \mathrm{K})$	$C_p(298\ K)$
Ru(OH)	263.086	40.351
Ru(OH)$_2$	308.693	73.670
Ru(OH)$_3$	325.224	87.2231
Ru(OH)$_4$	328.558	86.188
RuO(H$_2$O)	313.478	70.402
RuO(OH)	287.852	57.063
RuO(OH)(H$_2$O)	340.083	94.139
RuO(OH)$_2$	318.127	82.378
RuO(OH)$_2$(H$_2$O)	353.362	116.470
RuO(OH)$_3$	346.708	104.527
RuO$_2$(H$_2$O)	324.993	83.779
RuO$_2$(H$_2$O)$_2$	384.467	123.437
RuO$_2$(OH)	316.142	72.756
RuO$_2$(OH)(H$_2$O)	357.102	109.207
RuO$_2$(OH)$_2-$C$_{\mathrm{s}}$	326.705	92.507
RuO$_2$(OH)$_2-$C$_{2\mathrm{v}}$	323.256	94.531
RuO$_2$(OH)$_4$	372.147	143.758
RuO$_3$(H$_2$O)	349.971	102.081
RuO$_3$(OH)	328.577	86.197
RuO$_3$(OH)$_2$	328.577	111.216

Table 5.17 presents the standard molar entropies and heat capacities at constant pressure $C_p(298\ K)$ of most stable Ru oxyhydroxide compounds. Computed values are very close to those derived by Krikorian *et al.* [17]. We calculated coefficients for the heat capacity functions (equation 5.3) by curve fitting and reported them on Table C.6 of annex C.

Equilibrium thermodynamic calculations by Krikorian [17], Jackson [18], and Garisto [5] for ruthenium release in nuclear power plant severe accidents conditions conclude that only RuO$_3$(OH) and Ru(OH) species have an impact on Ru speciation at conditions relevant to an NPP severe accident. We also performed these calculations using literature data and our revised data to update these conclusions in Section 5.4.

5.3.3 Ru dimer species standard enthalpy of formation, molar entropy, and heat capacity

The Ru dimer standard enthalpies were derived using the following reactions:

$$R_1 : 2\,Ru + x\,O \longrightarrow Ru_2O_x \tag{5.5a}$$

$$R_2 : 2\,Ru + x\,OH \longrightarrow Ru_2O_x + xH \tag{5.5b}$$

$$R_3 : 2\,Ru + x\,H_2O \longrightarrow Ru_2O_x + xH_2 \tag{5.5c}$$

$$R_4 : 2\,RuO_4 \longrightarrow Ru_2O_x + (8-x)\frac{1}{2}O_2 \tag{5.5d}$$

$$R_5 : 2\,RuO_{\frac{x}{2}} \longrightarrow Ru_2O_x \tag{5.5e}$$
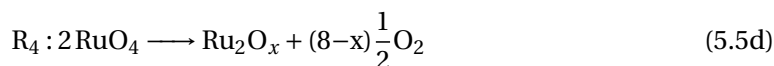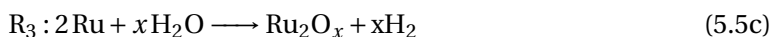
with x = 4 for Ru_2O_4 and 6 for Ru_2O_6 species. Resulting values are presented in Table 5.18.

Table 5.18: Standard enthalpies of formation for Ru_2O_4 and Ru_2O_6 in kJ mol^{-1} computed at the CCSD(T) level of theory using TPSSh-5%HF/aVQZ optimized geometries

Species	Method	R_1	R_2	R_3	R_4	R_5	$\overline{\Delta_f H°}$(298K) $\pm \sigma$
	CCSD(T)/aVTZ	140.54	101.11	87.93	70.05	63.85	92.70 ± 22.50
Ru_2O_4	CCSD(T)/aVQZ	97.72	83.80	83.58	70.62	66.03	80.35 ± 9.62
	CCSD(T)/aV5Z	82.99	75.29	77.63	71.91	67.58	75.08 ± 4.27
	CCSD(T)/CBS	69.79	68.27	73.21	72.14	68.97	70.48 ± 1.76
Ru_2O_6	CCSD(T)/aVTZ	-198.04	-257.19	-276.95	-290.39	-286.93	-261.90 ± 27.43
	CCSD(T)/aVQZ	-254.09	-274.96	-275.29	-289.90	-289.15	-276.68 ± 10.28

The deviation of computed standard enthalpies of formation is less than 2 kJ mol^{-1} at CBS level for Ru_2O_4 $\Delta_f H°$(298 K). Concerning Ru_2O_6 species, only the aVQZ level of theory has been achieved for computing total electronic energies. The deviation is equal to ~ 10 kJ mol^{-1}, quite similar to those obtained for Ru oxides and oxyhydroxides between CBS and aVQZ level of basis set. Furthermore, we also performed sensitivity analysis on the standard enthalpies of formation of Ru compounds discussed on the thermodynamic equilibrium calculations. Computed results show that no change are observed on speciation until the values of the standard enthalpy of formation deviate by 25 kJ mol^{-1} from their initial values. This range is larger than the aVQZ deviation towards CBS level. That leads to consider the computed $\Delta_f H°$(298 K) for Ru_2O_6 species at the aVQZ level of basis set as good approximation, close to CBS value.

5.4 Ru speciation calculations at thermodynamic equilibrium

To have a global estimate of the impact of oxyhydroxides and dimers species on ruthenium speciation, we present in this section equilibrium calculations performed by minimisation of the total Gibbs energy of system under constant pressure using the NUCLEA Tool Box software [19]. To reproduce representative conditions of a water reactor severe accident [20], the temperature range of simulations starts from ~ 1000 K, similar to those of steam generator

hot leg, to ~ 2500 K, similar to the outlet melt fuel temperature. Under ~ 1000 K, the temperature is too low to lead to a significant amount of gaseous ruthenium species. The pressure fixed to 2 bars is approximately corresponding to those of a Loss Of Coolant Accident (LOCA), about 2 days after the start of the accident. The reference value of initial ruthenium amount of 0.01 mol/m^3 is based on a reactor coolant system (RCS) volume of about 200 m^3, a residence time of about 100 s, and a release fraction of about 2% of the fuel inventory (~ 250 kg) per hour. A higher Ru concentration of 0.1 mol/m^3 is also studied to explore the influence of this parameter. The Gibbs functions database in the equilibrium simulation includes all most stable species of the Ru-O-H chemical system except for the species $RuO_2(OH)_2$, for which two isomers $RuO_2(OH)_2-C_s$ and $RuO_2(OH)_2-C_{2v}$ contribute equally to the Gibbs function in the temperature range of interest.

The first subsection present literature equilibrium calculations on ruthenium release in nuclear power plant severe accident conditions with the existing database for ruthenium oxyhydroxides. The same conditions of release are then used to perform equilibrium calculations using the revised thermodynamic data obtained from our theoretical calculations. The second subsection portrays equilibrium calculations using all our Ru oxides and oxyhydroxides species with sensitivity study of the amount released. Last subsection presents forecast including Ru oxides, oxyhydroxides and dimer species. The impact of Ru_2O_4 and Ru_2O_6 systems will be analysed.

5.4.1 Equilibrium calculations on Ru release using existing Ru-O-H database

To draw speciation, Garisto [5] database includes his derived thermodynamic properties for Ru oxides, and thermodynamic functions for Ru oxyhydroxides Ru(OH) and $RuO_3(OH)$ from Krikorian *et al.* [17] study. The conditions of simulations include the release of 0.01 mol of ruthenium into a 50 % steam-air mixture, at a pressure of 1 atm with 0.15 mol of steam. From his speciation calculation at high temperature, he concluded that Ru(OH) species is responsible for the enhanced ruthenium volatility, as compared to calculations without ruthenium hydroxides, even if the fraction of ruthenium release remains small, only 10^{-3} at 2000 K. At lower temperatures, the formation of $RuO_3(OH)$ into a pure steam or steam-air environment enhanced the volatility of ruthenium. In Fig. 5.7(a), we recalculated the thermodynamic equilibrium of Garisto's work under a steam-air environment using our simulation tool to ensure the reproducibility of Garisto's results when Krikorian's thermodynamic values are used for oxyhydroxides species. A similar result is observed with the formation of $RuO_3(OH)$ species at low temperature. In Fig. 5.7(b), the simulation of Fig. 5.7(a) is reproduced using our calculated thermodynamic data for the same species considered by Garisto. In particular, our calculated standard enthalpy of formation for $RuO_3(OH)$ is equal to -228.8 kJ mol^{-1}, less exothermic compared to those used by Garisto of -348.0 kJ mol^{-1}, and equal to 422.1 kJ mol^{-1} for Ru(OH), more endothermic to the one derived by Krikorian of 327.0 kJ mol^{-1}. The resulting speciation significantly changes, no oxyhydroxide is detected in the 800-2000 K temperature range. The formation of ruthenium trioxide and tetroxide governs mostly the ruthenium volatility.

In Fig. 5.7(c), the simulation is repeated including in Ru−O−H database all the oxyhydroxide species. No change is observed, the volatile speciation diagram is still dominated

(a)

(b)

(c)
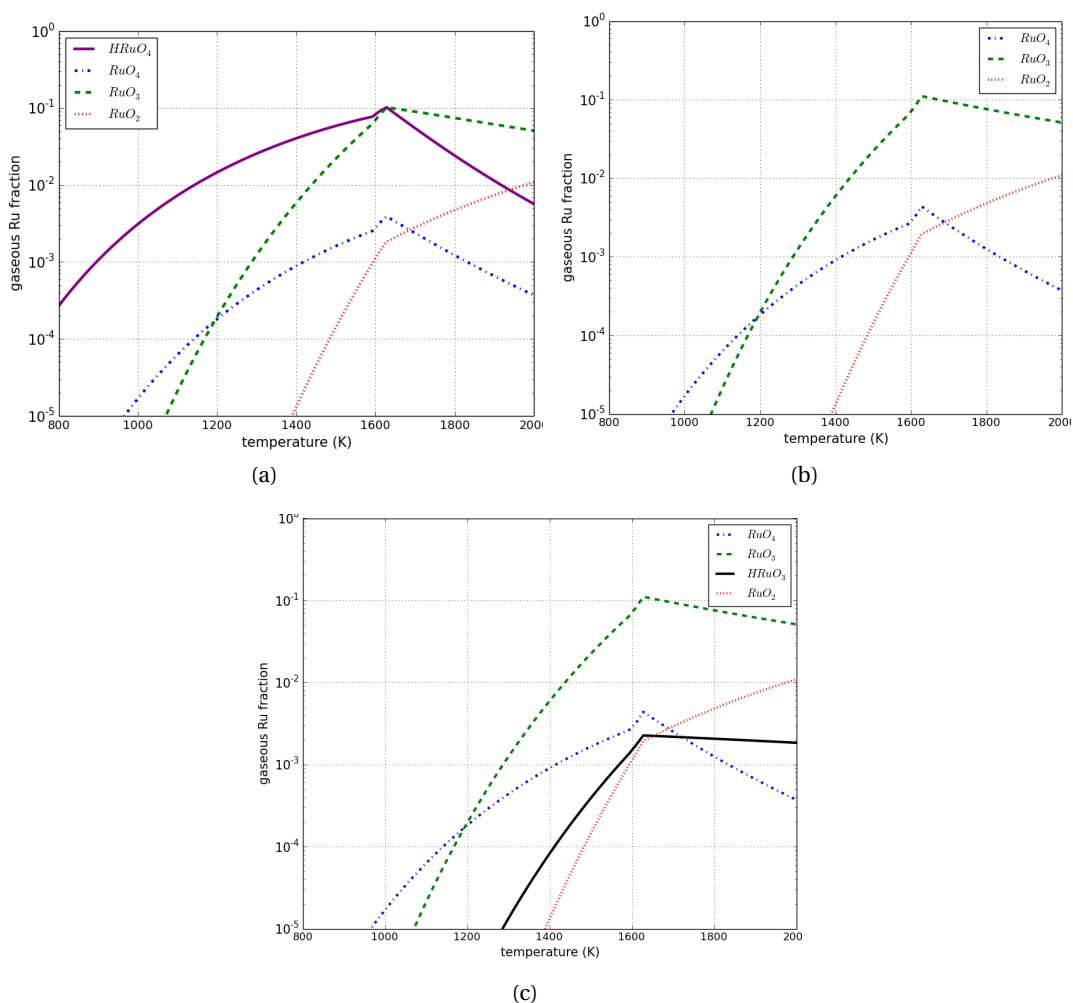
Figure 5.7:   Ruthenium speciation (HRuO$_4$ and HRuO$_3$ correspond respectively to RuO$_3$(OH) and RuO$_2$(OH) gaseous species) for the release of 0.01 mol of ruthenium into a 50 % steam-air mixture, at a pressure of 1 atm (0.15 mol of steam) [a].

[a] (a) including only the RuO$_3$(OH) and Ru(OH) species with the Krikorian's [17] thermodynamic data (cf Garisto's simulation displayed on Fig. 8 of ref. [5])
(b) including only the RuO$_3$(OH) and Ru(OH) species with our *ab initio* computed thermodynamic values
(c) including all ruthenium oxyhydroxide species with our *ab initio* computed thermodynamic values.

by the trioxide and tetroxide at low temperatures. For temperatures greater than 1200 K, the RuO$_2$(OH) species appears, reaching RuO$_2$ and RuO$_4$ quantities around 1600 K. However, these contributions are negligible in comparison with those of ruthenium trioxide.

5.4.2 Speciation of Ruthenium release using extended Ru-O-H database

Several sets of thermodynamic equilibria were performed and are illustrated in Fig. 5.8, changing the steam and air composition from 0, 50 to 100 %, at a pressure of 2 bar, and scanning the temperature from 1000 to 2500 K.

Initial amount of Ru is set to 0.1 (Figure 5.8(a)) and 0.01 mol/m^3 (Figure 5.8(b)). The results show that the oxidation of metallic ruthenium under an air atmosphere leads to the formation of gaseous ruthenium oxide species. Ruthenium oxyhydroxides appear beyond 2000 K in small quantities with mixed air/steam atmospheres. The ruthenium tetroxide is the dominating species for temperatures lower than 1000 K. The ruthenium trioxide becomes major in the 1000-2000 K range. The monoxide, dioxide, and trioxide species, with about 3 % of $RuO_2(OH)$ appears beyond 2000 K. Whatever the atmosphere composition and the initial ruthenium concentration, oxyhydroxide species are not stable at low temperature. The only relevant species emerging beyond 2000 K is $RuO_2(OH)$. These simulations with accurate theoretical thermodynamic values contradict the conclusions previously drawn by Garisto [5] and other authors [17, 18], who predicted $RuO_3(OH)$ to be present in significant amounts in conditions relevant to severe nuclear accidents.

The uncertainties of the results across the three chemical reactions considered, (reactions 5.4) does not exceed 3 kJ mol^{-1}. We should add to this standard deviation the uncertainty of the enthalpy of formation of RuO_4, 4.4 kJ mol^{-1} [5, 13, 14] used to derive that of all oxides and oxyhydroxides ruthenium species, that lead us to estimate the uncertainty of the calculated thermodynamic data to be about 10 kJ mol^{-1}. Sensitivity studies are performed to see the potential impact on Ru chemical speciation by varying the enthalpy of formation by -10, -25, -50, up to -100 kJ mol^{-1}.

Results reported in Table 5.4.2 were performed by varying the standard enthalpy of formation for one species at a time in a simulation environment of 50 % steam-air mixture with initial amount of metallic Ru equal to 0.01 mol/m^3. Massive amounts of oxyhydroxides appear when the values are shifted by -25 kJ mol^{-1}, the largest quantity (10.7 %) being observed for $RuO_2(OH)$ beyond 1500 K. Then the formation of the conformers of $RuO_2(OH)_2 - C_{2v}$ species, $RuO_2(OH)_2 - Cs$ is highlighted. The species $RuO_3(OH)$ found in large amount in literature Ru speciation release also appears, but in very negligible quantities. Calculations performed by shifting standard enthalpies of formation by -100 kJ mol^{-1} are shown in order to illustrate the importance of a slight uncertainty. In this case, the gaseous speciation becomes dominated by oxyhydroxides, reaching 100 % for temperatures greater than 1100 K. As nominal quantum chemical thermodynamic values are given with uncertainties less than 10 kJ mol^{-1}, thus oxyhydroxides cannot exist in significant amounts.

(a)

(b)
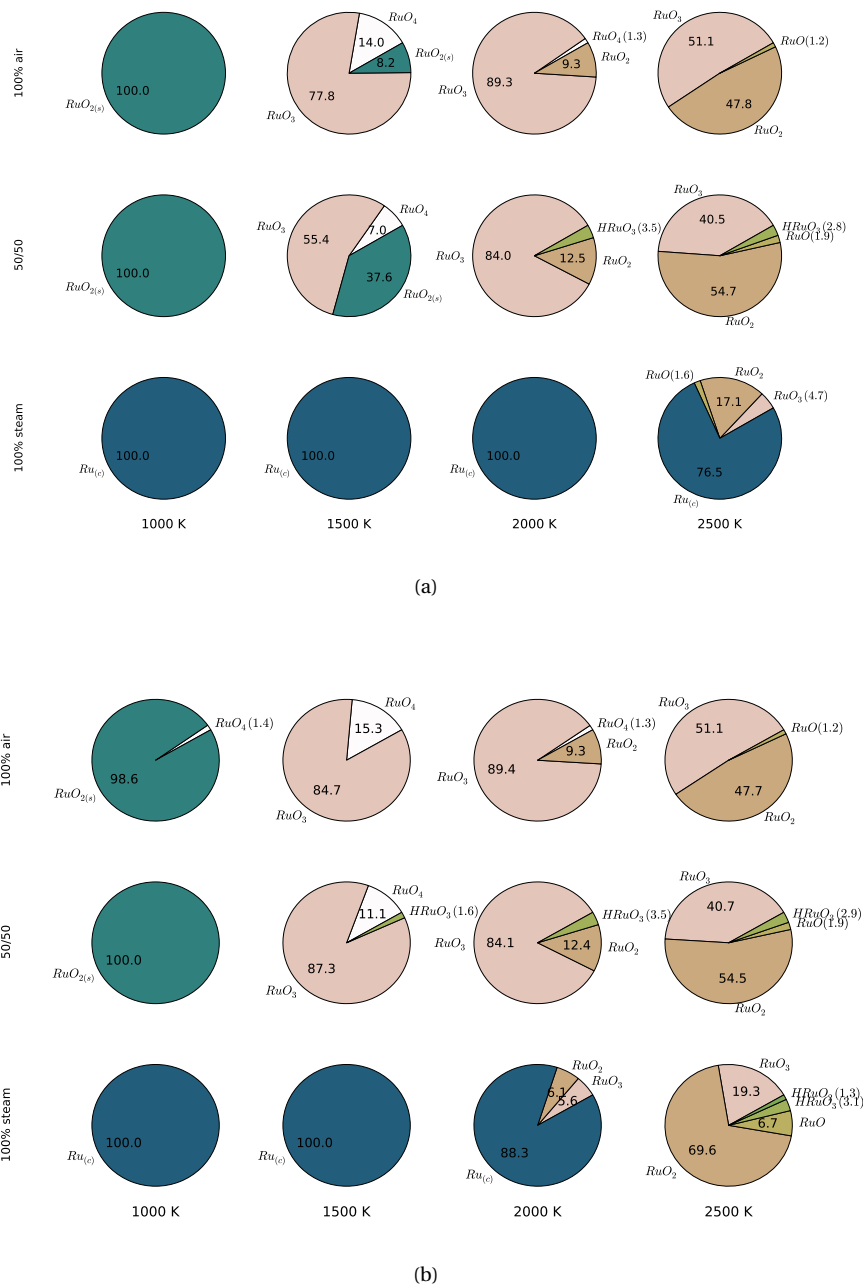
Figure 5.8: Ruthenium speciation ($HRuO_3$ and $HRuO_2$ correspond respectively to the $RuO_2(OH)$ and $RuO(OH)$ gaseous species) for the release of 0.1 (a) and 0.01 (b) mol of ruthenium into a 0, 50 and 100 % steam-air mixtures, at a pressure of 2 bar in volume equal to 1 m^3 at different temperatures [a].

[a]Species with concentrations smaller than 1 % are discarded. The state of a species is denoted by the letters: c (condensed state, solid or liquid), and s (solid). The gaseous state is implied if the state of a species is not explicitly indicated.

Table 5.19:   Sensitivity calculations on the standard enthalpies of formation of oxyhydroxides by varying their values by -10, -25, -50, and -100 kJ mol^{-1} in a 50 % steam-air mixture at 2 bar and in volume of 1 m^3 with initial amount of Ru equal to 0.01 mol/m^3. Only the resulting percentages of the released oxyhydroxide species are reported

Temperature (K)	900	1100	1300	1500
Initial % of oxyhydroxides	0.00	0.00	0.34	1.61
Variations of -10 kJ mol^{-1}				
Species	% of oxyhydroxides			
$RuO_2(OH)$			0.86	3.48
$RuO_3(OH)$			0.38	1.64
$RuO_2(OH)_2-C_{2v}$			0.36	1.64
Variation of -25 kJ mol^{-1}				
Species	% of oxyhydroxides			
$RuO_2(OH)_2-C_s$			0.37	1.63
$RuO_2(OH)$		0.05	3.46	10.67
$RuO_3(OH)$			0.52	1.78
$RuO_2(OH)_2-C_{2v}$			0.42	1.72
Variation of -50 kJ mol^{-1}				
Species	% of oxyhydroxides			
$RuO(OH)_2$				1.65
$RuO_2(OH)_2-C_s$		0.05	0.64	1.78
$RuO_2(OH)$		0.72	34.98	46.93
$RuO_3(OH)$		0.16	2.14	3.08
$RuO_2(OH)_2-C_{2v}$		0.06	1.12	2.41
Variation of -100 kJ mol^{-1}				
Species	% of oxyhydroxides			
$RuO(OH)_2$			1.22	3.68
$RuO_2(OH)_2-C_s$	2.16	10.77	31.05	10.36
$RuO(OH)$			0.37	2.25
$RuO_2(H_2O)$			0.66	2.55
$RuO_2(OH)$	1.80	98.17	98.64	97.99
$RuO_3(H_2O)$			0.47	1.74
$RuO_3(OH)$	3.42	37.75	78.86	46.91
$RuO_2(OH)_2-C_{2v}$	1.26	14.14	61.73	32.18

5.4.3 Ruthenium speciation release including Ru_2O_4 and Ru_2O_6 species in extended Ru–O–H database

Figure 5.9 presents calculations equilibrium of Ru speciation release in 50 % steam-air mixture at 1 atm with initial amount of Ru metallic atom equal to 0.01 mol/m^3, with Ru–O–H database including the thermodynamic functions of the dimers Ru_2O_4 and Ru_2O_6. Subfigure 5.9(a) illustrates results using this complete database. The calculation performed in subfigure 5.9(b) involved in database only Ru_2O_4, Ru_2O_6, RuO_4, and RuO_3 species without oxyhydroxide compounds and condensed phase of Ru. Subfigures 5.9(c) and 5.9(c) depict calculation done in order to analyse influence of dimers against oxides. Only Ru_2O_4 and RuO_3 species are included in database in 5.9(c), and only Ru_2O_4 and RuO_2 in 5.9(d).
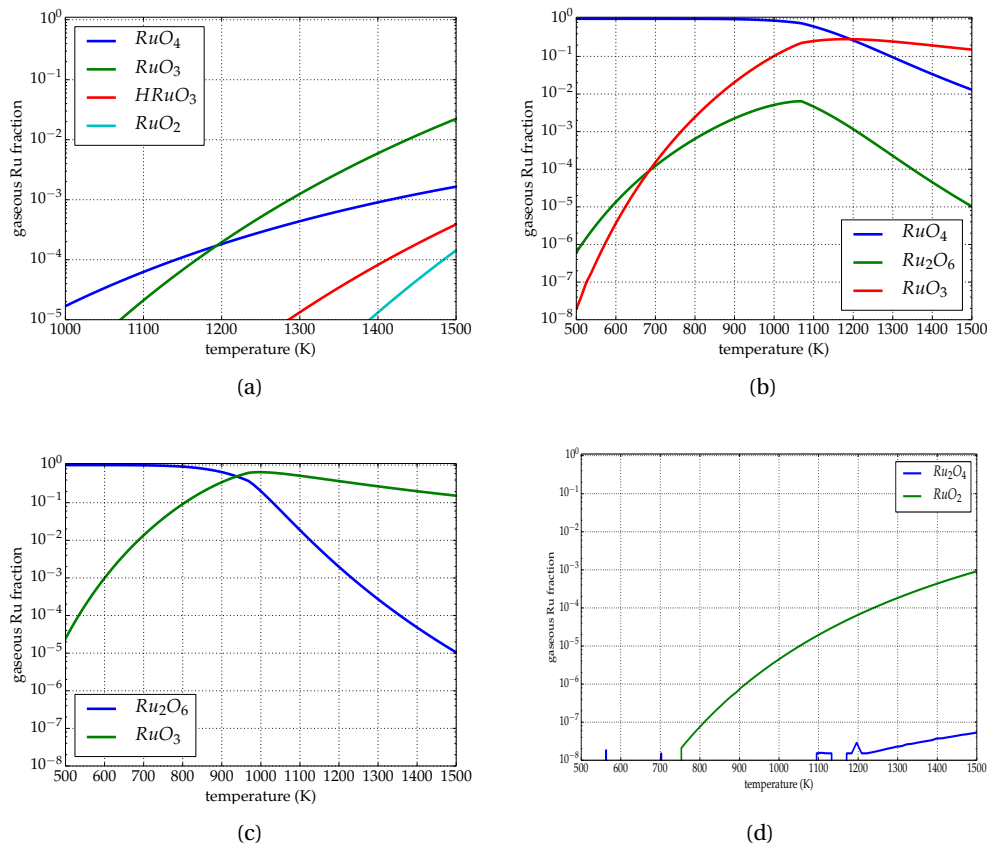
Figure 5.9: Ruthenium speciation ($HRuO_3$ correspond to $RuO_2(OH)$ gaseous species) for the release of 0.01 mol of ruthenium into a 50 % steam-air mixture, at a pressure of 1 atm (0.15 mol of steam): (a) including Ru_2O_4 and Ru_2O_6 dimer species with Ru oxides and oxyhydroxide species ; (b) including only the Ru_2O_4, Ru_2O_6, RuO_4, and RuO_3 species; (c) including only the Ru_2O_6 and RuO_3 species; (d) including only the Ru_2O_4 and RuO_2 species

Results in Fig. 5.9(a) highlight that the dimer species have no influence on ruthenium speciation, the volatility is still dominated by oxides species. In Fig. 5.9(b), we observe that formation of Ru_2O_6 species at low temperature is competitive to those of RuO_3 oxide, traducing the most stability of this species in temperature range closer to the cold leg break regarding nuclear severe accident scenario. At $\sim$ 700 K, formation of trioxide becomes dominating compared to those of Ru_2O_6. The formation of Ru_2O_4 is not observed, except in Fig. 5.9(b), even if such scenario is unlikely, the amount of this species remain negligible. As a conclusion, the dimer species have negligible influence at thermodynamic equilibrium on Ru speciation release.

5.5   Conclusions

Molecular structural study of Ru oxides highlights that the Ru-O bond length is a strong double covalent bond, with constant Ru-O bond distances due to the increasing Ru charge in competition with the decreasing delocalisation index at higher oxidation states. Oxyhydroxides complexes reveal covalent bond with hydroxyl group, in contrary to aqueous hydroxides species with ionic OH bonding. The ionic bonding of water ligand in oxyhydroxides complexes is formed by 4p oxygen lone pair orbital and 4d Ru orbital. Ru–Ru bond appear in Ru_2O_4 species as pure covalent bond, similar to ionic water ligand one. In Ru_2O_6, the Ru–Ru bond reveals no sharing of electrons between the two atoms, the bonding is made by repulsive attraction between Ru–O–Ru–O atoms forming a ring critical bond, according to the QTAIM analyses. The theoretical calculations predict the standard enthalpies of formation at 298 K of Ru oxides to be 639, 420, 140, and -50 kJ mol^{-1} for Ru, RuO, RuO_2, and RuO_3 gaseous compounds respectively, are in agreement with literature range values, revising value for Ru and RuO_3 species by shifted literature ones by ~ 10 kJ mol^{-1}. Derived thermodynamic values for oxyhydroxides species deviate towards literature ones up to 100 kJ mol^{-1}. The equilibrium calculations on Ru speciation release performed in conditions relevant to nuclear power plant accident reveal that ruthenium volatility is dominated by ruthenium tetroxide at lower temperatures, by ruthenium trioxide between 1000 and 2000 K. At higher temperatures gaseous ruthenium oxide, dioxide, and even Ru in gaseous phase are formed. Oxyhydroxide species $RuO_2(OH)$ appears at temperature range beyond 1500 K in negligible amount, contrary Garisto's assessments. Ru_2O_4 and Ru_2O_6 compounds are not longer detected in these simulations.

References

(1) Zhou, M.; Citra, A.; Liang, B.; Andrews, L. Infrared Spectra and Density Functional Calculations of MO_2, MO_3, $(O_2)MO_2$, MO_4, MO_2^- (M = Re, Ru, Os) and ReO_3^-, ReO_4^- in Solid Neon and Argon. *J. Phys. Chem. A* **2000**, *104*, 3457–3465, DOI: `10.1021/jp993026p`.

(2) Hameka, H. F.; Jensen, J. O.; Kay, J. G.; Rosenthal, C. M.; Zimmerman, G. L. Theoretical Prediction of Geometries and Vibrational Infrared Spectra of Ruthenium Oxide Molecules. *J. Mol. Spectrosc.* **1991**, *150*, 218–221, DOI: `10.1016/0022-2852(91)90204-N`.

(3) Siegbahn, P. E. M. Binding in Second-Row Transition Metal Dioxides, Trioxides, Tetraoxides, Peroxides, and Superoxides. *J. Phys. Chem.* **1993**, *97*, 9096–9102.

(4) Huang, W.; Xu, W.-H.; Schwarz, W. H. E.; Li, J. On the Highest Oxidation States of Metal Elements in MO4 Molecules (M = Fe, Ru, Os, Hs, Sm, and Pu). *Inorg. Chem* **2016**, *55*, PMID: 27074099, 4616–4625, DOI: `10.1021/acs.inorgchem.6b00442`.

(5) Garisto, F. *AECL-9552* **1988**.

(6) Kay, J.; Green, D.; Duca, K.; Zimmerman, G. L. *J. Mol. Spectrosc.* **1989**, *138*, 49.

(7) Morgan, D. J. Resolving ruthenium: XPS studies of common ruthenium materials. *Surface and Interface Analysis* **2015**, *47*, SIA-15-0179.R1, 1072–1079, DOI: `10.1002/sia.5852`.

(8) Marsh, B. M.; Zhou, J.; Garand, E. Charge Transfer in $MOH(H_2O)^+$ (M = Mn, Fe, Co, Ni, Cu, Zn) Complexes Revealed by Vibrational Spectroscopy of Mass-Selected Ions. *Phys. Chem. Chem. Phys.* **2015**, *17*, 25786–25792, DOI: `10.1039/C5CP01522G`.

(9) Michael; Kabrede, H. Geometries of Transition-Metal Complexes from Density-Functional Theory. *J. Chem. Theory Comput.* **2006**, *2*, 1282–1290, DOI: `10.1021/ct6001187`.

(10) Yamaguchi, K.; Koike, T.; Kim, J.; Ogasawara, Y.; Mizuno, N. Highly Dispersed Ruthenium Hydroxide Supported on Titanium Oxide Effective for Liquid-Phase Hydrogen-Transfer Reactions. *Chem. - Eur. J.* **2008**, *14*, 11480–11487, DOI: `10.1002/chem.200801655`.

(11) Magnera, T. F.; David, D. E.; Michl, J. Gas-Phase Water and Hydroxyl Binding Energies for Monopositive First-Row Transition Metal Ions. *J. Am. Chem. Soc.* **1989**, *111*, 4100–4101, DOI: `10.1021/ja00193a051`.

(12) Schiros, T.; Näslund, L.-Å.; Andersson, K.; Gyllenpalm, J.; Karlberg, G. S.; Odelius, M.; Ogasawara, H.; Pettersson, L. G. M.; Nilsson, A. Structure and Bonding of the Water-Hydroxyl Mixed Phase on Pt(111). *J. Phys. Chem. C* **2007**, *111*, 15003–15012, DOI: `10.1021/jp073405f`.

(13) Cordfunke, E. H. P.; Konings, R. J. M. Thermochemical Data for Reactor Materials and Fission Products: The ECN Database. *J. Phase Equilib.* **1993**, *14*, 457–464, DOI: `10.1007/BF02671964`.

(14) Barin, I.; Knacke, O.; Kubaschewski, O., *Thermochemical properties of inorganic substances*; Springer-Verlag: Berlin, Heidelberg, New York, 1977, p 861.

(15) Zimmerman, G. L.; Riviello, S. J.; Glauser, T. A.; Kay, J. G. Photochemical Decomposition of Ruthenium Tetroxide. *J. Phys. Chem.* **1990**, *94*, 2399–2404, DOI: `10.1021/j100369a039`.

(16) Miradji, F.; Souvi, S.; Cantrel, L.; Louis, F.; Vallet, V. Thermodynamic Properties of Gaseous Ruthenium Species. *J. Phys. Chem. A* **2015**, *119*, 4961–4971, DOI: `10.1021/acs.jpca.5b01645`.

(17) Krikorian, O. H.; Carpenter, J. H.; Newbury, R. S. A Mass Spectrometric Study of the Enthalpy of Sublimation of Technetium. *High Temp. Sci.* **1969**, *1*, 313–330.

(18) Jackson, D. D. Thermodynamics of the gaseous hydroxides, report UCRL-51137., Laurence Livermore National Laboratory, 1971.

(19) Piar, B. Nuclea Tool Box., Nuclea-Toolbox 1.2.0, IRSN.

(20) Dorsselaere, J.-P. V.; Auvinen, A.; Beraha, D.; Chatelard, P.; Herranz, L.; Journeau, C.; Klein-Hessling, W.; Kljenak, I.; Miassoedov, A.; Paci, S.; Zeyen, R. Recent Severe Accident Research Synthesis of the Major Outcomes from the SARNET Network. *Nucl. Eng. Des.* **2015**, *291*, 19–34, DOI: `10.1016/j.nucengdes.2015.03.022`.

REACTIVITY AND DETERMINATION OF KINETIC PARAMETERS

As presented in the previous chapter, Ru volatility in NPP severe accident conditions is dominated by the ruthenium trioxide and tetroxide volatile compounds. In this chapter, the aim is to find the mechanisms leading to the formation of both species. The first section presents the state of art regarding simulations of START tests with ASTEC/SOPHAEROS code, highlighting the need of kinetic in modelling. The choice of the selected reaction pathways leading to the formation of the products of interest is then detailed in Section 2. The structures of species involved in the selected reactions are then presented in Section 3, and their energetics are also discussed. The last part presents the kinetic parameters calculated using appropriate theories and discusses the comparison with experimental measurements.

6.1 Current modelling of START tests with ASTEC/SOPHAEROS code

The simulations of START tests with SA code ASTEC/SOPHAEROS[1] so far do not include kinetic parameters regarding the formation of Ru gaseous compounds. We choose to present here START tests 03 and 17 [2], performed in dry air with a quartz tube, leading to information of parameters involved in the formation of Ru gaseous species with different temperature gradients. An initial amount of anhydrous RuO_2 powder of 1 g was used in crucible. Final mass of Ru reported at the end was 78.56% in test 03 and 83.09% in test 17. Fig. 6.1 presents the thermal profiles of both tests. Aspects of primary circuit model tube at the end of the tests are also shown for both phases of the measurement (direct transport (vaporisation), and re-vaporisation of deposits). The START test 17 was performed with a smooth thermal profile. As explained in Chapter 2, such profile corresponds to a small temperature gradient. In fact, relatively high temperatures (∼ 1500 K) are imposed along the tube surfaces and decrease smoothly until the outlet (∼ 600 K). In START test 03, the thermal gradient is steeper; the tem-
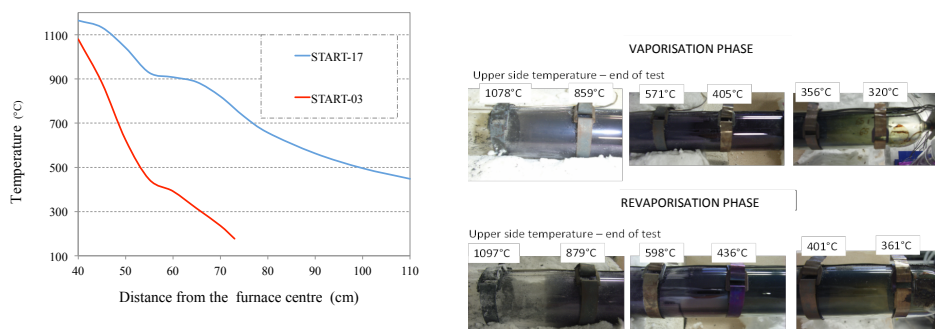
Figure 6.1: Thermal profiles of START-03 and START-17 tests (left)[2], with aspects of model tube at the end of tests (right).

Table 6.1: Current modelling for START tests 03 and 17 with ASTEC/SOPHAEROS

| | START-03: | | START-17: | |
	Gas (%)	Aerosols (%)	Gas (%)	Aerosols (%)
Vaporisation				
Models	1.4	0.1	0.1	0.1
Test	1.3	1.5	0.1	0.2
Revaporisation				
Models	0.8	0.5	0.6	0.0
Test	0.9	0.3	0.5	0.0

perature quickly decreases along the tube as it is shorter by comparison to the one used in test 17. The two sets of measurement reveal that most Ru is deposited on the tube surface in both tests, in slightly larger amounts with a smooth temperature profile. The above-mentioned tests were simulated with the ASTEC/SOPHAEROS module [3]. Table 6.1 presents the results of modelling and their comparisons to the experimental tests.

One can observe that with a small temperature gradient, the fraction of Ru gaseous compounds is smaller at the outlet. On the contrary, test performed with an abrupt temperature profile leads to a larger release of gaseous Ru. The modelling in overall reproduces the gaseous fractions observed in both tests. For the formation of aerosols, the model is less accurate for a steep temperature gradient. In fact, in the smooth temperature profile test, no aerosols are formed. The mechanisms involved in the formation of Ru compounds in the tests are schematically illustrated in Fig. 6.2. After RuO_3 was vaporised from crucible, it is transported along the the decreasing thermal profile, as drawn in Fig. 6.2. Around 1100K, that species become less stable, according to its thermodynamic stability (see Chapter 5, page 116). It can disappear according to two competing processes:

- by reduction to form RuO_2 condensed species;
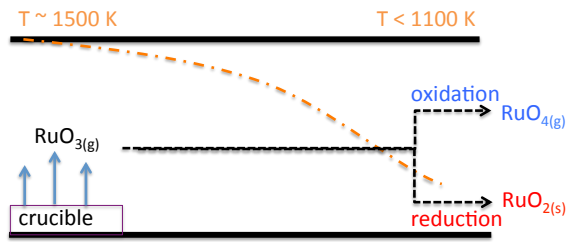
Figure 6.2: Schematic reproduction of RuO_3 mechanisms in gaseous phase during START tests.

- by oxidation to form RuO_4.

These two mechanisms are in competition. If a kinetic limitation is imposed on one of them, the other one is promoted. In our case, according to the experimental measurements, if we imposed kinetic limitations to the transformations in the gaseous phase, we can better reproduce the formation of aerosols. These difficulties in simulating the formation of aerosols are highlighted in the modelling of the deposit profiles: an offset on the deposit peak at high temperatures ($1000°$-$800°$) is obtained, in comparison with the experimental observations, this translating fewer amounts of deposits aerosols[3]. We thus need to study the possible reactions in the gaseous phase leading to the formation of RuO_3 and RuO_4 in conditions of NPP SA in the next section.

6.2 Selection of reactions pathways

The possible reactions involve air/steam species, but also air radiolysis products such as NO_2, N_2O, and NO volatile compounds, to be representative of a nuclear power plant severe accident. We calculated the Gibbs free reaction energies for several mechanisms, and listed them in Table 6.2. The corresponding curves are also illustrated in Fig. D.1 and D.2 in Appendix D. Reactions involving direct oxidation by H_2O or OH radical are not spontaneous at 1000 K. Those involving O radical are very spontaneous. Without radiation induced by SA conditions, reactions involving O radical are not suitable to occur, and if they are, no kinetic limitations will be encountered. With dimer species, the production of gaseous RuO_3 and RuO_4 is the only way to oxidise spontaneously with O_2 species. Oxidation with N_2O and NO_2 are also very spontaneous. Finally, we decided to focus on these latter mechanisms, involving dimerisation and air radiolysis products (N_2O and NO_2). Thus, we investigated the following reactions to form RuO_3 and RuO_4 by dimer species:

$$R_1 : 2\,RuO_2 \longrightarrow Ru_2O_4 \qquad\qquad (6.1a)$$
$$R_2 : 2\,RuO_3 \longrightarrow Ru_2O_6 \qquad\qquad (6.1b)$$
$$R_3 : Ru_2O_4 + O_2 \longrightarrow Ru_2O_6 \qquad\qquad (6.1c)$$
$$R_4 : Ru_2O_6 + O_2 \longrightarrow 2\,RuO_4 \qquad\qquad (6.1d)$$
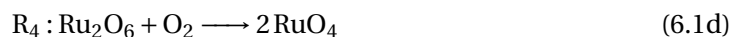
Table 6.2: Calculated Gibbs free reaction energies (in kJ mol^{-1}) at 1000 K obtained from molecular data computed at the TPSSh-5%HF.

Reactions	$\Delta_r G°$(1000 K), n=3	$\Delta_r G°$(1000 K), n=4
$RuO_{n-1} + H_2O \rightarrow RuO_n + H_2$	77.1	163.9
$RuO_{n-1} + OH \rightarrow RuO_n + H$	27.9	114.6
$RuO_{n-1} + O \rightarrow RuO_n$	-303.5	-216.7
$Ru_2O_{2(n-1)} + O_2 \rightarrow 2\,RuO_n$	-160.9	-84.2
$RuO_{n-1} + N_2O \rightarrow RuO_n + N_2$	-275.6	-188.8
$RuO_{n-1} + NO_2 \rightarrow RuO_n + NO$	-133.7	-46.9

And then oxidation by nitrous and nitrogen oxides:

$$R_5 : RuO_2 + N_2O \longrightarrow RuO_3 + N_2 \tag{6.2a}$$
$$R_6 : RuO_3 + N_2O \longrightarrow RuO_4 + N_2 \tag{6.2b}$$
$$R_7 : RuO_2 + NO_2 \longrightarrow RuO_3 + NO \tag{6.2c}$$
$$R_8 : RuO_3 + NO_2 \longrightarrow RuO_4 + NO \tag{6.2d}$$
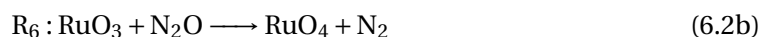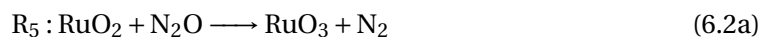
The structural properties and energetics of these chemical pathways are presented in next section.

6.3 Structural properties of potential energy surfaces and energetics

The potential energies surface have been explored to locate the stationary points corresponding to reaction intermediates, the transition states and molecular complexes. This procedure allows us to define the reaction mechanism between reactants and products. When a transition state structure has been located, internal reaction coordinates calculations (IRC) [4] have been performed using the algorithm implemented in the Gaussian09 software [4] to find the associated molecular complexes on the reactant and product sides. The nature of the intermediate species is revealed by the frequency check as a single imaginary frequency must be obtained for a transition state. The optimised reaction path starts from a transition state to connect intermediate molecular complexes namely the molecular complex reactant (MCR)
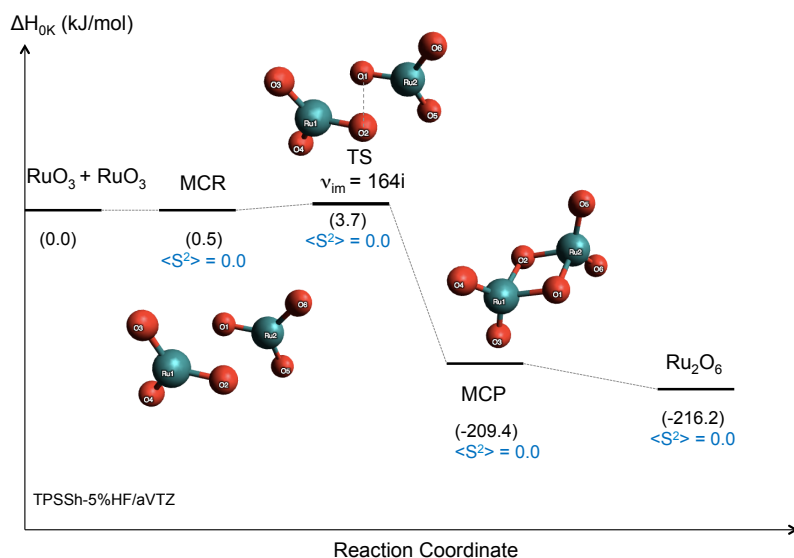
Figure 6.3: Reaction profile at 0 K calculated at the TPSSh-5%HF/AVTZ level of theory for reaction $2\,RuO_3 \longrightarrow Ru_2O_6$ with schematic representations of the intermediate species involved.

and the molecular complex product (MCP). Geometries were optimised with TPSSh-5%HF method. In this section, the structures and energetics reactions involving of dimer oxides (reactions 6.1a, 6.1b, 6.1c, and 6.1d) are presented in a first part, those involving nitrous oxides (reactions 6.2a and 6.2b) in a second part, and those with nitrogen oxides (reactions 6.2c and 6.2d) in the last one.

6.3.1   Reactivity with dimer species

We first investigated the reaction pathways leading to the formation of Ru_2O_4 or Ru_2O_6 species from two RuO_2 and RuO_3 gaseous molecules, respectively. No transition states was localised for Ru_2O_4 formation in reaction 6.1a. We consider this reaction as spontaneous. Regarding the formation of Ru_2O_6 from two RuO_3, the reaction profile at 0K is illustrated in Fig. 6.3. The essential geometric parameters and zero point energies (ZPE) for reactants, products, molecular complexes, and transitions state are provided in Table 6.3. The transition state appears with a negligible barrier($\sim$3.7 kJ mol^{-1}), connecting pro- and post-reactant molecules by forming ring critical points between the two oxygen of each trioxide. One can notice that no spin contamination is observed along the reaction pathway, all systems having a singlet ground state. Moreover, the bond lengths of the molecular complex reactant (r(Ru-O)$\sim$1.679 Å, r(Ru-O)[RCP]$\sim$1.923 Å, r(Ru-Ru)$\sim$3.053 Å) are similar to those found in the Ru trioxide dimer (r(Ru-O)$\sim$1.680 Å, r(Ru-O)[RCP]$\sim$1.900 Å, r(Ru-Ru)$\sim$2.970 Å, see Chapter 5, Section 5.1.3). θ(O-Ru-O) bond angle ($\sim$120.1°) and r(Ru-O) bond length ($\sim$1.685 Å) in MCR(6.1b) are similar to those of RuO_3 (θ(O-Ru-O)$\sim$120.0°, r(Ru-O)$\sim$1.690 Å, see 5.1.1.2). This reaction scheme can also be considered as spontaneous. According to the Gibbs energies diagram

Table 6.3: Structural parameters (bond lengths r are in Å, bond angles θ in °) imaginary vibrational frequency (cm^{-1}), and ZPE (kJ mol^{-1}), for the transition state and molecular complexes calculated at the TPSSh-5%HF/aVQZ level of theory, involved in the reaction $2\,RuO_3 \longrightarrow Ru_2O_6$

Parameters	MCR (6.1b)	TS (6.1b)	MCP (6.1b)
r(Ru-O)	1.685-1.695	1.684-1.715	1.679
r(Ru-O) [RCP]^a	3.032	2.645	1.918- 1.923
r(Ru-Ru)	3.941	3.586	3.053
θ(O-Ru-O)	119.6-120.7	118.5-122.8	110.7- 122.6
θ(O-Ru-O) [RCP]	70.3	71.2	74.7
θ(Ru-O-Ru)	109.7	108.7	105.2
ν_{im}		164 i	
ZPE	44.1	44.2	51.3

^{a} RCP: Ring Critical Point

Figure 6.4: Reaction profile at 0 K calculated at the CCSD(T)/aVQZ//TPSSh-5%HF/AVTZ level of theory for reaction $Ru_2O_4 + O_2 \longrightarrow Ru_2O_6$ with schematic representations of the intermediate species involved.

of reaction 6.1b shown in Fig. D.2(b), it can be stated that the formation of Ru_2O_6 through this mechanism is favoured at low temperatures. It could be one way to reduce the amount of RuO_3 gaseous compound in atmosphere during NPP SA.

The formation of Ru_2O_6 dimer through the oxidation of Ru_2O_4 by O_2 is drawn in Fig. 6.4. Table 6.4 gives the main geometric parameters of the species involved in this mechanism. The localised transition state is energetically lower, by $\sim$-55 kJ mol^{-1}, than the reactants. Otherwise, the multiplicity of this reaction pathway is triplet, without any spin contamination. The pro-reactant complex shows bonding between the metallic centre of Ru_2O_4 system and the O atoms of O_2 species. The molecular complex product is higher than the Ru_2O_6 product. Nevertheless, the bond lengths in the triplet MCP (6.1c) species are very close to those of

singlet product Ru_2O_6. The bond angles differ slightly being reduced by ~5°for θ(O-Ru-O) and θ(Ru-O-Ru), and increased by ~5°for θ(O-Ru-O)[RCP], compared to those of trioxide dimer (θ(O-Ru-O)~110.8-125.7°, θ(Ru-O-Ru)~102.7°, θ(O-Ru-O)[RCP]~77.2°). The bonding between the O atoms in O_2 is broken in the transition state complex, with an imaginary frequency of $461i \, cm^{-1}$. According to the Gibbs free energy diagram of reaction 6.1c, the formation of Ru_2O_6 is favoured at high temperatures, where $RuO_{2(g)}$ is more stable. In such conditions, this reaction can be considered almost spontaneous. In lower temperatures, Ru_2O_6 is formed by reaction 6.1b (dimerisation of RuO_3).

Table 6.4: Structural parameters (bond lengths r are in Å, bond angles θ in °) imaginary vibrational frequency (cm^{-1}), and ZPE (kJ mol^{-1}), for the transition state and molecular complexes calculated at the CCSD(T)/aVQZ//TPSSh-5%HF/aVQZ level of theory, involved in the reaction $Ru_2O_4 + O_2 \longrightarrow Ru_2O_6$

Parameters	MCR (6.1c)	TS (6.1c)	MCP (6.1c)
r(O-O)	1.422	1.711	
r(Ru-O)	1.662	1.672	1.682
r(Ru-O) [RCP]^a	1.946	1.910	1.910
r(Ru-Ru)	2.758	2.689	2.847
θ(O-Ru-O)	128.2	126.5	111.5- 121.7
θ(O-Ru-O) [RCP]	82.6	86.2	82.5-83.5
θ(Ru-O-Ru)	92.8	89.4	97.0
ν_{im}		461i	
ZPE	49.5	46.3	48.7

^{a} RCP: Ring Critical Point

The formation of RuO_4 through Ru trioxide dimer, as written in reaction 6.1d, is illustrated in Fig. 6.5. The corresponding geometric parameters are shown in Table 6.5. The search of this mechanism revealed several transition states. Two of them are presented in Fig. 6.5, including the one with the highest barrier. An intermediate TS is shown in Fig. D.3 of Appendix D. As for reaction 6.1c, the intermediate species calculated all have a triplet multiplicity without spin contamination. The first transition state TS1 (6.1d) shows the formation of Ru–O bonding between metallic centre of Ru_2O_6 species and O_{O_2} atom. We observe that the relative energy at 0 K is ~128 kJ mol^{-1} above the reactants. Ru_2O_8 species presents 2 RuO_4like compounds linked by the O atoms of the O_2 system. The second transition state lies ~93 kJ mol^{-1} above the reactants, with an imaginary frequency of 172i cm^{-1}. It depicts the breaking of centre O-O bonding in the intermediate Ru_2O_8 complex. We noticed that the MCP (6.1d) species presents bond angle and bond length (r(Ru-O)~1.737Å, θ(O-Ru-O)~97.2°) slightly different from those of RuO_4(r(Ru-O)~1.690Å, θ(O-Ru-O)~109.4°,see Section 5.1.1.1), corroborating a relative energy of ~160 kJ mol^{-1} above products. In conclusion, the large barriers to the transition states suggest that the formation of RuO_4via the formation of trioxide dimer in gaseous phase is a slow mechanism. Note that these reaction profiles have been computed at the TPSSh-5%HF/aVTZ level of theory, at a smaller computer ex-

Figure 6.5: Reaction profile at 0 K calculated at the TPSSh-5%HF/AVTZ level of theory for reaction $Ru_2O_6 + O_2 \longrightarrow 2\,RuO_4$ with schematic representations of the intermediate species involved.

Table 6.5: Structural parameters (bond lengths r are Å) imaginary vibrational frequency (cm^{-1}), and ZPE ($kJ\,mol^{-1}$), for the transition states and molecular complexes calculated at the TPSSh-5%HF/aVTZ level of theory, involved in the reaction $Ru_2O_6 + O_2 \longrightarrow 2\,RuO_4$

Parameters	MCR (6.1d)	TS1 (6.1d)	Ru_2O_8	TS2 (6.1d)	MCP (6.1d)
r(O-O)	1.214	1.240	1.443	1.772	3.876
r(Ru-O)	1.679	1.679- 1.691	1.687-1.732	1.688-1.726	1.688 - 1.786
r(Ru-O) [RCP][a]	1.904	1.763-2.348			
r(Ru-Ru)	2.973	3.061	4.042	4.099	4.428
θ(O-Ru-O)	110.8 -125.7	107.6 - 121.8	109.1- 119.2	110.9 - 115.7	82.5 - 111.9
θ(O-Ru-O) [RCP]	77.3	86.3			
θ(Ru-O-Ru) 102.7	107.2-109.2				
ν_{im}		178i		172i	
ZPE	62.0	61.2	63.7	59.7	62.9

[a] RCP: Ring Critical Point

pense than our reference CCSD(T)//CBS level. However, we are confident, that the energetic profile are correct. Moreover, we can expect that electronic calculations near to the transition state barrier often overestimate electronic energy due to the potential multi-configurational character of such compounds (see Section 3.2.1). The formation of Ru trioxide and tetroxide through nitrogen and nitrous oxide is discussed in the following subsections.
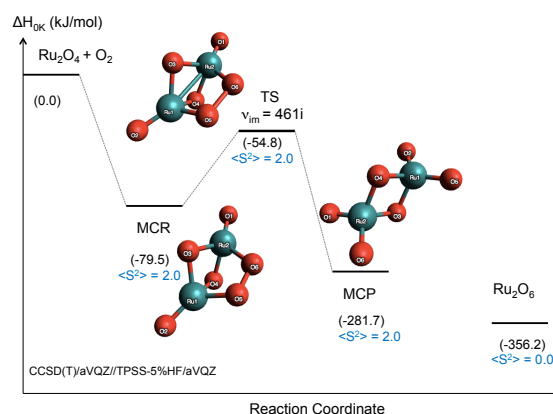
Figure 6.6: Reaction profile at 0 K calculated at the CCSD(T)/CBS//TPSSh-5%HF/AVTZ level of theory for reaction $RuO_3 + N_2O \longrightarrow RuO_4 + N_2$ with schematic representations of the intermediate species involved.

6.3.2   Oxidation with N_2O species

The formation of trioxide through N_2O oxidation is drawn in Fig.6.6. For the formation of RuO_4, the reaction profile is illustrated in Fig. 6.7. The main optimised geometric parameters and zero point energies (ZPE) for intermediate species are presented in Table 6.6, for the formation of RuO_3, and in Table 6.7, for the formation of RuO_4.

The provided r(N-N) bond length for N_2 species by DFA approximation of 1.097 Å is similar to the tabulated experimental value in the NIST database [5] (1.098 Å). In the linear N_2O species, this (N–N) bond length is found to be equal to 1.130 Å, and the (N-O) to 1.187 Å, in agreement with the literature values of 1.128 and 1.184 Å [6].

The TS (6.2a) structure relative to the formation of trioxide features a one-step mechanism with the breaking of (N-O) bond, stretched up to 1.351 Å from its equilibrium value in N_2O, to form the third Ru-O bonding, equal to 1.934 Å. This bond length is typical of ionic bonding, as observed between hydroxyl ligands and Ru oxides in the previous chapter. The value of the RuO_2 bond angle decreases as to favour the pyramidal structure leading to the formation of RuO_3. In the TS (6.2b) structure relative to the formation of tetroxide, the elongation of (N-O) bond distance is only 0.075 Å, much closer to the equilibrium value than the previous TS. The bond angles and bond distances are shrink from their equilibrium values, to lead to the formation of the tetrahedral structure of RuO_4.This reaction features the creation of the fourth Ru-O bonding of 2.101 Å, sharing fewer electrons between Ru and O_{N_2O} atoms compared to its counterpart in the previous TS. A bridge between O_{RuO_3} and N_{N_2O} is also observed, measuring 2.258 Å, indicating that the formation of RuO_4 implies large orbital mixings

Figure 6.7: Reaction profile at 0 K calculated at the CCSD(T)/CBS//TPSSh-5%HF/AVTZ level of theory for reaction $RuO_2 + N_2O \longrightarrow RuO_3 + N_2$ with schematic representations of the intermediate species involved.

from reactants.

Table 6.6: Structural parameters (bond lengths r are in Å) imaginary vibrational frequency (cm^{-1}), and ZPE ($kJ\,mol^{-1}$), for the transition state and molecular complexes calculated at the TPSSh-5%HF/aVTZ level of theory, involved in the reaction $RuO_2 + N_2O \longrightarrow RuO_3 + N_2$

Parameters	MCR (6.2a)	TS (6.2a)	MCP(6.2a)
r(N-N)	1.124	1.128	1.097
r(N-O)	1.222	1.351	
r(Ru-O$_{N_2O}$)	2.126	1.934	
r(Ru-O)	1.680	1.676	1.685
r(Ru-N$_{N_2}$)			4.527
θ(N-N-O)	173.4	148.8	
θ(O-Ru-O$_{N_2O}$)	109.8	113.9	
θ(O-Ru-O)	140.5	133.9	120.0
ν_{im}	590**i**		
ZPE	43.94	49.96	36.20

Connections of the TS(6.2b) to the $RuO_2 \cdots N_2O$ reactant complex (MCR (6.2a)) and to the $RuO_3 \cdots N_2$ product complex (MCP 6.2a) have been ensured in both forward and backward directions via IRC calculations at the TPSSh-5%HF/aVTZ level of theory. The ionic interaction (2.126 Å) between O_{N_2O} and Ru atoms allows RuO_2 and N_2O compounds to stabilise

Table 6.7: Structural parameters (bond lengths r are in Å) imaginary vibrational frequency (cm^{-1}), and ZPE (kJ mol^{-1}), for the transition state and molecular complexes calculated at the TPSSh-5%HF/aVTZ level of theory, involved in the reaction $RuO_3 + N_2O \longrightarrow RuO_4 + N_2$

Parameter	MCR (6.2b)	TS (6.2b)	MCP (6.2b)
r(N-N)	1.130	1. 121	1.098
r(N-O)	1. 187	1.262	
r(Ru-O$_{N_2O}$)	4.986	2.103	
r(Ru-O)	1. 684	1.762-1.688	1.684
r(Ru-N)			4.020
θ(N-N-O)	180	159.4	
θ(O-Ru-O$_{N_2O}$)	118.8	113.1-118.1	
θ(O-Ru-O)	120.0	108.1	109.3-109.5
ν_{im}		572**i**	
ZPE	50.73	49.96	48.62

themselves within the MCR (6.2a). In reaction 6.2b, this interaction becomes weaker and turns is of a van der Waals type (4.986 Å); we can see that bond angles and bond distances of reactant complex are similar to those in RuO_3 and N_2O species. Such interactions are also observed in MCP systems for both reactions, where the Ru–N bond length is equal to 4.527 and 4.020 Å, for $RuO_3 \cdots N_2$ and $RuO_4 \cdots N_2$ complexes, respectively. The relative enthalpies at 0 K in reaction profile curve reveal that N_2O and RuO_2 have to overcome the TS barrier of about 14 kJ mol^{-1} to form N_2 and RuO_3 products. The MCR (6.2a) is stabilised by ~ 43 kJ mol^{-1} with respect to the reactants. The post-reactive complex is similar to the products, differing only by 0.6 kJ mol^{-1}. For the reaction 6.2b, the TS barrier is larger, equals to ~114 kJ mol^{-1}, almost as large as the one with dimer oxide Ru_2O_6 (TS(6.1d)) to form 2 RuO_4. The pro- and post reactive complexes are similar to the reactants and products, respectively, differing only by ~ -4 kJ mol^{-1}.

6.3.3 Oxidation with NO$_2$ species

The structures of intermediate species involved in the formation of RuO_3 in reaction 6.2c and relative enthalpies at 0 K are shown in Fig. 6.8. For the formation of RuO_4, two parallel mechanisms were determined, presented in Fig. 6.10 for path 1 and Fig. 6.9 for path 2. Tables 6.8, 6.10, 6.9 and 6.10 present the essential geometric parameters and zero-point energies for intermediates species in the formation of RuO_3 and RuO_4, respectively. The optimised geometry parameters for NO(r(N-O)~1.154 Å) and NO_2 (r(N-O)~1.199 Å; θ(O-N-O)~134.2°) are in good agreement with their experimental counterparts (r(N-O)~1.514 Å for NO[7]; r(N-O)~1.193 Å; θ(O-N-O)~134.1°for NO_2[6]). The MCR (6.2c) complex adopts a ring-like structure in which RuO_2 and NO_2 interact with each other through two symmetric covalent bonds (1.316 Å) between O_{RuO_2}–N_{NO_2}, and Ru–O_{NO_2}. However, the bond distance N–O (1.191 Å) remains similar to its counterparts in nitrogen dioxide (1.199 Å). The bond angle θ(O-N-O) decreases by ca. 9°. These results suggest that the RuO_2 electrons are the ones mostly in-
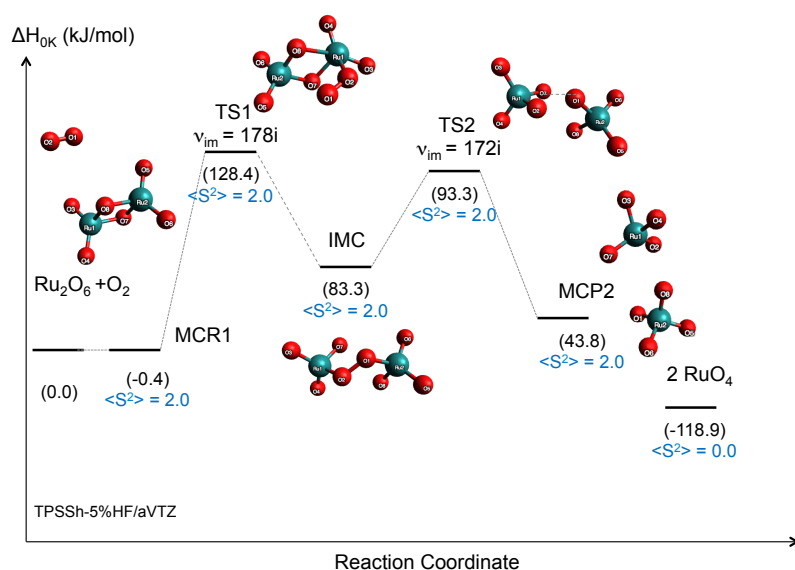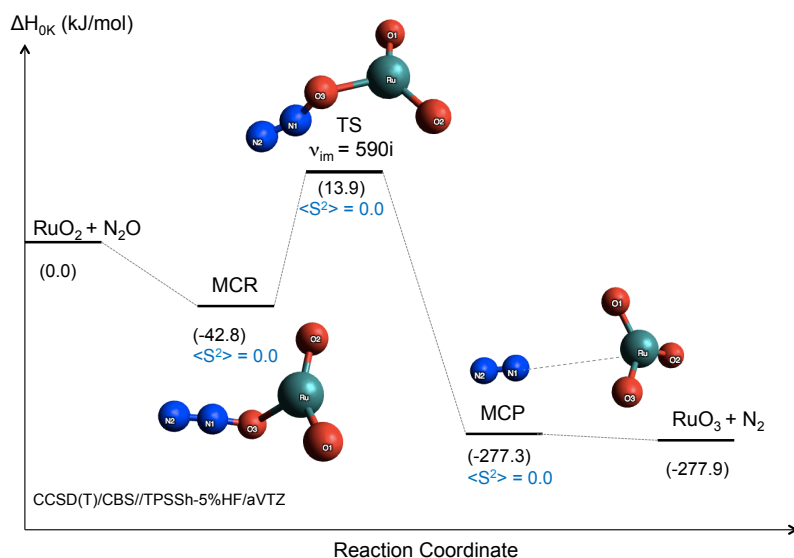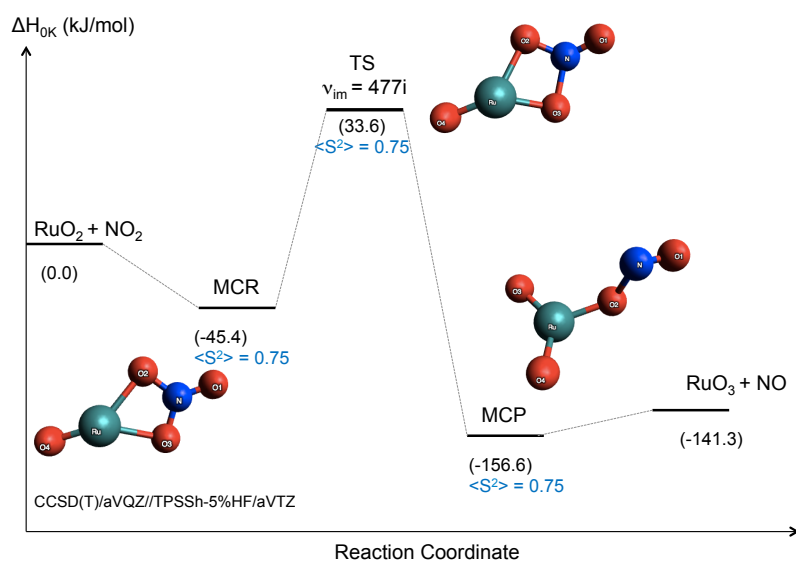
Figure 6.8: Reaction profile at 0 K calculated at the CCSD(T)/CBS//TPSSh-5%HF/AVTZ level of theory for reaction $RuO_2 + NO_2 \longrightarrow RuO_3 + NO$ with schematic representations of the intermediate species involved.
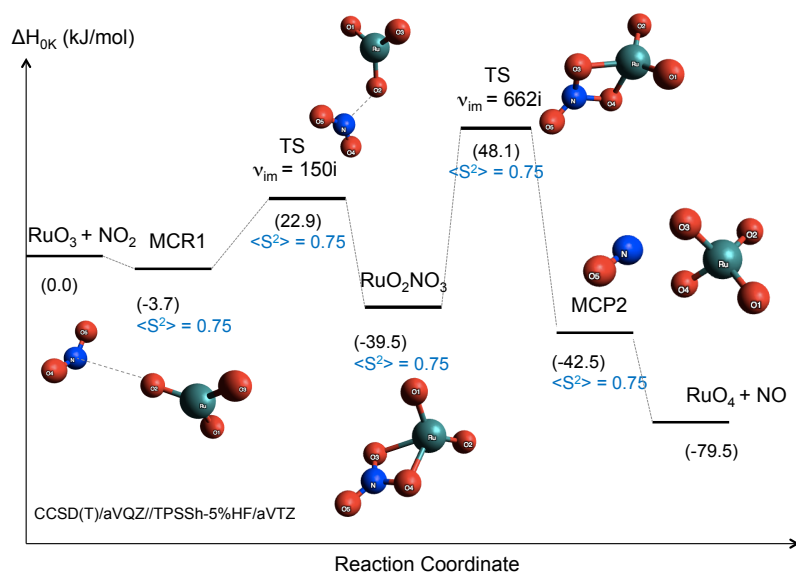
Figure 6.9: Reaction profile at 0 K calculated at the CCSD(T)/CBS//TPSSh-5%HF/AVTZ level of theory for reaction $RuO_3 + NO_2 \longrightarrow RuO_4 + NO$-path1, with schematic representations of the intermediate species involved.
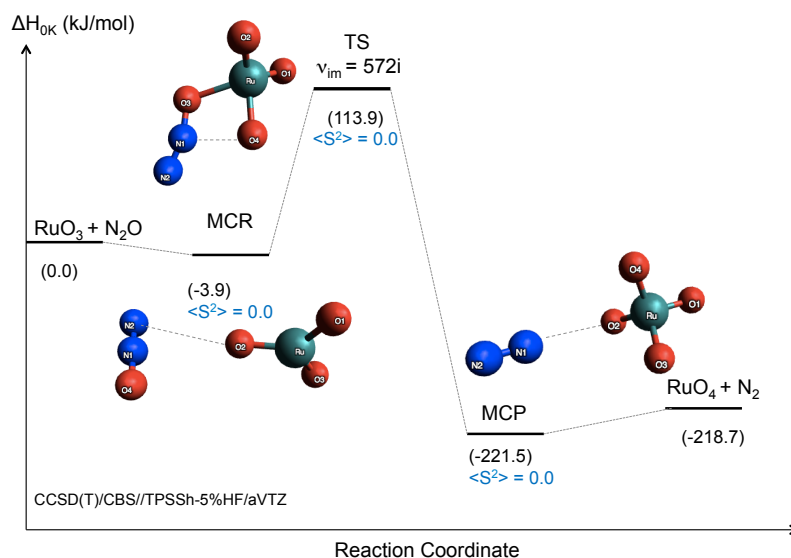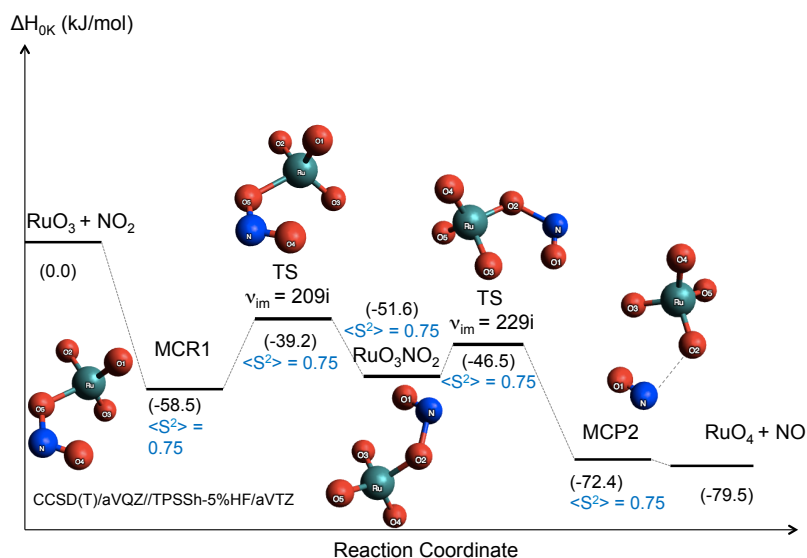
Figure 6.10: Reaction profile at 0 K calculated at the CCSD(T)/CBS//TPSSh-5%HF/AVTZ level of theory for reaction $RuO_3 + NO_2 \longrightarrow RuO_4 + NO$-path2, with schematic representations of the intermediate species involved.

Table 6.8: Structural parameters (bond lengths r are Å) imaginary vibrational frequency (cm^{-1}), and ZPE (kJ mol^{-1}), for the transition state and molecular complexes calculated at the TPSSh-5%HF/aVTZ level of theory, involved in the reaction $RuO_2 + NO_2 \longrightarrow RuO_3 + NO$

Parameters	MCR (6.2c)	TS (6.2c)	MCP (6.2c)
r(N-O)	1.191	1.175	1.145
$r(Ru-O_{NO_2})$	1.316	1.866-1.988	
$r(Ru-O_{NO})$			1.693
r(Ru-O)	1.648	1.661	1.673-1.847
θ(O-N-O)	124.8	124.7	110.8
θ(O-Ru-O_{NO_2})	93.0	72.9	
θ(O-Ru-O_{NO})			114.8
θ(O-Ru-O)		139.7	128.8
ν_{im}		472**i**	
ZPE	46.8	39.8	38.2

volved in these two symmetric bridging bondings in this complex; this is confirmed by the reduced Ru-O bond lengths of 1.648 Å, and the θ(O-Ru-O) bond angle of 140.2°, by comparison to the equilibrium geometric values in RuO_2 species. The molecular complex product associated with the formation of trioxide presents a Ru-O bond length lying between 1.692 and 1.847 Å, and a θ(O-Ru-O) bond angle of 128.8°, slightly larger than those related to the RuO_3 compound. In opposite, the N-O bond length is decreased by 0.368 Å from its equilib-

Table 6.9: Structural parameters (bond lengths r are Å) imaginary vibrational frequency (cm^{-1}), and ZPE (kJ mol^{-1}), for the transition state and molecular complexes calculated at the TPSSh-5%HF/aVTZ level of theory, involved in the reaction $RuO_3 + NO_2 \longrightarrow RuO_4 + NO$- path 1

Parameters	MCR (6.2d-P1)	TS1 (6.2d-P1)	RuO_2NO_3	TS2 (6.2d-P1)	MCP (6.2d-P1)
r(N-O)	1.197-1.200	1.184-1.188	1.184	1.183	1.125
r(Ru-O$_{NO_2}$)	4.008	3.523	2.109	1.910	
r(Ru-O)	1.687	1.686 -1.727	1.689	1.693	1.694 - 1.735
r(N-O$_{RuO_3}$)	2.893	2.13	1.134	1.402-1.483	
r(N-O$_{RuO_4}$)					2.198
θ(O-N-O)	134.7	137.6	124.2	125.3	
θ(O-Ru-O$_{NO_2}$)	104.0	103.8	62.3	70.9	
θ(O$_{RuO4}$-N- O$_{RuO4}$)					71.7
θ(O-Ru-O)	119.8-120.3	117.9-123.4	102.6-124.8	109.7-120.9	95.7-115.7
ν_{im}		150i		662i	
ZPE	44.6	47.2	54.2	48.0	

Table 6.10: Structural parameters (bond lengths r are Å) imaginary vibrational frequency (cm^{-1}), and ZPE (kJ mol^{-1}), for the transition states and molecular complexes calculated at the TPSSh-5%HF/aVTZ level of theory, involved in the reaction $RuO_3 + NO_2 \longrightarrow RuO_4 + NO$-path2

Parameters	MCR (6.2d-P2)	TS1 (6.2d-P2)	RuO_3NO_2	TS2 (6.2d-P2)	MCP (6.2d-P2)
r(N-O)	1.178-1.421	1.204-1.313	1.133	1.126	1.137
r(Ru-O$_{NO_2}$)	1.931	2.028	1.843		
r(O$_{RuO_4}$ -N$_{NO}$)			1.668	1.796	2.358
r(Ru-O)	1.688-1.725	1.685-1.723	1.692-1.733	1.693-1.728	1.696-1.711
θ(O-N-O)	114.8	114.5	115.0		
θ(O-Ru-O$_{NO_2}$)	109.3	115.9	100.6		
θ(Ru-O-N$_{NO}$)			123.9	119.7	114.9
θ(O-Ru-O)	109.7-121.5	108.9-120.9	108.0-120.1	107.7-116.7	106.7-110.7
ν_{im}		209i		229i	
ZPE	47.1	47.5	47.4	45.6	46.2

rium distance in NO species. These results are induced by the highly covalent bond between O$_{RuO_3}$ and N atoms of 1.693 Å, to stabilise RuO_3 and NO within MCP species. The TS (6.2c) found with an imaginary frequency of 477i cm^{-1} connects the MCR and MCP species. These intermediate complexes are found energetically more stable than the associated reactants and products, as shown in Fig. 6.8: the MCR one lies below reactants by ~ 45 kJ mol^{-1}, and the MCP one by ~ 16 kJ mol^{-1}. This confirms that the located TS (6.2c) ensures the mechanism to form RuO_3 and NO species starting from RuO_2 and NO_2 compounds. However, the TS barrier is larger by about 20 kJ mol^{-1} than the the one in reaction 6.2a, with N_2O species. This implies that this reaction will be energetically less favoured at 0 K.

For the formation of RuO_4 in reaction 6.2d, the two parallel mechanisms involve both two-step mechanisms, as observed for reaction 6.1d. The connexion of MCR(6.2d-P1) to intermediate RuO_2NO_3 species by TS1(6.2d-P1) corresponds to the formation of a ring-like structure between N, O_{NO_2}, Ru, and O_{RuO_3} atoms. The molecular complex RuO_2NO_3, which portrays a nitrogen trioxide combined with a ruthenium dioxide, reveals geometric parameters for N-O bond length (1.198 Å) and O-N-O bond angle (132.2°), smaller than their counterparts in NO_3 (1.238 Å and 120°, respectively [6]), and closer to those featuring in NO_2. In path 2, the TS1(6.2d-P2) ensures the bonding between O_{NO_2} to metallic centre of RuO_3, to form intermediate species RuO_3NO_2. The latter complex presents Ru-O and N-O bond lengths slightly longer to those of RuO_3 and NO_2. For the second step-mechanism, the breaking of the symmetric bondings between $O_{RuO_3} - N$, and $Ru - O_{NO_2}$, the shrinkage of Ru-O bonds, and finally the elongation of Ru-N bond distance, is ensured by TS2 (6.2d-P1), to form the $RuO_4 \cdots NO$ product complex. The TS2 (6.2d-P2) corresponds to the breaking of O_{RuO_4} -N_{NO} bonding in the intermediate complex RuO_3NO_2. This step leads to the formation of MCP(6.2d-P2) species, which has θ(O-Ru-O)(~108.7°) and r(Ru-O)(~1.702 Å) values close to those of RuO_4. This result contrasts with the ones obtained for MCP(6.2d-P1) system, which presents geometric parameters for θ(O-Ru-O)(~105.7°) and r(Ru-O)(~1.714 Å) slightly larger. Theses results are corroborated by the relative energies at 0 K , which are above products by 37 and 7.1 kJ mol^{-1} for MCP(6.2d-P1) and MCP(6.2d-P2), respectively. The highest TS2(6.2d-P1) barrier had relative energy above the reactants equal to ~50 kJ mol^{-1}, twice as small as those determined in reaction (6.2b) and (6.1d). The TS1(6.2d-P2) barrier, which is the highest barrier in reaction path 2, is below the reactants, and above the MCR(6.2d-P2) by ~19.3 kJ mol^{-1}. The latter had relative energy of ~-58.5 kJ mol^{-1} below the reactants. The reaction (6.2d) path 2 is found to be the one favoured to form RuO_4 in NPP SA conditions, in contrast to the thermodynamic calculations predicted by Gibbs free energies of reaction in Fig.D.1(b), which indicated that the reaction with nitrous oxide should be more spontaneous than the one with nitrogen oxide. The kinetic parameters of selected reaction pathways are investigated in next part.

6.4   Kinetic parameters

The calculations of the kinetic parameters were performed for reactions pathways involving N_2O and NO_2 species. Mechanisms imply dimer oxide to form RuO_4 were also investigated but presented in Appendix D (Tables D.1 and D.2) as the level of theory used for this reaction is not as accurate as the one used for reaction with N_2O and NO_2 molecules. For the formation of RuO_4 from NO_2 oxidation, only reaction path 2 results is presented. Those related to reaction path 1 are shown in Tables D.3 and D.4 of Appendix D. The extraction of the information from Gaussian output files and rate constant calculations over 250-2500 K were performed using the GPOP program [8]. The rate constants and Arrhenius fits are provided in following subsections.

6.4.1 Constant rates

The calculations of the temperature dependence of the rate constants have been performed at the CCSD(T)/CBS//TPSSh-5%HF for N_2O reactions and at the CCSD(T)/aVQZ//TPSSh-5%HF for the NO_2 reactions, including the zero point energies (ZPE). Their values are listed in Table 6.11, at different temperatures (250, 300, 400, 600, 800, and 1000 K). The computed rate constants related to the formation of ruthenium trioxide reveal that the oxidation of RuO_2 by N_2O is more favourable at higher temperatures, as we observed an increasing of the displayed values range from 10^{-16} at 250 K to 10^{-12} at 1500 K. The oxidation of RuO_2 by NO_2 shows a similar trend, with values varying from 10^{-22} to 10^{-15}. These results seem to reflect that the mechanism involving the nitrogen dioxide is slower than the one with the nitrous oxide, confirming the reactions profiles curves depicted in Fig. 6.8, revealing a higher TS barrier in reaction 6.2c, as compared to reaction 6.2a. The formation of tetroxide presents faster rate

Table 6.11: Rate constants in cm^3 molecule^{-1} s^{-1}, calculated at the CCSD(T)/aVQZ//TPSSh-5%HF level of theory.

Reactions		Temperature (K)							
		250	300	400	600	800	1000	1300	1500
Formation of RuO$_3$									
RuO$_2$ + N$_2$O $\longrightarrow$ RuO$_3$ + N$_2$		3.50×10^{-16}	1.08×10^{-15}	5.30×10^{-15}	3.75×10^{-14}	1.29×10^{-13}	3.12×10^{-13}	8.28×10^{-13}	1.37×10^{-12}
RuO$_2$ + NO$_2$ $\longrightarrow$ RuO$_3$ + NO		3.46×10^{-22}	4.83×10^{-21}	1.58×10^{-19}	7.5×10^{-18}	6.83×10^{-17}	3.02×10^{-16}	1.42×10^{-15}	3.08×10^{-15}
Formation of RuO$_4$									
RuO$_3$ + N$_2$O $\longrightarrow$ RuO$_4$ + N$_2$		1.07×10^{-37}	8.86×10^{-34}	8.16×10^{-29}	1.05×10^{-23}	4.77×10^{-21}	2.16×10^{-19}	8.48×10^{-18}	4.65×10^{-17}
RuO$_3$ + NO$_2$ $\longrightarrow$ RuO$_4$ + NO	TS1	2.53×10^{-07}	1.35×10^{-08}	4.03×10^{-10}	1.71×10^{-11}	4.59×10^{-12}	2.44×10^{-12}	1.63×10^{-12}	1.48×10^{-12}
	TS2	2.45×10^{-05}	6.93×10^{-07}	9.73×10^{-09}	2.03×10^{-10}	3.90×10^{-11}	1.70×10^{-11}	9.47×10^{-12}	7.92×10^{-12}

constants with increasing temperatures in the oxidation of RuO_3 by N_2O, with values varying from 10^{-37} to 10^{-17}. For reaction 6.2d, the rate constants are slow down with increasing temperatures, varying from 10^{-05} to 10^{-12} (TS2). We observe differences of several orders of magnitude at lower temperatures between the two oxidation reactions. The oxidation by the nitrogen dioxide is faster than the one with the nitrous oxide, as predicted by the reaction enthalpies profiles in Fig. 6.7, showing a higher TS barrier for the reaction 6.2b, as compared to reaction 6.2d.

6.4.2 Arrhenius parameters

The rate constants calculated at CCSD(T)/CBS level of theory for N_2O reactions and CCSD(T)/aVQZ for NO_2 reactions were fitted with the modified three-parameters Arrhenius equation of the form $k(T) = B \times T^n \exp(-E_a/RT)$. The values obtained for the pre-exponential factors B, activation energies (Ea), and n coefficients are reported in Table 6.12.

The negative values of the activation energies in reaction 6.2d-P2 underline that the limiting step is from MCR system to overcome TS1 barrier. In fact this species is more stable than the reactants. The above equations allowed us to derive $k(298K)$ values presented in Table 6.12. The values of $k(298K)$ reflect the previous trends, concerning the formation of trioxide and tetraoxide species. We compared the theoretical results with experimental tests described in Chapter 2, Section 2.3.3.2.

Table 6.12: Arrhenius parameters calculated over the temperature range 250–2500 K at the geometries at the CCSD(T)/aVQZ//TPSSh-5%HF level of theory.

Formation of RuO_3	B^a	n	E_a^b	$k(298K)^a$
$RuO_2 + N_2O \longrightarrow RuO_3 + N_2$	2.21×10^{-21}	2.85	8.0	9.79×10^{-16}
$RuO_2 + NO_2 \longrightarrow RuO_3 + NO$	4.01×10^{-24}	3.09	26.9	3.39×10^{-21}
Formation of RuO_4	B^a	n	E_a^b	$k(298K)$
$RuO_3 + N_2O \longrightarrow RuO_4 + N_2$	5.23×10^{-22}	2.72	106.4	6.14×10^{-34}
$RuO_3 + NO_2 \longrightarrow RuO_4 + NO$ (TS1)	6.43×10^{-24}	3.01	-43.9	8.92×10^{-09}
$RuO_3 + NO_2 \longrightarrow RuO_4 + NO$ (TS2)	8.78×10^{-24}	3.19	-51.5	7.27×10^{-07}

^{a} in cm^3 molecule^{-1} s^{-1}, ^{b} in kJ mol^{-1}

Table 6.13: Measurement of transported Ru fraction in function of carrier gas in VTT tests[9]. The model primary circuit are stainless steel tube or alumina tube samples. The gradient temperature varies from 1300/1500/1700 K to ca. 300 K.

Atmosphere (T)	Ru released rate (mg/min.)	Transported $RuO_{2(s)}$ (% Ru released)	Transported $RuO_{4(g)}$ (% Ru released)
Humid Air (1300 K)	0.3 ± 0.0	9.1 ± 0.5	0.0 ±0.0
Humid Air (1500 K)	3.2 ± 0.2	12.8 ± 0.6	0.0 ±0.0
Humid Air (1700 K)	20.3 ± 1.0	14.3 ± 0.7	0.0 ±0.0
Humid Air + NO_2 (1300 K)	0.3 ± 0.0	0.0 ± 0.0	13.9 ±0.7
Humid Air + NO_2 (1500 K)	3.2 ± 0.2	4.0 ± 0.2	9.9 ±0.5
Humid Air + NO_2 (1700 K)	20.3 ± 1.0	20.2 ± 1.0	0.0 ±0.0
Humid Air + N_2O (1300 K)	0.3 ± 0.0	6.0 ± 0.3	0.1 ±0.0
Humid Air + N_2O (1500 K)	3.2 ± 0.3	25.4 ± 1.7	0.1 ±0.0
Humid Air + N_2O (1700 K)	20.3 ± 1.0	15.5 ± 0.8*	0.0 ±0.0*

* measured for T = 1570 K

6.4.3 Comparison with experimental results

Table 6.13 presents experimental results reported in Kajan thesis [9], a part of the VTT programme[10]. The tests consisted in reproducing NPP SA conditions of temperature and atmosphere, and introduced in carrier gas percentage of air radiolysis products precursors, namely HNO_3, N_2O, and NO_2. The RuO_2 powder was vaporised from the crucible at 3 different temperatures (1300, 1500 and 1700 K). It is transported through primary circuit model tube with thermal a gradient profile, reaching an outlet temperature around 300 K. This experiment showed that the formation of $RuO_4$is favoured with atmosphere containing NO_2 precursors. In fact, the fraction of gaseous RuO_4 evidenced at the outlet of the facility was

about 14% with NO_2 precursors against 0.13% with N_2O ones, about the overall Ru released rate, at 1300 K. The collected gaseous fraction decreases with higher temperatures with NO_2 precursors. These observations are consistent with the theoretical calculations discussed in the previous sections.

According to the calculated kinetic parameters in this section, the formation of tetroxide presents kinetic limitations, that can explain in part the difficulties to quantify this species in severe accident code models, as our experimental conditions did not include atmosphere radiolysis (where the reaction with O radical will be spontaneous and dominant).

6.5   Conclusions

This chapter clarifies the mechanisms allowing the formation of RuO_3 and RuO_4 species, which were found as the dominating Ru gaseous compounds under severe accident conditions at NPP. Calculations of Gibbs free reaction energies for some possible mechanisms thought to occur in the gas phase to form the previous Ru compounds lead us to conclude that oxidation of trioxide by H_2O or OH species to form tetroxide is thermodynamically unfavourable. Oxidation of dimer species by O_2 gas is found thermodynamically favourable, however such species are in negligible amount in the conditions of a NPP severe accident. Air radiolysis products formed by the radiation of FPs, appear to be the most suitable reaction pathways to form RuO_4, in a case of severe accident conditions, (after the reaction with O radical). Current modelling of START tests do not include kinetic limitations, thus leading to overestimate the RuO_4 amount with accident code simulations. The overall provided kinetic parameters will hopefully soon be implemented in the models to evaluate their influences on the quantification of RuO_4 fraction at the breach of primary circuit sampling tests.

References

(1)   Van Dorsselaere, J. P.; Seropian, C.; Chatelard, P.; Jacq, F.; Fleurot, J.; Giordano, P.; Reinke, N.; Schwinges, B.; Allelein, H. J.; Luther, W. The ASTEC Integral Code for Severe Accident Simulation. *Nucl. Technol.* **2009**, *165*, 293–307.

(2)   Leroy, O.; Ohnet, M.; Planteur-Kieffer, S. Study of the Ruthenium transport under prevailing conditions in the primary circuit in case of a PWR severe accident., ERMSAR 2015, Marseille, March 24-26, 2015.

(3)   Souvi, S. Modélisation par ASTEC/SOPHAEROS des principaux essais START: Transport des espéces Ruthénium dans un milieu oxydant H2O/Air., Internal Communication, 2016.

(4)   Frisch, M. J. et al. Gaussian 09 Revision C.01., Gaussian Inc. Wallingford CT, 2009.

(5)   Huber, K.; Herzberg, G., *Molecular Spectra and Molecular Structure. IV. Constants of Diatomic Molecules*; Van Nostrand Reinhold Co.: 1979.

(6)   Herzberg, G. Electronic spectra and electronic structure of polyatomic molecules., New York, 1966.

(7)   NIST Diatomic Spectral Database., www.physics.nist.gov/PhysRefData/MolSpec/Diatomic/index.html.

(8)   Miyoshi, A. GPOP software revision 2013.07.15., available from the author.

(9)   Kajan, I.; Kärkelä, T.; Auvinen, A.; Ekberg, C. Ruthenium chemistry and transport in a RCS due to air radiolysis products., submitted to J. Radioanalytical and Nuclear Chem., 2016.

(10)   Kajan, I.; Kärkelä, T.; Tapper, U.; Johansson, L.-S.; Gouëllo, M.; Ramebäck, H.; Holmgren Stina andAuvinen, A.; Ekberg, C. Impact of Aerosols on the Transport of Ruthenium in the primary circuit of nuclear power plant., VTT Processes, Report No. AFT/NKS-R(14)111/1, Finland, 2015.

7

7.1   Sum-up of the main results

Consolidation of Ru oxides database

The thermodynamic properties of Ru, RuO, RuO$_3$, and RuO$_4$gaseous species in existing database comport large uncertainties, in main part due to assumptions on the structural properties of these compounds. Quantum chemistry calculations provided reliable geometric parameters, obtained at the DFT level (U-TPSSh-5%HF). We investigated the fundamental ground states thanks to highly correlated wave-function based approaches (CCSD(T), CAS-SCF, MRCI, CASPT2)). It appears that these compounds have a negligible amount of multi-reference character, despite their large number of electrons. The results stated the ground state of Ru to be a ^{5}F and the one of RuO a $^5\Delta$. RuO$_2$ has singlet multiplicity like RuO$_3$ and RuO$_4$. The thermodynamic properties of Ru oxides were obtained at the CCSD(T)/CBS//TPSSh-5% HF level of theory. The calculations predicted the standard enthalpies of formation Ru and RuO$_2$ (638 ± 2 and 140 ± 1 kJ mol^{-1}) in good agreement with the tabulated values in literature (640 ± 4 and 136 ± 10 kJ mol^{-1}). The predicted standard enthalpies of formation for RuO and RuO$_3$ species (420 ± 1 and -51 ± 1 kJ mol^{-1}) were revised.

Extension of gaseous Ru database

Oxyhydroxides species may play a role in the transport of Ru through RCS. In existing Ru database, only two oxyhydroxides were taking into account, namely RuO$_3$(OH) and RuOH species. Their standard enthalpy of formation comports large uncertainties that can amount to 100 kJ mol^{-1}. We thus investigate all possible stoichiometries of the RuO$_x$H$_y$ species, involving oxides, hydroxides and water ligands, and for each stoichiometry all possible conformers were studied. More than 30 oxyhydroxides gaseous species were determined. The

molecular properties were obtained by combining DFT (TPSSh-5%HF) geometries, partition functions and CCSD(T) electronic energies. The analysis of the chemical bonds within these species reveal that ruthenium forms both a covalent bond with the oxide and hydroxide ligands, and an ionic bond with the water ligands. To determine the standard thermodynamic properties of ruthenium oxyhydroxides gaseous species, we only consider the most stables isomers. The calculated standard enthalpies of formation differ from the literature values, by 10 up to 100 kJ mol^{-1}, the higher the oxidation state is the larger the difference. We also calculated the thermodynamic properties of two Ru dimers species, Ru_2O_4 and Ru_2O_6, as well as an isomer of ruthenium tetroxide O_2RuO_2. The standard enthalpies of formation of O_2RuO_2 and Ru_2O_6 were found exothermic (-50 and -276 kJ mol^{-1}), and the one of Ru_2O_4 endothermic (70 kJ mol^{-1}).

Determination of kinetic parameters

Experiments related to Ru transport through RCS concluded that kinetic limitations govern the formation and transport of Ru gaseous compounds. Investigations on reaction pathways leading to the formation of Ru trioxide and tetroxide reveal that oxidation by air radiolysis products such as N_2O and NO_2 are the most suitable reacting agents to form of RuO_3 and RuO_4 in the gaseous phase, in conditions relevant to nuclear power plant accident, without O radical. Reaction pathways involving H_2O or OH species were found not spontaneous. These conclusions corroborate experimental results which concluded that air radiolysis products in a gas stream affect the chemical composition of transported ruthenium, even in very low concentrations (50 ppm).

7.2   Main conclusions

Thanks to accurate quantum chemistry calculations, the Ru database has been consolidated and extended:

- the uncertainties on standard enthalpies of Ru oxides are reduced to less than 2 kJ mol^{-1}.

- the database was extended with the addition of 20 oxyhydroxides species, but with only two stable species in severe accident conditions.

The use of the herein highly correlated quantum chemistry computed thermodynamic data allows us to revise with a high degree of confidence the gaseous ruthenium chemical speciation. At thermodynamic equilibrium, the dominating Ru gaseous species were established to be:

- RuO_4 species at temperatures below ∼ 1000 K

- RuO_3 species the temperatures range from ∼ 1000 to ∼ 2000 K.

At higher temperatures, ruthenium dioxide, oxide and even Ru in gaseous phase are formed. The ruthenium oxyhydroxides species are formed only in negligible amounts, unlike the conclusions of previous thermodynamic calculations studies.

The derived kinetic parameters allow us to confirm that the transport of Ru gaseous compounds presents kinetic limitations, which can explain in part the overestimated fraction obtained with the simulations by accident code, assuming the thermodynamic equilibrium of Ru gaseous compounds.

7.3 Perspectives

The obtained kinetic parameters will be implemented in ASTEC, a severe accident simulation code, to evaluate their impact on the simulation of transported Ru species through RCS in NPP severe accident conditions.

In a following step, it will be interesting to study the chemical interactions between Ru species such as RuO_3, RuO_4, or either dimer species with sampling surface (quartz tube, SS, alumina) using quantum chemistry calculations. Indeed, small-scale tests are not representative of the ratio volume/surface, and interactions with surface should be better addressed.

In complement, the OCDE/STEM2 project is investigating the Ru transport in the RCS with an investigation of some parameters (gas content, thermal gradient, analytical, source of Ru, etc.). All these tests will be used to check the modelling and if needed to make some improvements. After being qualified the ASTEC modelling could be applied to predict more accurately severe accident scenarios.

A.1 Energy and partition function contributions

Translation degrees of freedom, ϵ_{trans} and q_{trans} are equal to:

$$
\epsilon_n = \frac{n^2 h^2}{8\pi^2 M}
$$
$$
q_{trans} = \left(\frac{2\pi M k_B T}{h^2}\right) V
$$

(A.1)

where n is the quantum number of the given state and M the total molecular mass. The rotation of the molecule is assumed to occur with a fixed geometry:

$$
\epsilon_J = J(J+1)\frac{h^2}{8\pi^2 \boldsymbol{I}}
$$
$$
q_{rot} = \frac{8\pi^2 I k_B T}{h^2 \sigma_r}
$$

(A.2)

where J is a quantum number running from zero to infinity, $\boldsymbol{I}$ is the moment of inertia and σ_r symmetry index equal to 2 for a homonuclear system and 1 for a heteronuclear system.

The vibrational degrees of freedom are decoupled in the normal coordinate system with the harmonic oscillator approximation, thus we obtain:

$$
\epsilon_n = (n+\frac{1}{2})h\nu
$$
$$
q_{vib} = \frac{e^{-h\nu/2k_B T}}{1 - e^{-h\nu/k_B T}}
$$

(A.3)

149

where n is a quantum number stands from zero to infinity and v is the vibrational frequency.

Regarding electronic degrees of freedom, the electronic partition function involves a sum over electronic quantum states with their degeneracy g_i. In almost all molecules, the energy difference between the ground and excited states is large compared with $k_B T$, which means that only the first term (the ground state energy) in the partition function summation is important. We thus obtain :

$$q_{elec} = \sum_{i=0}^{\infty} g_i e^{-\epsilon_i/k_B T} = g_0 e^{-\epsilon_0/k_B T} \tag{A.4}$$

If we set the energy of the reactant ground state to zero, the expression simplifies to:

$$\begin{aligned} q_{elec}^{reactant} &= g_0 \\ q_{elec}^{TS} &= g_0 e^{-\Delta E^{\ddagger}/k_B T} \end{aligned} \tag{A.5}$$

where $\Delta E^{\ddagger}$ is the difference in electronic energy between the reactant and TS, g_0 is the electronic degeneracy of the (ground state) wave function.

A.2 Enthalpy and entropy contributions

Given the partition functions, the enthalpy and entropy contributions for one mole of non linear molecules are:

$$\begin{aligned} H_{trans} &= \frac{5}{2}RT \\ H_{rot} &= \frac{3}{2}RT \\ H_{vib} &= R \sum_{i=1}^{3N-6(5)} \left(\frac{hv_i}{2k_B} + \frac{hv_i}{k_B} \frac{1}{e^{hv_i/k_B T}-1} \right) \\ H_{elec}^{reactant} &= 0 \\ H_{elec}^{TS} &= \Delta E^{\ddagger} \\ S_{trans} &= \frac{5}{2}R + R\ln\left(\frac{V}{N_A}(\frac{2\pi M k_B T}{h^2})^{3/2} \right) \\ S_{rot} &= R\left(\frac{3}{2} + \ln\left(\frac{\sqrt{\pi}}{\sigma})(\frac{8\pi^2 k_B}{h^2})^{1/2} \sqrt{I_1 I_2 I_3}T^{3/2} \right) \right) \\ S_{vib} &= R \sum_{i=1}^{3N-6(7)} \left(\frac{hv_i}{KT} \frac{1}{e^{hv_i/k_B T}-1} - \ln(1 - e^{-hv_i/k_B T}) \right) \\ S_{elec}^{reactant} &= S_{elec}^{TS} = R\ln g_0 \end{aligned} \tag{A.6}$$

For linear systems, rotational contributions are defined as follows:

$$H_{rot}(linear) = RT$$

$$S_{rot}(linear) = R\left[1 + ln\left(\frac{8\pi^2 \boldsymbol{I} k_B T}{\sigma h^2}\right)\right]. \tag{A.7}$$

B.1 Ru compounds electronic spectra

B.1.1 Ru

Figure B.1: Ru electronic spectra derived with MCSCF calculations. Fundamental energy is equal to -93.80139924 au for the 7 degenerated states $^5\Delta A_g$, $^5\Delta B1_g$, $^5\Sigma B1_g$, $^5\Phi B2_g$, $^5\Pi B2_g$, $^5\Phi B3_g$ and $^5\Pi B3_g$
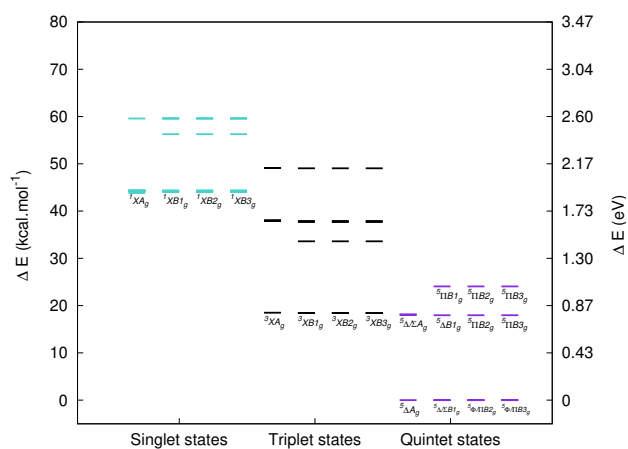
Figure B.2:   Ru electronic spectra derived with MRCI calculations. Fundamental energy is equal to -94.00866876 au for the 7 degenerated states $^5\Delta A_g$, $^5\Delta B1_g$, $^5\Sigma B1_g$, $^5\Phi B2_g$, $^5\Pi B2_g$, $^5\Phi B3_g$ and $^5\Pi B3_g$
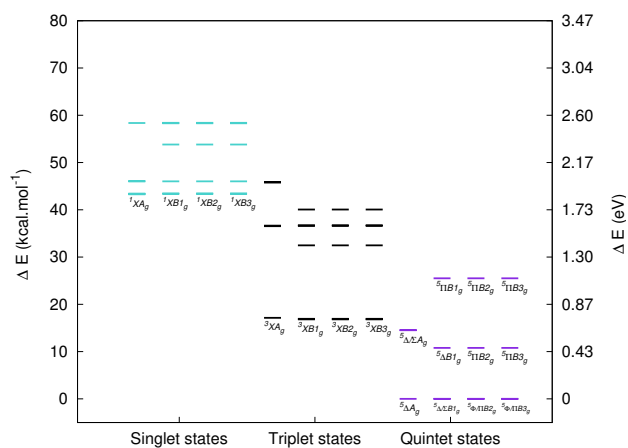
Figure B.3:   Ru electronic spectra derived with CASPT2 calculations. Fundamental energy is equal to -94.00733919 au for the 7 degenerated states $^5\Delta A_g$, $^5\Delta B1_g$, $^5\Sigma B1_g$, $^5\Phi B2_g$, $^5\Pi B2_g$, $^5\Phi B3_g$ and $^5\Pi B3_g$

B.1.2 RuO
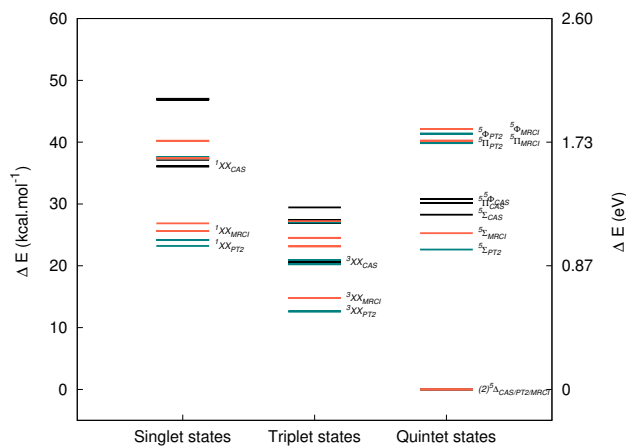
Figure B.4: RuO electronic spectra derived with MCSCF, CASPT2 and MRCI calculations. Fundamental energy of doubly degenerated state $^5\Delta$ is equal to -168.71007012 au, -169.14614294 au and -169.13754268 au in CASSCF, CASPT2, and MRCI+Q theory respectively. Black is for CASSCF states, blue for CASPT2 states and tomato for MRCI states.

B.1.3   RuO$_2$ electronic spectra
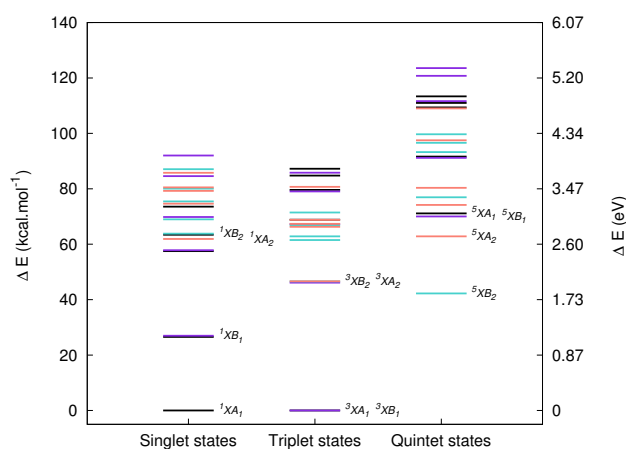
Figure B.5:   RuO$_2$ electronic spectra derived with MCSCF calculations. Fundamental energy is equal to -243.6786587 au in $^1A_1$ state, $^3A_1$ state, and $^3B_1$ state. Black is for A_1 symmetry states, violet for B_1 symmetry states, turquoise for B_2 symmetry states and pink for A_2 symmetry states
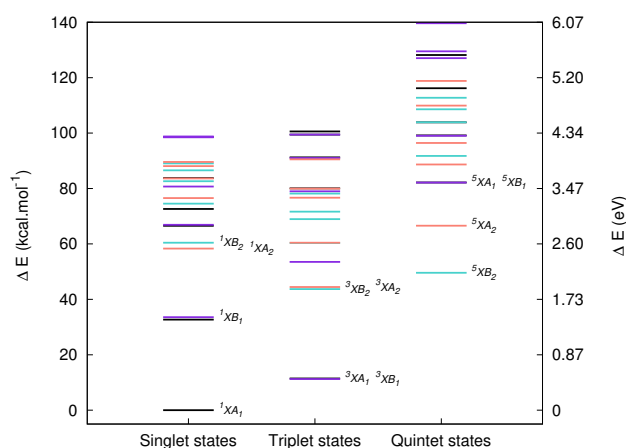
Figure B.6:   RuO$_2$ electronic spectra derived with MRCI calculations, fundamental energy is equal to in -244.3069747 au in $^1A_1$ state. Black is for A_1 symmetry states, violet for B_1 symmetry states, turquoise for B_2 symmetry states and pink for A_2 symmetry states
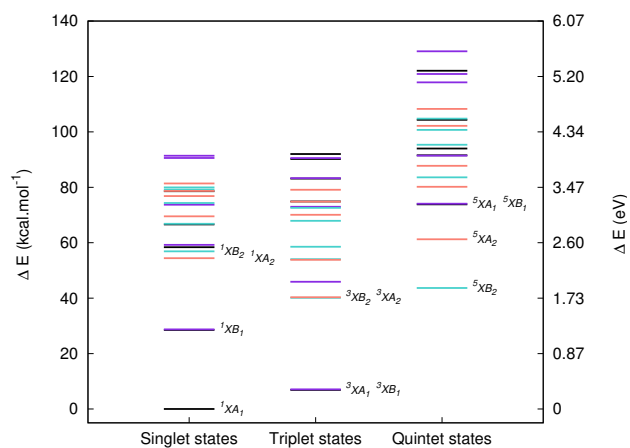
Figure B.7: RuO$_2$ electronic spectra derived with CASPT2 calculations, fundamental energy is equal to in -244.3232158 au $^1A_1$ state. Black is for A_1 symmetry states, violet for B_1 symmetry states, turquoise for B_2 symmetry states and pink for A_2 symmetry states

B.2   Cluster expansions procedures

Table B.1: Direct UHF/CCSD(T) and UDFTBS-UHF/CCSD(T) calculations performed with G09 software.

Species	Method	E_{UHF} [au]	ΔE (UHF)^a [kJ mol^{-1}]	$E_{CCSD(T)}$ [au]	ΔE(CCSD(T) ^{a} [kJ mol^{-1}]
Ru	UHF/CCSD(T)/AVTZ	-93.7928443	-	-93.9903723	
	UHF/CCSD(T)/AVQZ	-93.793437	-1.56	-94.0031567	-33.57
	UHF/CCSD(T)/AV5Z	-93.7936822	-0.64	-94.0079291	-12.53
	UDFTBS-UHF/CCSD(T)/AVTZ	-93.8159914	-	-94.0181158	-
	UDFTBS-UHF/CCSD(T)/AVQZ	-93.8168198	-2.17	-94.0333398	-39.97
	UDFTBS-UHF/CCSD(T)/AV5Z	-93.8169793	-0.42	-94.0392364	-15.48
RuO	UHF/CCSD(T)/AVTZ	-168.6116967	-	-169.1306254	-
	UHF/CCSD(T)/AVQZ	-168.6169848	-13.88	-169.1638278	-87.17
	UHF/CCSD(T)/AV5Z	-168.6185062	-3.99	-169.1756324	-30.99
	UDFTBS-UHF/CCSD(T)/AVTZ	-168.6662858	-	-169.1677708	-
	UDFTBS-UHF/CCSD(T)/AVQZ	-168.6717003	-14.22	-169.2024922	-91.16
	UDFTBS-UHF/CCSD(T)/AV5Z	-168.6733042	-4.21	-169.2150545	-32.98
RuO$_2$	UHF/CCSD(T)/AVTZ	-243.4562694	-	-244.3433707	-
	UHF/CCSD(T)/AVQZ	-243.4674989	-29.48	-244.399320	-146.89
	UDFTBS-UHF/CCSD(T)/AVTZ	-243.4655583	-	-244.3404692	-
	UDFTBS-UHF/CCSD(T)/AVQZ	-243.4766968	-29.24	-244.3962621	-146.48

^{a} Difference in total energies derived at AVXZ and AV(X-1)Z basis set level

B.3   CASPT2 and MRCI ruthenium 5d shell orbital calculations

Table B.2: Computed electronic energy for Ru and RuO with MRCI+Q and CASPT2 method by increase active space with one 5d shell of ruthenium d orbitals.

Species	Method	E_{CASSCF} [au]	E_{corr} [au]	E_{TOT} [au]	Δ (E_{with5d} - $E_{without5d}$) [kJ mol^{-1}]
Ru	CASPT2//AVTZ	-93.84574826	-0.1591779	-94.00492616	-5.814
	CASPT2//AVQZ	-93.84593286	-0.17475689	-94.02068975	-7.276
	CASPT2//AV5Z	-93.8459485	-0.18150167	-94.0274502	-8.069
	CASPT2//CBS	-93.84594998	-0.18857816	-94.03452814	-8.917
	MRCI+Q//AVTZ		-0.16519324	-94.0109415	-11.068
	MRCI+Q//AVQZ		-0.17911219	-94.02504505	-11.725
	MRCI+Q//AV5Z		-0.18454322	-94.03049175	-11.887
	MRCI+Q//CBS		-0.19024135	-94.03619133	-12.04169
RuO	CASPT2//AVTZ	-168.840712	-0.312195308	-169.1529073	-6.271
	MRCI+Q//AVTZ		-0.32129023	-169.1620022	-55.999

B.4 Computational considerations

B.4.1 DFT results

Table B.3: Comparison of computational resources used by DFT TPSSh-5% HF method to derive electronic structure for Ru compounds using G09 -RevC.01 package[1]. Optimized geometries and stabilization for non stable wave function are tabulated with all basis set level.

Species	Method	Nproc	CPU(s)	Disk (GBytes)
Ru	Energy calculation			
	TPSSh-5% HF/AVTZ	8	30	0.01
	TPSSh-5% HF/AVQZ	8	88.4	0.02
	TPSSh-5% HF/AV5Z	8	1242.2	0.05
RuO	Optimization calculation			
	TPSSh-5% HF/AVTZ	8	106.5	0.02
	TPSSh-5% HF/AVQZ	8	1228.3	0.05
	TPSSh-5% HF/AV5Z	8	17816	0.13
	Single point energy in TPSSh-5%HF/AVTZ geometries			
	TPSSh-5% HF/AVQZ	8	311	0.04
	TPSSh-5% HF/AV5Z	8	227083.2	0.11
RuO_2	Optimization calculation			
	TPSSh-5% HF/AVTZ	8	470	0.04
	TPSSh-5% HF/AVQZ	8	7133.9	0.31
	TPSSh-5% HF/AV5Z	8	45961.7	0.24
	Stabilization			
	TPSSh-5% HF/AVTZ	8	2102.6	0.08
	TPSSh-5% HF/AVQZ	8	18129.8	0.21
	TPSSh-5% HF/AV5Z	8	110111.7	0.46
	Single point energy in TPSSh-5%HF/AVTZ geometries			
	TPSSh-5% HF/AVQZ	8	4703.1	0.09
	TPSSh-5% HF/AV5Z	8	29142.7	0.20
	Stabilization			
	TPSSh-5% HF/AVQZ	8	23598.4	0.21
	TPSSh-5% HF/AV5Z	8	94610.7	0.46

B.4.2   HF and MCSCF computational analysis

Table B.4:   Comparison of computational resources used by HF and MCSCF methods to compute electronic energies of Ru compounds using Molpro package [2] for ground state orbitals. Single point calculations were performed using optimized geometries in TPSSh-5%HF/AVTZ.

Species	Method	Nproc	Total CPU (s) [a]	Disk (GB)
Ru	HF/AVTZ	8	1.20	0.28
	HF/AVQZ	8	2.73	0.30
	HF/AV5Z	8	6.55	0.54
	MCSCF/AVTZ	8	1.75	0.04
	MCSCF/AVQZ	8	3.58	0.28
	MCSCF/AV5Z	8	7.94	0.52
RuO	HF/AVTZ	8	1.78	0.34
	HF/AVQZ	8	8.98	1.06
	HF/AV5Z	8	44.11	4.12
	MCSCF/AVTZ	8	5.90	0.14
	MCSCF/AVQZ	8	17.52	1.07
	MCSCF/AV5Z	8	59.82	4.20
RuO_2	HF/AVTZ	8	3.44	0.80
	HF/AVQZ	8	22.43	4.31
	HF/AV5Z	8	140.68	21.78
	MCSCF/AVTZ	8	82.95	0.60
	MCSCF/AVQZ	8	111.54	4.07
	MCSCF/AV5Z	8	261.87	21.51

[a] Total CPU times take into account method and matrix integrals building cost. Average time cost for the MCSCF method is about 0.5 and 7 s to derive Ru and RuO calculations against 3 and 35 s to build the matrix integrals with higher basis set level. For RuO_2 system, the cost time of the MCSCF calculation took at AV5Z basis set level around 2 min and 30 s, similar to the matrix building about 2 min.

B.4.3 Variational methods computational analysis

Table B.5: Comparison of computational resources used by variational methods to derived electronic energy for Ruthenium compounds using Molpro package[2]. Single point energy were performed using optimized geometries in TPSSh-5%HF/AVTZ.

Species	Method	Nproc	Total CPU (s) [a]	Disk (GB)
Ru	MRCI/AVTZ	8	0.47	0.02
	MRCI/AVQZ	8	1.99	
	MRCI/AV5Z	8	29.2	
	ACPF/AVTZ	8	2.01	0.04
	ACPF/AVQZ	8	4.33	0.28
	ACPF/AV5Z	8	9.58	0.52
	AQCC/AVTZ	8	2.15	0.04
	AQCC/AVQZ	8	4.33	0.28
	AQCC/AV5Z	8	9.45	0.52
RuO	MRCI/AVTZ	8	15.10	0.14
	MRCI/AVQZ	8	43.85	1.07
	MRCI/AV5Z	8	127.14	4.20
	ACPF/AVTZ	8	33.73	0.034
	ACPF/AVQZ	8	92.63	1.09
	ACPF/AV5Z	8	248.95	4.23
	AQCC/AVTZ	8	25.17	0.34
	AQCC/AVQZ	8	73.58	1.09
	AQCC/AV5Z	8	209.84	4.22
RuO_2	MRCI/AVTZ	8	5346.98	0.80
	MRCI/AVQZ	8	11316.21	4.46
	MRCI/AV5Z	8	19898.37	22.26
	ACPF/AVTZ	8	13588.73	0.80
	ACPF/AVQZ	8	29190.33	4.46
	ACPF/AV5Z	8	51004.20	22.24
	AQCC/AVTZ	8	9663.29	0.80
	AQCC/AVQZ	8	21602.49	4.46
	AQCC/AV5Z	8	38107.50	22.28

[a] Total CPU times take into account method and matrix integrals building cost. Average time cost of the MRCI calculations is around 0.5 and 44 s to compute Ru and RuO electronic energies, respectively, at AV5Z basis set level. For RuO_2, the MRCI calculation took ca. 2 h. The AQCC and ACPF methods took around 2 min to compute Ru and RuO electronic energies, and 5 h for RuO_2 system, at AV5Z basis set level. Time used to construct the matrix integrals are equal to those discussed in Table B.4.

B.4.4 Perturbation methods computational analysis

Table B.6: Comparison of computational resources used by perturbation theory methods to derive electronic energies of Ru species. Single point energy calculations were performed using optimized geometries in TPSSh-5%HF/AVTZ.

Species	Method[a]	Nproc	CPU (s)[b]	Disk (GB)
Ru	CASPT2/AVTZ	8	1.10	0.04
	CASPT2/AVQZ	8	2.55	0.15
	CASPT2/AV5Z	8	6.71	0.38
	QDNEVPT2-PC/AVTZ	1	7.39	0.03
	QDNEVPT2-PC/AVQZ	1	15.74	0.09
	QDNEVPT2-PC/AV5Z	1	41.19	0.32
RuO	CASPT2/AVTZ	8	8.14	0.23
	CASPT2/AVQZ	8	21.03	0.92
	CASPT2/AV5Z	8	67.15	4.04
	QDNEVPT2-PC/AVTZ	1	92.22	0.16
	QDNEVPT2-PC/AVQZ	1	170.70	0.84
	QDNEVPT2-PC/AV5Z	1	604.05	3.85
RuO_2	CASPT2/AVTZ	8	580.15	0.65
	CASPT2/AVQZ	8	1359.86	4.28
	CASPT2/AV5Z	8	2794.25	21.98
	QDNEVPT2-PC/AVTZ	1	419.37	0.62
	QDNEVPT2 -PC/AVQZ	1	874.12	4.14
	QDNEVPT2-PC/AV5Z	1	3118.62	21.63

[a] CASPT2 calculations were carried out with Molpro package [2]. The QDNEVPT2-PC calculations were performed with one node and a single processor, in two steps with two programs: the CASSCF references states are provided by Molpro software, then the output is coupled with QDINTERFACE program [3], which performed the perturbative excitations. [b] Total CPU times take into account the method and the matrix integrals building cost. To compute Ruand RuOelectronic energies at the AV5Z basis set level, the CASPT2 calculations took less than 0.1 s and 5 s; the QDNEVPT2-PC calculations took 27 s and 7 min, respectively. For RuO_2, the CASPT2 calculation took ca. 41 min at the AV5Z basis set; the QDNEVPT2-PC calculations is in the same order. Time used to construct the matrix integrals are equal to those discussed in Table B.4.

B.4.5   Coupled Cluster methods computational considerations

Table B.7: Comparison of computational resources used by the Coupled Cluster approaches to compute electronic energy for Ru compounds using Molpro package [2]. Single point energy were performed using optimized geometries in TPSSh-5%HF/AVTZ.

Species	Method [a]	Nproc	Total CPU (s) [b]	Disk (GB)
Ru	UCCSD(T)/AVTZ	8	0.70	0.12
	UCCSD(T)/AVQZ	8	2.46	0.19
	UCCSD(T)/AV5Z	8	7.92	0.46
	MR-UCCSDT/AVTZ	8	338.24	0.03
	MR-UCCSDT/AVQZ	8	2258.92	0.09
	MR-UCCSDT/AV5Z	8	4779.75	0.32
	MR-UCCSDTQ/AVTZ	8	63351.54	0.03
	MR-UCCSDTQ/AVQZ	8	850141.56	0.09
	MR-UCCSDTQ/AV5Z	8	1637063.55	0.32
RuO	UCCSD(T)/AVTZ	8	8.52	0.47
	UCCSD(T)/AVQZ	8	448.57	1.54
	UCCSD(T)/AV5Z	8	230.08	5.47
	MR-UCCSDT/AVTZ	8	103040.76	0.16
RuO_2	CCSD(T)/AVTZ	8	9.86	0.74
	CCSD(T)/AVQZ	8	70.14	4.78
	CCSD(T)/AV5Z	8	361.83	24.11
	BCCD(T)/AVTZ	8	20.74	0.74
	BCCD(T)/AVQZ	8	167.59	4.79
	BCCD(T)/AV5Z	8	980.38	24.12
	MR-CCSDT/AVTZ	8	813088.12	0.62

[a] Total CPU times take into account the method and the matrix integrals building cost. To compute Ruand RuOelectronic energies at the AV5Z basis set level, the UCCSD(T) calculations took 0.70 s and 2 min, respectively; the UCCSDT calculation a computational cost at least 10 times higher than the UCCSD(T) calculations. For RuO_2 species, the CCSD(T) calculation took 3 min at the AV5Z basis set level; The BCCD(T) calculation took 7 min. The UCCSDT calculation a the AVTZ basis set took around 15 days. Time used to construct the matrix integrals are equal to those discussed in Table B.4.

B.4.6   Computational resources with spin-orbit correction
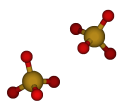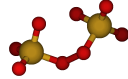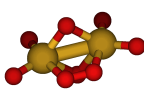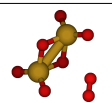
Table B.8:   Comparison of computational resources used by relativistic calculations RASSI-SO to compute electronic energies for Ru compounds using Molpro package [2] and Molcas package. Single point energy calculations were performed using optimized geometries in TPSSh-5%HF/AVTZ.

Species	Method	Nproc	CPU (s)	Disk (GB)
Ru	Spin-orbit calculations with pseudo-potentials basis set using Molpro Package			
	RASSI-SO/MCSCF/AVTZ	4	47.92	0.02
	RASSI-SO/MCSCF/AVQZ	4	32.24	0.07
	RASSI-SO/MCSCF/AV5Z	4	69.72	0.30
	RASSI-SO/CASPT2/AVTZ	2	23.13	0.28
	RASSI-SO/CASPT2/AVQZ	4	34.72	0.11
	RASSI-SO/CASPT2/AV5Z	4	70.10	0.35
	MRCI/AVQZ	4	138.50	0.02
	MRCI/AVQZ	4	303.51	0.07
	MRCI/AVQZ	4	710.14	0.30
RuO	Spin-orbit calculations with pseudo-potentials basis set using Molpro Package			
	RASSI-SO/MCSCF/AVTZ	4	141.18	0.27
	RASSI-SO/MCSCF/AVQZ	4	218.25	0.97
	RASSI-SO/MCSCF/AV5Z	4	436.97	4.13
	RASSI-SO/CASPT2/AVTZ	4	4089.42	0.27
	RASSI-SO/CASPT2/AVQZ	4	7577.36	0.97
	RASSI-SO/CASPT2/AV5Z	4	17669.96	4.22
	RASSI-SO/MRCI/AVTZ	7	64946.81	0.41
	RASSI-SO/MRCI/AVQZ	4	365097.76	0.97
	Spin-orbit calculations with all electrons basis set using Molcas Package			
	RASSI-SO/CASPT2/AVTZ	1	2106.00	1.02
RuO_2	Spin-orbit calculations with pseudo-potentials basis set using Molpro Package			
	RASSI-SO/MCSCF/AVTZ	4	13453.78	0.60
	RASSI-SO/MCSCF/AVQZ	4	16131.84	4.07
	RASSI-SO/MCSCF/AV5Z		16935.29	21.48
	RASSI-SO/CASPT2/AVTZ	4	240535.16	0.60
	RASSI-SO/CASPT2/AVQZ	4	322885.01	4.07
	RASSI-SO/CASPT2/AV5Z	4	613102.22	21.63
	RASSI-SO/MRCI/AVTZ	4	25574.26	0.60

C.1   Research of RuO$_4$ dimer

Table C.1: Electronic energies (au) with average $<S^2>$ amount derived in TPSSh-5%HF//aVTZ theory for Ru$_2$O$_8$ complexes comparing with 2 tetraoxides energy, RuO$_6$ + O$_2$ equivalent properties, and 2 trioxides + O$_2$ derived energies

Species	Figure	Singlet state			Triplet State		
2(RuO$_4$)		E_{elec}	=	-791.2014808			
Ru$_2$O$_8$-A		E_{elec}	=	-791.202403	E_{elec}	=	-791.1380867
		$<S^2>$	=	0.00	$<S^2>$	=	2.01
Ru$_2$O$_8$-B					E_{elec}	=	-791.1233658
					$<S^2>$	=	2.01
Ru$_2$O$_8$-C		E_{elec}	=	-791.10878	E_{elec}	=	-791.105013
		$<S^2>$	=	0.57	$<S^2>$	=	2.03
Ru$_2$O$_8$-D					E_{elec}	=	-791.154524
					$<S^2>$	=	2.01
Ru$_2$O$_6$ +O$_2$ [a]		E_{elec}	=	-791.1541584	E_{elec}	=	-791.1251079
2(RuO$_3$) +O$_2$ [b]		E_{elec}	=	-791.0682732			

[a] O$_2$ multiplicity is triplet, only Ru$_2$O$_6$ multiplicity varying
[b] O$_2$ multiplicity is triplet and RuO$_3$ is singlet

C.2   Optimized RuO$_x$H$_y$ species

Table C.2:   RuO$_x$H$_y$ species nuclear and electronic energy (au) with average S^2 amount derived in TPSSh-5%HF theory (part 1)
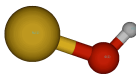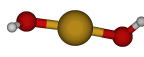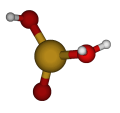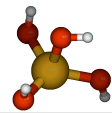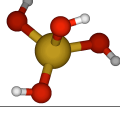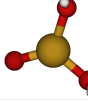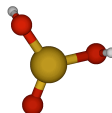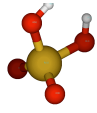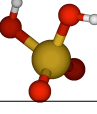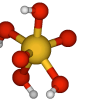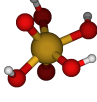
Species/level of theory	Figure	Data for initial Symmetry			Data with Loose Symmetry		
		Oxydation +I					
Ru(OH)		C$_s$			C$_s$		
TPSSh5%HF//AVQZ		E$_{nucl}$	=	43.47757479	identical		
		E$_{elec}$	=	-170.3619968			
		S^2	=	3.776			
		Oxydation +II					
Ru(OH)$_2$		C$_1$			C$_s$		
TPSSh5%HF//AVQZ		E$_{nucl}$	=	97.15211387	identical		
		E$_{elec}$	=	-246.2918027			
		S^2	=	0.768			
RuO(H$_2$O)		C$_1$			C$_1$		
TPSSh5%HF//AVQZ		E$_{nucl}$	=	94.34146153	identical		
		E$_{elec}$	=	-246.2542872			
		S^2	=	6.006			
		Oxydation +III					
Ru(OH)$_3$		C$_1$			not done		
TPSSh5%HF//AVQZ		E$_{nucl}$	=	171.2836206072	/		
		E$_{elec}$	=	-322.193820584	/		
		S^2	=	0.754	/		
RuO(OH)		C$_2$			C$_2$		
TPSSh5%HF//AVQZ		E$_{nucl}$	=	96.68950696	identical		
		E$_{elec}$	=	-245.6746396			
		S^2	=	6.005			
RuO(OH)(H$_2$O)		C$_1$			C$_1$		
TPSSh5%HF//AVQZ		E$_{nucl}$	=	170.9382999	identical		
		E$_{elec}$	=	-322.163328			
		S^2	=	0.785			
		Oxydation +IV					
Ru(OH)$_4$		C$_1$			C$_1$		
TPSSh5%HF//AVQZ		E$_{nucl}$	=	262.5982143	E$_{nucl}$	=	262.5894923662
		E$_{elec}$	=	-398.0840963	E$_{elec}$	=	-398.0840685
		S^2	=	0.000	S^2	=	0.000
Ru(OH)$_4$		C$_1$			C$_1$		
TPSSh5%HF//AVQZ		E$_{nucl}$	=	262.5947253	E$_{nucl}$	=	262.5893483
Conformer		E$_{elec}$	=	-398.0840952	E$_{elec}$	=	-398.0840685
H rotation		S^2	=	0.000	S^2	=	0.000
RuO(OH)$_2$		C$_s$			C$_s$		
TPSSh5%HF//AVQZ		E$_{nucl}$	=	166.7303463	identical		
		E$_{elec}$	=	-321.5907626			
		S^2	=	0.478			
RuO(OH)$_2$		C$_1$			C$_1$		
TPSSh5%HF//AVQZ		E$_{nucl}$	=	166.7282866	identical		
Conformer		E$_{elec}$	=	-321.5907909			
H rotation		S^2	=	0.547			

Table C.3: RuO$_x$H$_y$ species nuclear and electronic energy (au) with average $<S^2>$ amount derived in TPSSh-5%HF theory (part 2)

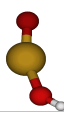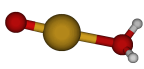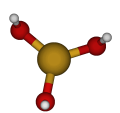| Species/level of theory	Figure	Data for initial Symmetry			Data with Loose Symmetry		
		Oxydation +IV					
RuO(OH)$_2$(H$_2$O)		C$_1$			C$_1$		
TPSSh5%HF//AVQZ		E$_{nucl}$	=	259.1269797	identical		
		E$_{elec}$	=	-398.0735814			
		$<S^2>$	=	0.000			
RuO$_2$(H$_2$O)		C$_s$			C$_s$		
TPSSh5%HF//AVQZ		E$_{nucl}$	=	165.7086340	identical		
		E$_{elec}$	=	-321.572011			
		$<S^2>$	=	0.000			
RuO$_2$(H$_2$O)$_2$		C$_1$			C$_1$		
TPSSh5%HF//AVQZ		E$_{nucl}$	=	254.5424080	identical		
		E$_{elec}$	=	-398.0541592			
		$<S^2>$	=	0.000			
RuO$_2$(H$_2$O)$_2$		C$_1$			C$_1$		
TPSSh5%HF//AVQZ		E$_{nucl}$	=	255.1815017	identical		
Conformer		E$_{elec}$	=	-398.0567598			
OH$_2$ trans-rotation		$<S^2>$	=	0.000			
		Oxydation +V					
RuO(OH)$_3$)		C$_1$			C$_1$		
TPSSh5%HF//AVQZ		E$_{nucl}$	=	253.1561409	identical		
		E$_{elec}$	=	-397.4732064			
		$<S^2>$	=	0.756			
RuO(OH)$_3$)		C$_1$			C$_1$		
TPSSh5%HF//AVQZ		E$_{nucl}$	=	254.3529109	identical		
Conformer		E$_{elec}$	=	-397.4808845			
H rotation		$<S^2>$	=	0.756			
RuO$_2$(OH)		C$_s$			C$_s$		
TPSSh5%HF//AVQZ		E$_{nucl}$	=	161.3430401	E$_{nucl}$	=	161.0736964
		E$_{elec}$	=	-320.9571773	E$_{elec}$	=	-320.977759
		$<S^2>$	=	0.754	$<S^2>$	=	0.754
RuO$_2$(OH)(H$_2$O)		C$_1$			C$_1$		
TPSSh5%HF//AVQZ		E$_{nucl}$	=	250.4539277	E$_{nucl}$	=	250.48826049
		E$_{elec}$	=	-397.4617118	E$_{elec}$	=	-397.4616898
		$<S^2>$	=	0.761	$<S^2>$	=	0.761
		Oxydation +VI					
RuO$_3$(H$_2$O)		C$_1$			C$_1$		
TPSSh5%HF//AVQZ		E$_{nucl}$	=	239.5739347	identical		
		E$_{elec}$	=	-396.8252953			
		$<S^2>$	=	0.133			
RuO$_3$(H$_2$O)		C$_1$			not done		
TPSSh5%HF//AVQZ		E$_{nucl}$	=	241.2616598	/		
Conformer		E$_{elec}$	=	-396.8285465	/		
OH$_2$ rotation		$<S^2>$	=	0.477	/		

Table C.4: RuO_xH_y species nuclear and electronic energy (au) with average $< S^2 >$ amount derived in TPSSh-5%HF theory (part 3)

Species/level of theory	Figure	Data for initial Symmetry			Data with Loose Symmetry
		Oxydation +VI			
$RuO_2(OH)_2$		C_{2v}			C_{2v}
TPSSh5%HF//AVQZ		E_{nucl}	=	247.7397996	identical
		E_{elec}	=	-396.8648915	
		$< S^2 >$	=	0.000	
$RuO_2(OH)_2$		C_2			C_2
TPSSh5%HF//AVQZ		E_{nucl}	=	247.2587411	identical
Conformer 1		E_{elec}	=	-396.862867	
2 H trans-rotation		$< S^2 >$	=	0.000	
$RuO_2(OH)_2$		C_s			C_s
TPSSh5%HF//AVQZ		E_{nucl}	=	248.2305717	identical
Conformer 2		E_{elec}	=	-396.869955	
1 H trans-rotation		$< S^2 >$	=	0.000	
		Oxydation +VII			
$RuO_3(OH)$		C_1			C_1
TPSSh5%HF//AVQZ		E_{nucl}	=	239.4746484	identical
		E_{elec}	=	-396.2330796	
		$< S^2 >$	=	0.756	
		Oxydation +VIII			
$RuO_2(OH)_4$		C_1			not done
TPSSh5%HF//AVQZ		E_{nucl}	=	461.7242439	/
		E_{elec}	=	-548.4979008	/
		$< S^2 >$	=	0.000	/
$RuO_2(OH)_4$		C_1			C_1
TPSSh5%HF//AVQZ		E_{nucl}	=	461.7294061	identical
Conformer		E_{elec}	=	-548.4979008	
H rotation		$< S^2 >$	=	0.000	
$RuO_3(OH)_2$		C_1			C_1
TPSSh5%HF//AVQZ		E_{nucl}	=	338.4413688	identical
Conformer		E_{elec}	=	-472.0232168	
H rotation		$< S^2 >$	=	0.000	

C.3 Standard entropies, heat capacities and Cp fit coefficients of Ru compounds

C.3.1 Ru oxides

Table C.5:   Standard molar entropies at 298 K ($S°(298\,\mathrm{K})$), heat capacities at constant pressure ($C_p(298\,K)$) in $\mathrm{J\,K^{-1}\,mol^{-1}}$ computed at the TPSSh-5%HF/aug-cc-pVTZ level of theory with unscaled vibrational frequencies, together with the heat capacity coefficients for the expansion $C_p(T) = a + b\,T + c\,T^2 + d\,T^{-2}$

Species	$S°(298\,\mathrm{K})$	$C_p(298\,K)$	T range (K)	a $\mathrm{J\,K^{-1}\,mol^{-1}}$	b $\mathrm{J\,K^{-2}\,mol^{-1}}$	c $\mathrm{J\,K^{-3}\,mol^{-1}}$	d $\mathrm{J\,K\,mol^{-1}}$
Ru	186.6	21.5	298-800	1.313×10^1	2.791×10^{-2}	-1.520×10^{-5}	1.264×10^5
$\sigma^1 = 1$			800-2000	3.495×10^1	-7.255×10^{-3}	1.103×10^{-6}	-2.509×10^6
RuO	242.3	31.2	298-800	2.792×10^1	1.778×10^{-2}	-9.639×10^{-6}	-1.022×10^5
$\sigma = 1$			800-2000	3.695×10^1	3.619×10^{-4}	-8.039×10^{-8}	-8.740×10^5
RuO$_2$	266.4	44.5	298-800	3.620×10^1	4.049×10^{-2}	-2.167×10^{-5}	-1.681×10^5
$\sigma = 2$			800-2000	5.693×10^1	9.904×10^{-4}	-2.202×10^{-7}	-1.993×10^6
RuO$_3$	291.0	60.8	298-800	4.988×10^1	6.142×10^{-2}	-3.295×10^{-5}	-3.985×10^5
$\sigma = 2$			800-2000	8.127×10^1	1.457×10^{-3}	-3.239×10^{-7}	-3.151×10^6
RuO$_4$	287.5	73.5	298-800	6.159×10^1	8.601×10^{-2}	-4.621×10^{-5}	-8.572×10^5
$\sigma = 2$			800-2000	1.055×10^1	2.002×10^{-3}	-4.446×10^{-7}	-4.694×10^6

C.3.2   Ru oxyhydroxides species

Table C.6:   Heat capacity coefficients for the expansion $C_p(T) = a + b\,T + c\,T^2 + d\,T^{-2}$ computed at the TPSSh-5%HF/aug-cc-pVQZ level of theory with unscaled vibrational frequencies for the ruthenium oxyhydroxides species

Species	T range (K)	a $J\,K^{-1}\,mol^{-1}$	b $J\,K^{-2}\,mol^{-1}$	c $J\,K^{-3}\,mol^{-1}$	d $J\,K\,mol^{-1}$
Ru(OH)	0-500	2.18×10^1	8.10×10^{-2}	-6.87×10^{-5}	4.15×10^4
	600-3000	4.37×10^1	7.78×10^{-3}	-1.21×10^{-6}	-4.98×10^5
Ru(OH)$_2$	0-500	3.39×10^1	1.82×10^{-1}	-1.66×10^{-4}	-2.86×10^3
	600-3000	7.97×10^1	1.48×10^{-2}	-2.25×10^{-6}	-7.57×10^5
Ru(OH)$_4$	0-500	3.14×10^1	2.43×10^{-1}	-1.93×10^{-4}	-6.17×10^4
	600-3000	1.15×10^2	1.06×10^{-2}	-1.76×10^{-6}	-3.75×10^6
RuO(H$_2$O)	0-500	4.67×10^1	1.08×10^{-1}	-8.65×10^{-5}	-7.23×10^4
	600-3000	7.47×10^1	1.85×10^{-2}	-2.96×10^{-6}	-1.12×10^6
RuO(OH)	0-500	2.67×10^1	1.35×10^{-1}	-1.13×10^{-4}	1.97×10^4
	600-3000	6.75×10^1	8.40×10^{-3}	-1.31×10^{-6}	-1.39×10^6
RuO(OH)(H$_2$O)	0-500	3.50×10^1	2.67×10^{-1}	-2.27×10^{-4}	-5.52×10^4
	600-3000	1.10×10^2	2.67×10^{-2}	-4.26×10^{-6}	-2.55×10^6
RuO(OH)$_2$	0-500	2.34×10^1	2.63×10^{-1}	-2.21×10^{-4}	1.11×10^4
	600-3000	1.02×10^2	1.67×10^{-2}	-2.65×10^{-6}	-2.64×10^6
RuO(OH)$_2$(H$_2$O)	0-500	2.84×10^1	3.96×10^{-1}	-3.30×10^{-4}	-6.36×10^4
	600-3000	1.44×10^2	3.60×10^{-2}	-5.81×10^{-6}	-4.19×10^6
RuO(OH)$_3$	0-500	2.02×10^1	3.73×10^{-1}	-3.05×10^{-4}	8.70×10^2
	600-3000	1.36×10^2	2.61×10^{-2}	-4.19×10^{-6}	-4.30×10^6
RuO$_2$(H$_2$O)	0-500	4.59×10^1	1.70×10^{-1}	-1.33×10^{-4}	-9.94×10^4
	600-3000	9.81×10^1	1.96×10^{-2}	-3.17×10^{-6}	-2.43×10^6
RuO$_2$(H$_2$O)$_2$	0-500	6.07×10^1	2.81×10^{-1}	-2.25×10^{-4}	-1.06×10^5
	600-3000	1.40×10^2	3.75×10^{-2}	-6.04×10^{-6}	-3.29×10^6
RuO$_2$(OH)	0-500	3.46×10^1	1.69×10^{-1}	-1.32×10^{-4}	-3.44×10^4
	600-3000	9.12×10^1	9.46×10^{-3}	-1.53×10^{-6}	-2.45×10^6
RuO$_2$(OH)(H$_2$O)	0-500	4.08×10^1	3.07×10^{-1}	-2.51×10^{-4}	-9.08×10^4
	600-3000	1.33×10^2	2.79×10^{-2}	-4.50×10^{-6}	-3.67×10^6
RuO$_2$(OH)$_2$ – C$_s$	0-500	2.22×10^1	3.09×10^{-1}	-2.45×10^{-4}	-2.31×10^4
	600-3000	1.24×10^2	1.90×10^{-2}	-3.11×10^{-6}	-4.38×10^6
RuO$_2$(OH)$_2$ – C$_{2v}$	0-500	2.68×10^1	3.00×10^{-1}	-2.40×10^{-4}	-5.23×10^4
	600-3000	1.25×10^2	1.90×10^{-2}	-3.12×10^{-6}	-4.18×10^6
RuO$_2$(OH)$_4$	0-500	6.43	6.18×10^{-1}	-5.27×10^{-4}	-4.42×10^4
	600-3000	1.94×10^2	3.53×10^{-2}	-5.69×10^{-6}	-6.75×10^6
RuO$_3$(H$_2$O)	0-500	5.31×10^1	2.21×10^{-1}	-1.76×10^{-4}	-1.21×10^5
	600-3000	1.23×10^2	2.00×10^{-2}	-3.27×10^{-6}	-3.16×10^6
RuO$_3$(OH)	0-500	3.14×10^1	2.43×10^{-1}	-1.93×10^{-4}	-6.17×10^4
	600-3000	1.15×10^2	1.06×10^{-2}	-1.76×10^{-6}	-3.75×10^6
RuO$_3$(OH)$_2$	0-500	1.93×10^1	4.13×10^{-1}	-3.50×10^{-4}	-4.44×10^4
	600-3000	1.50×10^2	1.86×10^{-2}	-3.03×10^{-6}	-4.98×10^6

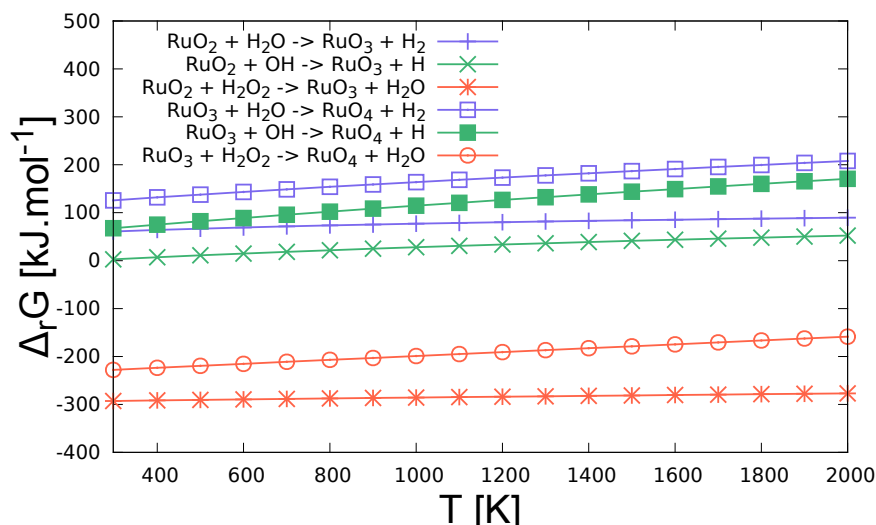## D.1 Gibbs free reaction energies

D.2 Reactivity and kinetic rates

Table D.1: Rate constants in cm^3 molecule^{-1} s^{-1}, calculated at the TPSSh-5%HF level of theory.

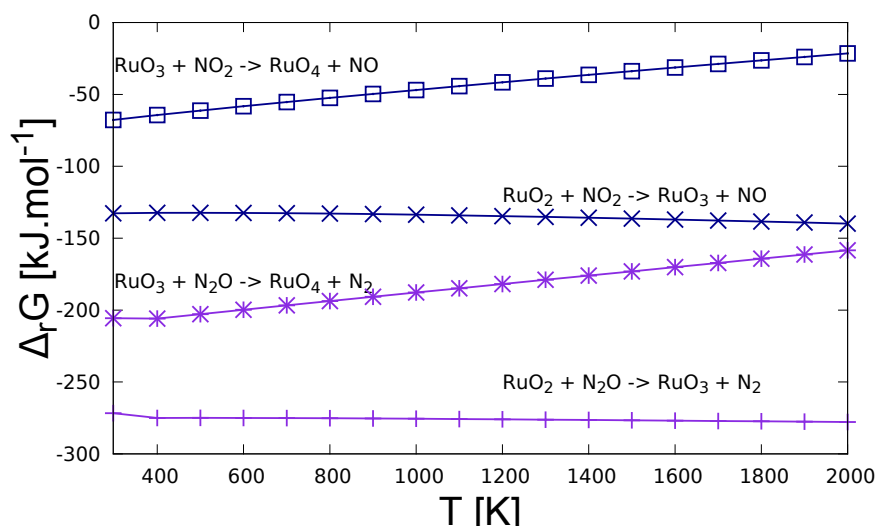| Reaction		Temperature (K)							
		250	300	400	600	800	1000	1300	1500
	TS-178i	6.55×10^{-41}	2.57×10^{-36}	1.67×10^{-30}	1.49×10^{-24}	1.76×10^{-21}	1.41×10^{-19}	9.29×10^{-18}	6.40×10^{-17}
$Ru_2O_6 + O_2 \longrightarrow 2\,RuO_4$	TS-150i	1.07×10^{-38}	1.36×10^{-34}	2.12×10^{-29}	4.49×10^{-24}	2.60×10^{-21}	1.35×10^{-19}	6.04×10^{-18}	3.50×10^{-17}
	TS-172i	3.48×10^{-33}	8.07×10^{-30}	1.52×10^{-25}	4.01×10^{-21}	8.27×10^{-19}	2.33×10^{-17}	5.92×10^{-16}	2.67×10^{-15}

Table D.2: Arrhenius parameters calculated over the temperature range 250–2500 K at the geometries at the TPSSh-5%HF level of theory.

Formation of RuO$_4$		B^a	n	E$_a^b$	$k(298K)$
	TS-178i	7.24×10^{-21}	2.62	126.1	1.73×10^{-36}
$Ru_2O_6 + O_2 \longrightarrow 2\,RuO_4$	TS-150i	1.02×10^{-21}	2.65	111.7	9.69×10^{-35}
	TS-172i	7.69×10^{-21}	2.74	90.5	9.34×10^{-30}

^{a} in cm^3 molecule^{-1} s^{-1}, ^{b} in kJ mol^{-1}
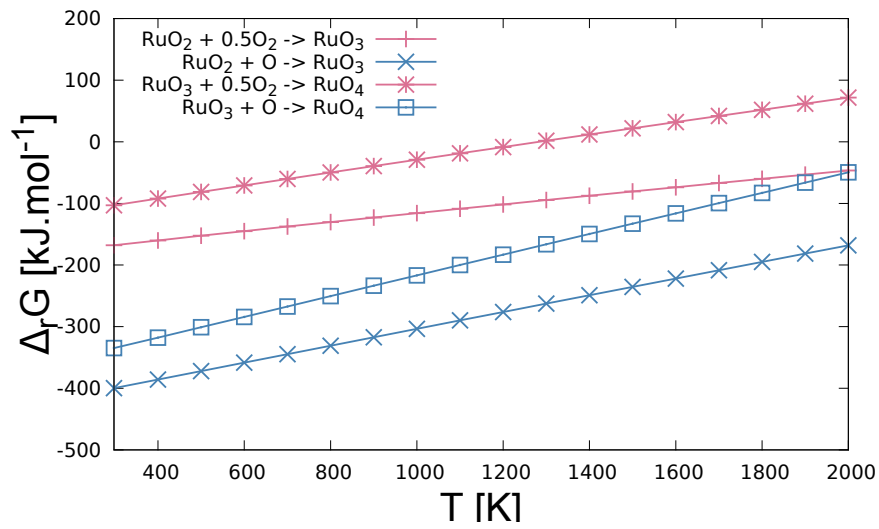
(a)
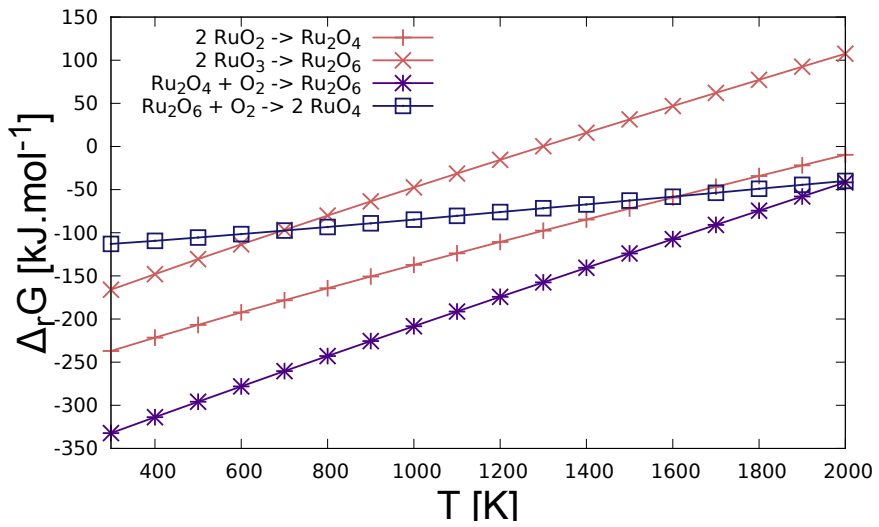

(b)

Figure D.1: (a) H_xO_y species reactions; (b) N_xO_y reactions.

Table D.3: Rate constants in cm^3 $molecule^{-1}$ s^{-1}, calculated at the TPSSh-5%HF level of theory.

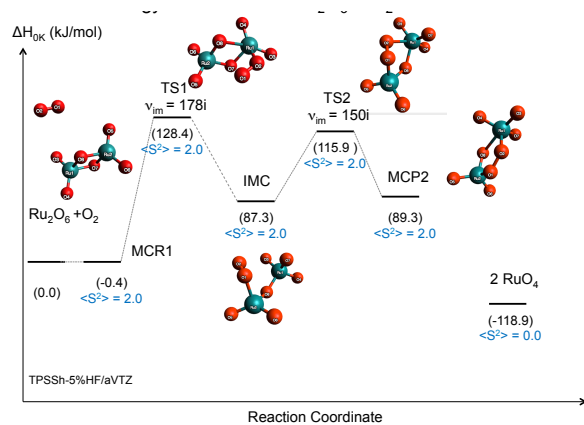| Reactions		Temperature (K)							
		250	300	400	600	800	1000	1300	1500
$RuO_3 + NO_2 \longrightarrow RuO_4 + NO$	TS1	1.10×10^{-18}	9.03×10^{-18}	1.49×10^{-16}	3.49×10^{-15}	2.19×10^{-14}	7.66×10^{-14}	2.88×10^{-13}	5.63×10^{-13}
	TS2	1.42×10^{-25}	6.93×10^{-24}	1.05×10^{-21}	2.25×10^{-19}	4.33×10^{-18}	3.00×10^{-17}	2.13×10^{-16}	5.54×10^{-16}

Figure D.2: (a) Ox reactions; (b) Dimers reactions

Figure D.3: Reaction profile at 0 K calculated at the TPSSh-5%HF/AVTZ level of theory for reaction $Ru_2O_6 + O_2 \longleftrightarrow 2\,RuO_4$ with schematic drawing of intermediate species involved.

Table D.4: Arrhenius parameters calculated over the temperature range 250–2500 K at the geometries at the CCSD(T)/aVQZ//TPSSh-5%HF level of theory.

Formation of RuO_4	B^a	n	E_a^b	$k(298K)$
$RuO_3 + NO_2 \longrightarrow RuO_4 + NO$ TS1	7.51×10^{-22}	3.01	19.3	8.67×10^{-18}
$RuO_3 + NO_2 \longrightarrow RuO_4 + NO$ TS2	1.72×10^{-24}	3.13	41.1	5.91×10^{-24}

^{a} in cm^3 molecule^{-1} s^{-1}, ^{b} in kJ mol^{-1}